Departamento de Física Teórica
Facultad de Ciencias
Universidad Autónoma de Madrid

European Southern Observatory
Adaptive Optics Department

Junio 2011

Extreme Adaptive Optics system optimization for High Contrast Imaging with the High Order Test bench

Memoria que presenta para optar al grado de Doctor en Ciencias Físicas:

Emmanuel Aller Carpentier

Dirigida por:

Dr. Markus Kasper

Investigador del Dpto. Óptica Adaptativa de la ESO.

Dirección académica:

Dr. Carlos Eiroa de San Francisco

Profesor Titular del Dpto. Física Teórica de la Universidad Autónoma de Madrid.

To my mom

Acknowledgements

First of all I would like to thank my thesis supervisor Carlos Eiroa and my supervisor at ESO Markus Kasper for their support and their guidance along these years. I would also like to acknowledge the Univesidad Autónoma de Madrid and the European Southern Observatory which offered me the opportunity to develop the work of this thesis. In particular thanks to all the members of the Adaptive Optics group, past and present. Without their help and answers to all my questions I would not have been able to improve my knowledge in Adaptive Optics and instrumentation. I would also like to thank Norbert for his confidence in me and Francoise for her support and patience regarding the finalization of my thesis.

I am grateful to the people involved in the HOT experiment: Elise and Christophe, who helped me during my very first steps; Patrice, for his companionship in the laboratory work; Enrico and Christian for their support in electronics. I also want to mention our Italian colleagues in *Arcetri*, namely Simone, Enrico, Alfio and Fernando: your collaboration and advices were essential for the success of the project. Moreover, I would like to thank Sebastien and Christophe for their precious help and teachings.

I would like to acknowledge my friend Jesús for his help with the administrative issues at the University in Madrid, and Johann, Richard and Antonio for their corrections to the manuscript. I am also very grateful for the financial assistance from the Spanish government international fellowship and the European Framework programs FP6 and FP7.

Finally, but not less important, I appreciate the support and encouragement from my family and my girlfriend. Thanks Elisabetta to be at my side ...

A todos, muchas gracias.

Contents

List of Figures

List of Tables

Abstract

Direct detection of extrasolar planets is one of the most exciting but also one of the most challenging aim of the next 20 years. High-contrast imagers dedicated to the search for extrasolar planets are currently being developed for present-day 8-10 meter telescopes (SPHERE, GPI ...) or in design phase for the next generation of Extremly Large Telescopes (EPICS).

Direct imaging of extrasolar planets requires contrast levels better than 10^{-6} at a few tenths of an arcsecond from the central star. Scattered light from optical aberrations introduced by atmospheric turbulence (seeing) and the diffraction pattern of the telescope apertures limit this contrast by masking the faint planet with light from the star. To achieve the required contrast it is necessary to implement eXtreme Adaptive Optics systems (XAO) in order to work on diffraction limit and coronagraphs to suppress the light coming from the star. Simulations predict good performances but XAO systems still need to be proven.

The High Order Testbench, currently installed at ESO laboratories in Munich, implements an experimental XAO system. This test bench is the first to incorporate simultaneously all the components of a real XAO system and simulating real telescope conditions using a turbulence generator with phase screens. The 32x32 actuator MEMS deformable mirror, two types of wave-front sensors (Shack-Hartmann and pyramid) using the essentially read-noise free EMCCD, and the ESO SPARTA real-time-computer (RTC) provide an ideal testbed to study XAO implementation.

The aim of this work is to study and characterized the different components of an XAO system confirming expected performance. In addition several experiments were carried out, including coronagraph characterization with real XAO conditions and high contrast techniques.

Resumen

La búsqueda directa de planetas extrasolares es uno de los desafíos más excitantes de los próximos 20 años. Instrumentación de alto contraste para la búsqueda de planetas extrasolares está siendo desarrollada para los actuales telescopios de 8-10 metros (SPHERE, GPI ...) o en fase de diseño para la próxima generación de telescopios de gran diámetro (EPICS).

La observación directa de planetas extrasolares requiere un contraste superior a 10^{-6} a pocas fracciones de segundo de arco de la estrella central. El contraste se ve limitado debido a la luz dispersada por las aberraciones ópticas introducidas por la turbulencia atmosférica (seeing) y debido a los efectos de difracción debidos a la abertura del telescopio. Para obtener el contraste exigido es necesario implementar sistemas de Óptica Adaptativa eXtrema (XAO) con la intención de trabajar en el régimen difractivo y coronógrafos para suprimir la luz de la estrella. Las simulaciones predicen un alto rendimiento pero los sistemas XAO tienen que ser todavía probados.

Los laboratorios de la ESO albergan un prototipo para la verificación de sistemas de Óptica Adaptativa Extrema, el "*High Order Test bench*" (HOT). Este banco de pruebas es el primero en incorporar simultáneamente todos los elementos de un sistema real XAO incluyendo generadores de turbulencia atmosférica que permiten el desarrollo y caracterización en condiciones normales de observación. En HOT se dispone de un espejo micro-deformable 32x32, el sistema de cálculo en tiempo real SPARTA y una cámara de alta sensibilidad S/N (E2V CCD 60) para estudiar la implementación de la Óptica Adaptativa Extrema.

El objetivo de este trabajo es estudiar y caracterizar los diversos componentes de un sistema XAO demostrando el rendimiento previsto. Además varios experimentos se han llevado a cabo incluyendo el estudio de coronógrafos con XAO y otras técnicas de alto contraste.

1

Introduction

Astronomical telescopes are devices which collect as much radiation from astronomical objects and put it in as sharp an image as possible. Both collecting area and angular resolution play an important role and will be determined by the telescope diameter. But, It has long been realized that the spatial resolution of images obtained with astronomical telescopes is limited by the effects of atmospheric turbulence. In fact, this was realized not long after the invention of the telescope, and Newton himself suggested that telescopes would provide clearer images if used at mountaintop observatories.

The atmosphere limitation comes from temperature variations of the air that produce two effects: air masses of various sizes to move with different velocities and in different directions (i.e. wind effect) and local fluctuations of the air refractive index along the propagation path through the atmosphere (since, refractive index is proportional to density, so, to temperature). Air density decay exponentially with height, being the ground layer the most turbulent.

Random distortions are induced on the phase of the incoming electric field and consequently on the amplitude after propagation, leading to a degraded image. The wavefront distortion spreads the energy received from a point source into a diffuse disk, considerably reducing its peak intensity and making is characteristics more difficult to measure.

At visible wavelengths, it is found that the resolution obtained with a telescope varies during the night, and typically corresponds to the diffraction limit of a telescope with diameter in the range 10-20cm. This means that modern giant, ground-based telescopes, which have a diameter of 8-10m, have the same resolution as small amateur telescopes.

In the 1950s, Horace Babcock [1] (and independently by Linnik) proposed that wavefront aberrations introduced by the atmosphere might be corrected in real time using an active optical element (such as a deformable mirror). The wave-front distortions would be measured by a wave-front sensor which delivers the signals necessary to drive the correcting element. Babcock ideas were not technically feasible in the 1950s. Theoretical work by David Fried and Darryl Greenwood provided the seminal papers with which to define the spatial and temporal requirements of such *Adaptive optics* system. It was on this period, 1970s and early 1980s, that adaptive optics systems were developed as a practical technology. The first operational astronomical AO system was built in France and successfully tested in October 1989 in Observatoire d'haute provence. It was later installed on the 3.6 m telescope at the European Souther Observatory. Since 1994, a growing number of observatories have been equipped with AO systems.

In the last decade astronomy discoveries benefits from the AO developments and now the different science fields impose specific requirements to the instruments driving the future technical developments. The new generation of AO systems are designed either to improve the on-axis performance of the correction (Extreme AO) or extend the size of the corrected Field of View (wide field AO like Multi Conjugate AO or Ground Layer AO). The improvement on performance will allow to achieve the spatial resolution

limit of the telescope aiming direct extrasolar planets imaging, while an increase of sensitivity over a wide field of view will be fundamental on extragalactic astronomy and the early universe study.

Direct imaging of extrasolar planets requires contrasts levels better than 10^{-6} a few tenths of an arcsecond from the central star. Scattered light from optical aberrations introduced by atmospheric turbulence (seeing) and the diffraction pattern of the telescopes aperture limit this contrast by masking the faint planet with light from the star. To achieve the contrast required it is necessary to implement eXtreme Adaptive Optics systems (XAO) in order to work on diffraction limit and coronagraphs to suppress the light coming from the star.

Simulations predict good performances but XAO systems still need to be proven. It is why laboratory experiments are required in order to check the performance predicted, study new technologies and possible limitations which could reduce XAO correction. Shack-Hartmann and Pyramid wavefront sensors appear to be suitable to deliver the correction expected from XAO systems but still need to be characterized under realistic conditions.

The High Order Testbench, currently installed at ESO laboratories in Munich, implements an experimental XAO system. This test bench is the first to incorporate simultaneously all the components of a real XAO system and simulating real telescope conditions using a turbulence generator with phase screens. The 32x32 actuator MEMS deformable mirror, two types of wave-front sensors (Shack-Hartmann and pyramid) using the essentially read-noise free EMCCD, and the ESO SPARTA real-time-computer (RTC) provide an ideal testbed to study XAO implementation.

The aim of this work is to study an characterized the different components of a XAO system (chapter 3 - 4) proving the performance predicted (chapter 5). In addition several experiments were carried out, including coronagraph characterization for real XAO conditions, high contrast techniques and impact study of a primary segmented mirror on the AO performance (chapter 6).

1.1 Science motivation

The development of AO over the last years has increased the capacity of ground-base observations and opened to the astronomers a world of possibilities, that in other case, it would be only possible with space telescopes. AO will be a fundamental part of next generation of extremely large telescopes (30 - 50 m) ([2],[3],[4]) aiming a real advantage of the diameter increase. The new generation of imagers and spectrographs instruments ([5],[6],[7]) will take advantage of the increased angular resolution an image contrast to expand our knowledge in many scientific areas. Some general areas of interest are summarized in this section.

Galaxy Assembly and Star Formation History. At redshifts z > 1, galaxies have shrunk to angular sizes of approximately 1 arc sec, so that seeing based observations are not useful at uncovering morphologies and internal kinematics. At the epoch of greatest star formation and AGN activity around z $\tilde{2}$.5, traditional optical lines of Hα OIII and OII are nicely shifted into the K, H and J bands respectively. Integral field spectrographs such as SINFONI at the VLT and OSIRIS at Keck are now starting to dissect some of the brightest galaxies at this epoch using the increased sky coverage provided by laser guide stars. With the sensitivity gain and increased sky coverage new science topics can be addressed. These include the relationship between AGN and their host galaxies: radio galaxies and quasars have very strong emission lines and complex kinematics. In ”normal” galaxies, the redshift range from 1.5 to 2.5 is the key era for the birth of their first stars and the formation of the major architectural components of the galaxy, the bulge and disk. Measuring the morphology of star formation, the kinematics of proto-disks, the internal velocity dispersions and metallicity gradients (e.g. from the NII/Hα ratio) will allow us to witness the birth of galaxies like the Milky Way.

VLT next generation of imagers and spectrographs (Hawk-I and MUSE) would benefit from the increase of corrected field of view provided by GLAO systems (GRAAL and GALACSI, respectively). This is an astounding advance to complete deep spectroscopic surveys of the distant universe giving the possibility of simultaneously observing many targets within a several square arc minute field. Moreover, the improvement of signal to noise ratio will increase the achieved depth. As example, GRAAL will increase the capacity of Hawk-I by 0.5 mag for a fixed exposure time.

Nearby Active Galactic Nuclei. It has become increasingly clear that black holes play a key role in galaxy formation and evolution. The most important evidence for a close connection between black hole growth and galaxy evolution comes from the observed correlations between black hole mass and the bulge velocity dispersion of the host, galaxy and from the correlation between black hole mass and bulge mass. Simulations and theory have highlighted the importance of feedback from active galactic nuclei (AGNs), in the form of winds or outflows which can serve to shut off AGN fueling and potentially expel a significant fraction of the host galaxy's gas into the intergalactic medium following a major merger. AGN feedback is frequently invoked as a mechanism to limit black hole growth and to shut off star formation in early-type galaxies, but observational evidence for this scenario remains sketchy.

Key observational goals in this field include the accurate determination of the demographics of black holes in nearby galaxies over the widest possible range in black hole mass, investigations of the redshift evolution, and studies of the host galaxies of AGNs out to high redshifts to determine bulge luminosities, stellar populations, and emission-line kinematics. AO observations will be crucial in addressing these issues over the next decade. in the near-IR, LGS AO improved PSF quality and stability will significantly reduce the measurement uncertainty in black hole masses. On the other hand, AO capability in the I band will open up the possibility of using the Ca II triplet lines, giving a PSF core that is narrower than in the near-IR, and which will extend the distance out to which the most massive black holes can be detected.

Precision Astrometry in the Galactic Center. The proximity of our Galaxy's center presents a unique opportunity to study a massive black hole and its environs. In the last decade, near-IR astrometric observations have enabled the measurement of orbital motions for several stars near the Galactic Center. Due to the crowded stellar environment at the Galactic Center and the strong line-of-sight optical absorption, tracking the stellar orbits requires the high angular resolution in near-IR provided by AO. An improvement on the astrometric and radial velocity precision would show deviations on the orbits stars from pure Keplerian motion offering a unique opportunity to test General Relativity in the strong gravity regime.

AO improvements to measurements at the Galactic Center could be summarize as:

- Higher Strehl at K-band will reduce confusion, improving both photometric and astrometric accuracy because the previously undetected faint star population will cause less of a bias in the positions and magnitudes of brighter stars.

- Higher Strehl at K-band will allow the detection of new stars, some of which may pass close enough to the black hole to contribute to the obtainable accuracy and precision of General Relativistic effects.

- Use of multiple laser guide stars will decrease the field dependence of the PSF, thereby increasing both photometric and astrometric accuracy.

- The accuracy of current radial-velocity measurements is limited by signal to noise. Higher Strehl and lower sky background will materially improve the radial-velocity contribution to orbit determinations.

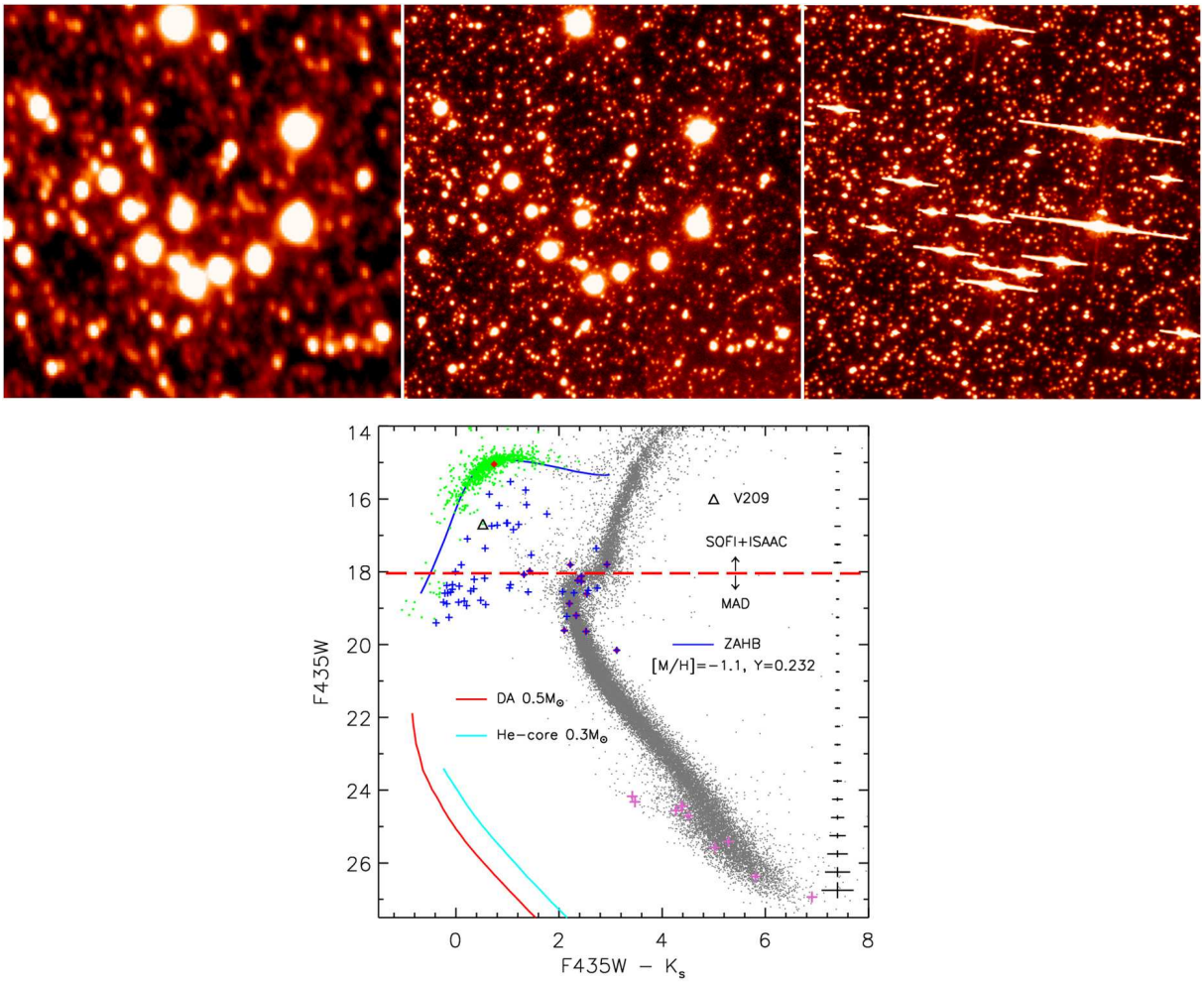

Figure 1.1: **Top:** 20 x 20 arcseconds region nearby the centre of the globular cluster Omega Centauri. The image on the left was obtained in K-band by ISAAC and has an average FWHM of 0.6 arcseconds. The center-hand image was obtained at the same wavelength by MAD with MCAO correction. In the latter case the FWHM is often below 0.1 arcsecond, a remarkable value taking into account that the closest guide star is ∼ 1 arcmin away. The angular resolution improvement is dramatic and allows very close and faint stars to be distinguished. The limiting magnitude in K is ∼ 20.5. On the right ,Same field of view observed by HST, in this case the FWHM is also around 0.1 arcsecond. **Bottom:** HR diagram of ω Cen based on MAD data. The red line split the objects only observed by non AO instrument (ISAAC, SOFI) and the new objects found by MAD. MS stars with mass values $M \approx 0.3 M_{\odot}$ ($Ks \approx 21$) were observed.

Globular clusters. It has been clear for more than a decade that globular clusters do not consist merely of passively evolving old stars. The complexity of their stellar populations, kinematics, and chemical abundances has shown that globular clusters can yield clues to the merger and star formation history of galaxies, and in turn that they suffer tidal disruption from the galaxies around which they live. For the decade or more to come, key questions will involve the relation of globular cluster evolution to galaxy formation, understanding the relative ages of globular clusters, tracking their formation environment, and understanding if clusters and their galaxies are connected by a common star formation and chemical enrichment history.

Image compensation achieved uniformly over large fields by MCAO and GLAO will allow to ascertain cluster membership and to infer their kinematical and dynamical properties.

Substellar-mass objects. High-contrast near-IR imaging will enable direct imaging surveys for Jovian-mass planets around nearby young low-mass stars and brown dwarfs. Both the Gemini Observatory and ESO are developing highly specialized planet-finding AO systems with extremely high contrast for direct imaging of young planets. The specific science cases for these XAO instruments will be discussed on section 1.3.2. Even if extreme AO systems are very powerful, their design restricts them to searches around bright, solar-type stars (e.g. I < 9 mag). Fainter substellar objects could be also study by other AO systems. By number, low-mass stars (M $\leq$ 0.5 M_{Sun}) and brown dwarfs dominate any volume-limited sample, and thus these objects may represent the most common hosts of planetary systems. Such cool, optically faint targets will be unobservable with specialized extreme AO systems because their parent stars are not bright enough to provide a high order wavefront reference. But thousands of cool stars in the solar neighborhood can be targeted by LGS-AO systems. the same problem is found for the very youngest stars in star-forming regions such as Taurus or Ophiuchus, generally too faint for extreme AO systems.

In the context of the formation of planetary systems and additional science case is suitable for spectroscopic measurements supported by AO. We know that a sizable fraction of nearby stars are surrounded by dust disks or debris disks. While these disks clearly contain lots of dust, it is yet unknown if circumstellar disks harbor also significant amounts of gas. High resolution integral field spectroscopy at optical wavebands would be a powerful way to study the gas content in circumstellar disks. The 5% SR correction offered by GALACSI, the GLAO module of MUSE, will allow to study these disks of several arcsec size at distances of a few tens of pc.

Multiplicity of Minor Planets in our Solar System. While space missions largely drove early progress in planetary astronomy, we are now in an era where ground-based telescopes can efficiently perform the regular observations needed for monitoring planetary atmospheres and geology, and can quickly respond to transient events. Improved angular resolution and corrected field of view will enable detailed images to be obtained of planets, asteroids, comets, and satellites. Example of the improvement on planetary ground-based observations are Jupiter images either obtained by multiconjugated AO demonstrator (MAD) at the VLT or by the AO Keck module.

1.2 Adaptive optics overview

AO Concept

All adaptive optics systems generally use the principle of phase conjugation. An optical beam is made up of both an amplitude A and a phase ϕ component and is described mathematically by the electric field $Ae^{-i\phi}$. Adaptive optics reverses the phase to provide compensation for the phase distortion. The reversal of the phase, being in the exponent of the electric field vector, means changing the sign of the

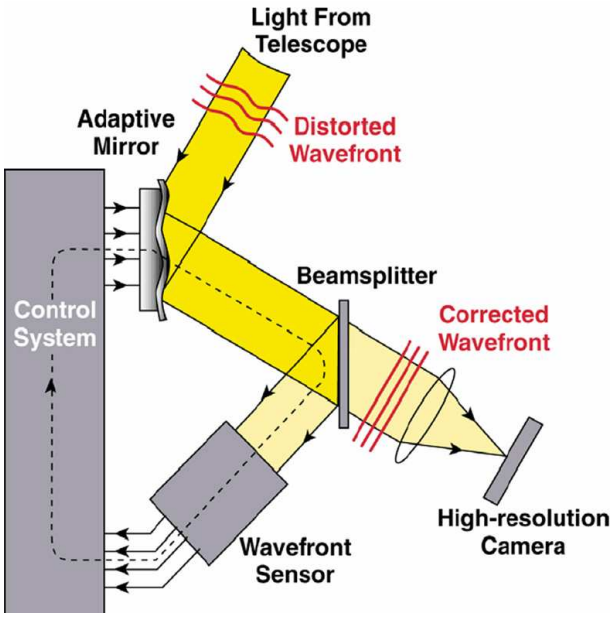

Figure 1.2: Schematic diagram of a typical astronomical adaptive optics system.

term behind the imaginary number. This mathematical conjugation corresponds to phase conjugation of the optical field.

An AO system basically consists of three main components: a wave-front corrector, a wave-front sensor and a control system. Figure 1.2 outlines the basic astronomical AO system. Lightwaves from a distant reference source, initially undistorted, pass through the turbulent atmosphere and are collected by the telescope. The distorted optical beam passes through the wavefront corrector, usually a deformable mirror, with the capacity of modify its shape, thereby, introducing compensating optical paths to cancel the phase errors. Then a beam splitter diverts part of the light toward the scientific camera and part toward the wave-front sensor to estimate the residual wave-front distortions. The control system uses the indirect wave-front sensor measurements to compute the electrical signals that are fed back to the deformable mirror, thus closing the control loop. This loop process must be executed faster than the rate of change of the atmosphere, typically between 100 and 1000 Hz.

Several books have been written during the 1990s on the fundamentals of astronomical AO ([8], [9], [10], [11]). In addition, several updated review papers show the improvement of the last decade ([12],[13],[14],[15]).

Atmospheric turbulence characterization: The Fried parameter

Non stationary random functions as atmospheric turbulence could be described statistically using the so-called structure functions (Tatarski, 1961) used by Kolmogorov to implement a model of the turbulence:

$$D_\phi = \left\langle \left| \phi(\mathbf{r}' + \mathbf{r}) - \phi(\mathbf{r}') \right|^2 \right\rangle = 6.88 \left(\frac{|\mathbf{r}|}{r_0} \right)^{5/3} \tag{1.1}$$

where $\mathbf{r}, \mathbf{r}'$ are lateral displacement vectors, $\phi(\mathbf{r})$ is the wavefront phase, $\langle ... \rangle$ denotes the ensemble average and r_0 is the Fried parameter.

The aberration effect of the turbulent atmosphere on wavefronts passing through it is described easily using this last Fried parameter. It is defined as the area over which the root-mean-square (rms) wavefront aberrations is 1 radian. A telescope of diameter less than r_0 will be diffraction-limited when observing

through the turbulence, while a telescope of diameter larger than r_0 will be seeing-limited. Using the Kolmogorov model for the refractive index fluctuations in the atmosphere the Fried parameter is given by the expression:

$$r_0 = \left[0.423k^2(cos\gamma)^{-1} \int C_n^2(h)dh\right]^{-\frac{3}{5}} \tag{1.2}$$

where $k = 2\pi/\lambda$ is the wavenumber, γ is the angle of observation measured from the zenith. C_N^2 is the refractive index structure function dependent of altitude h. The integral of C_N^2 along the line of sight gives the integrated strength of turbulence. One of the consequences of 1.2 is that r_0 is proportional to the six-fifths power of the wavelength, $r_0 \propto \lambda^{6/5}$. The typical value of r_0 in the visible is between 10 and 20 cm, this corresponds to values in the range 50-100 cm in the K band (for excellent observing site). The full-width at half-maximum of a seeing-limited image could be define from r_0 as:

$$FWHM_{seeing} \cong 0.97\lambda/r_0 \tag{1.3}$$

which implies that the FWHM depends on wavelength as $\lambda^{-1/5}$.

Using equation 1.1 Noll (1976) calculated the spatial power spectrum of phase fluctuations due to Kolmogorov turbulence:

$$\Phi(\mathbf{k}) = \frac{0.0023}{r_0^{5/3}} |\mathbf{k}|^{-11/3} \tag{1.4}$$

where $\mathbf{k}$ is a two-dimensional spatial frequency vector. The infinite amount of energy in this spectrum du to the divergence at the origin is not physical. In reality, low order frequencies are truncated by the *outer scale* of turbulence (defined as the scale of the largest turbulent structures), as modeled by the more realistic von Karman spectrum.

Atmospheric turbulence is a dynamic process where the wavefront aberrations are constantly changing. A characteristic timescale may be defined as the time over which the rms in wavefront error is less than $1rad^2$. If the turbulence were concentrated in a single layer of r_0 , moving with a horizontal speed of v m/s then the characteristic time, τ_0, is given by:

$$\tau_0 = 0.314r_0/v \tag{1.5}$$

A layer with r_0 =10cm at 0.5 μm moving at a speed of 10m/s will give $\tau_0 = 3.1ms$, the corresponding value at K band will be 19 ms.

AO limitations

The high frequency required imposes to the WFS a temporal sampling of the order of milliseconds. Which such small integration time an additional problems appears: the leak of photons. Most of all WFS concepts measures the local wavefront splitting the pupil in several elements (subpupils). The degree of correction depends on the number of subpupils, thus, a higher correction would imply few photons per subpupil. Because the science target is often too faint to be used as a reference star a nearby brighter guide star can be used instead. Since the atmospheric turbulence evolves spatially on rather small scales this guide star must be located close to the astronomical object in order to avoid the isoplanatic effect: as the wave coming from the two objects does not cross the same part of the atmosphere (i.e. the same turbulence),the aberrations are different in the two directions, while the correction is optimized only for one (figure 1.3). The angular size of the patch over which the wavefront is fairly uniform is called isoplanatic angle. For a single layer with a given value of r_0 at a height h and zenith angle γ, the isoplanatic angle is given by:

$$\theta_0 = 0.314r_0cos(\gamma)/h \tag{1.6}$$

corresponding to a mean square difference in the wavefront errors equal to 1 rad^2. Typically, for infrared observations the guide star must lie within about 30 arcseconds of the astronomical target, while for visible-light observations the guide star must be within about 10 arcseconds. These limitations are quite severe, and mean that the fraction of objects in the sky that are favored with a suitable guide star is a few percent or less.

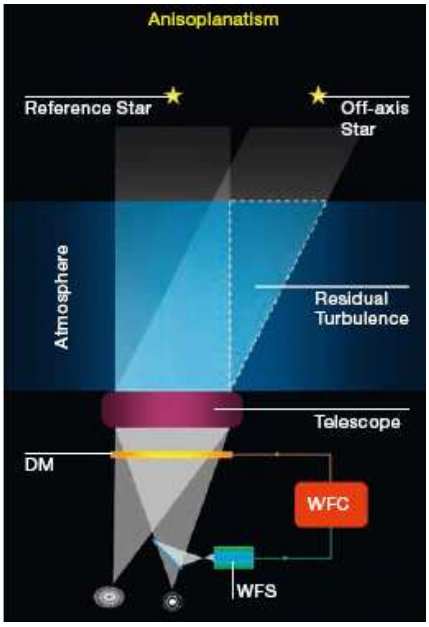

Figure 1.3: Graphical representation of the atmospheric anisoplanatism effect for a classical Adaptive Optics system. The stars not in the direction of the correction see a different portion of the atmosphere, which is partially corrected.

Laser guide stars

The idea of using a laser to generate an artificial guide star was first proposed in the astronomical literature by Foy and Labeyrie in 1985 although the principle had already been tested on a military system. The advantage of using a laser guide star (LGS) is that it allows a bright reference source for the AO wavefront sensor to be placed anywhere in the sky. Laser guide stars can be generated using either Rayleigh scattering off air molecules or resonant scattering from sodium atoms which make up a sodium layer at an average altitude of 90 km. Rayleigh guide stars, which can be generated at altitudes up to about 30km, are not suitable for large telescopes, and most development work is now concentrated on sodium guide stars. Some fundamental limitations of LGS are:

- An LGs cannot be used to measure tip and tilt of the wavefront. This is because the guide star position is affected by the tip-tilt on the up path, or jitter in the projected laser beam. An NGS with reduced demands on its brightness and distance to the object is still required for this purpose.
- Since the laser guide star is formed at a finite distance above the telescope, the light from the LGS traverses a conical volume defined by the telescope pupil and the LGS altitude, while light from astronomical objects traverses a cylinder in the turbulent atmosphere. The resulting difference between the wavefront aberration induced on a natural star and that measured by the laser guide star is referred to as the ”cone effect”, or ”focal anisoplanatism”.
- The laser guide star is seen to be elongated if observed with an aperture that is not coincident with the laser launch telescope producing elongated spots on the WFS. The centroiding sensitivity of

the WFS depends on the spot size, and so the sensitivity is reduced by spot elongation. This effect is more severe for larger apertures.

- Variations in the height of the sodium layer can occur over short timescales and this will introduce focus errors forcing the use of a natural guided star to estimate the focus. In addition, variations in the concentration of sodium ions cause variations in the intensity of the photon return from the sodium layer.

System performance estimation

In adaptive optics systems it is customary to use the wavefront variance residual error or the Strehl ratio as a measure of the image quality. The main error sources that limited the AO performance are:

- Noise in the wavefront sensor measurement: photon noise, readout noise and background noise.
- Imperfect wavefront correction due to the finite number of actuators. Because a deformable mirror cannot exactly match the shape of Kolmogorov turbulence a fitting error results.
- Bandwidth error due to the finite time required to measure and correct the wavefront error.
- Isoplanatic error.

Other errors include errors in the telescope optics which are not corrected by the AO system (e.g. high frequency vibrations, high spatial frequency errors), residual calibration errors and non-common path errors. The latter are wavefront errors introduced in the corrected beam after light has been extracted to the wavefront sensor. Since the wavefront sensor does not sense these errors they will not be corrected. Since the non-common path errors are usually static, they can be measured off-line and taken into account in the wavefront correction.

Assuming that these errors are uncorrelated and are essentially Gaussians random variables. Their variances can be addend to determine the global system error:

$$\sigma^2_{system} = \sigma^2_{WFS\,noise} + \sigma^2_{fitting} + \sigma^2_{temporal} + \sigma^2_{isoplanatic} \tag{1.7}$$

With σ^2 in units of square radians.

The performance of an adaptive optics system is usually characterized by the Strehl Ratio (SR), which is defined as the ratio of the peak image intensity to the peak intensity of a diffraction-limited image. The SR is related to the residual wavefront phase variance, σ^2, by:

$$SR = e^{-\sigma^2} \tag{1.8}$$

A typical design goal for a high-performance AO system (non XAO system) on an 8-10m telescope would be to obtain SR=0.8 when observing in the K band. In astronomy is common to describe images by the FWHM. If the SR is high then the fwhm should approximate to the theoretical value for a diffraction-limited image. For moderate values of SR (> 0.1) there is a fairly monotonic relation between SR and FWHM, while a low value of SR may correspond to a wide range of FWHM.

The Strehl ratio is not a unique descriptor of AO performance since the corrected point spread function has a complicated core-halo structure. The corrected wavefront produces a coherent diffraction-limited core, while the residual uncorrected wavefront gives rise to a halo of size somewhat less than the long-exposure image size. For planet finder instruments this residual halo limits the detectability of the planet, even for high SR. In this case the contrast level between core and halo gives a better estimation of the performance.

1.2.1 Wavefront sensing

The purpose of the wavefront sensor in an adaptive optics system is to measure the wavefront with the required spatial and temporal sampling [16]. Direct sensing of a wave-front is not possible at optical frequencies, because the wavefront phase does not interact with matter in any measurable way, instead, the wavefront must be deduced from intensity measurements at one or more planes.

Optical instruments for laboratory measurements employs a direct approach where there is an explicit determination of the phase or OPD (*optical path difference*) of the wave using interferometry with narrow-band lasers. Because of the need to use broadband, direct measurements of optical phase are not feasible in astronomical AO. Instead, an indirect approach is used where the information related to the phase is translated into signals that are used to compensate for the wavefront.

Wavefront sensors can be divided into pupil plane and image plane sensors depending on where the intensity is measured by the detector. Pupil plane methods split the pupil up into subapertures in some way, then use intensity in each subaperture to deduce either the first of the second derivatives of the wavefront phase. On this group are included the most common AO sensors: Shack-Hartmann, pyramid and curvature. For the focal plane methods, wavefront properties are deduced from whole aperture intensity measurements made at or near the focal plane Image plane. Phase diversity and speckle nulling are examples of this methods.

Shack-Hartmann sensor

The Hartmann method (1900) is a way of testing a lens or mirror that employs an opaque mask with holes placed behind the optical element under test. Each of the holes acts as an aperture, and since the light passing through the lens is converging, the image produced is an array of spots. The position of the spots is a direct indication of the local wavefront tilt at each hole. Shack improved the concept including lenses on the hole to focus the spot and optimize the light.

The Shack-Hartmann sensor is shown in figure 1.4. The SHS divided the wavefront on the pupil plane into subapertures using an array of lenses (i.e. lenslet array). Each of the beams in the subapertures is focused onto a detector placed on the focal plane. if the WF is plane, the spots are focused on the optical axes of its corresponding lenslet. On other hand, if the WF is disturbed, each lenslet receives locally a tilted WF that produces and angular displacement α of the spot respect to the centered reference position.

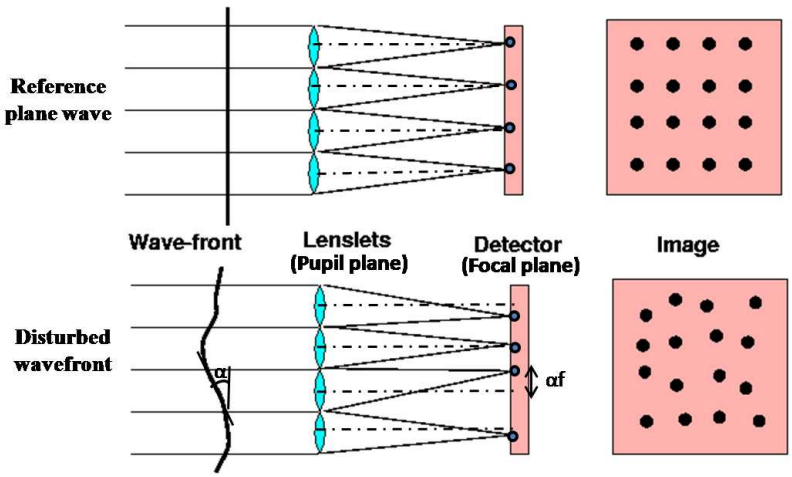

Figure 1.4: Principle of the Shack-Hartmann wavefront sensor. **Top:** plane wave. **Bottom:** disturbed.

The angular displacement gives an slope estimation for the average wavefront on each subapertures by measuring the displacement of the spot in both x and y directions. It could be defined as:

$$\alpha_x = \frac{c_x}{fM} = \frac{\lambda}{2\pi A_{sa}} \int_{sa} \frac{\partial \phi}{\partial x} dxdy \tag{1.9}$$

where c_x is the spot displacement (i.e. centroid), f the lenslet focal length, M the magnification between the lenslet plane and the telescope entrance plane and A_{sa} the subaperture area. The same equation can be write for the y-axis. Several methods are used to determine the spot position. A simple estimation is the center of gravity position (c_x, c_y):

$$c_x = \frac{\sum_{i,j} x_{i,j} I_{i,j}}{\sum_{i,j} I_{i,j}} \quad c_y = \frac{\sum_{i,j} y_{i,j} I_{i,j}}{\sum_{i,j} I_{i,j}} \tag{1.10}$$

where $I_{i,j}$ and $(x_{i,j}, y_{i,j})$ are the signal and the position coordinates of the detector pixel (i, j).

The spot width on the detector is compute from the subaperture diffraction equation:

$$\Delta x = \frac{2\lambda f}{d} \tag{1.11}$$

A displacement of the spot radius corresponds to a wavefront tilt of one wavelength over the subaperture (phase shift of one λ). (figure 1.5).

When designing a WFS it is important to enlarge as much as possible the dynamical range (i.e. turbulence strength that could be sensed) over which the sensor is linear. Several factors constrain it as maximum number of pixels available, photon noise, computation complexity, etc. So, a compromise is always necessary taking into account the wavefront sensing requirements.

The smallest detector size per subaperture is a 2x2 array, called a quad-cell. For this sensor the effect of the read noise is minimized but on other hand it has a limited dynamical range and a non linear response.

For this case the angular displacement of the spot can be simplified by:

$$\alpha_x = \frac{\theta_*}{2} \frac{I_1 + I_2 - I_3 - I_4}{I_1 + I_2 + I_3 + I_4} \tag{1.12}$$

where θ_* is the angular spot size in radians (i.e. equal to λ/d in the diffraction-limited case or λ/r_0 in the seeing limited case). In terms of the tilt angle, the linear range of each subaperture is limited by:

$$\alpha = \pm \frac{\lambda}{2d} \quad \text{rad} \tag{1.13}$$

Equation 1.12 and 1.13 show that the sensor signal does not depend on the focal length. Thus, the quadcell lacks of flexibility with a range of tilt over the subaperture restricted to about ± 0.5 waves. Moreover, the gain (i.e. the response versus the measured wavefront deformation) for the quadcell is fixed by the spot size of the spot. A way to improve the dynamic range is to use more detector pixels for each subaperture. In this case the dynamical range and linearity of the tilt measurement is determined by the geometry of the detector (focal length, ratio of pixel size to spot width and number of pixels). As example, small pixels compare to the spot width gives good linearity but, small dynamical range, while a bigger pixel increase the dynamical range but suffers from linearity problems.

A 4x4 array has greater flexibility and provides a good compromise between performance and complexity. As the response are identical in the x and y directions, the pixels are summed across the array in the direction orthogonal to the scan to obtain the ”four-bin” elements a_1 through a_4 for each axis. Thus, the basic center of gravity algorithm has the form:

$$c = \frac{w_1 a_1 + w_2 a_2 + w_3 a_3 + w_4 a_4}{a_1 + a_2 + a_3 + a_4} \tag{1.14}$$

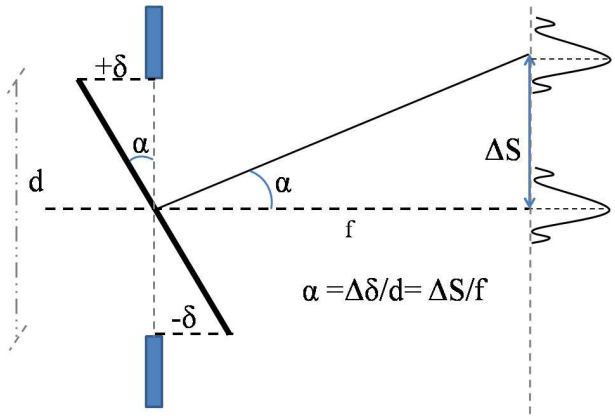

Figure 1.5: Principle of wavefront tilt sensing over a subaperture. A displacement of the radius spot ($\Delta S = \frac{2\lambda f}{d}$) corresponds to a wavefront tilt ($\Delta\delta$) of one wavelength over the subaperture.

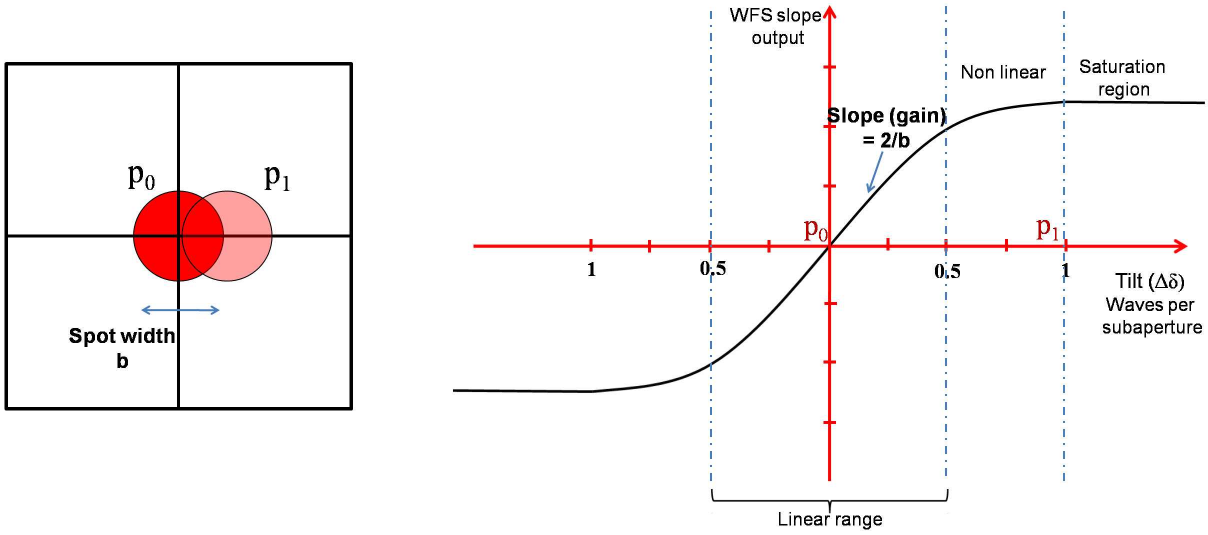

Figure 1.6: Transfer function of a Shack-Hartmann sensor using a quadcell. One wave of subaperture tilt displaces the central core of the spot entirely into one cell for the detector array (left). For higher tilt wavefront errors the sensor will saturate, although the linear range is restricted only to about ± 0.5 waves. The gain of the system is obtained from the curve slope of the linear range, for the quadcell case is fixed by the spot size

.

where $w_1 ... w_4$ are the pixel position (-1.5,-1,+1,+1.5). A 4x4 cell SHS could be used as a quadcell changing the w values to (-1,-1,+1,+1).

Pyramid sensor

The pyramid wavefront sensor was recently introduced by Ragazzoni in 1996 [17]. It is based on the same principle as the Foucault knife-edge test used for optical lens testing. The principle of operation is shown in figure 1.7. The wavefront coming from the telescope is focused into the focal plane, where a four face pyramidal prism is placed with its vertex at the focal point.

The four faces of the pyramid deflect the light in slightly different directions. A lens relay placed after the pyramid is used to produce four images of the exit pupil on a CCD detector allowing the adjustment of the scaling (number of pixels across the pupils). The vertex angle of the pyramid must be slightly less

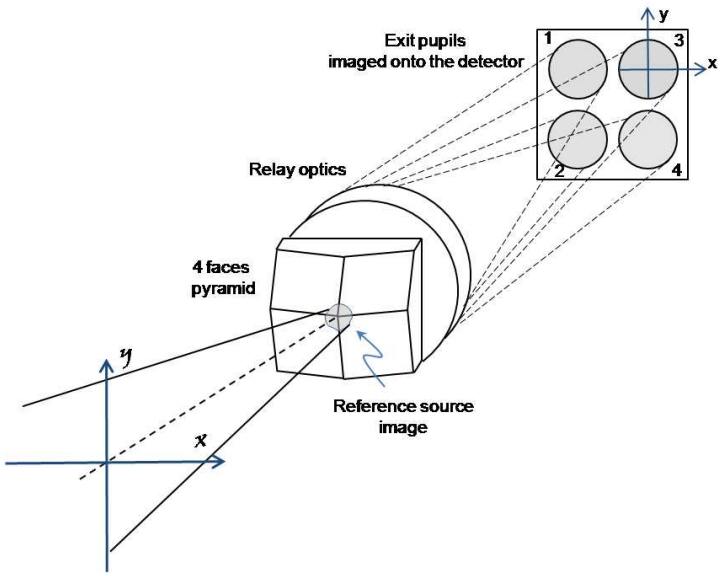

Figure 1.7: Schematic diagram of the pyramid wavefront sensor concept. The reference source is imaged on the pyramid vertex, afterwards the light is deflected in four directions and reimaged in four exit pupils by the relay optics.

than 180^0 to avoid overlap between the pupil images. The difference intensity between pairs of pupils is related with the wavefront gradient along the x and y axes.

Let's consider the two faces pyramid case (two exit pupils, only one sensing direction) on figure 1.8 to explain the sensing principle. In the absence of aberrations, all the rays coming from the pupil will be focused on the center of the pyramid vertex, so the light will be split equally onto the two pupils. If there is a global tilt across the entrance pupil, the focal plane will be shift respect the vertex center, thus, one pupil would be more illuminated than the other, but homogeneity illuminated. The illumination difference between the two pupils is related with the wavefront slope, thereby, with the global tilt (equivalent principle of a quadcell detector for the four faces pyramid).

Let's consider now a local phase gradient on a small area of the entrance pupil A (e.g. of size r_0), on the geometrical approach, the aberrated rays coming from A will miss the vertex of the pyramid and will cross only one of the prism faces being projected only onto one of the reimaged pupils. In this way, the area A'_2 will be higher illuminated than A'_1. However, the intensity distributions in the pupil images are only a measure for the sign of the ray's slopes (the ray goes either in the up or down pupil, thereby the pupil illumination is independent of the tilt strength). This simply means that the signal of the PWFS saturates as soon as small aberrations appears. As shown in figure 1.9 (left), the linearity range is extremely small.

The sensitivity (refers to the ratio between the sensor signal rms and the incoming wavefront rms) could be reduced by modulating the position of the input beam on the pyramid using a tip-tilt mirror ([18],[19]). If we consider an aberrated ray which strikes the pyramid as shown in figure 1.9 (right), then circular modulation of the beam will cause the ray to trace out a circle over the sides of the pyramid. Over one modulation cycle, the time spent on each face, and hence the intensity at the corresponding point in each of the four pupil images, will depend on the modulus of its slope. The relation between intensity and wavefront for the 4 sided pyramid is given by:

$$S_x(x,y) = \frac{(I_1(x,y) + I_2(x,y)) - (I_3(x,y) + I_4(x,y))}{I_1 + I_2 + I_3 + I_4} \qquad S_y(x,y) = \frac{(I_1(x,y) + I_3(x,y)) - (I_2(x,y) + I_4(x,y))}{I_1 + I_2 + I_3 + I_4} \tag{1.15}$$

$$\frac{\partial w(x,y)}{\partial x} = \frac{R}{F} sin\left(\frac{\pi}{2} S_x\right) \qquad \frac{\partial w(x,y)}{\partial y} = \frac{R}{F} sin\left(\frac{\pi}{2} S_y\right) \tag{1.16}$$

where R is the amplitude of the modulation and F the linear distance between the exit pupil (reimaged on the tip-tilt mirror) and the pyramid vertex (focal plane).

Figure 1.9 (center) shows that the sensor response is approximately linear in the regime of small wavefront slopes. It can be seen that the sensor sensitivity is inversely proportional to the modulation amplitude R. In closed-loop operation the initial amplitude corresponds to the seeing size and then can be reduced in order to increase the sensitivity. Changing the amplitude modulation would be equivalent to change the focal length of the lenslet array in a SHS sensor. Hence, the PWS principle is highly flexible and can be adjust depending onto the observation conditions.

Curvature sensor

The curvature sensor applies more directly the idea of using propagation of intensity to measure wavefront errors given by the Irradiance Transport Equation (continuity equation for light beams):

$$\frac{\partial I}{\partial z} = -(\nabla I \cdot \nabla \phi + I \nabla^2 \phi)) \tag{1.17}$$

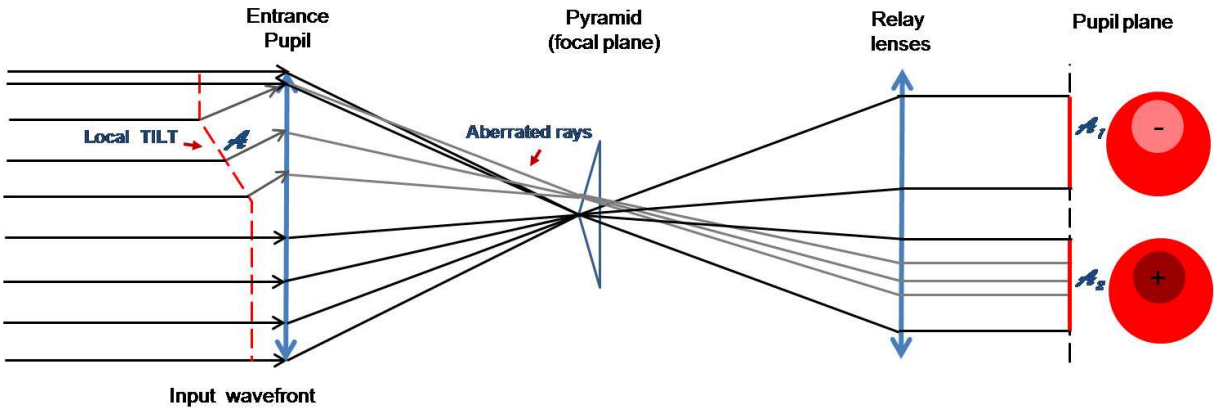

Figure 1.8: PWS sensing concept. A local phase tilt causes that the aberrated rays hit the pyramid on either side of its tip and appears only in one of the multiple pupils causing the corresponding zone to be brighter in one pupil image and darker in the other.

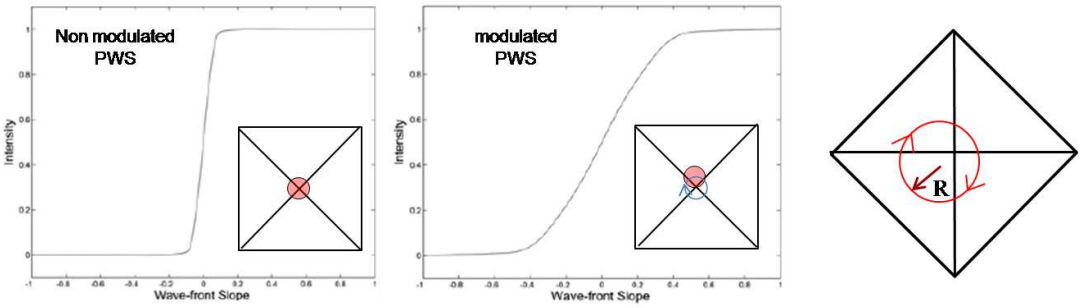

Figure 1.9: **Left:** Transfer function of a non modulated PWS, the sensor is only linear over the spot width. **(Middle:)** Transfer function of a modulated PWS, the sensor is linear over modulation width. **Right:** Path of a tilted single ray due to tip-tilt modulation.

The first term represents the transverse shift of the beam due to local wavefront tilt (concept used on the SHS and PWS) while the second term may be interpreted as the change in irradiance due to focusing or defocussing of the beam caused by local wavefront curvature (used on the CWS).

The curvature wavefront sensor was developed by F. Roddier in 1988 ([20]). The principle in shown in figure 1.10. Two intensity distributions are recorded in the planes P_1 and P_2, at a distance l before and behind the telescope focal plane. These intensity distributions can be considered as defocused images of the telescope pupil. A local curvature on the wavefront modified the rays convergence and divergence in both planes leading to a local excess of illumination in plane P_1 and a lack of illumination at the corresponding position in P_2. While the difference between the two illuminations gives the local WF curvature (second derivative) inside the beam, at the edges of the beam gives the WF radial slope (first derivative).

In the geometrical approximation, the irradiance transport equation can be developed to find the relation between the normalized intensity difference and the WF phase ϕ:

$$c(\vec{r}) = \frac{I_1(\vec{r}) - I_2(-\vec{r})}{I_1(\vec{r}) + I_2(-\vec{r})} = \frac{\lambda f(f-l)}{2\pi l}\left[\frac{\partial\, phi}{\partial n}\left(\frac{f\vec{r}}{l}\delta_c\right) - \nabla^2\phi\left(\frac{f\vec{r}}{l}\right)\right] \tag{1.18}$$

where $\partial\phi/\partial n$ is the radial first derivative of the WF at the edge, δ_c a linear impulse distribution around the pupil edge and ∇^2 the laplacian operator. The CWS signal $c(\vec{r})$ can be amplified by reducing l, which makes gain adjustment possible.

On real implementation of CWS, a vibrating membrane mirror is placed at the telescope focus, followed by a collimating lens, and a lens array. The defocused distance can be chosen by adjusting the vibration amplitude in order to conjugate the defocalized sensing planes on the lenslet array. Optical fibers are attached to the individual lenses of the LA, and each fiber leads to an avalanche photodiode (APD) with zero readout noise.

1.2.2 Deformable mirrors

In order to compensate for the distortions in the wavefront, a phase correction device is introduced into the optical beam. Such devices introduce an optical phase shift ϕ by producing an optical path difference δ (where $\phi = (2\pi/\lambda)\delta$). The quantity δ is the variation of the optical path ne, where n is the refractive index and e the geometrical path. The easiest way to introduce a geometrical path difference is using a deformable mirror or a tip-tilt mirror.

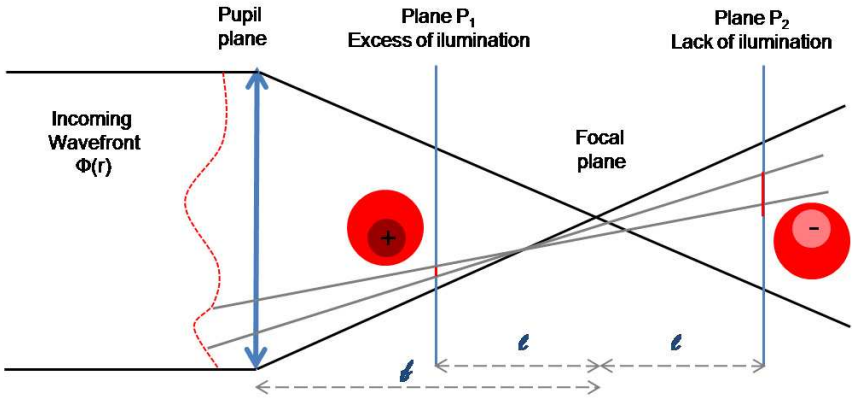

Figure 1.10: Principle of the curvature wavefront sensor.

Deformable mirrors (DMs) basically consist of a segmented or continuous reflective faceplate (i.e. surface mirror) coupled to an array of electromechanical actuators that perform the deformation. The main characteristics which determine the performance of a wavefront corrector are:

- **Number of actuators.** The number of actuators represents the degrees of freedom within the active area and is the basic descriptor. The actuator pitch d in relation to the value of r_0 determines the fitting error. Full wavefront compensation requires an effective actuator spacing of 1 - 1.5 r_0. This implies than larger is the telescope, higher is the number of actuators required.

- **Actuator stroke.** The dynamic range of the deformation is defined by the stroke. We can difference two types of stroke: The *interactuator stroke* corresponds to the maximum displacement between two adjacent actuators (individual actuator stroke) and is always less than or equal to the *mechanical stroke* defined as the maximum range over which all of the actuators can move collectively, i.e., simultaneously applied with the same driving voltage. The stroke required is defined by the standard deviation of the turbulent wavefront:

$$\sigma = 0.06\left(\frac{D}{r_0}\right)^{5/6} \quad (waves) \tag{1.19}$$

  The DM should be able to correct the PTV specified as $\pm 2.5\sigma$. The stroke of a mirror is 1/2 the phase change placed on the beam; thus, the total stroke (mechanical) required is:

$$stroke = 0.15\left(\frac{D}{r_0}\right)^{5/6} \quad (waves) \tag{1.20}$$

  Note that the stroke required is independent of the wavelength being corrected. The results showed are considered for a tip-tilt free turbulence since this modes could be corrected independently by a tip-tilt mirror in order to reduce the stroke required by the DM.

- **Influence functions.** The shape of a deformable mirror surface, when it is pushed by an actuator, is called its influence function (IF). The influence function defines the spatial response of each actuator and is a function of mirror faceplate parameters, as thickness, stiffness or modulus of elasticity. The shape of the IF determines how well the DM is able to take on the shape of the turbulence. The IF for each actuators is recorded into a Matrix by applying a fixed voltage to each actuator sequentially and recording the wavefront phase produced (usually using an interferometer to have high accuracy). The knowledge of the IF is necessary for a modal control where the modal decomposition of the turbulence wavefront is projected onto the IF (section 1.2.3).

- **Actuator coupling**. Actuator coupling shows how much the movement of one actuator will displace its neighbors. It is defined as the ratio of the faceplate deflection produced by an actuator A_i at the position of an adjacent actuator A_{i+1}, to that of the maximum peak deflection of A_i.

- **Temporal frequency response**. Temporal response of the deformable mirror shows how quickly the mirror will react to the control signal. Small mirrors usually have higher bandwidth.

The actuators employed in deformable mirrors are usually either piezoelectric or electrostive. An electric field applied to a permanently polarized piezoelectric ceramic induces a deformation of the crystal lattice and produces a strain proportional to the electric field. The most commonly used piezoelectric material is lead zirconate titanete: Pb(Zr,Ti)O3, referred as PZT. The poling in the material is created by applying an intense field to the ceramic, aligning the randomly oriented dipoles parallel to the field. The response of PZT to applied voltage is linear and bipolar (i.e. can be made to both expand and contract).

In the case of a disk actuator, the effect of a longitudinal electric field E parallel to the poling axis (axis of deformation) is given by:

$$\frac{\Delta e}{e} = d_{pzt}E \qquad \Delta e = d_{pzt}V \tag{1.21}$$

Where e is the thickness of the PZT disk and d_{pzt} is the piezoelectric coefficient. Thus the relative thickness variation is proportional to the field E and, hence, the variation of thickness is proportional to the voltage applied.

The main disadvantage of PZT, being ferroelectric material, is that they exhibits 10-20% hysteresis. This mean, that when a voltage is applied and then removed, the actuator does not return to exactly the same length it had before the voltage was applied. The effect in a closed-loop AO system is to reduce te effective bandwidth.

One type of PZT deformable mirror is the bimorph mirror, in which electrodes are placed between two sheets of oppositely poled actuator material. Applying a voltage to an electrode causes one sheet to contract and the other sheet to expand in the vicinity of the electrodes. This results in a local curvature of the deformable mirror surface. This type of mirror is usually employed in systems having a curvature sensor (since the curvature sensed by the WFS is directly compensated by the Laplacien IF of the DM). A disadvantage of bimorph mirrors is that it is difficult to have a large number of actuators ($\approx$ 100 actuators max).

The second physical process used to produce stroke is the electrostrictive effect that generates a relative deformation which is proportional to the square of the applied electric field E:

$$\frac{\delta}{e} = aE^2 = a\left(\frac{V}{e}\right)^2 \tag{1.22}$$

where a is the electrostrictive coefficient. Note that with electrostive material, the change in thickness is thickness dependent.

Micro deformable mirrors

A new type of deformable mirror was developed during the last decade using micro-electronics fabrication process. These devices have not yet been used in astronomical instrumentation, but this technology will provide the key to small, low-cost, light, and scientifically efficient instruments.

These deformable mirrors are fabricated as microelectromechanical systems (MEMS) ([21]). the fabrication process consist on the deposition of various materials on the surface of a substrate, and using masks, their localization on the substrate is precisely defined in order to ensure their specific tasks. In MEMS, there are two kinds of layers: structural layers and sacrificial layers. The structural layer materials are polysilicon or metal, and the sacrificial layers are silicon oxides or organic materials. The sacrificial layers are chemically dissolved at the end of the fabrication process in order to create air gaps between the remaining structural layers. Fabrication process is shown in figure 1.11.

Micro-mechanical actuation is obtained using electrostatic effect. The electrostatic actuator consists of two electrodes of metal heavily, isolated from each other by a gap of thickness g filled with dielectric medium, usually air. When a voltage V is applied between the electrodes, an attractive force F is generated, and if one of the electrodes is mobile, it moves towards the other. Since the electrostatic effect has only one attraction sense it is necessary to set up the actuator at half range as zero point operation, in this way is possible to obtain two stroke directions by increasing the voltage (attract the electrodes, negative stroke) or decreasing the voltage (separate the electrodes, positive stroke).

A micro deformable mirror (MDM) is usually a continuous mirror formed by a single mirror membrane supported by multiple post attachments to an electrostatic actuator array (figure 1.11b) ([22],[23]).

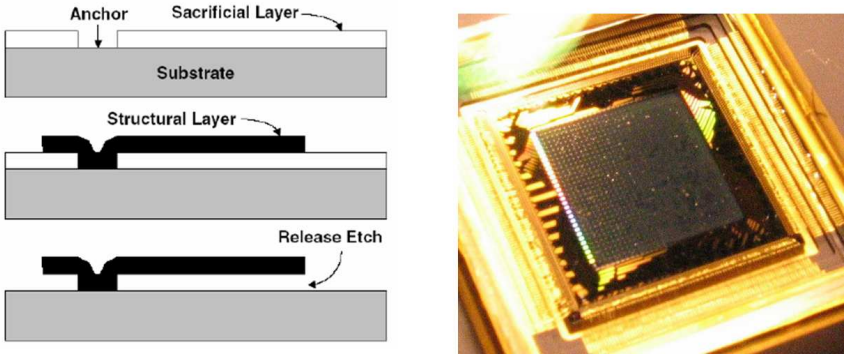

Figure 1.11: **Left:** Schematic of the microelectromechanical fabrication process. **Right:** MEMS deformable mirror, the size of the reflective surface is around 10 mm

The typical actuators consists of a 300 x 300 x 2 μm silicon layer anchored to a substrate along two opposite edges. The actuator flexible membrane serves as the upper electrode of the parallel plate capacitor. A lower, stationary pad of polycrystalline silicon was deposited over an electrically insulating 0.5 μm thick silicon nitride layer that covers the silicon substrate. This pad serves as the other capacitor electrode. Applying a voltage between the lower capacitor electrode and the grounded upper actuator membrane causes the latter to deflect downward, in turn moving its 3 μm post and point of attachment to the mirror. An airgap, typically 5 μm thick, separates the actuator membrane from its voltage activation pad.

The physical behavior of the actuator could be described by an attractive force between the membrane and the pad that is balanced by a restoring force of the spring due to the membrane stress (figure 1.11a). The equilibrium equation is given by:

$$F_m = kz = \frac{\epsilon_0 A V^2}{2(g-z)^2} = F_e \tag{1.23}$$

where F_m is the restoring force, F_e the electrostatic force, k is a constant related to the membrane thickness, elastic modulus and physics geometry, ϵ the dielectric constant of the gap space (normally vacuum), g the gap spacing, z the height of the segment above the substrate, A the area of the segment and V the voltage applied. Thus, the relation between displacement (stroke) and V is given by:

$$V = \left[\frac{2kz(g-z)^2}{\epsilon_0 A}\right]^{1/2} \tag{1.24}$$

note that the stroke displacement is dependent on the square of the voltage.

The two main advantages are the size of the device (for a 32x32 actuators array will measured only around 10 mm) that will allow to build small high density actuators mirrors, and the speed (up to several kHz). In addition, MDM are not affected by hysteresis.

Although, they present a main restriction on the stroke, actual devices produces stroke around 2 μm and future developments are limited by construction to a few microns since an stroke increase implies to increase the size of the actuator and thereby the size of the membrane that would give problems on the equilibrium forces. The solution is to use simultaneously two deformable mirrors on the AO system; a woofer DM with few stroke but large stroke will be used to correct the spatially low order disturbance while a MDM with large number of actuators and few stroke will be used to compensated the high order disturbance.

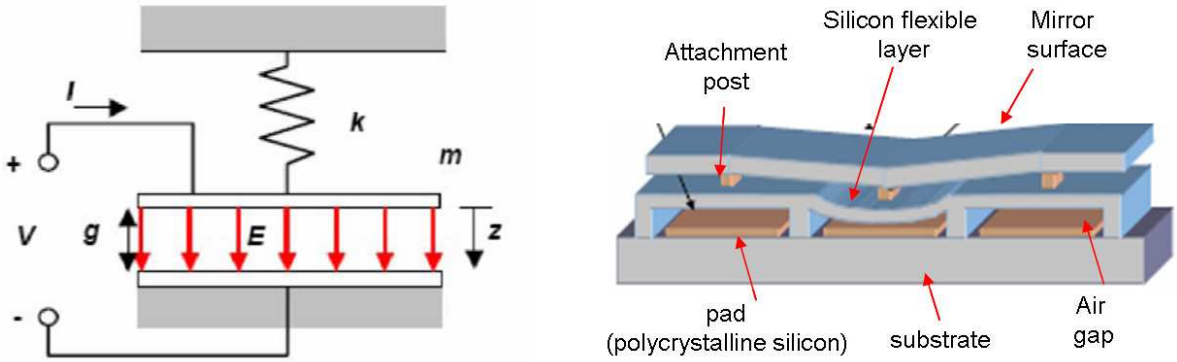

Figure 1.12: **Left:**Electrostatic actuation principle. **Right:** Scheme of a MEMS deformable mirror.

1.2.3 Wavefront reconstruction and control

On an AO system the gradient (or laplacian) data delivered by the WFS is converted into commands for the deformable mirror:

$$\mathcal{S}_{x,y} \xrightarrow{\mathcal{R}} C \tag{1.25}$$

where $\mathcal{S}_{x,y}$ represents the slope space, C the commands space, and $\mathcal{R}$ is a linear application that goes from slope to commands space.

This linear relation can be expressed using matricial formalism as:

$$\mathbf{c} = R\mathbf{s} \tag{1.26}$$

where $\mathbf{s}$ is the slopes vector $\{s_x^1, ..., s_x^{ns}, s_y^1, ..., s_y^{ns}\}$, ns the number of subapertures, $\mathbf{c}$ the commands vector $\{c^1, ..., c^{na}\}$, na the number of actuators and R is the reconstructor or control matrix.

The mathematical computation of $\mathcal{R}$ and the conversion between slopes and commands is known as *wavefront reconstruction*. This process restores the absolute phase values on the whole-aperture that are lost when local wavefront slope is measured.

The complete process of sensing, reconstruction and commands deployment is done in a feedback loop process within a short time, termed latency, that must be less than the change time of the wavefront being compensated. Adaptive optics control may use either open-loop or closed-loop operation. In the open-loop operation (feed-forward configuration) the WFS is placed before the DM, thus, the received wavefront is first measured in its raw or uncorrected state. The required corrections are then computed and fed to the DM.

In the closed-loop configuration the first component in the optical system is the DM. which compensates the wavefront errors on the incoming beam before it is sampled and measured by the WFS. The WFS therefore sees only the residual error; that is, the difference between the current incoming wavefront and the last correction applied to the DM. This error is processed to update the control signals applied to the DM. On this arrangement, the wavefront sensor needs only to detect small deviations away from the null.

Open loop configuration are more instable and depends on accurate WFS measurements and deformable mirror calibration. Any error in the response of these components shows up as a wavefront error in the optical output. For this reason, closed-loop configuration are used in most AO system, and open loop systems are used only when closed-loop configuration is not feasible like in MOAO (section 1.2.4).

Using the closed-loop approach, an AO system can be defined (following control theory) as a multi-variable servoloop system (figure 1.13) where the input is the wavefront phase perturbation and the output is the residual after correction. In most cases, is used a first-order servoloop containing an integrator as feedback law. This integrator in a discrete time system corresponds to summation:

$$\mathbf{c}(i) = \mathbf{c}(i-1) + \alpha R\mathbf{s}(i) \tag{1.27}$$

where $\mathbf{c}(i)$ is the commands vector for the actual iteration, $\mathbf{c}(i-1)$ is the commands vector applied on the previous iteration, $\mathbf{s}$(i) is the slopes vector on the actual iteration and R is the reconstructor or matrix gain (using the control theory term). α is a scalar gain between 0 and 1 used to decrease all the matrix gains in the closed loop, giving stability but reducing performance (the control bandwidth and transfer function are directly related to this parameter). This gain is adjusted depending on the observing conditions.

The integrator induces memory of previous aberrations on the system, since the actual commands computed take into account the commands history applied.

On this way the output residual phase in each iteration is given by:

$$\phi_{res} = \phi_{tur} - \phi_{corr} \tag{1.28}$$

The corrected phase, expressed in slopes, is linearly related to the commands by:

$$\mathbf{s} = M\mathbf{c} \tag{1.29}$$

Where the matrix M is the Interaction Matrix of the system (IM) that links the deformations of the DM to the WF distortions measured by the WFS. The matrix M could be obtained experimentally from the system: the basic idea for recording it is to deform the DM by pushing its actuators one after the other (zonal approach), and for each of them record the slopes vector produced on the WFS. This process is known as *calibration* since what we do is to ”calibrate” the WFS response to the DM.

In this way, for a system with *na* actuator and *ns* subapertures an interaction matrix of N_{2ns}xN_{na} is

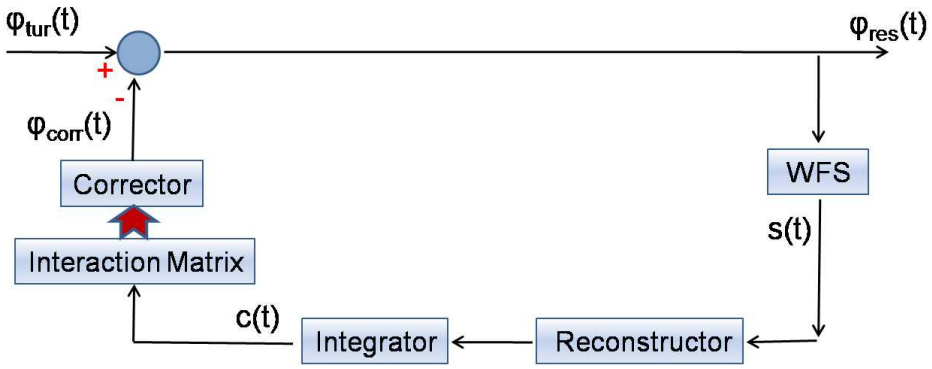

Figure 1.13: Basic block diagram of the AO control loop.

obtained:

$$M = \left(\begin{pmatrix} s_{x,1} \\ s_{x,2} \\ \vdots \\ s_{x,ns} \\ s_{y,1} \\ s_{y,2} \\ \vdots \\ s_{y,ns} \end{pmatrix}_{act=1} \begin{pmatrix} s_{x,1} \\ s_{x,2} \\ \vdots \\ s_{x,ns} \\ s_{y,1} \\ s_{y,2} \\ \vdots \\ s_{y,ns} \end{pmatrix}_{act=2} \cdots \begin{pmatrix} s_{x,1} \\ s_{x,2} \\ \vdots \\ s_{x,ns} \\ s_{y,1} \\ s_{y,2} \\ \vdots \\ s_{y,ns} \end{pmatrix}_{act=na} \right) \tag{1.30}$$

To compute the commands the reconstructor matrix is required. Looking at equations 1.26 and 1.29, it is shown that matrix M and R are inverse one of each other. Since the interaction matrix is known, the reconstructor could be obtained inverting M. But, the linear system that represents actuators and slopes is overdetermined (there are more wavefront sensor signals than actuators). Hence, matrix M is not invertible since it is not square and normally is bad conditioned: this is known as the *inverse problem*. There are many approaches to finding R.

In the standard square approach, the wavefront sensor error $(s - Mc)^2$ has to be minimized. It can be shown that the theoretical control matrix that accomplishes this condition is:

$$R = [M^T M]^{-1} M^T \tag{1.31}$$

In practice, this reconstructor implies the diagonalization of the matrix $[M^T M]^{-1}$, that in this case is a square matrix, but is normally affected by noise propagation and unseen modes and thereby badly conditioned. The most common way to inverted M is to use the so-called *singular value decomposition*. Where M can be written as a product of three matrices:

$$M = U \Lambda V^T \tag{1.32}$$

where U is an N_{2ns}xN_{2ns} orthogonal matrix, V is an N_{na}xN_{na} orthogonal matrix and Λ is an N_{2ns}xN_{na} diagonal matrix. equation 1.32 can be expressed as:

$$M = \begin{pmatrix} \mathbf{u}_1 & \mathbf{u}_2 & \dots & \mathbf{u}_{2ns} \end{pmatrix} \begin{pmatrix} \lambda_1 & & & \\ & \lambda_2 & & \\ & & \ddots & \\ & & & \lambda_{na} \end{pmatrix} \begin{pmatrix} \mathbf{v}_1^T \\ \mathbf{v}_2^T \\ \vdots \\ \mathbf{v}_{na}^T \end{pmatrix} \tag{1.33}$$

where the vectors $\mathbf{u}_i$ and $\mathbf{v}_i$ form complete sets of modes for the sensor signal and mirror control spaces respectively. The diagonal elements of Λ, λ_i, are the singular values of the matrix M. Each non-zero value of λ_i relates the orthogonal basis component $\mathbf{v}_i$ in **c**, the control signal space, to an orthogonal basis component $\mathbf{u}_i$ in **s**, the sensor signal space. We can now distinguish two types of modes:

- **Correctable Modes.** For these modes, $\lambda_i \neq 0$, the actuator control signal c = $\mathbf{v}_i$ results in the sensor signal $\mathbf{s} = \lambda_i \mathbf{u}_i$. These modes can be corrected by applying the actuator model $\mathbf{c} = \lambda_i^{-1} \mathbf{v}_i$, (the singular value could be understood as the sensitivity of the mode).

- **Unsensed mirror modes.** There are modes for which $\lambda_i = 0$. These modes produce zero signal on the detector. This is the case of piston mode, moving all the actuators together do not produce any slopes measurement.

  These unseen modes depend on the geometry distribution between actuators and subapertures. Considering the usual Fried geometry (actuators are placed in the corner of the subapertures), an

important unseen mode is the *waffle*, figure 1.14a shown the waffle pattern as ”chess” distribution. this mode is equivalent to piston, because it produces a constant phase displacement over the whole-subaperture (there is decophasing on the wavefront), thereby the slope measurement is not affected.

In real systems unseen modes are related to λ_i values that are not exactly zero, but are very small. For these modes the sensor is practically blind and clearly susceptible to noise. These modes should be discarded in the reconstruction in order to avoid noise propagation. This is the case of the partially waffle modes shown in figure 1.14b.

The final Reconstructor matrix is now given by:

$$R = M^{+} = V\Lambda^{+}U^{T} \tag{1.34}$$

where + denotes *pseudo-inverse*, Λ^{+} is the least-squares pseudo-inverse of Λ formed by transposing Λ and replacing all non-zero diagonal elements by their reciprocals λ_i^{-1}, which now can be interpreted as the gains of the system modes.

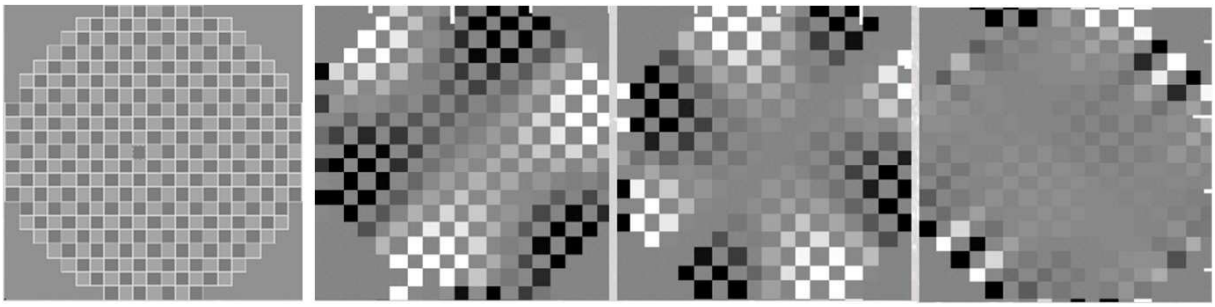

Figure 1.14: Unseen mirror modes **Left:** Waffle mode. **Right:** Three examples of partially waffle modes.

Modal control

The perturbated wavefront over the pupil may be considered as the superposition of spatial modes with increasing spatial frequency and showing different temporal behavior, while the correcting system is described by a zonal approach where the aperture is divided into independent subapertures and the wavefront is compensated by an array of discrete actuators. Despite the zonal geometry, modal algorithms could be used in the reconstruction in order to compute the drive signals.

The turbulent phase $\phi(x, y)$ could be decomposed on a set of whole-aperture basis functions (modes) given by:

$$\phi(\mathbf{r}) = \sum_{k=1}^{N_a} a_k Z_k(\mathbf{r}) \tag{1.35}$$

where a_k are the coefficients of the basis functions $Z_k(x, y)$. The base of modes is assumed to be orthogonal (linearly independent, i.e., the decomposition presents a unique solution):

$$\int_P Z_i(\mathbf{r}) Z_j(\mathbf{r}) d^2 r = \delta_{ij} \tag{1.36}$$

Using the orthogonality property of the basis functions, the a_k coefficients are given by the wavefront projection onto the base:

$$a_k = \int_P \phi(\mathbf{r}) Z_k(\mathbf{r}) d^2 r \tag{1.37}$$

Since wavefront aberrations are a random process, coefficients a_k are also random and we are interested in their statistical properties. The statistical covariance matrix is given by:

$$\left\langle a_i a_j \right\rangle = \int_P \langle \phi(\mathbf{r}) \phi(\mathbf{r}') \rangle \, Z_i(\mathbf{r}) Z_j(\mathbf{r}) d^2 r \tag{1.38}$$

The diagonal elements of this matrix are the variances of the modes and describes their contribution to the atmospheric turbulence.

The most used base is the Zernike polynomials because they can be computed by simple analytic expressions. These polynomials keep the properties of orthogonality and normalization on a unit circular aperture. The first few modes correspond to familiar optical aberrations, such as overall tilt, defocus, astigmatism, and coma.

The covariance matrix could be computed taking into account the statistical properties of the phase. For the Zernike modes the diagonal elements are given by the approximate expression:

$$\left\langle a_i^2 \right\rangle = 0.294 i^{-1.9} \left(\frac{D}{r_0} \right)^{5/3} (rad^2) \tag{1.39}$$

Also non diagonal components appears on the covariance matrix for the Zernike case. This means that all modes are not statistically independent. a set of basis functions orthogonal and statistically independent could be obtained in terms of the Zernike modes by diagonalization of the Zernike covariance matrix. It is the so-called Karhuhen-Loeve expansion. If $A_{sta} = aa^t$ is the covariance matrix, since it is hermitian, there is always a unitary matrix U that verify that

$$UAU^t = \Lambda \tag{1.40}$$

The coefficients b_j of the K-L expansion are given by:

$$\mathbf{b} = U\mathbf{a} \tag{1.41}$$

From equation 1.40 and 1.41 The K-L covariance matrix given by $\mathbf{b}\mathbf{b}^t$ is diagonal and thereby, statistically independent. Using equation 1.35 and 1.41 the phase could be expressed as:

$$\phi(x, y) = \sum_{k=1}^{N_a} \sum_{j=1}^{N_m} u_{kj} b_j Z_k(\mathbf{r}) \tag{1.42}$$

And the K-L functions could be expressed as linear combination of Zernike functions with the vector columns of U as coefficients:

$$K = \sum_{k=1}^{N_a} u_{kj} b_j Z_k(\mathbf{r}) \tag{1.43}$$

The computation of a K-L modal basis statistically independent could be done from any set of functions, not necessarily from the Zernike polynomials as we will see on section 4.

To apply the modal approach on the AO control it is necessary to come back to the mirror space, since it is the space where the phase is compensated. The mirror space is defined by the DM influence functions or wavefront distortions produced by each individual actuator (section 1.2.2). Projecting the modal basis onto the IF space it could be found a matrix relationship between commands and modal coefficients given by:

$$\mathbf{c} = B\mathbf{m} \quad B = FZ; \tag{1.44}$$

Where F is the IF matrix, Z the modes matrix and (*m*) are the mode coefficients of the modal basis (Zernike, K-L or other). Matrix B gives the voltage pattern to recreate each of the modes by the DM. Applying sequentially each of this mode patterns to the DM and recording the slopes vector produced on the WFS the modal calibration matrix *D* is obtained. The modal IM converts mode coefficients vector into slopes vector:

$$\mathbf{s} = D\mathbf{m} \tag{1.45}$$

The reverse equation could be found trough the pseudoinverse of B (using SVD).

$$\mathbf{m} = D^{+}\mathbf{s} \tag{1.46}$$

In this way any WF measured by the WFS could be described by its modal coefficients.

From equation 1.45 and 1.46 the modal control matrix required to compute the feedback commands is given by:

$$\mathbf{c} = \underbrace{BD^{+}}_{\mathrm{R}}\,\mathbf{s} \tag{1.47}$$

Modal control could be performed recording a zonal IM and taking into account the modal basis B. In this case the reconstructor is given by:

$$\mathbf{c} = \underbrace{BB^{+}M^{+}}_{\mathrm{R}}\,\mathbf{s} \tag{1.48}$$

Modal control is useful because it is possible to decide a priori which modes of the turbulence to control taking into account the observing conditions. When working in low flux conditions it is convenient to control only low order modes and avoid high order modes more affected by noise propagation or to set individual control gains for each mode. In addition it is possible to take into account the spatial structure of the turbulence on the construction of the modal basis. Specific issues about modal control as the computation of the modal basis will be treated on chapter 4.

1.2.4 Adaptive optics systems zoology

Several AO concepts have been developed in the last years to achieve the different scientific goals explained before specially for the next generation of extremely large telescopes (as explained in Hubin *et al.* 2005 [24]). The main differences consist on the corrected FoV: higher correction imply smaller FoV, while higher FoV are obtained reducing the performance over the corrected field. The classical AO concept explained before, consisting of one deformable mirror and one WFS, is called Single Conjugated Adaptive Optics (SCAO). In this case, the maximum performance is achieved in the guide star direction while science targets suffers from anisoplanatism. The new adaptive optics systems proposed for the next instruments generation are hereafter briefly reviewed from the largest to the smallest corrected FoV.

Ground layer adaptive optics

Ground Layer Adaptive Optics (GLAO) is a new AO concept based on the fact that most of the atmospheric turbulence is generated in the first few hundred meters above the ground (at least for the best observing sites). The correction of only this ground layer of turbulence allows us to achieve a moderate level of correction (since only a fraction of the turbulence is corrected), but over a very large field (up to 8-10 arcmin). The atmospheric turbulence volume (3D) is measured using several guide stars (natural or lasers) and therefore several wavefront sensors. The guide stars are distributed on the edges of the FoV of interest. A single deformable mirror at the ground is controlled by averaging the signals from the multiple widely spaced wavefront sensors.

Multi-object adaptive optics

The aim of MOAO (Multi-Object Adaptive Optics) is to allow the survey of a large number of objects spread over a wide field of view. Each object is separately corrected by an independent deformable mirror performing single conjugate correction in different directions. Control signals are provided to each deformable mirror based upon a tomographic reconstruction of the atmosphere using multiple laser beacons.

These separates correctors might share a global woofer mirror (as a secondary deformable mirror). The multiple DMs of MOAO systems are currently envisioned to be operated in open-loop since the DMs are placed after the WFS in the control loop.

The final result is an optimization of the AO correction in very specific areas, typically smaller than 1 arcsec, but spread over a very large FoV, up to 10 arcmin in the NIR.

Multi-conjugated adaptive optics

Multi-Conjugate Adaptive Optics (MCAO) can be seen as an extension of GLAO, where several layers at various altitudes are corrected, using additional deformable mirrors optically conjugated to these different layers. This systems achieve a diffraction-limit over a medium sized FoV, typically 1 to 2 arcmin with corrections of the order of 50% SR in K-band. Multiple LGS are required to improve sky coverage. The main differences with GLAO and MOAO systems is the fact that they can provide good PSF uniformity over the corrected FoV, typically a few % of SR variation.

Laser Tomography Adaptive Optics

Laser Tomography Adaptive Optics (LTAO) was developed to improve the actual SCAO concept limited by anisoplanatism and limited sky coverage. Several LGS are used to correct the whole turbulent volume above the telescope. In opposite to GLAO, the signal from the multiple WFS is not averaged, instead, it is used to do a tomographic reconstruction to optimize the correction over the direction of interest.

1.3 From classical AO to XAO

1.3.1 XAO concept

Adaptive optics developments go in two main directions: increase correction over a wide field of view or extremely high correction on axis depending on the specific science targets. High contrast imaging (HCI) looks for the detection and characterization of extrasolar planets, an the main pre-requisite is the need for high angular resolution. Direct planets imaging requires contrast levels up to 10^{-6} very close to the parental star. Thus, almost perfect PSF is required in order to concentrate the light on the PSF core while reducing the intensity of the halo, where planets are susceptible to be detected. the light from the star could be removed efficiently by high performing coronagraphs only if the energy is well concentrated.

To observe at very high-contrast levels leads to the so-called ”Extreme Adaptive optics” systems (XAO) which objective is to achieve high performance not only improving the central peak (SR > 90%), but supressing the halo of scattered light that surrounds any AO-corrected star. XAO systems have a characteristic PSF with a sharp peak and a relatively flat halo out to a control radius given by λ/d, where d is the actuator spacing.

XAO basic concept is identical to a standard AO system (SCAO), but each single component is pushed to its ultimate capacities to mitigate each of the possible error source (everything but anisoplanatism) and the whole system needs to break a number of conceptual and technological barriers.

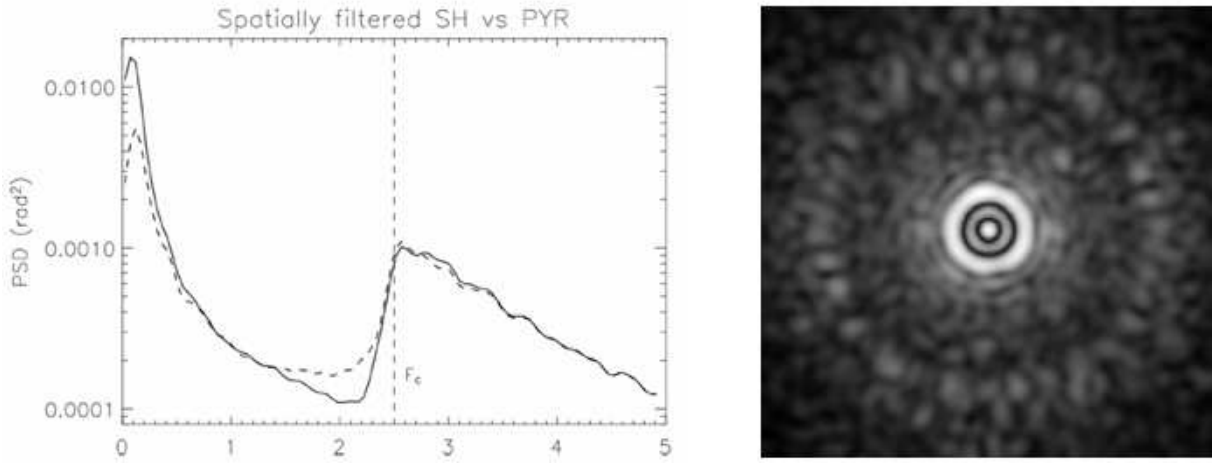

Figure 1.15: **Left:** PWS (dashed line) vs SFSHS (solid line) in terms of spatial distribution of the residual error. PWS performs better at low frequencies while the SHS achieves better performance at frequencies closer the AO control radius. **Right:** Simulated postcoronagraphic images for an APLC coronagraph (Carbillet, 2006 [25]). the image show the limit of the control area as a visible external ring, as well as a sea of speckles within the control area that limit the detectability of possible exoplanets.

There are two types of errors: evolving an static [26]. Planets will almost always be fainter than even the most extreme of XAO halos, so the ability to detect the small deviation in the halo caused by a planet depends on the smoothness of the halo. In instantaneous images the halo is completely non-smooth, consisting of a pattern of diffraction-limited speckles, but over long exposure these speckles move around and average out. This halo limits the contrast performance (ratio between core peak and halo level) but can be removed by a postprocessing low frequency filter, thus the halo limits the image contrast but not the detectability of the planet.

On other hand, static errors (e.g. non-common path aberrations) produce a static (or quasi-static) speckle pattern on the final image that could not be averaged. In this case the detectability of the instrument is limited by the intensity level and distribution of this speckles since it is not possible a priori to distinguish between speckle and planet.

Although, two methods are used to deal with these errors; removing them by measuring the phase or/and the amplitude of the individual speckles on the final image (speckle nulling, phase diversity ...) and then offsetting the DM commands, or implementing postfocal techniques to discriminate the planet by using the differential properties respect to the speckle (Differential imaging ([27],[28]), spectral deconvolution ([29]), stochastic speckle discrimination ([30]),([31])).

In this way, a HCI instrument will consist of three fundamental modules: The XAO system to compensate the turbulence, the coronagraph to suppress the PSF core and reduce the diffraction pattern (increase contrast) and the high contrast modules that implement themself a subinstrument (IFS, differential imaging, polarimetry) working simultaneously with postprocessing techniques (increase detectability).

XAO error budget

The wavefront error variance after AO correction is defined by equation 1.7. For XAO we should take into account an overall global error:

$$\sigma^2_{XAO} = \sigma^2_{atmosphere} + \sigma^2_{AO\ system} + \sigma^2_{others} \tag{1.49}$$

The two first terms corresponds to errors not due to the limited adaptive optics correction. The atmospheric term reagroup errors origined on the turbulence that the standard WFS are not able to sense:

scintillation, diffraction effects, chromatic effects. ”Others” considers telescope and instrument errors mainly coming from aberrations within the light path not seen by the AO system: non-common path aberrations between sensor and scientific path, calibration and reconstruction errors, etc.

The AO system term corresponds to the standard error variance due to the limited adaptive optics correction. For XAO the main limiting factors are given by:

$$\sigma^2_{AOsystem} = \sigma^2_{fitting} + \sigma^2_{aliasing} + \sigma^2_{measure} + \sigma^2_{temporal} \tag{1.50}$$

The fitting error translates the fact that a limited range of spatial frequencies, and hence atmospheric turbulence modes, can be physically corrected by the mirror, and then the possible mirror modes. This error is consequently expressed in function of the ration between the inter-actuators mean distance d and the Friend parameter:

$$\sigma^2_{fitting} \propto \left(\frac{d_{DM}}{r_0}\right)^{5/3} \tag{1.51}$$

Hence, increasing the number of actuators the fitting errors is reduced. For XAO it is necessary to achieve an actuator spacing of the order of the Fried parameter. This implies that bigger the mirror, higher number of actuators (and thereby subapertures) are required to achieve XAO corrections. Also, bigger is the telescope, higher is the AO system complexity. the actuator pitch will also determine the angular radius λ/d of the area around the PSF over which the AO performs corrections.

The aliasing error is due to the finite number of wavefront analysis elements. Spatial frequency errors higher than the subaperture size are unseen by the WFS. In addition this produce an aliasing error: Uncorrected high order spatial frequencies are mis-understood as low order frequencies introducing an error on the measurements. Supposing that the size of the analysis element is d_{WFS}, the aliasing variance error is given by:

$$\sigma^2_{aliasing} \propto \left(\frac{d_{WFS}}{r_0}\right)^{5/3} \tag{1.52}$$

Aliasing could be mitigate reducing the subaperture size or filtering the high spatial frequencies before the WFS. This is done using a field stop on the focal plane. Since the focal plane is the Fourier transform of the pupil plane, image information far away from the PSF center will corresponds to high order frequencies on the pupil plane. Covering this area of the focal image we remove the spatial frequencies not sensed by the WFS. The size of the spatial filter (so-called pinhole) depends on the size of the subaperture.

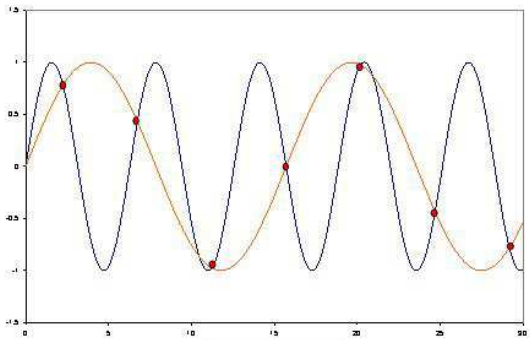

Figure 1.16: Aliasing error. When measuring or digitalizing a signal if the sampling frequency (given by the WFS subaperture size) is lower than the signal frequency, the signal will be misunderstood as a lower frequency signal. On a continuous spectral signal, low order frequencies will be overestimated.

The measure error is related to the light detection by the CCD device used on the WFS. Photon noise is an intrinsic property of the radiation and inversely proportional to the photons received. On other hand, it is possible to mitigate the other two components, read-out noise and dark-current, by improving the CCD design. Read-out noise is one of the most important noise source that limits the reference star magnitude, since for low magnitudes the read-out noise is quite higher than the photon noise.

Electro multiplicative CCDs (EMCCD) begin to be widely used for WFS and short exposure astronomy observations. The improvement consist on an intermediate step between the photon detection and the amplifier read-out. On this step the electrons are multiplied by a voltage (as on photomultiplier detectors). In this way, the read-out noise on the amplifier is the same (is an intrinsic property of the amplifier design), but since the number of electrons now is higher the relative or equivalent read-out noise is smaller.

Last error is related to the global AO system temporal error. This error could be mitigated increasing the WFS frequency (but, increasing the photon noise) or reducing the commands computation time by optimizing the reconstructor algorithms and using faster digital processor (FPGA, DSP ...). The speed system required is defined by the turbulence coherence time. For XAO, system speeds of 1 - 3 kHz are mandatory.

As other AO system the basic parameters to measure the performance of an XAO system are the Strehl ratio and the residual variance (section 1.2). But, in this case the SR range is around $90 - 95\%$ and small errors as speckle are not well take into account. in addition to SR, other parameters and factors should be considered. Contrast level between central peak and halo at different angular distance is more suitable specially when working with coronagraphy. As well has to be considered the capability to obtained well-reconstructed images (e.g., shape of the airy rings).

Wavefront sensor for XAO

WFS using high number of sensing elements is required for XAO. Two wavefront sensors are suitable for high order sensing where the spot is diffraction-limited [32]. Conventional SHS sensibility is limited by the spot angular size on each subaperture λ/d given by the diffraction of the subaperture of size d. This implies that the sensibility is constant from low to high order modes. On the other hand, the PWS takes advantage of the full-aperture diffraction limited spot, so PWS sensibility to low order modes is higher than for the SHS, and decrease until reach the limit of the SHS for high order modes. As shown in Ragazzoni *et al.* 1999 [18], the sensibility improvement should permit a gain of 2 magnitudes over the SHS. In addition, as explained on section 1.2.1, the PWS is more flexible since the sampling and the gain are easily adjustable.

SHS could be improved diminishing the aliasing error by introducing a spatial filtering in the focal plane. This concept, so-called *spatial filter Shack-Hartmann* (SFSHS), was proposed originally by L.A. Poyneer and B. Macintosh in 2004 ([33]). Another degree of improvement could be achieved by optimizing the centroid signal calculations. Simulations show that the new SFSHS and PWS performance are of the same order. Verinaud *et al.* 2003 ([34]), using a interferometric approach for the PWS, demonstrated that while the PWS better performs around the center of the diffraction patterns (i.e. around the core itself of the PSF), the SFSHS gives better results towards the edges of the AO control area (figure 1.15).

1.3.2 Extrasolar planets finder: Science objectives

A summary of the main science objectives of extreme AO systems could be found in [35],[36],[37]. The primary goal of extra-solar planet science of the next decade will be a better understanding of the mechanisms of formation and evolution of planetary systems. The fundamental observational parameter is the frequency of planets as a function of mass and separation.

Theoretical models of planet formation predict that the peak of formation of giant planets is found close to the snowline, thanks to the availability of a larger amount of condensate in the protoplanetary disk. In outer regions, the longer timescales involved should make planet formation a less efficient process. Migration mechanisms and long term orbit instabilities will alter the original distribution. Determination of the frequency of giant planets in wide orbits (5-10 AU) will allow testing basic aspects of the planet formation models.

Over 400 extrasolar planets are known so far, most of all discovered in radial-velocity (RV) surveys. This indirect technique measures the Doppler shift induced by the companion onto its parent star, and thus provides an indirect estimate of the projected mass of this companion, as well as orbits parameters. The RV method is mostly sensitive to F,G,K,M bright stars characterized by slow rotation periods and low activity. This technique is the most suitable to find companions with larger masses and shorter orbits (< 5 UA), hence, allowing the study of the inner side of the planet distribution.

Nowadays statistical results are extremely biased by the observation capabilities of RV. For example, within the observation period of few years, the brown dwarf companions are rare events, it is the so-called brown dwarf desert. But this could only means that substellar objects more massive than 10 Jupiter masses are mostly located at large distances from the star, and thereby, no observed by RV.

High resolution and contrast imaging is expected to be the most efficient technique to discover planets in the outer regions of planetary systems giving a clear view of the frequency of giant planets in wide orbits. For it, HCI instruments need to resolve large contrast of luminosity between the star and the planet (larger than 12.5 mag or 10^5 flux ratio) at very small angular separations, typically inside the seeing halo.

Imaging gives access to the planets photon, so to intrinsic properties not observable by indirect methods. We may distinguish two regimes of planets emission:

- Intrinsic emission of the planet due to residual cooling after their formation. It is larger for high-mass and young planets. The star planet flux ratio of this emission is independent of the orbital distance (since the planet is self-luminous), however, the planet gets hotter and thus its infrared emission can be significantly enhanced. On the other hand, the flux ratio strongly depends on the star spectral type, being later types more favorable.

  Due to the planet effective temperature (100-1000K), the intrinsic emission increases towards the mid-infrared (Y,J,H,K and L bands), giving a typical ration peak between star and planet of 10^{-6}-10^{-7}. It is also characterized by spectral features, mostly due to CH_4 and H_2O, and thus commonly found in spectra over an extended mass range, from Saturn mass up to brown dwarfs (0.3-30M_j).

- Emission due to the reflection of starlight by the atmosphere of the planet. It is given by:

$$\frac{F_{reft(t)}}{F_*} = \frac{A_{pl}}{4}\left(\frac{R_{pl}}{a}\right)^2 \phi(t) \tag{1.53}$$

  The reflected light is strongly dependent on the star-planet distance a (figure 1.17), being only significant at short star-planet distance (below 1.5 AU for a G star). It also depends on the the planet radius (R_{pl}), albedo (A_{pl}) and is strongly modulated with the phase $\phi(t)$, such that the planet is the brightest when it is situated behind the star, and thus at smallest angular separations. Most of the light is reflected in the visible (where the star is bright) and it is strongly polarized providing the possibility for detecting using differential polarimetry.

  This emission is not easily accessible (star-planet ratio peak $10^{-9} - 10^{-10}$) and so concerned observations is limited to the closest bright stars for the actual telescopes ($\approx$ 8 m diameter). To increase the number of targets on this regime will require observations with extremely large telescopes (40 m) to increase the sensibility and the angular resolution, as well as more efficient XAO and HCI instruments.

Consequently, the direct imaging of planets will allow some characterization of their atmospheric components: effective temperature, depth of methane and water features using near-IR-low-resolution spectrophotometry, dust grain size and cloud characteristics (degree of polarization),planet radius and geometric albedo.

The contrast and angular resolution required constrain the targets suitable for planet search:

- Star magnitude: For a 8 m telescope with 1k actuator DM, the limit is a magnitude V $\approx$ 10 in order to achieve 90% SR (on K-band). This limits the planet magnitude to 25 magnitudes, limiting the range of achievable planets.
- Stellar type: So far all planets were imaged around A stars, so early type stars. Planets around late-type stars are more likely to be discovered by direct imaging (the star-planet magnitude contrast is more favorable by 2 magnitudes with a M0V star compared to a G0V star).
- Star distance: Limitations in angular resolution and sensitivity points towards stars within $\approx 100pc$, in order to probe the internal 50 to 100 AUs around stars. This corresponds with the planet formation region specially around stars typically cooler that the Sun.
- Star age: The intrinsic cooling of giant planets makes them easier to detect when young and hot. Stars within nearby young associations are thus prime targets of planet search surveys.

Hence, for next generation of planet finders on 8 m class telescope, star targets could be grouped as:

- The most nearby stars: 3 - 20 pc. Evolved planets of M_J could be detected around stars within 20 pc, at a typical contrast of 10^{-6}. It also allow some discoveries through the reflected light.
- The youngest stars: 20 - 70 pc, 1-100 My. Located in star-forming regions.
- Intermediate age stars: 3 - 50 pc, 0.1-1 gy. It will include stars with planets known by RV and also active stars discarted in RV surveys but whose activity may indicate a relatively young age.

1.3.3 Next generation of High contrast instruments

SPHERE: Spectro-Polarimetric High-contrast Exoplanet Research

The SPHERE instrument (Beuzit *et al.* 2008) [38]) is an extrasolar planet imager belonging to the second generation instruments of the European VLT (Very Large Telescope) foreseen to be operative in 2012. SPHERE is an IR and visible instrument feed by a high performing XAO system. It is divided in four systems: the Common Path and Infrastructure and the three science channels, a differential imaging camera (IRDIS, Infrared Dual Imager and Spectrograph), an Integral Field Spectrograph (IFS), and a visible imaging polarimeter (ZIMPOL, Zurich Imaging Polarimeter).

The Common Path includes pupil stabilizing fore optics (tip-tilt and rotation), the SAXO extreme adaptive optics system, a NIR coronagraphic device and a separate visible coronagraphic device. The two NIR instruments (IRDIS and IFS) are fed with the coronagraphed NIR beam and ZIMPOL gets the visible coronagraphed beam, after it has shared the visible photons with the AO wavefront sensor. A photon sharing scheme has been agreed between IRDIS and IFS, allowing IFS to exploit the NIR range up to the J band, leaving the H-band for IRDIS.

The SPHERE adaptive optics system (SAXO) combine new technological aspects. The 41x41 piezo-actuator DM of 180 mm diameter provides a maximum stroke of $5\mu m$ combined with a 2-axis tiptilt mirror (TTM) with ± 0.5 mas resolution. The wavefront sensor used is a 40x40 lenslet Shack-Hartmann sensor, with a spectral range between 0.45 and 0.95 μm equipped with a focal plane filtering device of

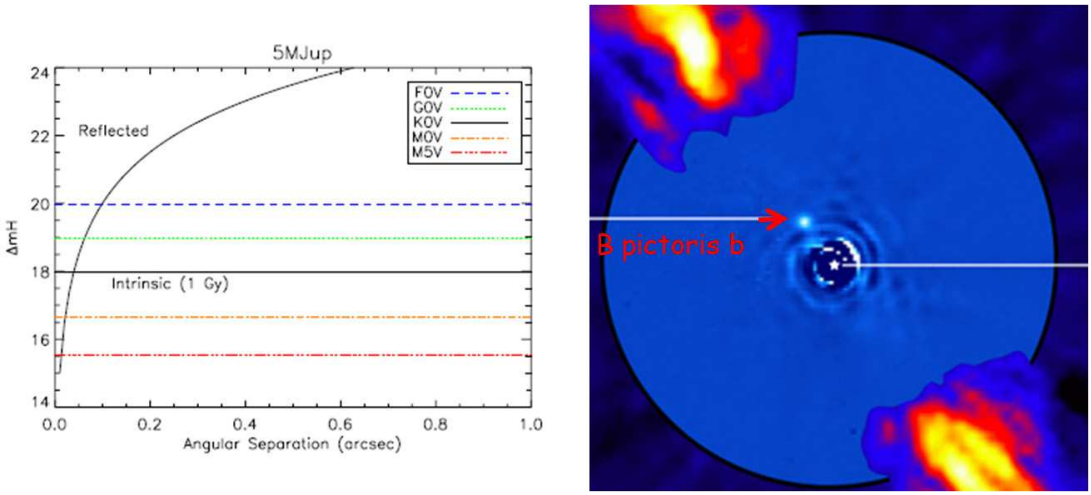

Figure 1.17: **Left:** H-band planet-to-star flux ratio in both regimes of planet emission, intrinsic light (horizontal lines) and reflected light, for a 5 M_{Jup} planet on a system of 1 Gy at 10 pc. The star spectral type induces more than 4 magnitudes variations in contrast, from F0V to M5V, while the reflected light drops by orders of magnitude with increasing orbital distance. **Right:** Deep adaptive-optics L-band image of β Pic recorded using the NaCo instrument at the Very Large Telescope showing a companion of $\approx$ 8 M_{Jup} mass at 8 AU and typical temperature of $\approx$1500 K (Lagrange *et al.* 2009 [39]).

variable size for aliasing control. A temporal sampling frequency of 1.2 kHz is achieved using a 240 x 240 pixel electron multiplying CCD detector with a readoutnoise < 1 electron. The global AO loop delay is maintained below 1 ms.

Image and pupil stability are also essential in high-contrast instruments. Differential image movements due to thermo-mechanical effects and displacement mechanism precision are therefore measured in realtime using an auxiliary NIR tip-tilt sensor located close to the coronagraphic focus and corrected via a differential tip-tilt mirror in the WFS arm. Likewise, pupil run-out is measured by analysis of the WFS sub-pupil intensity along the pupil edge and corrected by a pupil tip-tilt mirror close to the telescope focal plane at the entrance of the instrument. Non-common path aberrations are measured off-line using a phase diversity algorithm and compensated on-line by reference slope adjustments.

Efficient coronagraphy is critical for reaching reduction in the intensity of the stellar peak by a factor of at least 100 and eliminate the diffraction features due to the pupil edges. The baseline coronagraph suite will include an achromatic four-quadrant phase mask coronagraph (A4Q) based on precision mounting of four half-wave plates (HWP), an apodized Lyot coronagraph (APLC) as well as Classical Lyot coronagraphs (CLC).

The Infra-Red Dual-beam Imaging and Spectroscopy (IRDIS) science module covers a spectral range from 950-2320 nm with an image scale of 12.25 mas. The FOV is 11" x 12.5", both for direct and dual imaging. Dual band imaging (DBI) provides images in two neighboring spectral channels. Two parallel images are projected onto the same 2kx2k detector. A series of filter couples is defined corresponding to different spectral features in modeled exoplanet spectra. The classical imaging mode allows high-resolution coronagraphic imaging of the circumstellar environment. In addition to these modes, it also provides long-slit spectroscopy.

The second science channel of SPHERE is an integral field spectrograph (IFS). While an IFS for planet imaging is conceptually challenging, it is widely recognized as a potentially extremely useful for a planet-searching instrument. The multiple spectral channels allow for better correction of speckle chromaticity and even data analysis strategies that do not rely on the presence of a-priori assumed features in the planets spectrum. The spectral range of the IFS covers the Y-J bands (0.95-1.35 μm), allowing the use of a single detection channel and parallel operation of IRDIS and IFS.

On the visible, ZIMPOL (Zurich Imaging Polarimeter) will study the reflected light of planets using differential polarimetry. It is located behind SAXO and a visible coronograph. ZIMPOL is specified with a bandwidth of 600 to 900 nm. The ZIMPOL optical train contains a common optical path that is split with the aid of a polarizing beamsplitter in two optical arms. Each arm has its own detector. The common path contains a switchable half wave plate and a ferro electric liquid crystal polarization modulator (FLC). The two arms have the ability to measure simultaneously the two complementary polarization states in the same or in distinct filters.

The basic ZIMPOL principle for high-precision polarization measurements includes a fast polarization modulator with a modulation frequency in the kHz range, combined with an imaging photometer, which demodulates the intensity signal in synchronism with the polarization modulation. The polarization modulator and associated polarizer convert the degree-of-polarization signal into a fractional modulation of the intensity signal, which is then measured in a demodulating detector system by a differential intensity measurement between the two modulator states.

GPI: Gemini planet imager

GPI (Macintosh *et al.* 2006 [40]) is the american counterpart of SPHERE being designed and built for the Gemini Observatory. Since it is also foreseen for 2012 and theoretical performance are similar it will imply a big competition to be the first HCI on sky. The basic concept is quite similar, an extreme adaptive optics feeding a NIR spectro-imager. But there are several differences both, on the XAO system and the subsystems.

GPI combines precise and accurate wavefront control, diffraction suppression, and a speckle suppressing science camera with integral field and polarimetry capabilities. The wavefront correction is done using a MEMS deformable mirror of 64x64 elements (but, smaller pupil size). The MEMS DM will have only 3-4 microns stroke, insufficient to fully correct the atmosphere on a 8-m telescope. It will therefore operate on a woofer/tweeter architecture, offloading low-frequency modes from the MEMS to bimorph DM which will also provide tip/tilt correction.

As on the sphere case a spatially-filtered Shack-Hartmann wavefront sensor (44 subapertures across the pupil) is used and a APLC coronagraph is set as baseline. In this case, a second high-precision IR wavefront sensor will be integrated after the coronagraph focal plane. For this purpose a modified Mach-Zehnder interferometer is used where the light from the core of the PSF removed at the coronagraph focal plane provides the reference wavefront. A beamsplitter forwards part of the science light to the interferometer while the main part is sent to an IFS.

The GPI science instrument is a lenslet-based IFS with a low-resolution 1-2.5 μm. It is used both, speckle noise rejection and spectral characterization of the planet. In addition the IFS will also include a polarimetric mode used to characterize circumstellar dust. In this mode, a cryogenic Wollaston prism will be inserted in the reimaging optic path. This will produce two images of orthogonal polarization states, each covering half the field of view. An external half-wave plate will be used as a polarization modulator. By taking simultaneous images the unpolarized halo of starlight scattered by the atmosphere can be removed to see the polarized light reflected off circumstellar dust.

EPICS: The exoplanet imager for the E-ELT

The Exo-Planet Imaging Camera and Spectrograph (EPICS) (Kasper *et al.* 2010 [41]) is an instrument project for the direct imaging and characterization of extra-solar planets with the European ELT (E-ELT). The project has been kicked off in October 2007 and is currently on phase-A study. EPICS will be optimized for observations in the visible and the near-IR and will have photometric, spectroscopic and polarimetric capabilities. The increase on the mirror size (42 m) will imply an increase on the pos-

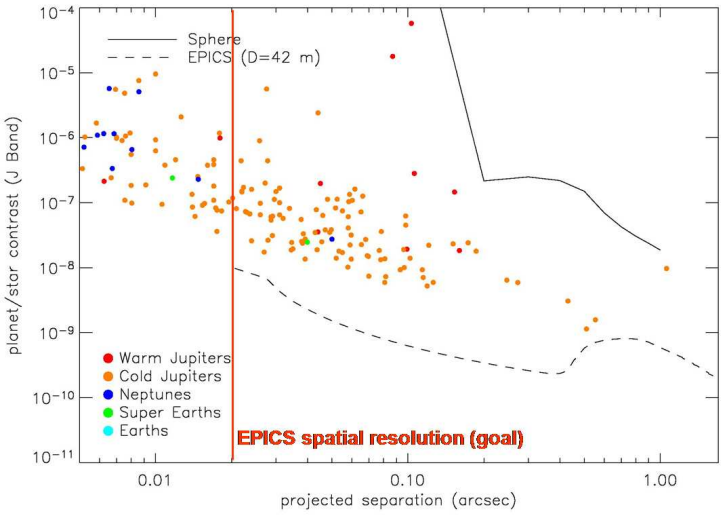

Figure 1.18: Comparison of SPHERE and EPICS contrast goal.

sible targets, specially for planet search using reflected light, as well as an improvement on the contrast achievable. On the other hand, such big mirror will be segmented and will introduce new problems and technological challenge.

The basic concept of EPICS follows the standard approach to the high-contrast imaging problem, including a high performing XAO system, coronagraph, IFS and differential polarimetry. The baseline for the XAO system include a non modulated roof-pyramid wavefront sensor (2 two-sides pyramids on two optical arms split by an beamsplitter). This concept allows the use of 4 independent CCDs (that could be 4 EMCCD as the one used on sphere). Since the temporal bandwidth error is dominating the AO budget, high frame-rates of about 2-3 kHz are needed to reduce the turbulent halo to the adequate level.

The EPICS XAO will have to control two deformable mirrors, the telescope M4 ([42]) with about 6000 - 8000 actuators on the 42 m pupil correcting for large stroke low order aberrations and the internal high order DM with more than 30000 actuators (actuator spacing less than 0.2 m). M4 mirror will be used on SCAO mode controlled by a low order wavefront sensor (in this case a 4-sided pyramid). This low-order loop will feed the XAO system with a diffraction-limited PSF for the a second step correction (residual low order aberrations not corrected with high temporal frequency and the high order aberrations).

Table 1.1: EPICS science cases.

Brightness ratio at distance (mas)	30	100	300
Young self-luminous gas giants in star forming regions	10^{-6}	10^{-6}	10^{-6}
Mature jovian gas giants in reflected light	-	$2 \cdot 10^{-9}$	$4 \cdot 10^{-10}$
Warm Jupiters known by radial velocity	10^{-8}	10^{-9}	10^{-8}
Warm Neptunes and massive rocky planets	$2 \cdot 10^{-9}$	$4 \cdot 10^{-10}$	$5 \cdot 10^{-10}$

Quasi static aberrations have a dramatic impact and will be measured by a dedicated focal plane wavefront sensor at the XAO focus and scientific wavelengths and feed back the required correction to either the XAO system or to a dedicated 2nd stage corrector located after the XAO. the so called Self-Coherent Camera (SCC) is being considered for the speckle suppression stage. The principle of

the Self-Coherent Camera has been described for example in Baudoz *et al.* 2006 [43]). The SCC takes advantage of the coherence of the speckle with the stellar beam in two ways: to extract the uncorrected residual phase directly from the final science image, or to extract the image of the planet from the residual speckles.

Contrast requirements for the different science cases are resumed on table 1.1. A new science case is included covering the detection and 1st order characterization of Neptune mass planets and massive rocky planets around nearby stars (10 pc) with the ultimate goal of detecting such planets located in the habitable zone (for late type stars and very nearby systems < 4 pc).

2

HOT: The High Order Test Bench

2.1 Objectives and requirements

Several high contrast instruments were foreseen for the actual 10 m telescopes (SPHERE, GPI) and next generation of extreme large telescopes (EPICS). As well, other AO systems (GRAAL, GALACSI, LBT-AO) will be high order systems (over 1000 actuators). In all cases, Shack-Hartmann or pyramid concepts will be used for wavefront sensing.

Simulations confirm the performance expected for HCI instruments but no experiments were carried out to study an end-to-end XAO system that also includes coronagraphic setup.

The HOT bench (Vernet E. *et al.* 2006 [44]) was born with the idea to cover the gap between simulations and fulfilled instruments in order to obtain an experimental feedback. It implements a full XAO system on the MACAO (Multi-application curvature adaptive optics for the VLT [45]) testbench which includes star and turbulence generator mimicking realistic conditions at telescope (spiders geometry, F number ...).

The main objectives can be summarized as ([46]):

- Study and characterize all the possible limitations which could reduce XAO correction.
- Characterize two kinds of WFS, Shack-Hartmann and Pyramid, for XAO. Study the different behavior in terms of linearity, sensitivity to calibration errors and noise propagation. Spatial filtering on the SHS case or modulation for the pyramid, will be taken into account.
- Test bench for new components. New deformable mirrors (MEMS) or EMCCDs are foreseen on next generation XAO systems, as well as new control techniques. It is necessary to check in laboratory their performance and limitations.
- XAO bench for High contrast techniques. It will allow to test and compare the performance of several different types of coronagraphs and new post focal sensing techniques in order to achieve high contrast levels under realistic AO conditions.

The main characteristics to be investigated in order to achieve the previous goals are listed hereafter:

- Reach the ultimate correction on axis using both very high order DM and very high accuracy wave front sensors (optimization).
- Characterize PSF and residual aberrations.
- Study system performance (Strehl, sensitivity, robustness).
- Study contrast level performance and halo suppression.

The bench is designed to fulfill the requirements of extreme adaptive optics ([47]) including:

- Equivalent 8 m telescope (f/50 input beam) design.
- Light source and turbulence generator simulating 0.5” and 0.85” arcsec seeing. Due to limited DM stroke, the low order aberrations are reduced either by phase screen design or low-order first stage correction.
- Pupil mask mimicking VLT or E-ELT spiders shape.
- Low order DM; 60 actuators in order to allow static aberrations correction and turbulence low-order first stage correction.
- High order DM; over 650 actuators and subapertures covering the pupil to achieve a Strehl ratio over 90% in H-band.
- The setup allow separation of NIR science channel, PWS and SHS:
  - SHS wavefront sensor: 31x31 subapertures, 4x4 pixels per subaperture, 2” subaperture field of view, spatial filtering (between 0.3” and 1.5 ” diameter) in the entrance focal plane. Read-noise free CCD.
  - Pyramid wavefront sensor: 4 sided pyramid, tip-tilt mirror for modulation, relay optics allowing 31x31 or 40x40 subapertures. Read-noise free CCD.
- Scientific path including infrared camera (> 5″ FoV to get PSF wings) and achromatic optics for reimaging pupil and focal plane in order to place coronagraphic components (apodizer, Lyot, mask).
- Interfaces that allow DMs and wavefront sensors to be controlled through MATLAB in order to implement a flexible RTC that enhances test capabilities.

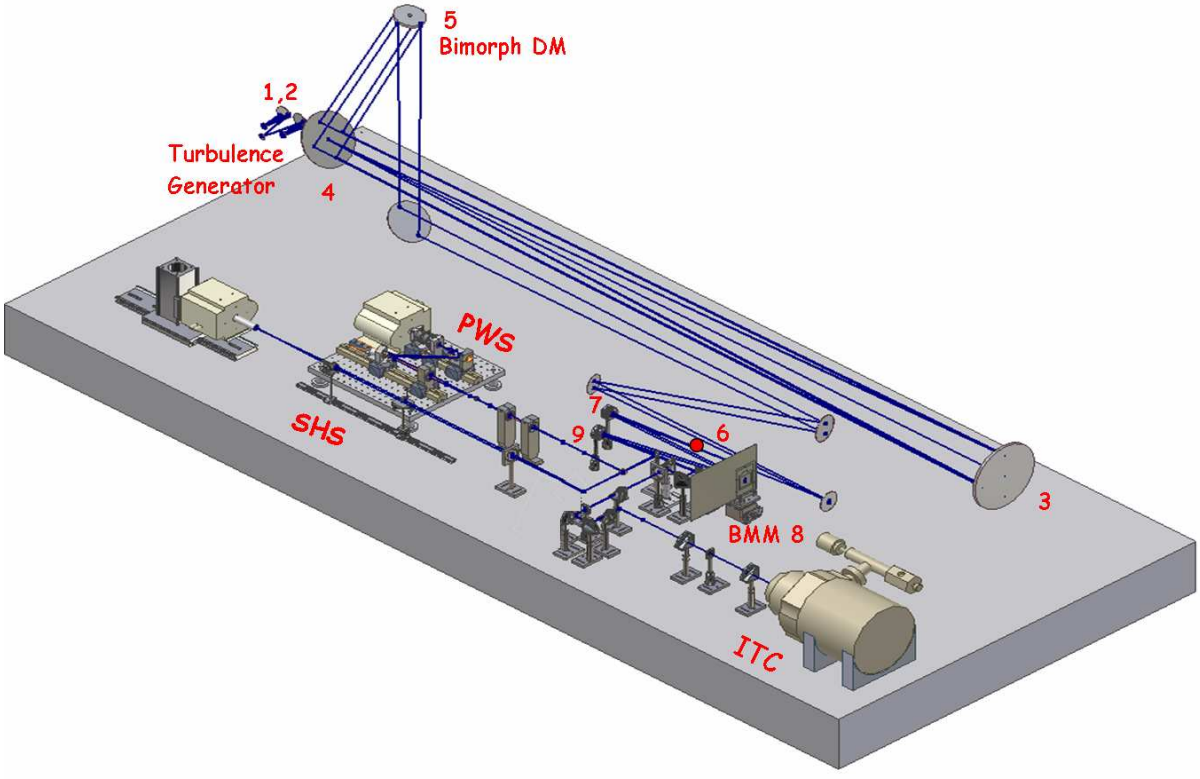

Figure 2.1: 3D view of the *High Order Test bench* optomechanical setup. The test bench table size is 3500 m x 1500 m.

2.2 System overview

2.2.1 Optical setup

The optical set up is described in figure 2.1 and figure 2.2 [48]. The first part of the setup is composed by the original MACAO bench optics that simulate the VLT input beam [49]. Reference sources can be chosen from a number of optical fibers with variable diameters mounted on a wheel (1). Dynamical optical aberrations are generated by a source module with two rotating phase screens which produces an f/16.8 beam (2). A spherical mirror (3) on axis transforms this beam into a converging f/50 beam.

A flat mirror (4), with a central hole simulating the VLT central obstruction (14%), send the beam to the MACAO bimorph DM (5) located at about 1010 mm above the table level, and has its axis tilted of 13.26 degrees (like in the VLT Coudé train). This DM defines the pupil, where different pupil masks can be installed close to its surface. This design provides a field of view of 10 ” in diameter and a diffraction limited image quality with a wavefront error of about 70 nm rms.

The MACAO DM resends the converging beam again to the table level (150 mm). After several folder mirrors the beam converge on the first focal plane (6) where the HOT optical setup begins. Afterwards the beam is collimated with an spherical mirror (f=500 mm) (7) that reimages the pupil plane on the micro DM (8) with an equivalent pupil size of 10.42 mm. A second identical spherical mirror (9) generated a telecentric beam f/47.9.

A cube beamsplitter (50%) (10), placed on the converging beam before the second focal plane, divers the beam in two channels: The sensing channel (visible light, 650-900 nm) and the scientific channel (NIR, > 900 nm). A SHS or a PWS could be chosen on the sensing channel using a folder mirror installed on a magnetic mount (the folder mirror sends the beam to the PWS setup, while without it the beam enters on the SHS setup). The entrance focal plane is placed after this folder mirror (independent focal planes for each sensor).

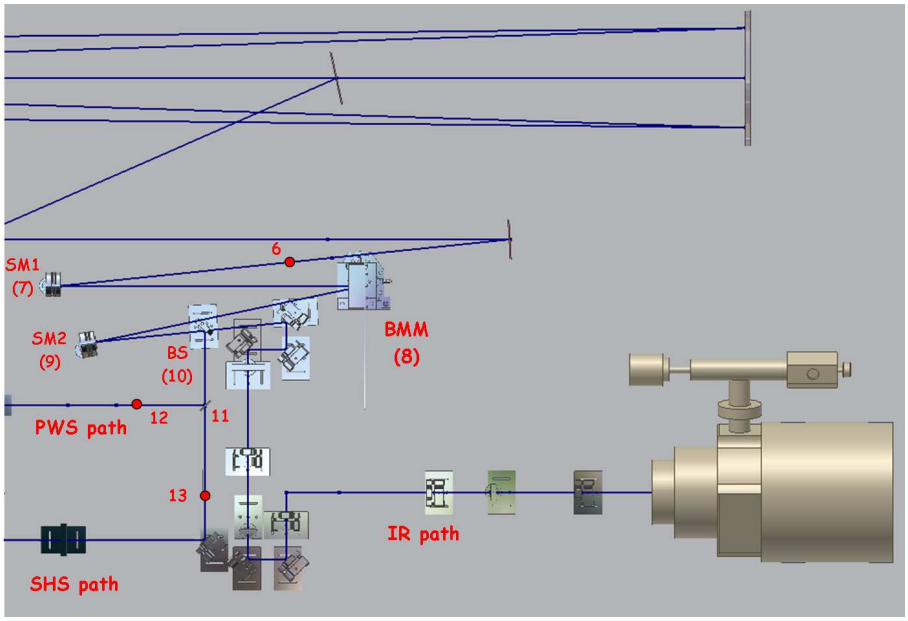

Figure 2.2: Schematic view of the inner HOT setup.

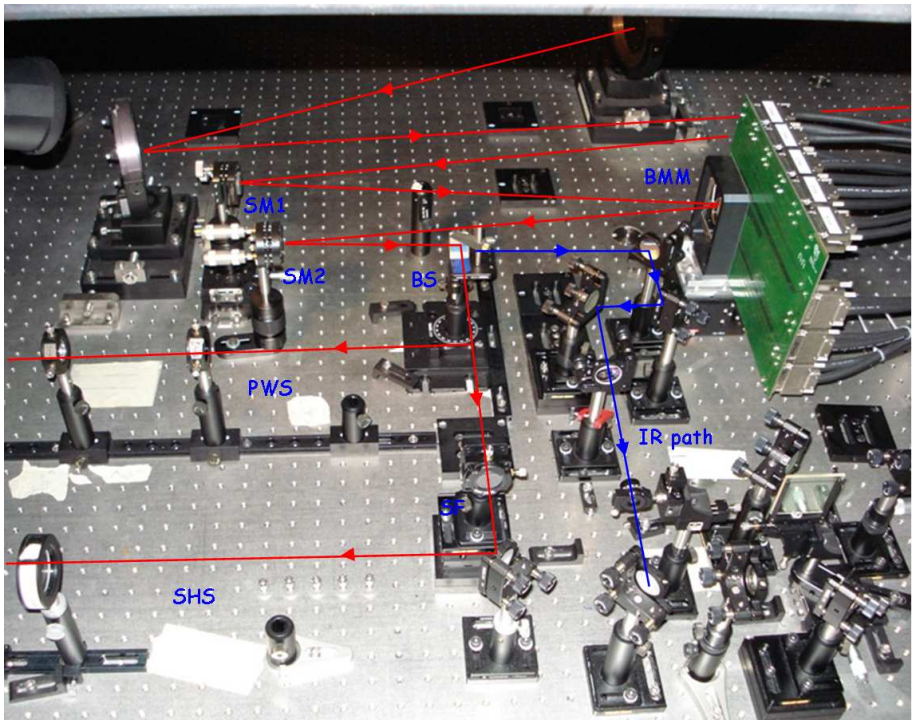

Figure 2.3: Picture view of the inner HOT setup.

2.2.2 Turbulence generator

The turbulence is generated using two phase screens ([50]) in reflection with a diameter of 50 mm. figure 2.4 shows the optical setup which provides an f/16.8 beam. The phase screens can rotate independently so that the atmospheric coherence time can be adjusted. Two spherical mirrors allow to conjugated both phase screens with the pupil plane of the system defined by the bimorph deformable mirror. The diameter of the beam on the phase screens is $\approx$ 6.7 mm.

Phase screens have been calculated for different kinds of seeing:

- 0.5” seeing with reduced low order aberrations.
- 0.85” seeing with reduced low order aberrations.
- 0.65” seeing with full Kolmogorov turbulence.

The low order reduced phase screens are required to drive the micro-DM alone avoiding saturation since the limited actuator stroke (about two microns). The low spatial frequency spectrum of turbulence in this case is the one that would be left after correction by the 60 actuator bimorph DM. The full kolmogorov turbulence phase screens are designed to study the woofer-tweeter concepts where both DMs are driven. The wavefront maps as well as the power spectra of the imprinted turbulence are shown in figure 2.4.

2.2.3 Deformable mirrors

Bimorph DM and tip-tilt mount

The low-order deformable mirror is a 60 element bimorph deformable mirror provided by CILAS company [49]. This mirror was designed for the MACAO adaptive optics systems installed on the VLTI coude focus. The main characteristics of the mirror are listed hereafter:

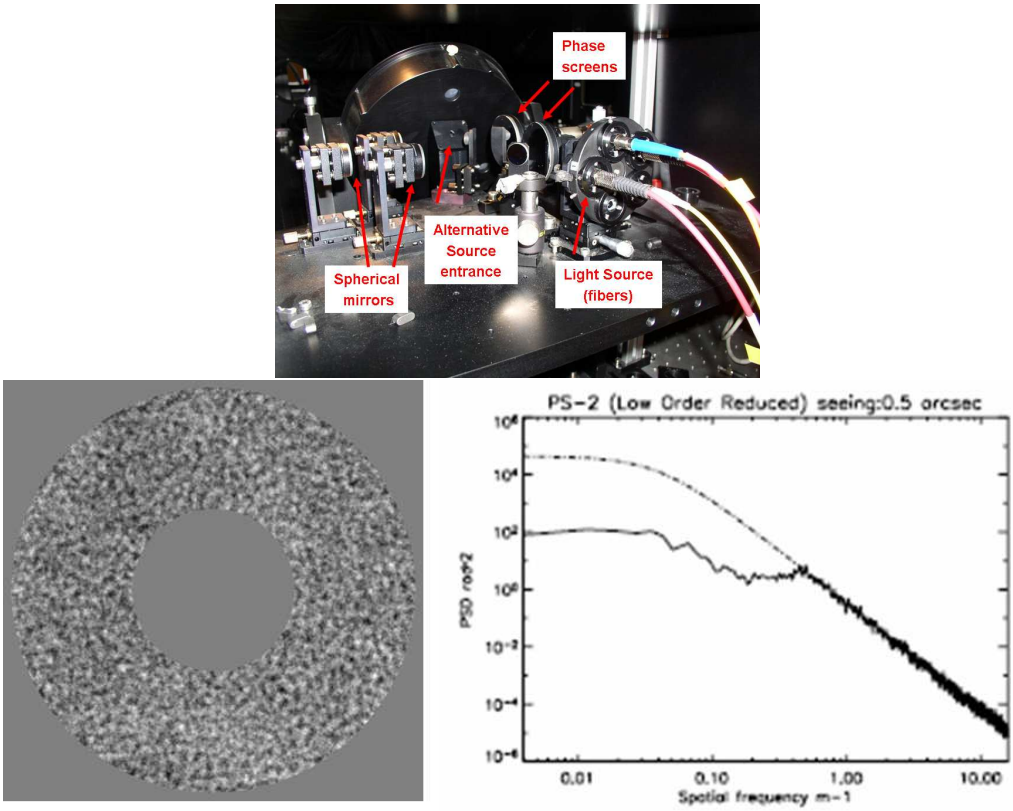

Figure 2.4: **Top:** Picture of the input light source and turbulence generator. **Bottom:** Spatial distribution of the imprinted turbulence for the phase screen (left) and power spectra (right).

- Pupil diameter 98.3 - 101.1 mm.
- Voltages range ± 400V.
- 10 nm rms surface quality.
- Minimum curvature radius: 27 m.
- Curvature stroke to correct a 1” seeing (stroke ≈ 6 um).

The DM is mounted in a Tip/Tilt mount supplied by Observatoire de Paris allowing a correction of up ±3″ at 100 Hz bandwidth.

Micro-deformable mirror

The micro-DM (figure 2.5) is an electrostatic MEMS 32x32 device from Boston Micromachines (BMM) ([51]). Its main characteristics taken from the specifications sheet are listed below:

- 10.8 mm edge length.
- Actuator pitch 340 μm.
- 1.7 mm PTV surface stroke.
- Voltages range 0 - 200V.
- Influence functions with 15% coupling.
- Aluminium coating.
- Surface finish ≈30 nm rms (better in center, worse at the edges).
- 7 kHz bandwidth in atmosphere.

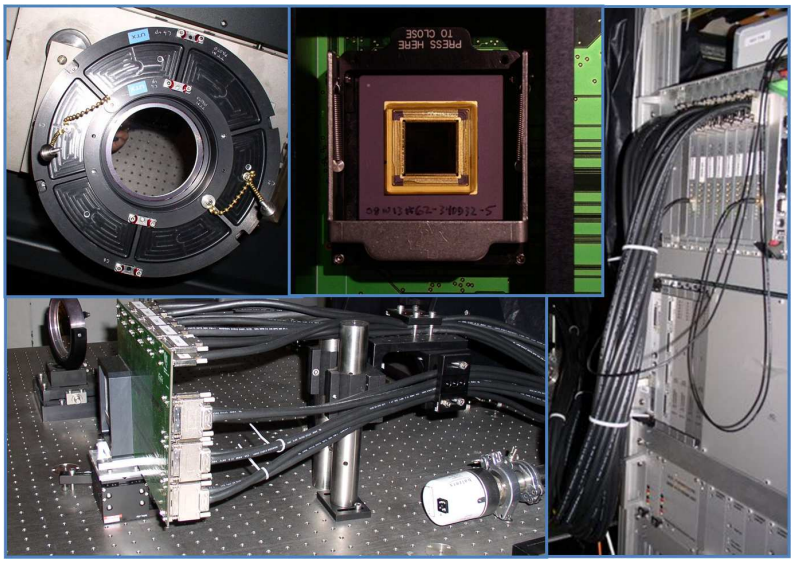

Figure 2.5: **Top-left:** Bimorph DM on the Tip-tilt mount **Bottom:** BMM interface card and wires connections to the HVA. On the front part of the card we could see the black socket where the BMM is placed. **Top-middle:** BMM installed on the card socket **Right:** Electronic cabinet including the BMM, bimorph DM and TTM high voltage amplifiers (HVA).

The BMM is covered by a protective window to keep vacuum conditions since the DM electrodes are susceptible of oxidation under high voltage conditions. Initially two BMM were acquired for the testbed (BMM1 and BMM2). BMM2 present less defective actuators and was selected to carry on the experiments (section 3.2.2). After two years oxidation problems appeared on the BMM and it was not more usable (section 3.2.6). A new device (BMM3) was acquired including an IR coating on the protective window to avoid the ghost problematic found on the previous devices.

By design, 4 actuators are fixed, used as pin connectors for ground and external control. Two of them are placed on the corners, while the other two are placed on the center of the last column, being inside the HOT pupil. BMM3 design is slightly different and all four fixed actuators are placed on the corners of the device allowing a full cleared pupil.

The electronics to drive the micro-DM have been produced by Shaktiware, France. The delay to update the 1024 channels is less than 1 ms and the noise is around 0.02 V (rms). Besides commanding the MEMS1024, Shaktiware also provided a small electronics box that can command the MACAO TTM with ±10V.

The BMM is installed on a customized board and connected to the electronics HVA using 16 cables (2 cables per high voltage board). The high voltage electronics are driven through the *Code Test Tool*, software included on the real time computing *SPARTA platform*, developed to control the next generation of ESO adaptive optics systems. On addition the BMM electronics are reachable trough TCP connection, allowing to be controlled under Matlab.

2.2.4 SHS wavefront sensor

The HOT Shack-Hartmann wavefront sensor designed by the University of Durham ([52]), is modeled with an input beam from a 8 m class telescope with a 400 m focal length (F/50). The WFS provides a plate scale of 0.5 arcsec/pixel, with 31x31 subapertures, each detected on 4 x 4 pixels of a 24 μm pixel CCD.

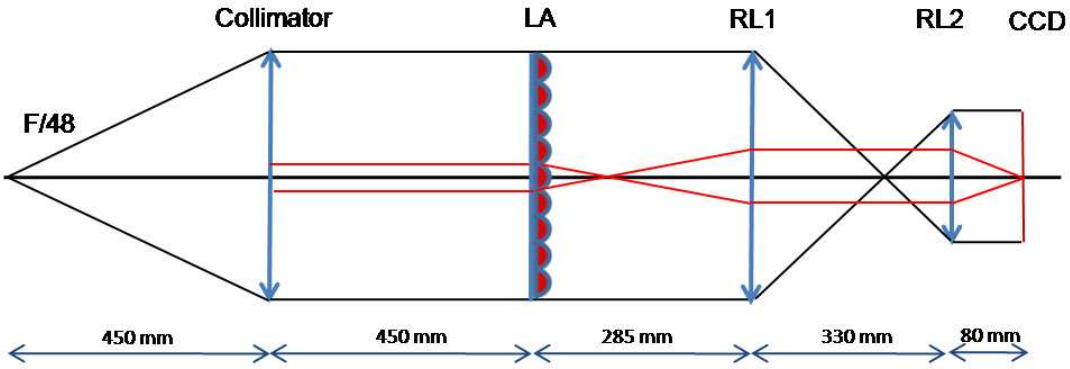

Figure 2.6: SHS design.

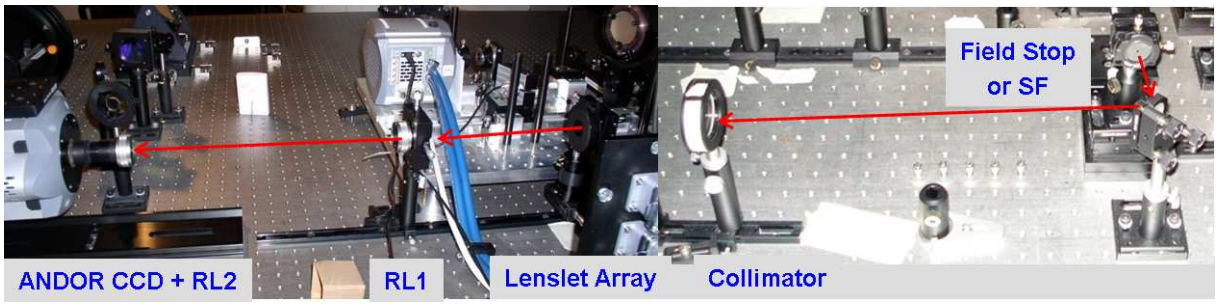

Figure 2.7: Picture of the SHS setup.

Table 2.1: SHS optical parameters

Component	Configuration
Input beam	F/48 (measured on the bench)
Plate scale	0.52 arcsec/pix
Collimator	f=450 mm Pupil size=9.395 mm
Lenslet array	f=35 mm pitch= 0.3 mm subapertures = 31x31
RL1	f=450 mm
RL2	f=80 mm
CCD	pixel=24 μm 4x4 pix per subaperture

The SHS optical design is shown in figure 2.6, and compose of first a collimating lens used to collimate the F/50 input beam. Afterwards, the lenslet array is placed in a position such that it is conjugated with the DM. A couple of lenses are needed as reimaging optics in order to resample the SHS spots onto the CCD at the correct pitch. All optics are placed on a linear rail, allowing easy adjustment of the Z position.

There are three constraints witch determine the characteristics of the optical components used. The input beam (F/50), the plate scale (0.5 arcsec/pix) and the sub-aperture pitch must be 4 pixels (96 μm). Commercial components should have been used in order to reduce costs. This added also a limitation on the pitch/focal length combination of the lenslet array and the range of possible collimating lens focal length.

In order to reduce the effects of aberrations it is recommended to use as long focal lengths as possible for the two reimaging lenses (short focal lengths can result in distortions of the pixel grid at the edge of the array). The final optical parameters found to fit the SHS specifications are summarized on table 2.1.

The detector chosen for the SHS is a 128 x128 pixel electron multiplying CCD Andor iXON L3 ([53]). This camera is a subelectronic readout noise at 400 Hz frames rate working under L3 multiplication gain and a maximum readout rate of 10 Mhz. The camera was characterized to be under specifications, a readout noise value of 0.07 e- rms was measured for the optimum operate mode.

The WFS will also work as a SFSHS (Spatial Filter Shack-Hartmann wave front Sensor) adding pinholes with different sizes on the entrance focal plane of the SHS setup. 1.25, 1.5 and 1.8 λ/d are foreseen to study the performance of the sensor. In addition, a pinhole covering the full 2 arcseconds subaperture will be use on the normal SHS operation to reduce crosstalk between subapertures (the so-called *Field Stop*).

2.2.5 Pyramid wavefront sensor

The PWS for the HOT bench ([54],[55]) is based on the PWFS developed for LBT AO system([56]). The Arcetri Observatory is responsible for the design, integration and first laboratory test of the PWFS. The PWS is an independent module installed on a separate board that match on the HOT bench. The PWS has two possible pupil sampling configurations which are selected by changing the final camera lens. These are a low sampling mode with 31x31 subapertures and a high sampling mode with 48x48 subapertures.

The PWS is designed to have a telecentric input beam with an f-ratio of 16.7. This ensures the correct pupil positions and shape on the final PWS CCD camera. In order to pass from the delivered f/50 beams to the f/16.7 beams the PWS has an auxiliary refocusing system made up of two achromatic lenses (labeled L1 and L2 in figure 2.8 and 2.9).

The PWS design is shown of figure 2.8. The first component is a refocusing triplet (L3) used to converges the beam. Then, a tip-tilt mirror (TT) produces the modulation and send the beam into a folder mirror used to bend the beam. Finally, the converging beam is focused onto the vertex of the pyramid, afterwards a camera lens (L4) adjusts the sampling on the ixon andor CCD (same model used for the SHS).

All the components except the refocusing lenses L1 and L2 are installed on the wavefront sensor board. All mounts can be positioned along the optical axis translating them on the rectified rails. The mounts for the glass pyramid and the camera lens L4 have x and y adjustment to easily achieve the correct sensor alignment.

The Pyramid is designed so to have an angularly well-packed set of four pupils coming out from the pyramid. The base angle of a single pyramid that introduces this separation, for an f/50 input is found to be about 2^o. On our design, the pyramid used is made up of two square base pyramids attached for the base. The double pyramid introduces an angular separation between the two opposite outcoming beams

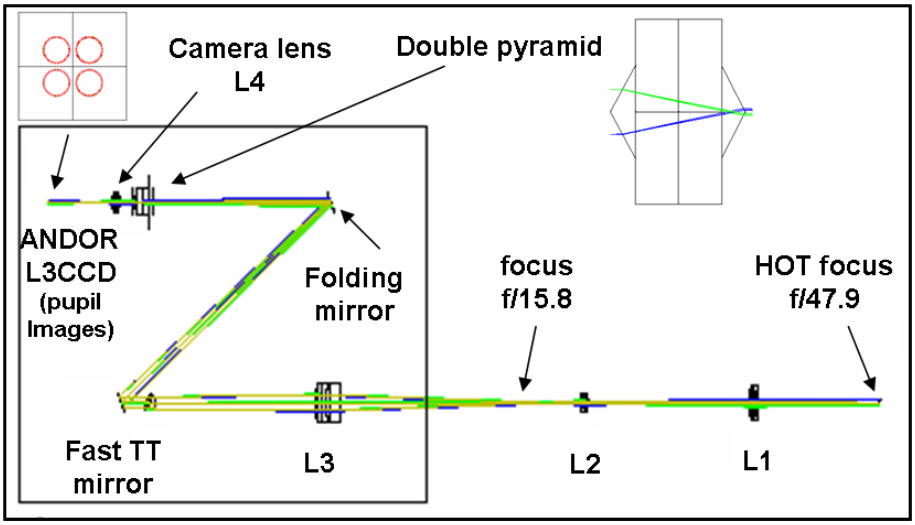

Figure 2.8: PWS design.

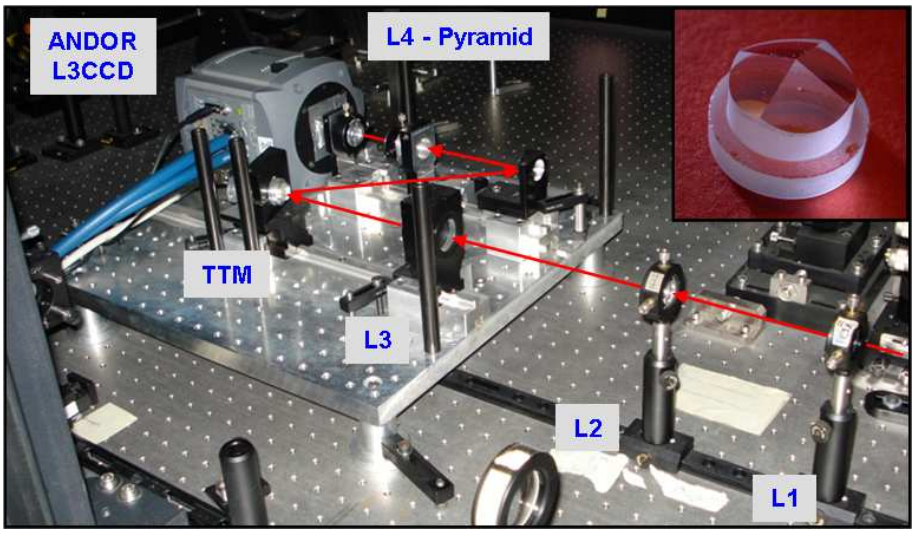

Figure 2.9: Picture of the PWS optomechanical table integrated on the HOT bench. On the up-right, picture of one of the pyramid.

given by:

$$\delta = 2\alpha_1(n_1 - 1) - 2\alpha_2(n_2 - 1) \tag{2.1}$$

where δ is the angular separation, α_1 and α_2 are the two base angles for the two pyramids and n_1 and n_1 are the refractive indexes of the two glasses. The two pyramids are made of N-SK11 and N-PSK53 with respectively refractive index of 1.56 and 1.62 (at 0.6 μm) and they have base angles $\alpha_1 = 30^0$; $\alpha_2 = 28.31^0$. The uses of a double pyramid allows to reduce chromatic effects as well as reducing the confusion circle of the pupils and simplify the manufacturing.

The 36 mm focal length of the camera lens allows to create pupil images having a nominal diameter of 744 μm (31 pixels of the PS CCD having a pixel size of 24 μm). The set of four pupil images created after the pyramid by the camera lens are nominally placed on a square having a side of 985 μm. This corresponds to 41.0 pixels of the CCD detector.

2.2.6 Coronagraph and IR camera

The coronagraphic concept for exoplanets search is described in appendix A. Four types of coronagraph are foreseen to be study on the HOT bench. A classical Lyot coronagraph, an APLC (*Apodized Lyot Coronagraph*), a four quadrant phase mask (FQPM) and a band limited coronagraph.

Classical Lyot and APLC

A detailed description of the Lyot and APLC coronagraphs could be found in Patrice *et al.* 2008 ([57]). A large range of Lyot mask diameters have been manufactured (for the classical Lyot and APLC) using wet etch lithography process on BK7 glass by Precision Optical Imaging. They are made by Cr deposit (+Al) to reach an OD of 6.0 at 1.65 microns.

Nine different Lyot masks have been developed with diameter starting from 2.25 λ/D to 14.40 λ/D. All these masks were deposited on the same glass substrate (λ/4) (figure 2.10 with AR coating on both faces and allows the selection of a different mask simply by translation along the x and y directions. In parallel GEPI (company) has produced individuals Lyot masks (4.5, 4.9, 7.5 λ/D) using Cr deposition (+Au) with the same requirements for the OD. In both case accuracy on the mask is close to 1 micron on the diameter and each mask are perfectly circular and clean.

The second component of the Lyot coronagraph is a pupil stop placed after the Lyot mask. The pupil stop reproduces the pupil shape of the VLT (defined by the mask placed at the MACAO DM) where the inner and outer radii have been increased or cut by 80% respectively. It was manufactured with laser-cutting technique (substrate diameter is 12.7 mm and the pupil size is 3 mm). The Apodized Pupil Lyot

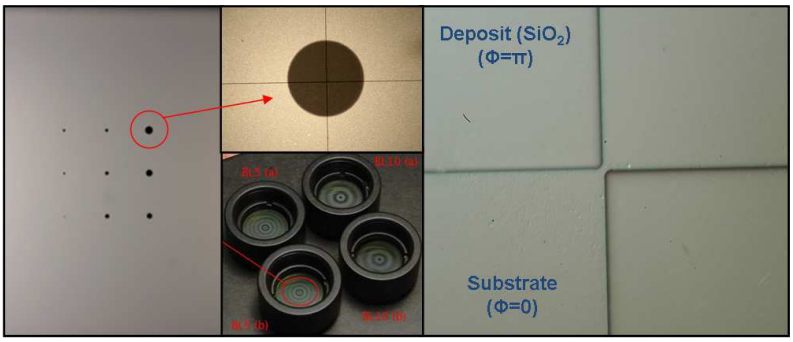

Figure 2.10: **Left:** Set of 9 Lyots manufactured on the same substrate. **Top-middle:** Microscopic inspection of one of the Lyot masks. **Bottom-middle:** Band-Limited prototypes in microdots **Right:** Microscopic inspection of the FQPM center showing the transitions.

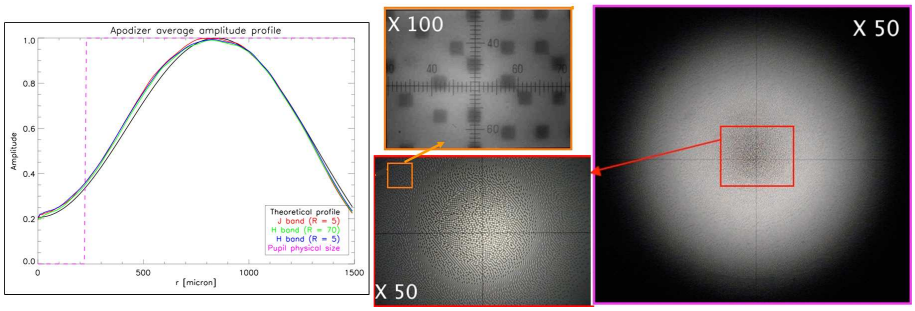

Figure 2.11: **Left:** Apodizer azimuthally average profile (from center to the edges) using different filters (J, H and narrow H band) compared to specification. **Right:** Metrology inspection of the microdot apodizer of the APLC (3mm diameter on a 12.7 mm substrate). Profile accuracy is about 3%.

Coronagraph (APLC) combines a pupil apodization with a small hard-edged focal plane occultor (Lyot mask) and an undersized pupil-plane stop (annexe A).

The APLC configuration (focal mask diameter and corresponding pupil apodization function) usually refereed with the mask size diameter (here 4.5 λ/D) has been selected taking into account HOT characteristics such as the ratio of the central obscuration of the VLT-pupil. This configuration is representative of the one developed for the SPHERE instrument (IRDIS) defined as a 4.0 λ/D APLC.

The apodizer was manufactured with a halftone-dot process, using a binary pattern instead of the classical continuous deposit. Such *"microdots apodizer"* is an array of pixels that are either blocking or letting through the incident light. It is fabricated by lithography of a light-blocking Cr layer deposited on a transparent glass substrate (BK7, λ/20). The transmission profile could be find on figure 2.11. More details of the design and performance of microdots apodizer could be find in Patrice *et al.* 2009 ([58],[59],[60]). The APLC pupil-stop is very similar to the entrance pupil. In principle the APLC pupil stop is identical to the entrance pupil. However a slight adjustment for alignment error issue is required.

Four-Quadrant Phase Mask

As well as the APLC, the Four-quadrant phase mask (FQPM) is one of the coronagraph foreseen on SPHERE. Although on the SPHERE case is achromatic, while the device develop for HOT is chromatic ([57]) .

The four-quadrant phase mask, being a focal plane phase mask, split the focal plane into four equal areas, two of which are phase-shifted by π. The mask consists of a glass substrate (INFRASIL 301) of 3 mm with a 2 μm thick SiO_2 layer deposited on two of the quadrants (figure 2.10). this design ensures the desired phase shifting for an operating wavelength of $\lambda = 1.65\mu m$. In addition anti reflection coating was added to the two faces. For this case, the pupil stop is mostly reduced in diameter with respect to the VLT-like pupil.

Band limited

The microdots technique have been also extended for the manufacture of a Band-Limited coronagraph (BLC), not considered in the first place for HOT experiment. Like the APLC, BLCs are improvements of the Lyot coronagaph. Two BLC coronograph were designed applying a function (1-sinc) and with inner working angles of 5 and 10 λ/D respectively. Assuming availability of adapted pupil-stop, the BLC prototypes can be used with any kind of entrance pupil.

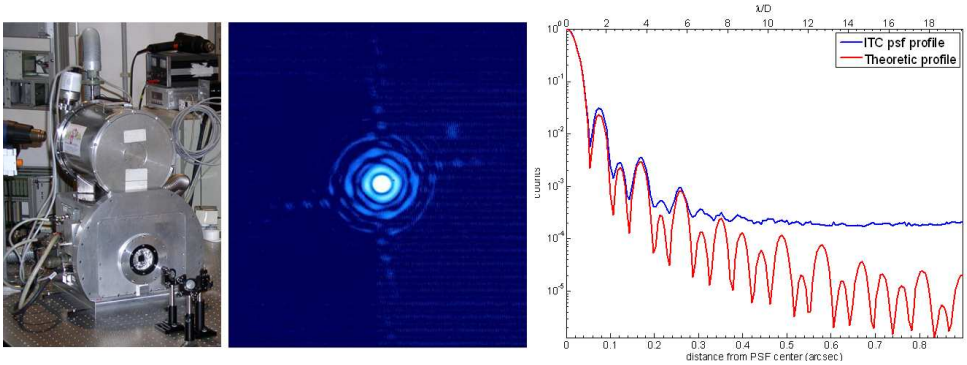

Figure 2.12: **Left:** *Infrared test camera (ITC)* including the cryogenic circuit. **Middle:** PSF imaged obtained with the ITC on the IR path showing an optical quality of 95% SR. **Right:** PSF profile (blue) compare with the theoretic one (red).

IR camera

The original infrared camera *RASOIR* foreseen for HOT, was substituted with the Infrared Test Camera (ITC) because of vacuum leak problems. The ITC detector is a Hawaii array (1K x 1K) with 4 quadrants (512 x 512). The camera incorporate internal optics designed to enable a pixel-scaled of 5.3 mas/pix. The camera is cooled until 103 - 107k with nitrogen under vacuum conditions of 10^{-5} – 10^{-6} mbar for optimal performance.

The camera software control offers a continuous image mode. It gives the possibility to record individual frame sequences and for long exposure time the camera records short images and give the mean image as result.

The ITC offers the possibility to use different filters (J,H,K) narrow and broadband placed on an internal wheel. For the HOT bench is used the broadband H filter (centre at 1.6 μm $\nabla\lambda/\lambda$ = 20%) combined with a H narrow external filter placed in front of the ITC window (centre at 1.6 μm $\nabla\lambda/\lambda$ = 1.4%).

Since the light intensity will be defined by the WFS, it will be necessary to place different neutral densities in front of the ITC to avoid saturation but ensuring the maximum signal.

IR optical setup

The IR optical setup is designed to reimage several times the pupil and focal plane, thanks to a set of achromatic lenses, in order to place the different coronagraphic components. In addition the IR setup could work independently from the rest of the HOT bench installing a fiber on the input focal plane, allowing to test the coronagraphic components on ideal conditions. An optical quality of 95% SR was measured (figure 2.12) for the independent IR setup.

Figure 2.13 shows the scheme of the IR setup. After the beamsplitter the F/48 beam converged on a new focal plane. Afterwards a lens collimates the beam and a new pupil plane is reimaged (3 mm of diameter) where the apodizer is placed (for the APLC case). A new achromatic lens converge again the beam on a focal plane where the lyot or FQPM mask block the light. The beam is collimated a last time to recover the pupil plane where the coronagraph stop is superimposed to the VLT pupil mask. Finally a new lens is used to reimaged the focal plane on the ITC.

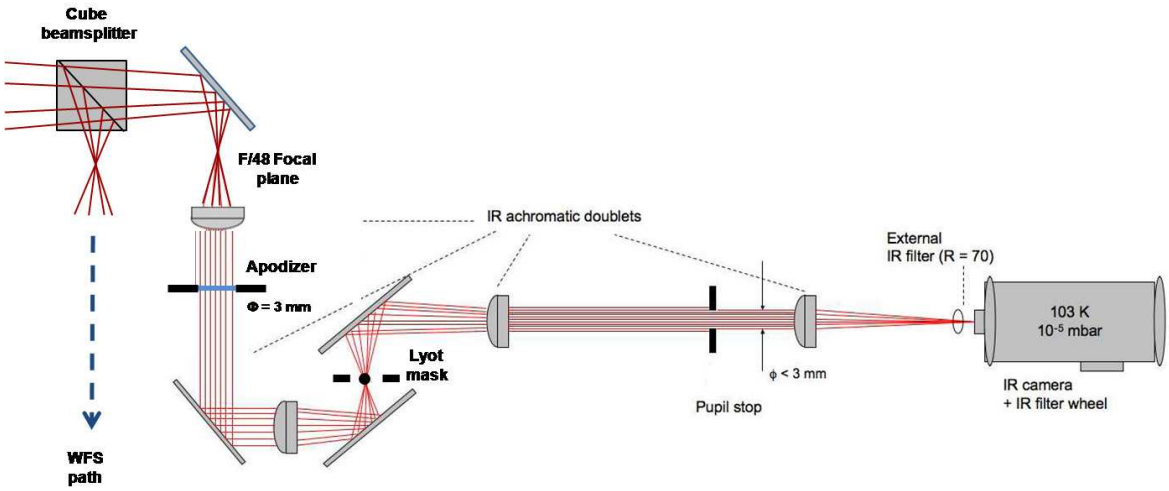

Figure 2.13: SHS design.

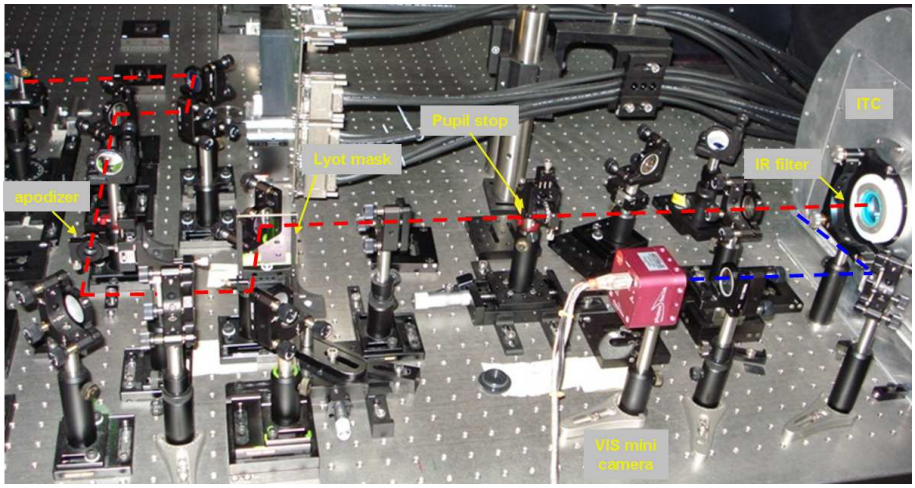

Figure 2.14: Picture of the IR setup showing the beam path. The blue path corresponds to an alternative path (thanks to a flat mirror in front of the ITC) used to reimaged the pupil on a visible camera in order to align the different pupil components.

2.2.7 System interface and Real time computing

The RTC interface design for HOT is based on the ESO *SPARTA light platform* ([61]). The idea of the *light* version is to achieve a full RTC system at low cost and complexity using CPUs. In addition the control has to be flexible to allow easily testing of different configurations, all controlled through high level languages (Matlab, IDL, python ...).

The complete interface scheme of the HOT RTC is showed on figure 2.15. The RTC is implemented on a linux PC with access to the different subsystems. The control system requires communication with 3 subsystems: the bimorph DM, the BMM, the TT mount and the ANDOR CCD. The voltage output signals applied to the BMM and the TTM are drive through the HVA (High voltage amplifiers) controller. In the other hand, the input ANDOR CCD signals are driven through the internal controller card.

The access to the HVA is done through a TCP connection. The HVA controller accepts two types of connections: HKL or HSDL. The HKL (*House-Keeping Link*) allow to apply the state commands (online, standby, voltage status, offline) and it also allows to apply voltage patterns, but at low speed. The HSDL (*High Speed Data link*) is designed to send voltage patterns at high speed in order to achieve RTC requirements. In addition the HVA can be controlled externally using the *Code Test Tool* software to apply status commands and load voltage configurations through *fits* files.

The ANDOR controller is accessible through a FPDP connection (Front Panel Data Port). The data stream coming from the CCD is received by the *WPU emulator* on the linux PC. This WPU (Wavefront Processing Unit) computes, on real time, the slopes from the CCD pixels frame allowing slopes and pixels to be accessible to the RTC using a set of C functions. This job is done by software in the same way as a FPGA processor card. The pixels coming from the WPU are also accessible to the VLT software RTD (*Real Time Display*) for visualization on real time.

The control of the bimorph HVA is integrated on the RTC software of the MACAO instruments. Thus, it is only possible to set commands of status, apply voltage patters using fits files and apply different zernike shapes to the DM. With this configuration it is not possible to perform a close loop control between bimorph and WFS. Only in the last phase of the project the HVA was modified to allow access through FPDP, hence controlled by the HOT RTC. Quite all the experiments showed on this work were performed without this option.

The user control of the different subsystems and the RTC software is foreseen to be developed under MATLAB. MATLAB can performed a TCP connection through internal functions (*pnet*), allowing the

HVA access. MATLAB has the possibility to link to C code using MEX function. A set of this functions where already developed to allow access to the slopes computed by the WPU emulator.

To simplify the control it will be necessary to developed with MATLAB a higher control layer through two *classes*. The *HVA* class will include the functions to perform the TCP access and will allow to send voltages to the HVA on the correct units. On the other hand, the *WPU* class allow the connection and control of the WPU, allowing access to the slopes and pixels, configure the background, etc. In addition, a set of general functions will be developed for different actions as the slope visualization, calibration, alignment.

The development of A GUI (*Graphical User Interface*) will be necessary for the loop control of the RTC: close loop, load configuration, gain control, offsets, etc. The MATLAB utilities developed for HOT RTC will be described deeply on section 4.6.

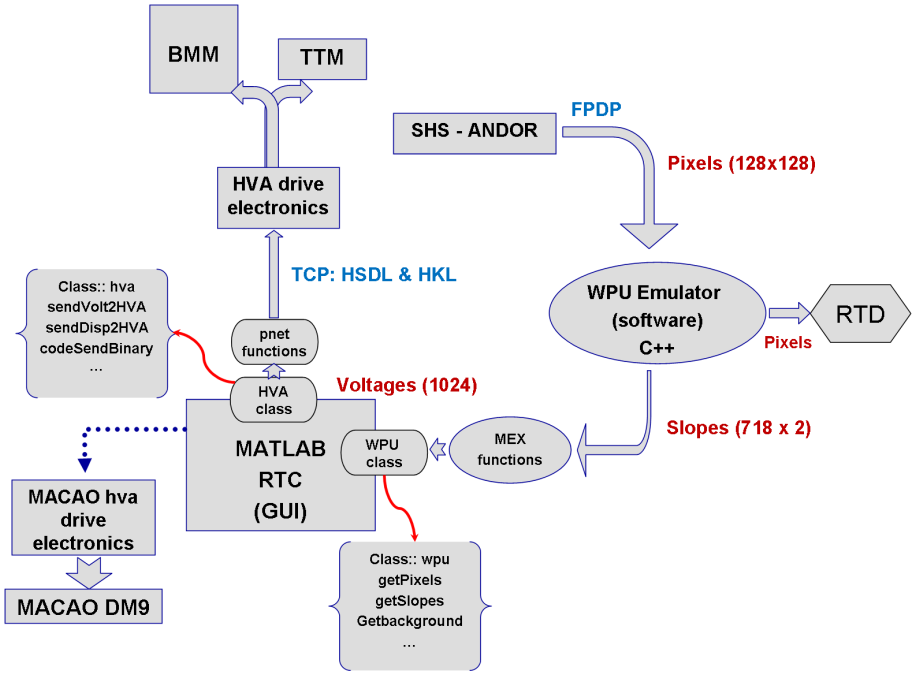

Figure 2.15: HOT RTC interface scheme.

3

Subsystems integration and characterization

In this chapter we will describe the different steps followed to obtain a full operating system. A summary of the integration and characterization can be found in Aller-Carpentier *et al.* 2008 and 2009 ([62], [63]). On the actual bench status, the MACAO bench components are already installed and aligned. Instead of the phase screens, two flat mirrors are used in the turbulence generator during the installation and characterization phase.

The spherical mirrors are placed in the HOT common path and the BMM is conjugated with the pupil. Instead of the beamsplitter, a flat mirror is currently used to redirect the beam to the wavefront sensing arms. The PWS is installed and aligned on the bench and initial tests were performed ([55]). Initial characterization tests for the BMM and the ANDOR camera were already done ([51] and [53]).

The different subsystems operations required are listed hereafter:

- Measurement of the bimorph influence functions and flattening the mirror with the techniques already developed for the MACAO bench. The IF information is necessary to estimate the voltage patterns to compensate static wavefront aberrations.
- Characterization of the BMM including: Stroke vs voltage behavior, bias voltage, coupling, bad actuators, BMM flatness and IFs. This information is required for the modal control.
- Testing of the optical quality of the bench. It is necessary to minimize static aberrations to avoid actuator saturation in closed loop operations.
- Installation, alignment and characterization of the Shack-Hartmann wavefront sensor.
- MATLAB utilities development for measurement, characterization, calibration, analysis and control.
- Once the system is operative, the flat mirrors in the turbulence generator will be substituted by the real phase screen. Characterization of the turbulence in terms of speed using the SHS will be necessary.
- Installation of the beamsplitter and IR path.

3.1 MACAO bimorph deformable mirror

An independent optical setup installed on the bench allows to reimage the bimorph DM on a commercial SHS wavefront sensor: the HASO 64x64. This WFS is used to measure the shape of the DM and the influence functions. The IF are measured by applying 64 Hadamard patterns (see section 4.2.1) and recording the wavefront measured by the HASO. This process is done on a loop thanks to a trigger

signal. Afterwards the IF are used to compute a Zernike base for the mirror. This modal base is loaded by the SPARTA RTC software of the DM which can apply different Zernike shapes to the DM.

The next step is to flatten the DM. The HASO software offers on real time a Zernike decomposition of the aberrated wavefront sensor. In this way we could flatten the DM by applying different Zernikes. The flatness accuracy obtained is around **50 nm** rms. The voltage pattern obtained afterwards was recorded and used as a bias pattern for the DM.

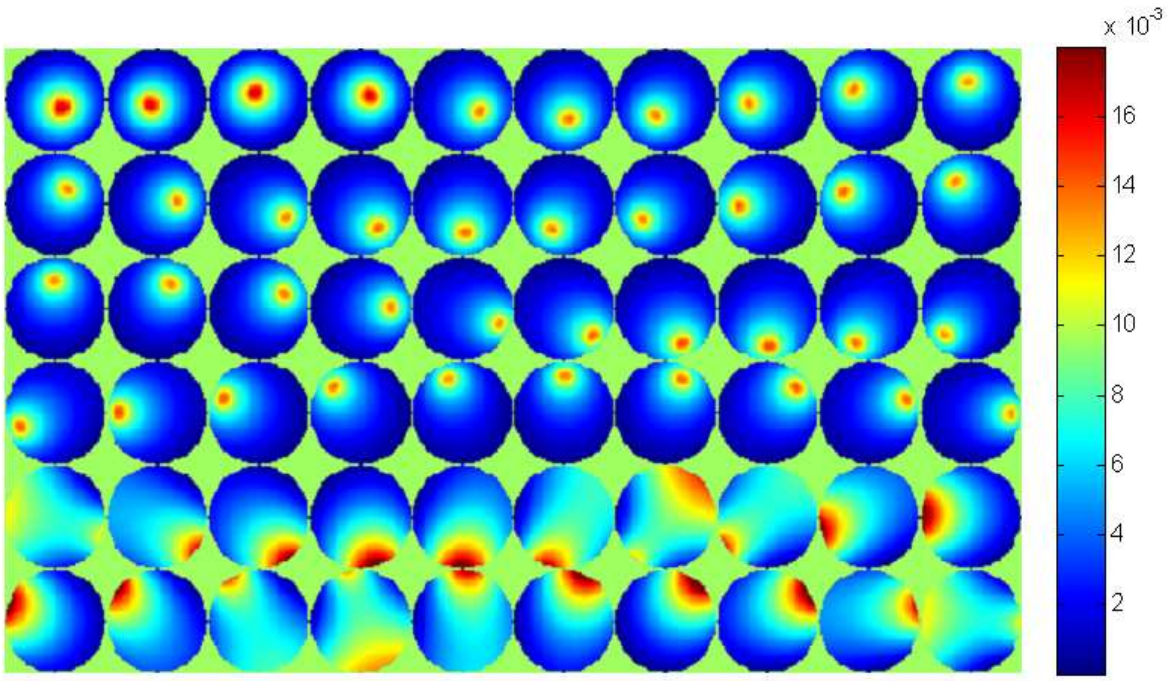

Figure 3.1: Measurements for the 60 IF of the bimorph DM. Colorbar in $\mu m/V$.

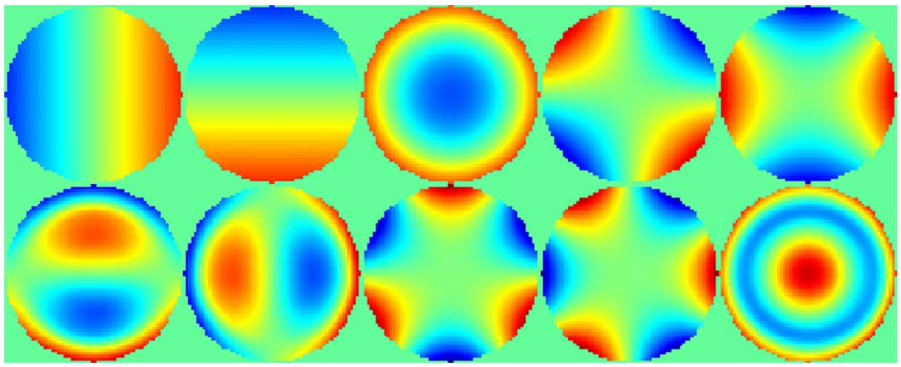

Figure 3.2: Wavefront reconstruction for the first 10 Zernikes using the bimorph IF (Tip, tilt, focus, astigmantism X and Y, coma X and Y, trefoil X and Y and second order spherical).

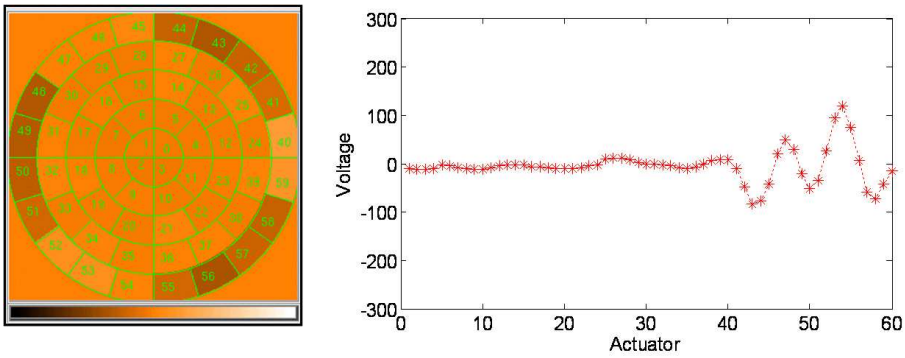

Figure 3.3: **left:** Actuator map distribution for the bimorph DM. **right:** Actuators voltage pattern applied to flatten the DM.

3.2 BMM's mirror characterization

As explained on section 2.2.3, three BMM's were acquired for the bench. BMM1 and BMM2 at the beginning of the project while BMM3 was purchased at the end. To avoid confusions, it will be specified for each experiment in this thesis which BMM is used. We will introduce in this section the characterization of the micro-DM's in terms of:

- Mirror flatness.
- Defective actuators.
- Stroke behavior.
- Bias determination.
- Influence functions measurements.

BMM1 and BMM2 characterization was done using the interferometer uPhase 2 HR from FISBA optik. The FISBA is a Twyman-Green phase-shifting interferometer with a camera of 1024x1024 pixels (HeNe laser, λ =632.8 nm). Since the FISBA pupil size (10 mm) is smaller than the BMM and no reimaging optical setup was foreseen, the DM was measured in four sectors, displacing the FISBA along the DM. Each time a sector is measured, an additional reference image is recorded in order to recover the relative position between sectors and reconstruct a full BMM image (since a common area is always measured in the four sectors). The reference image is obtained applying a voltage pattern to the DM that reproduces a cross within a frame covering the first and last row and column (figure 3.4).

After reconstruction, the final image of the BMM surface covering the 32x32 actuators has a resolution of 986x986 pixels. This resolution corresponds to an interactuator distance of 31.5 pixels (1pix = 10.8 μm).

3.2.1 Mirror flatness

MEMS deformable mirrors show a strong slope in the edge caused by the manufacturing process. This effect normally limits the useful mirror area and reduces the number of available actuators. The mirror surface is measured on the rest position at 0 V. Figure 3.4 shows a 3D view of the mirror surface. An inner region of $\approx$ 6.7 mm is flat to $\pm 50nm$, while the edges show an increasing slope whose maximum difference in height reach 700 nm (figure 3.5). This mirror slope will produce an aberrated wavefront and the optical quality of the bench will be reduced since it is foreseen to use a circular pupil covering the maximum BMM area.

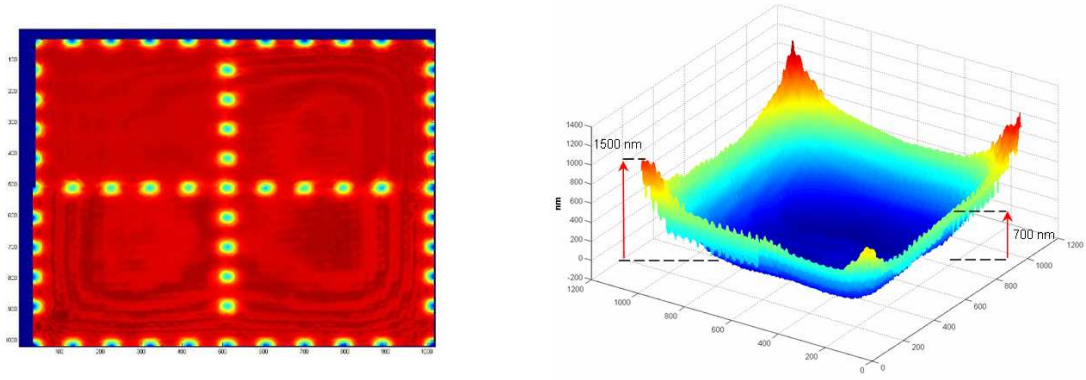

Figure 3.4: **Left:** Reconstructed BMM surface image showing the voltage pattern used as reference. **Right:** 3D view of the BMM1 surface showing a flat area in the center and an increasing slope in the edges with a maximum difference of 1500 nm in the corners and 700 nm in the edges .

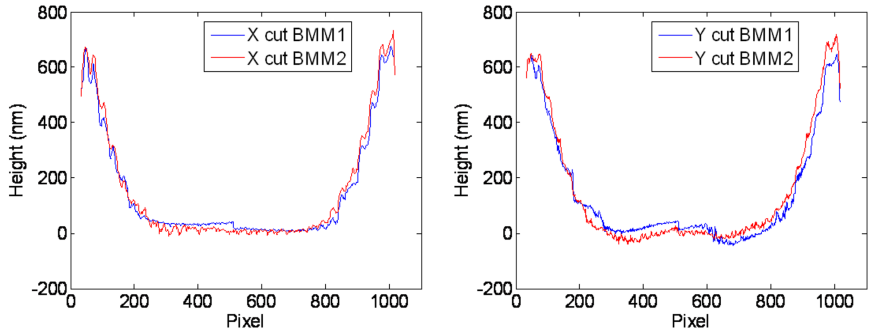

Figure 3.5: BMM1 and BMM2 profile cuts along the X and Y axes showing a flat area in the center covering about 12x12 actuators.

3.2.2 Defective actuators

As explained before, Boston Micro-deformable mirrors are designed with 4 inactive actuators used as pin connectors (two for ground and two for TT control). In the case of BMM1 and BMM2, two of these actuators are placed on column 31, row 15 and 17, and therefore on the mirror edge but inside the pupil.

Two types of defective actuators are found on the devices: stuck and floating actuators. Stuck actuators are blocked at 0 V position, thus when the mirror is settled at the bias (mid voltage range) a peak appears in the wavefront since the actuator remains alone on the rest position (inactive actuators also produce this effect in the wavefront since they behave as stuck actuators).

On the other hand, floating actuators do not respond to the voltage applied and therefore are uncontrollable, but they are free-moving since they are linked to the mirror membrane moving together with the rest of the actuators. Some of these actuators are linked to a neighbor actuator, moving in pairs. These type of actuators are less harmful since they do not aberrate the wavefront even if they cannot be used to correct the wavefront.

A stuck actuator was found on BMM1 inside the pupil, while BMM2 shows only some floating actuators. BMM2 was chosen to be used on the bench for our experiments and we will refer to it in the next sections.

Figure 3.6 shows the distribution of defective actuators. A pair and a group of three linked actuators are found inside the pupil. In addition, a floating actuator and a pair of linked actuators are found outside the pupil.

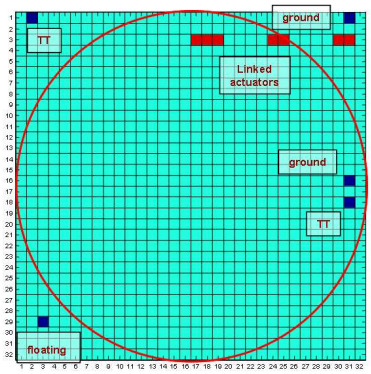

Figure 3.6: BMM2 actuator map showing the defective actuators distribution.

3.2.3 Characterization of a standard actuator

An actuator in the center of the mirror (actuator 690, row 22 column 18) was chosen somewhat arbitrarily for response investigation. The response curve should be obtained by pushing only a single actuator while all others are left at the ground potential (0 V). In our case, this is not possible due to interferometer limitations for measuring the stroke curve for the higher voltages. Instead, another option consists in pushing one actuator while the others were left at a bias voltage (mid range of the response curve). An approximate bias value is used initially (100 V by manufacturer specifications). The real bias value could only be found after knowing the actuator stroke response.

The stroke versus voltage curve was measured applying voltages between 0 and 200V (figure 3.7). A quadratic response was found between **0 and 163V**, at higher voltage this behavior is lost due to non linearity effects on the membrane stress. The quadratic range defines the working range of the BMM. The response curve measured by the manufacturer shows a full working range between 0 and 200V, which is not true from our measurements.

Now it is possible to find the correct bias position by applying different bias voltages to all actuators (between 109 and 116V). For each bias position we measure the stroke produced by a single actuator when applying the maximum and minimum voltage (0 and 163 V). The correct bias is found when the stroke produced on both directions is the same. This condition is fulfilled for a bias of **114 V**.

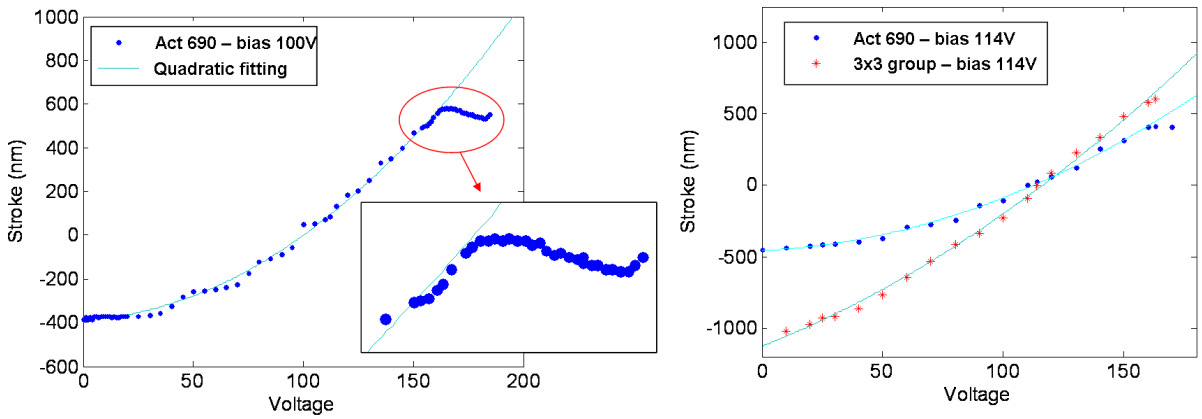

Figure 3.7: **Left:** Stroke response for the actuator 690 (bias 100V), the solid line shows the quadratic fitting. At high voltage the quadratic behavior is lost as shown on the window zoom. **Right:** Stroke response curves showing the differences between a single actuator and a group of 3x3 actuators. For a group of actuators the response is less quadratic.

The response curve of the actuator is measured again setting the bias at 114V. A second curve (figure 3.7) was measured activating a group of 3x3 actuators. The curve shows a quadratic behavior but less strong than for a single actuator. This effect is normal since the membrane restoring force depends on the surface area displaced (section 1.2.2, equation 2.1).

The interactuator stroke (single actuator) measured is **0.86** μm, while the mechanical stroke (group of 3x3 actuators) corresponds to **1.53** μm. Actually, these values are only approximate since the real interactuator and mechanical stroke should be measured at the ground potential as defined on section 1.2.2.

3.2.4 Influence functions measurement

Influence functions correspond to the measurement of the spatial response for each actuator. Two images are recorded, the first with positive displacement (up) and another with negative displacement (down). The down position is obtained by applying 75% of the voltage range, i.e. 151V. To obtain the up position we look for the voltage that produce the same displacement, but positive, in this case, 60V (remember, a voltage higher to the bias, corresponds to an actuator contraction, i.e. negative wavefront, while a lower voltage corresponds to a relaxation, i.e. positive wavefront).

The final IF for the actuator i is obtained as the subtraction of the up and down images following the equation:

$$IF(x,y;i) = \frac{up\_IF(x,y;i) - down\_IF(x,y;i)}{2} \tag{3.1}$$

In this way, the static errors are removed from the measurements. Afterwards, the influence functions are expressed in units of nm/V.

It is necessary to measure 1024 actuators (2048 images), but an automatic trigger system was not foreseen. Since the influence function area is not bigger than 3 actuators pitch, it is possible to measure simultaneously several IF without coupling problems. 9 actuators were measured simultaneously for each quadrant, (placed at a distance of 5 pitches from each other) (figure 3.8). In this way, the number of images recorded is reduced to 292.

The images are post-processed to recover the individual IF. Each image is corrected of residual tip-tilt, afterwards, the IF for each actuator is copied from the original image and placed on an empty matrix taking into account the relative position between actuators. The final result (equivalent to record an image

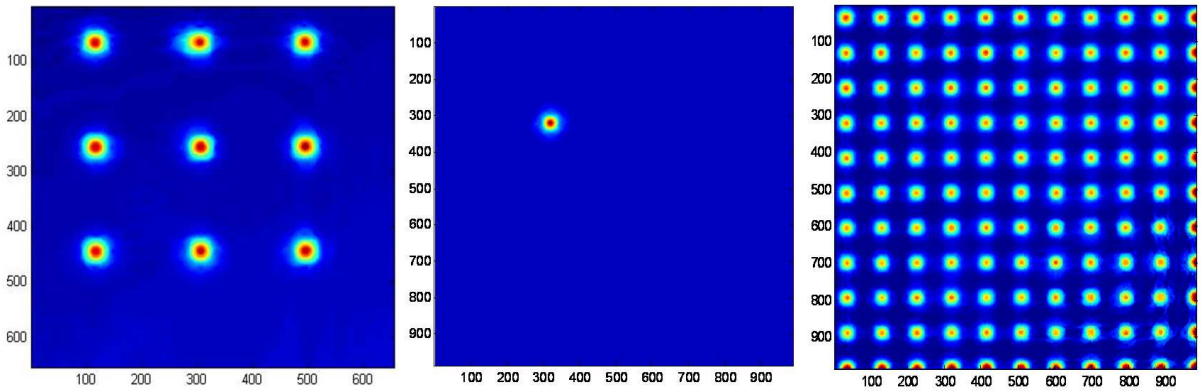

Figure 3.8: **left:** IF raw image of the up-left quadrant showing the 9 actuators configuration in the up position. **center:** Example of one of the processed IF (actuator [11,11]), the image size corresponds to the full BMM. **right:**. Montage image showing the IF's of several actuators together.

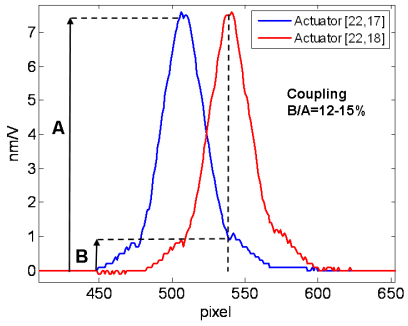

Figure 3.9: Y profiles of two contiguous actuators showing an actuator coupling of 12-15%.

for each individual actuator) is a datacube of 1024 images with a resolution of 986x986 pixels. The data cube is resize to a lower resolution of 248x248 pixels in order to reduce memory and time computing requirements.

The coupling between actuators could be measured superimposing the IF profiles of two contiguous actuators as shown in figure 3.9. 12-15% of coupling was measured for the BMM (as defined on section 1.2.2).

3.2.5 The third Boston micro-machine mirror

A new BMM was acquired to solve the problems of dead actuators (section 3.2.6) and ghosts. The new BMM characteristics are the same as previous BMM's, but with a good IR coating in the window (R_{avg}<1.5%, 550-1800 nm) and a stronger wedge (angle of 6 degrees between protective window and mirror) in order to avoid the ghosts. Another difference is the position of the 4 inactive actuators, now all are placed outside the pupil, in the corners of the mirror.

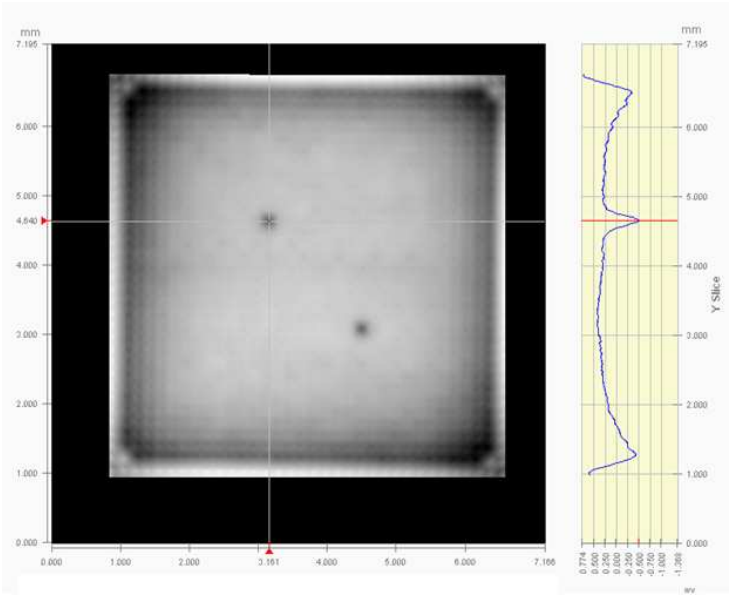

Figure 3.10: Surface image of the BMM3 obtained with the 4D interferometer. The BMM was placed at the bias position while two actuators are set at maximum stroke. The curve on the edge shows the profile along the x axis through one actuator revealing the shape of the mirror (surface in waves, $nm = wv * \lambda, \lambda = 632.8nm$.

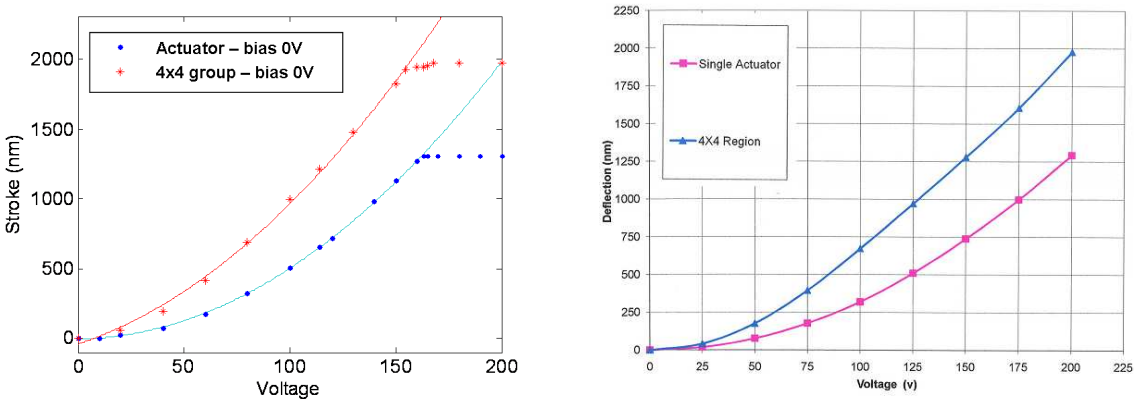

Figure 3.11: **Left:** Stroke response curves for a single actuator and a group of 4x4 actuators. In this case the rest of actuators are kept at the ground position (0 V). **Right:** Same curves provided by the manufacturer. In this case, the actuator response is quadratic until 200V which is not true from our measurements.

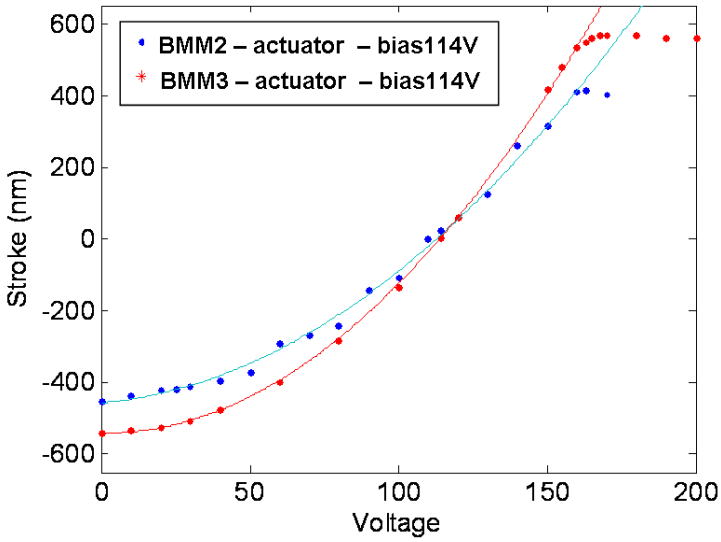

Figure 3.12: Stroke response curves comparing BMM2 and BMM3 for the case of a single actuator at the bias voltage. The curves show that BMM3 has a stroke 0.25 μm higher than BMM2.

BMM3 was characterized using a new interferometer, the PhaseCam 4020 from 4D technology. The PhaseCam is a phase-shift interferometer insensitive to vibrations based on a Twyman-Green design and a camera of 1kx1k pixels. The laser source is a HeNe center in 632.8 nm. The main advantage of this interferometer is the high accuracy (rms precision better than 0.002 waves). The collimator beam diameter is 7 mm, although for this case a reimaging system was implemented to expand the beam in order to cover the full mirror.

No stuck actuators were found and only a group of 3 floating actuators were detected on row 31 close to the pupil edge. The flatness of the mirror keeps the same properties as before with a maximum difference on height of **670 nm**. If the mirror is set to the bias value (114 V) the maximum difference found is **582 nm** (figure 3.10). The response curve of the mirror was measured for a single actuator and a group of 4x4 actuators (figure 3.11). In this case, the measurement could be done setting the mirror at the ground position (instead of the bias value) since the 4D interferometer does not have the limitations of the previous one. The quadratic range is again kept until 163V (while, as before, manufacturer curves

in figure 3.11 show a full 200 V range). The bias voltage was checked to be 114V, as for BMM2.

Now, the real stroke values could be obtained. The interactuator stroke (single actuator) measured is **1.3** μm, while the mechanical stroke (group of 4x4 actuators) corresponds to **1.97** μm.

In addition, another curve for a single actuator was measured using the bias value of 114V. The maximum stroke obtained In this case is 1.1 μm, which shows a smaller value with respect to the real interactuator stroke measured at the ground level **1.3** μm.

Using this last curve it is possible to compare both mirrors. Figure 3.12 compares the response curve for a single actuator measured at the bias value. It is shown how the stroke is higher for the BMM3 by about 0.25 μm.

3.2.6 MEMS deformable mirror problems

For two years the BMM2 was used on the bench for normal AO operations (sensor calibration, close loop ...). After this time, defective actuators began to appear. First, the HVA boards were checked to rule out electronic causes. The problem consisted of loss of actuator stroke. Most of the defective actuators lose all the stroke capacity from the first moment, while others seem to keep some movement capacity until they stick completely at resting position.

The BMM manufacturing company was contacted in order to have some information about this problem but they could not help. Contacting other BMM users, a possible explanation was found on an oxidation process as explained in Shea *et al.* 2000 ([64]) and Shea *et al.* 2004 ([65]).

A combination of high voltage and water vapor inside the actuator produce the electrolysis of the H_20 molecule. The negatively charged $OH-$ ions are attracted to the anode, and then form $SiOH$, which combines with more $OH-$ to make SiO_2 (glass, which is not conductive), releasing molecular hydrogen. Thus, the actuator lost the stroke since it could not create the electrostatic force. The protective window in front of the BMM should provide a vacuum atmosphere. A leak in the window's interface could be the origin of the presence of the water vapor. The mirror was imaged with a microscope to confirm the oxidation, as shown in figure 3.13.

The number of defective actuators increased until it was not possible to drive the mirror (up to 30 defective actuators). The BMM2 was ruled out and BMM1 was installed temporarily on the bench until BMM3 was received.

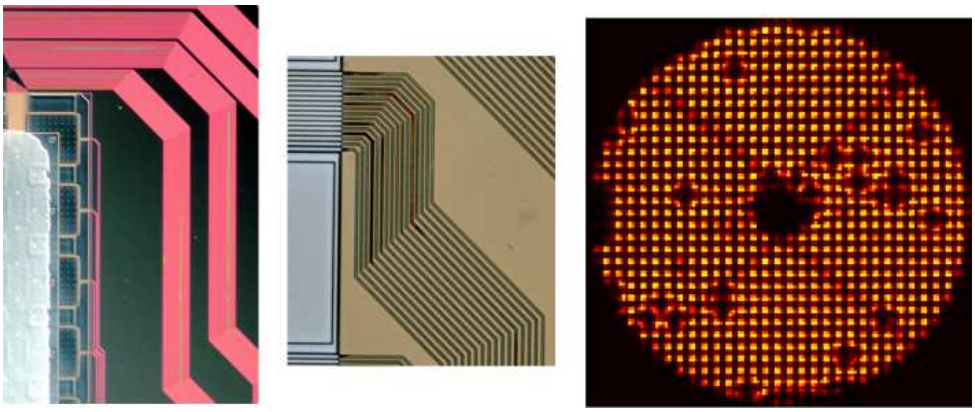

Figure 3.13: **Left-middle:** . Microscope images of BMM2 connections done by the LESLIA laboratories. Differential interferential contrast interferometer image (left) and direct microscopic inspection (center). The different colors between electronic lines(green compare to the pink on the left image, brown compare to the green on the center image) is a clear sign of oxidation. **Right:** SHS CCD image showing the effect of the defective actuators. When the BMM actuators are set to the bias voltage the defective actuators stay at 0 volt position producing a high slope in the surrounding subapertures (shown as holes on the image).

3.3 Common path

3.3.1 Optical quality

The optical quality of the bench was checked by measuring the wavefront error with the HASO 64x64 and acquiring PSF images with a visible CCD camera (PCO camera). Three beam positions were selected for the wavefront measurements: after the turbulence generator, after the MACAO bench optics (between the first focal plane and the first spherical lens) and before the WFS's. An auxiliary lens is used to reimage the pupil plane on the HASO. PSF images are obtained in the first focal plane (MACAO bench) (figure 3.14 up-left) and WFS focal plane.

Wavefront error measurements are summarized on table 3.1. No errors were found in the optical quality of the MACAO bench ($\approx$ 100 nm rms), especially if we take into account that the bimorph flatness is around 50 nm. Also the PSF image do not show specific errors.

On the other hand, the WFE measured after the BMM is higher, around 200 nm. Viewing the PSF image (figure 3.14 top-right) a clear cross structure can be seen, i.e, a square diffraction. The error could come from the BMM shape, due to the high slope in the edges (other possible source errors were ruled out). A PSF image was simulated (figure 3.14 down-right) using the wavefront measurement of the BMM shape (section 3.2.1, figure 3.4). Similar structures could be seen on both, the real and simulated PSF.

This error could be solved reducing the pupil size in order to use only the inside flat area, but in this case, the optical parameters of the bench would change. Another possibility is to flatten the BMM (in open or closed loop), but it would reduce the available stroke for turbulence compensation. The better option is to use the bimorph mirror to compensate both the BMM shape and other static aberrations.

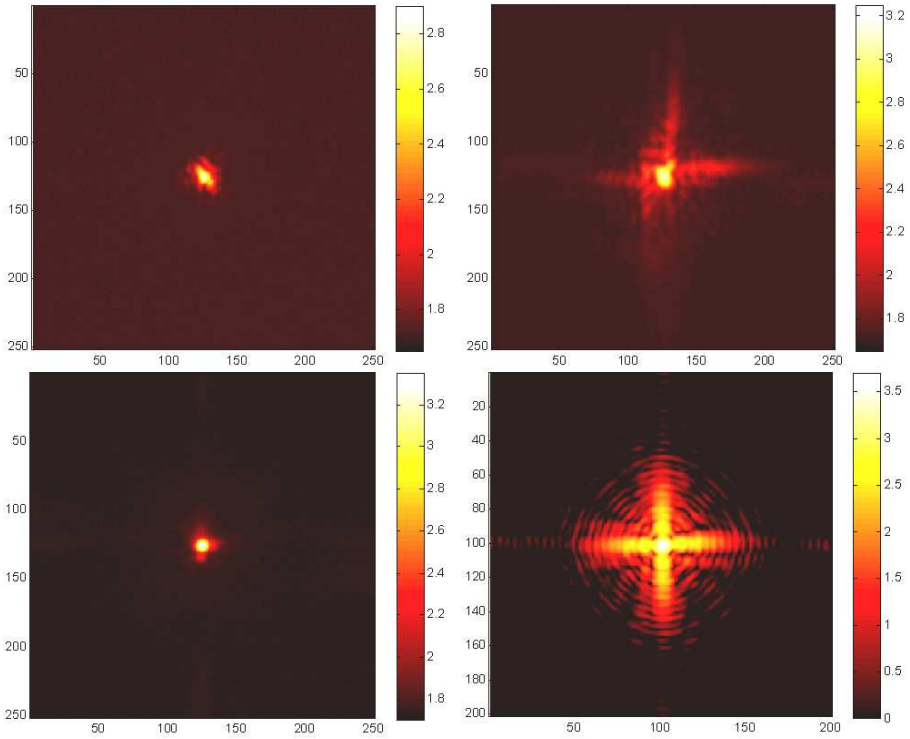

Figure 3.14: Visible PSF images. **Top-left:** Macao bench, first image plane. **Top-right:** WFS image plane, showing the cross pattern due to the BMM shape. **Bottom-left:** WFS image plane after correction using the bimorph DM. **Bottom-right:** Simulated PSF taking into account the surface error due to the BMM.

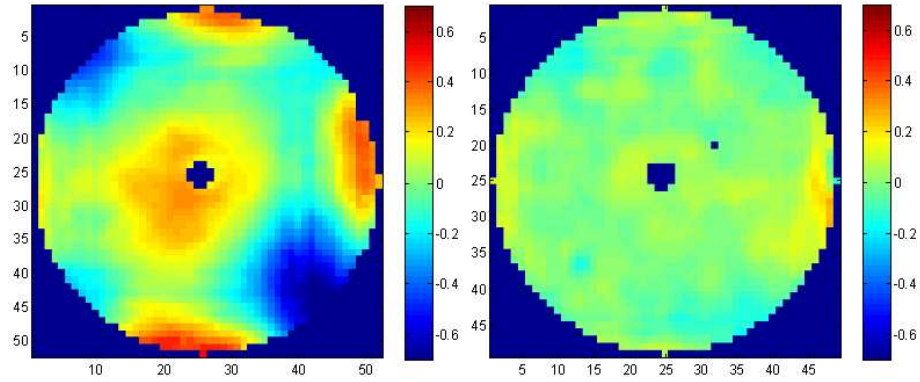

Figure 3.15: **Left:** WFE measured over the SHS pupil plane before bimorph correction.(≈ 200 nm rms). **Right:** WFE measured over the SHS pupil plane after bimorph correction (≈ 50 nm rms).

Bimorph mirror correction

The bimorph mirror and the HASO wavefront sensor are used to correct the static wavefront error (on open loop). The WFE is measured in the SHS pupil plane (after the collimator). Firstly, rotation and resolution between WFS measurement and bimorph influence functions had to be adjusted. Then, the WFE is projected onto the IF's to recover the corrective voltage pattern following:

$$V_{corr} = V_{flat} + IF^{+} S_{WFE} \tag{3.2}$$

where V_{flat} is the initial voltage pattern that flattens the bimorph DM, IF is the influence function matrix, S_{WFE} is the WFE vector, and V_{corr} is the voltage pattern that compensates the aberrations.

The WFE measured after applying the corrective voltage is ≈ 50 nm (rms). Figure 3.15 compares the wavefront error before and after correction. As expected the cross pattern on the PSF disappears as shown in figure 3.14 (bottom-left).

Table 3.1: Optical quality (wavefront error)

	Turbulence generator	**Macao bench**	**SHS pupil plane** (before correction)	**SHS pupil plane** (after correction)
RMS (nm)	60	120	210	52
PTV (nm)	300	700	1250	420

3.3.2 Pupil masks

A mask with the VLT pupil shape (including a 0.14% central obscuration and spiders) is placed in front of the bimorph DM. The mask also includes a rectangular metal patch to cover the pupil area (5x2 subapertures) corresponding to the two inactive actuators at the edge of BMM2 in order to avoid diffraction effects. For the case of BMM3, a different mask was used without this covered area. Figure 3.16 shows pupil images acquired with a visible camera on the SHS pupil plane for both masks.

The pupil mask was installed on the bench once the alignment of the common path and initial SHS alignment were finished. The fine alignment of the SHS was done using the pupil mask as reference.

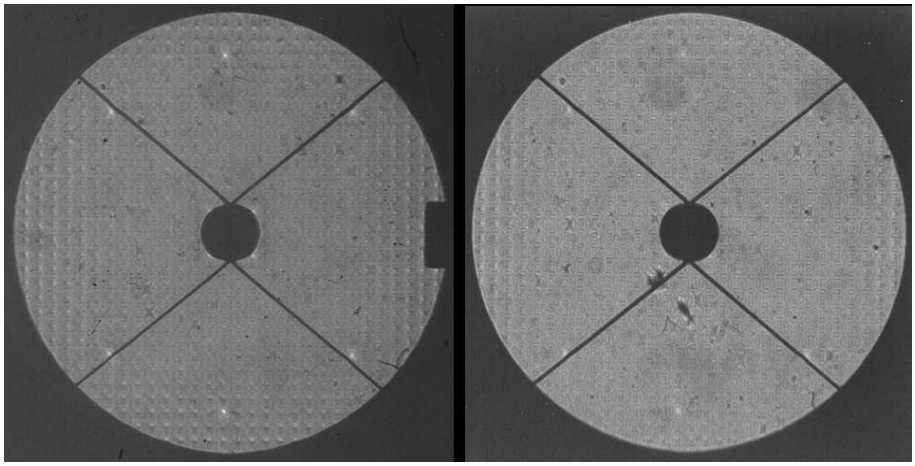

Figure 3.16: **Left:** VLT pupil mask used with BMM2 (a rectangular metal path covers the area surrounding the inactive actuators). **Right:** VLT pupil mask used with BMM3. In both images a set of actuators are pushed for alignment purpose.

3.4 SHS wavefront sensor

3.4.1 Optical alignment

The SHS optical setup is designed with commercial components (lens, mounts ...) which introduces limitations on the stability and alignment capabilities. The optical components are positioned following the distances given by the optical design (figure 2.6) and geometrical optics considerations. No alignment telescope tools were used, so, a more accurate alignment was not performed.

The SHS setup is placed on a linear rail, allowing easy z positioning of the optical components. The folding mirror, which redirects the beam on the SHS setup, was aligned in order to have the beam at the correct height (15 cm) and parallel to the rail.

The first collimator lens is installed at the theoretical distance. To find the correct position of the lens, the defocus of the collimated beam is measured using the HASO. The lens is displaced on the rail while minimizing the defocus measured by the HASO, so a good collimation is assured.

The next step consists of finding the pupil plane where the lenslet array (LA) will be placed (therefore, pupil mask, BMM and LA will be conjugated). A compact CCD camera (the so-called ”minicam”) mounted on the rail is used to find the pupil by imaging the VLT mask.

The second reimaging lens is a focus lens, so objects at the infinite should be imaged on the Andor CCD, allowing an easy positioning between CCD and lens. The andor CCD camera is set at the theoretical distance on the rail (no accurate positioning for the andor CCD is foreseen). The RL2 is installed on a tube joined to the CCD with a fine z movement. On the collimated beam, without other optics, the RL2 position is adjusted in order to focus the PSF on the CCD (maximizing the PSF peak).

Afterwards, the first reimaging lens is positioned (in the theoretical position) in order to match the focal planes of both reimaging lenses. This lens is installed on a mount with X and Y accurate movement.

Finally the lenslet array is set on the pupil plane found before. The LA is installed on a mount with tip-tilt movement for positioning the LA perpendicular to the beam, rotation movement to avoid rotation between ccd pixels and subapertures and X and Y movement to match subapertures and actuators on the correct Fried geometry.

Once all the optical components are set on the rail an accurate alignment is required to place pupil, actuators, subapertures and CCD pixels in the correct position. In addition to the CCD pixel display image (RTD), a matlab piece of code (RSD, *”Real Slope Display’*), was programmed to display in real time the slopes map (figure 3.18).

The CCD camera is adjusted in X and Y to center the pupil on it. The CCD camera has 128x128 pixels where only 124x124 are used to image the pupil. Then, the centroid of the subapertures are adjusted on the CCD. The subaperture focal point has to produce a symmetric light distribution on the 4x4 pixels used to image each subaperture. The RL1 is displaced in X and Y until the 4 central pixels (for each subaperture) are equally illuminated. This operation corresponds to setting the initial tip-tilt to zero.

The slopes map shows a small rotation between LA and CCD which is corrected by rotating the LA mount. Afterwards, a second adjustment of the RL2 is performed in order to sharpen the centroids reducing its size, therefore, improving the pixel scale. The fine adjustment is done looking for the position where the central pixels have maximum light, and the external ones have minimum light.

Pushing a group of actuators, following a defined geometry, the relative positions between pupil mask, BMM and LA are deduced. Installing a folding mirror, the BMM is imaged on the minicam showing the relative position between the mask and BMM. The BMM is shifted in X and Y until the

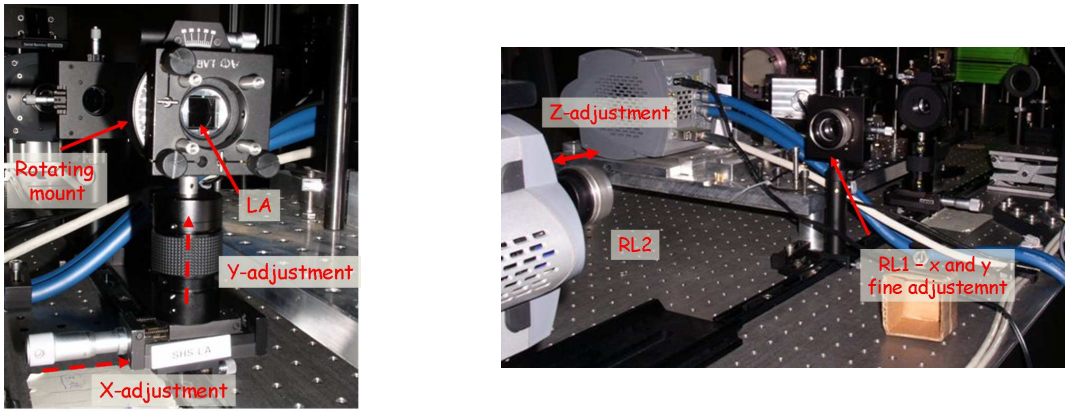

Figure 3.17: **Left:** Lenslet array integrated in the mount, allowing axis and rotation adjustment. **Right:** RL1 and RL2. The RL2 is mounted on a tube joined to the CCD.

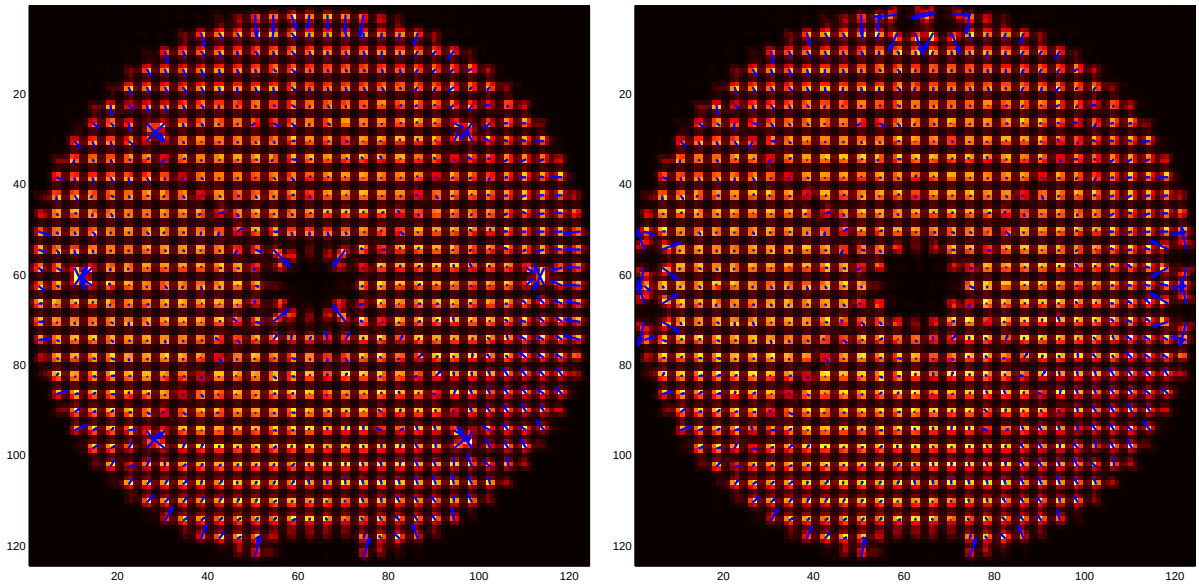

Figure 3.18: SHS slopes map. A configuration of actuators are pushed or pulled in order to align the LA respect to the BMM. **Left:** Configuration of 10 actuators pushed. **Right:** Configuration of 6 pulled actuators placed on the pupil edges.

pupil is centered on the actuator pattern (figure 3.16).

Using two different actuators patterns, the relative position between actuators and subapertures is adjusted. The LA is displaced in X and Y until a symmetric distribution of the slopes produced by the pushed actuators is obtained (checking both, the CCD image and the RSD).

If the actuators are well centered on the LA and on the pupil, it is expected that the LA is also well centered on the pupil. This could be easily checked verifying that the intensity distribution for the partial illuminated subapertures on the edges is symmetric.

The slopes map shows a clear magnification of the actuators grid respect to the subapertures. This magnification is computed to be a factor ≈ 1.03.

The last operation is to install on the SHS entrance focal plane a magnetic mount with a fiber. Thus, it will be possible to acquire reference slopes measurements of the SHS setup in order to not take them into account on the close loop. This also allows to verify the quality and stability of the alignment.

3.4.2 Slopes reconstruction

The slopes computation is done by the WPU software unit (2.15). The slopes are computed with a standard centroid algorithm as explained in section 1.2.1 with weighting factors {-1.5 -0.5 0.5 1.5}. The slope is computed only for the valid subapertures inside the pupil.

The WPU use three configuration files. The first includes the configuration for the valid subapertures (718 or 728 subapertures depending on the pupil mask used). The other two files include the configuration for the X and Y weighting factors used for each subapertures (in our case all valid subapertures use the same factors).

The matlab MEX functions recovering the WPU data were encapsulated in a class: *WPU*. The *WPU* class allows access to pixels and slopes checking the frame counting necessary to avoid lost frames. The class also implemented specific methods to measure and apply the background subtraction.

3.4.3 SHS characterization

SHS linearity

In order to achieve an optimal performance of the AO system, it is necessary to know the SHS behavior in terms of linearity and crosstalk. The linearity study requires an incident flat wavefront in order to have zero offsets on the centroid positions. The BMM voltage pattern and TTM position that flatten the wavefront in the SHS is obtained in closed loop (in order to remove static errors on the common path and SHS path). Closed loop implementation will be described in the next chapter.

The TTM is used to obtain the response curve of the sensor since we need to produce known variances tilts on the wave front. Hence, the response for each subaperture is obtained by recording the slope measurements at different positions of the useful range of the two TTM axes and subtracting the slope reference at zero TTM position.

The two TTM axes will be called channel 0 (Y slopes) and channel 1 (X slopes). Both channels are controlled in the range -1 to 1 (where 0 is the zero position). It will be called ”normalized unit” (nu). These values correspond to a voltage range from -10 to 10 volts. The amplitude of the mount is 570 mas per 0.1 nu (measured experimentally in the ITC infrared camera). Linearity plots are expressed in normalized units, since it will be the natural units used by the AO loop control.

The SHS is characterized for two cases: without field stop in the focal plane and with field stop (covering the full 2 arcseconds subaperture) to reduce the crosstalk between subapertures.

Linearity characterization without field stop.

First we check the SHS pixel scale by finding the TTM range necessary to displace the subaperture spot by 1 pix. This value is approximately 0.082 nu, giving a pixel scale of 0.47 arcsec/pix. On the other hand, the centroid variation measured is around 0.6 pix instead of 1 pix as expected. This effect is mainly caused by a clear aliasing between subapertures. The criterion used to estimate the crosstalk is the rate between the max pixel value and the min pixel value of the subaperture. In this case $\approx$ 6% is measured.

Figure 3.19 shows the superimposed response curves for all the subapertures (on both, X and Y directions). A variance between subapertures in terms of gain and dynamical range could be seen from the graph. To see better the difference between subapertures, we plot the subaperture map showing the max and min value of the response curve, as well as the global range (figure 3.20). The behavior per subaperture is quite homogeneous except for specific areas; for the channel 0 (Y direction) on the top and bottom edge, while for the channel 1 (X direction) it is localized on the right side.

The linearity range of the response curve is defined as $\approx$ 70% of the slope dynamical range (i.e. the

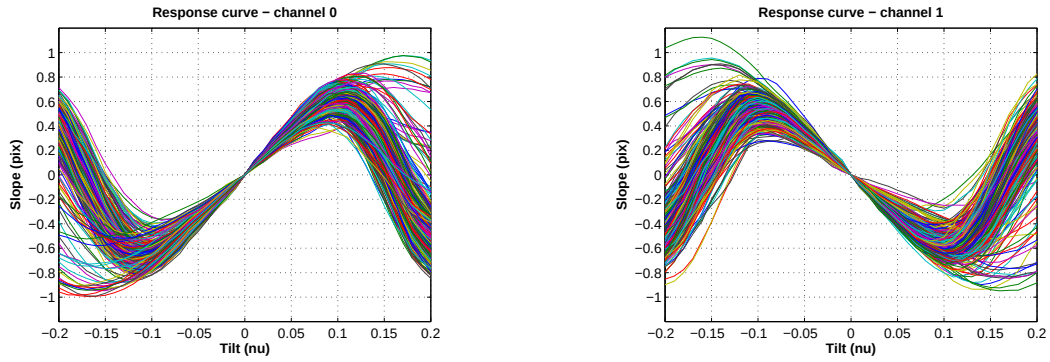

Figure 3.19: Response curve for all valid subapertures without field stop. **Left:** Channel 0 **Right:** Channel 1.

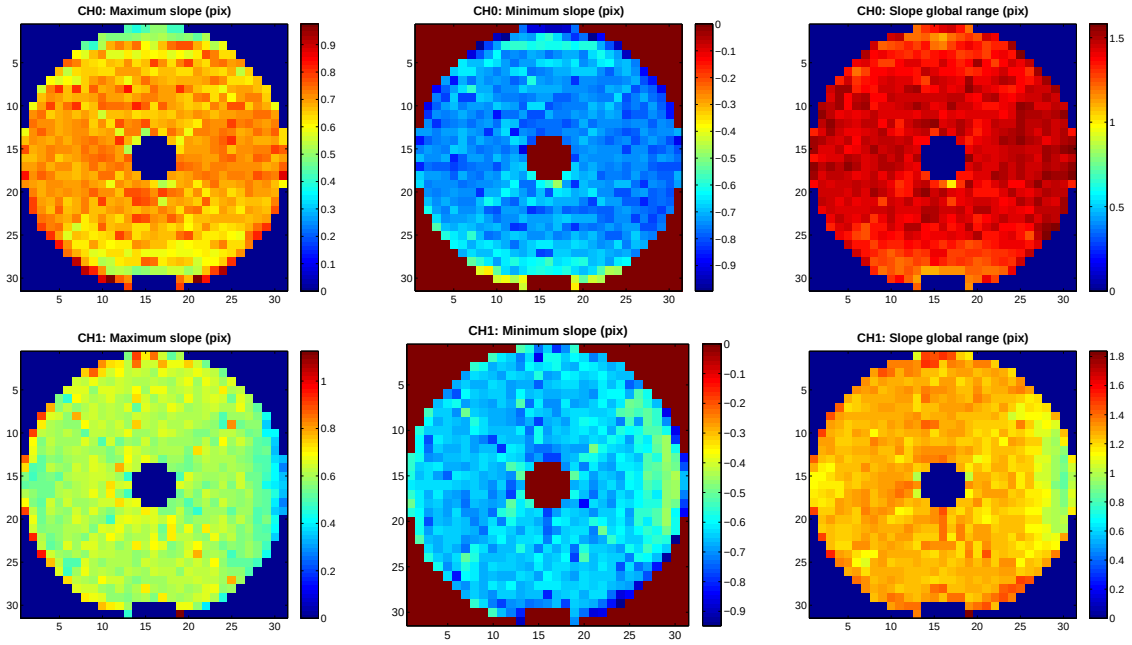

Figure 3.20: Subaperture map showing the maximum, minimum and dynamical range (max-min) from the response curve. **Top:** Channel 0 **Bottom:** Channel 1.

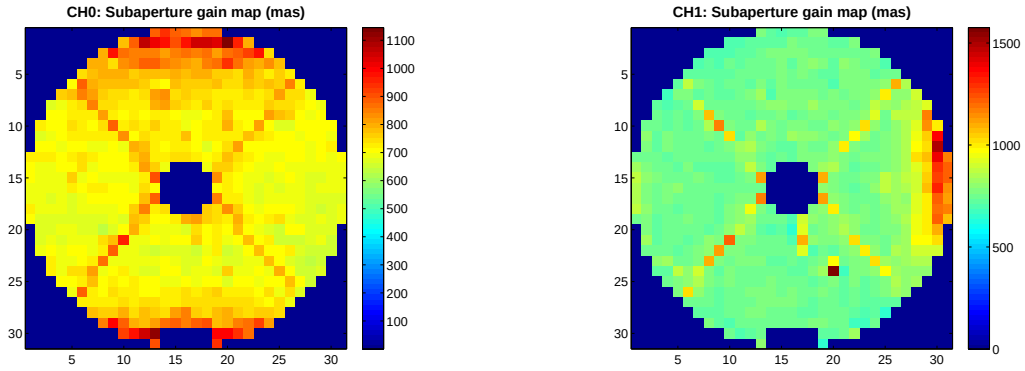

Figure 3.21: Subaperture map showing the gain (slope) over the linear range of the response curve. **Left:** Channel 0 **Right:** Channel 1.

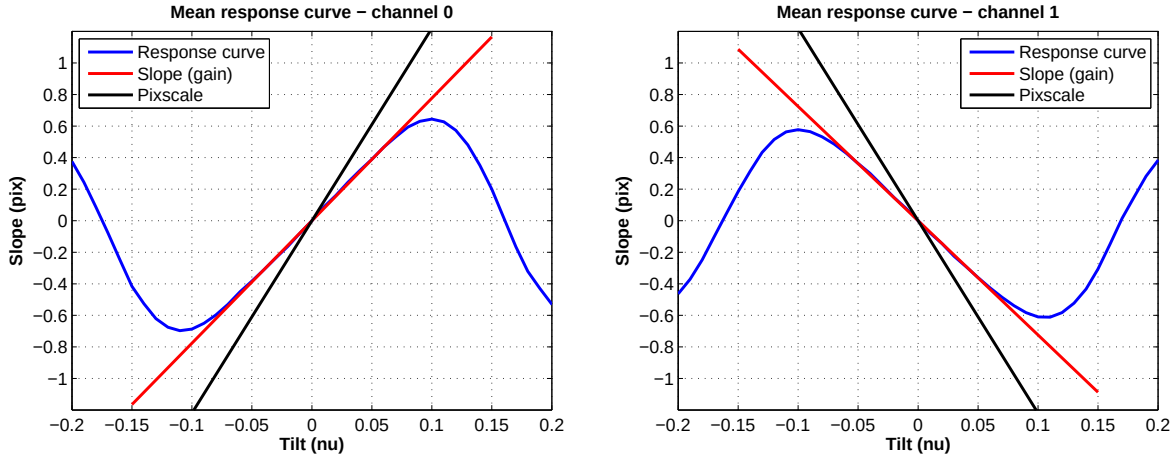

Figure 3.22: Mean response curve (blue line) and slope of the curve (red line) fitted in the linear range (corresponding to a 70% of the max-min difference). The pixscale is also included (black line). **Left:** Channel 0 **Right:** Channel 1.

difference between max and min). The slope (gain) per subaperture over the linear range is measured by applying a linear fit. The gain map per subaperture in figure 3.21 show that for some subapertures the gain is higher, corresponding again with the same problematic areas as before. Although, in this case, it is clear that the gain for the subapertures covered partially by the spider are also higher.

The mean gain values are: **0.73** arcsec/pix (CH0) and **0.78** arcsec/pix (CH1) (taking into account only the internal subapertures and removing the spiders). As mentioned before, the main difference between pixscale and gain is explained by the big crosstalk between subapertures.

A mean response curve (figure 3.22) is obtained from all subaperture responses in order to find some mean parameters. The linear range covers 70% of the max-min difference (same value for both channels). The slopes of the linear fitting for both channels are **0.73** arcsec/pix and **0.78** arcsec/pix. Dynamical range values can be found in table 3.2.

Table 3.2: SHS linearity parameters without field stop

	channel 0	**channel 1**
Max slope	0.64 pix	0.58 pix
Min slope	-0.70 pix	-0.61 pix
Slope dynamical range	0.95 pix	0.84 pix
Linear range/global range	70%	70%
Max tilt	0.10 nu	0.11 nu
Min tilt	-0.11 nu	-0.10 nu
Tilt dynamical range	0.13 nu	0.12 nu
gain	0.73 arcsec/pix	0.78 arcsec/pix

Table 3.3: SHS linearity parameters with field stop

	channel 0	**channel 1**
Max slope	0.70pix	0.70 pix
Min slope	-0.73 pix	-0.71 pix
Slope dynamical range	0.99 pix	0.99 pix
Linear range/global range	70%	70%
Max tilt	0.10 nu	0.10 nu
Min tilt	-0.11 nu	-0.11 nu
Tilt dynamical range	0.12 nu	0.14 nu
gain	0.68 arcsec/pix	0.73 arcsec/pix

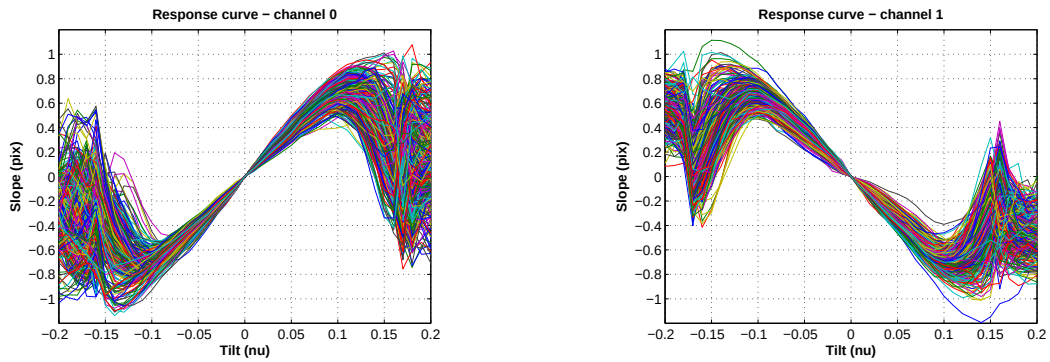

Figure 3.23: Response curve for all valid subapertures with field stop. **Left:** Channel 0 **Right:** Channel 1.

Linearity characterization with field stop.

A field stop (FiS) of 3.8 mm has been installed on the SHS entrance focal plane to reduce crosstalk between subapertures. The intensity rate between brightest and faintest pixel inside the subaperture is reduced from 6% to 3%.

Figure 3.23 shows the superimposed response curves for the FiS case, while figure 3.24 shows the max, min and global range subaperture map. It could be seen that the behavior is more homogeneous between subapertures. On the other hand, as before, there are specific regions with a different dynamical range.

A difference on the partially illuminated subapertures can clearly been seen. The max and min values are not symmetric. This is because a partially illuminated subaperture has only crosstalk contribution from one of the contiguous subapertures, thus, the behavior is different if the TT channel displaces to the plus or minus direction (i.e. moving to the pupil or outside the pupil).

Figure 3.25 shows the gain map per subaperture. The map distribution is similar to the previous case, also showing areas with higher gain (specially for channel 1). On the other hand, the mean values decrease; **0.68** arcsec/pix (CH0) and **0.73** arcsec/pix (CH1), which represents a decrease of 8% and 6%, respectively.

The mean parameters (table 3.3) are obtained from the mean response curves shown in figure 3.26. The linear range is again 70%. This parameter is important in the calibration step because, together with the max and min slope value per subaperture, it is used to find the stroke that maximizes the signal to avoid saturating the subaperture linear range.

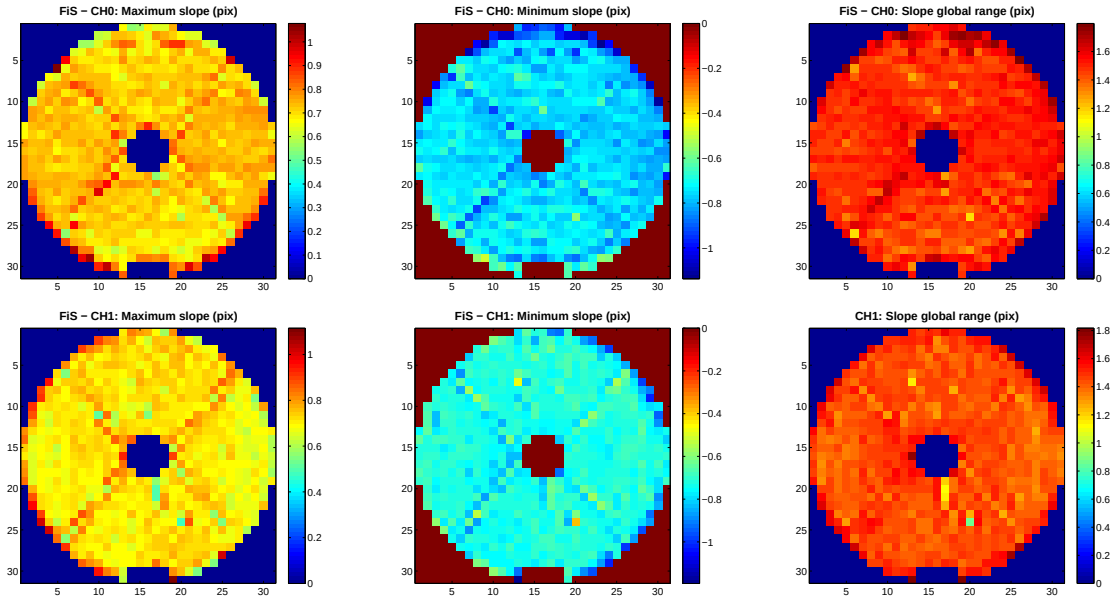

Figure 3.24: Subaperture map showing the maximum, minimum and dynamical range (max-min) from the response curve for the field stop case. **Top:** Channel 0 **Bottom:** Channel 1.

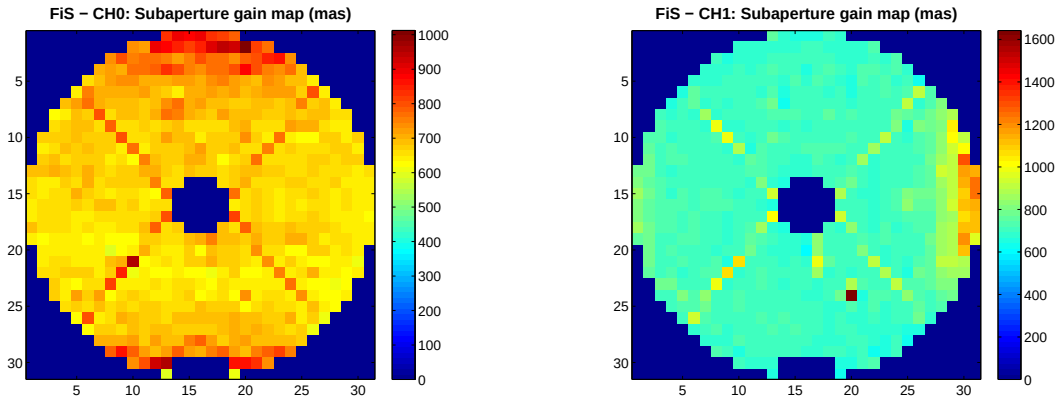

Figure 3.25: Subaperture map showing the gain (slope) over the linear range of the response curve for the field stop case. **Left:** Channel 0 **Right:** Channel 1.

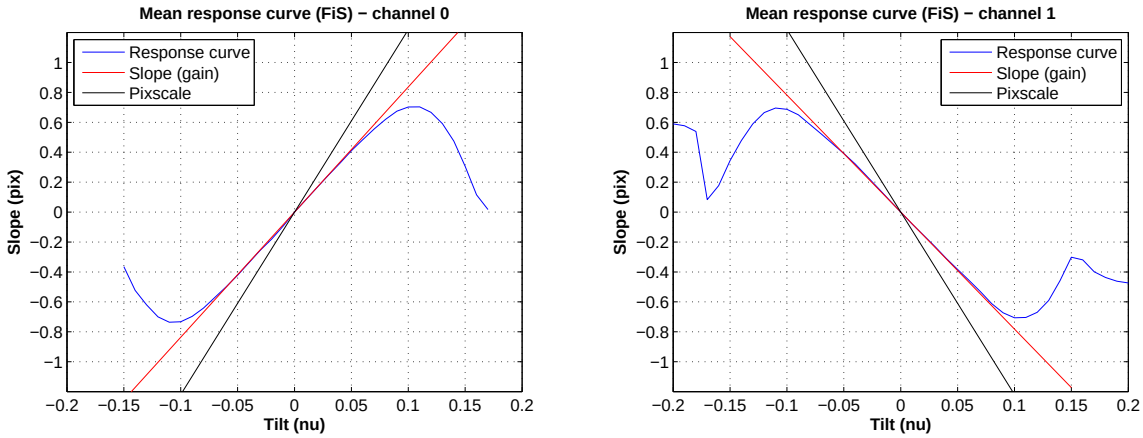

Figure 3.26: Field stop configuration. Mean response curve (blue line) and slope of the curve (red line) fitted in the linear range (corresponding to a 70% of the max-min difference). The pixscale is also included (black line). **Left:** Channel 0 **Right:** Channel 1.

We can summarize the conclusions from both cases, with and without the field stop:

- The tilt dynamical range gives the maximum turbulence the WFS is able to measure. For both cases it is similar since this parameter depends on the SHS design.
- In the field stop case, the slope dynamical range increases ≈ 9%, while the gain decreases (≈ 8%). These parameters depend on the crosstalk between subapertures. Since, by design, there is not a guard band between the 4x4 pixels of each subaperture, the sensor suffers from an important crosstalk that is clearly mitigated by the use of a field stop.
- Even using the field stop, some residual crosstalk remained. The loss of linearity (linear range ≈ 70% of the global range) is due to the residual crosstalk together with the truncation of the PSF (only 4x4 pixels per subaperture).
- The difference in behavior between subapertures is not important, except for some specific regions (including the subapertures covered by the spiders) where the gain is quite higher. These subapertures could give problems depending on the strength of the turbulence.
- Partially illuminated subapertures do not show a different behavior on terms of linearity and gain.

Linearity characterization with field stop: new set of measurements.

On december 2009 a new set of linearity measurements was done. The differences between sets of measurements are due to several improvements on the optical conditions:

- The new BMM3 replaced BMM2, thus no optical ghosts are added to the system. In addition, the full pupil mask is used (728 subapertures) and several realignments were carried out.
- Now, the Bimorph DM is controlled by *matlab*, so a close loop is performed to correct all static errors on the system including BMM shape errors. Thus, a flat wavefront is ensured for the measurements.

Hereafter, only the field stop measurements are shown, since this is the standard operation mode of the SHS. Figure 3.27 shows the subapertures gain map, while, figure 3.28 shows the mean response curve. Now, the full pupil is homogeneous. The anomalous high gain areas seen before have disappeared. From the mean parameters (table 3.4), we can see that now both channels do not show differences in gain (**0.665** arcsec/pix for both). The gain value is similar as before, but the slope dynamical range increased by about 0.22 pix (20%). Also the linear range is larger, ≈ 80% of the global range.

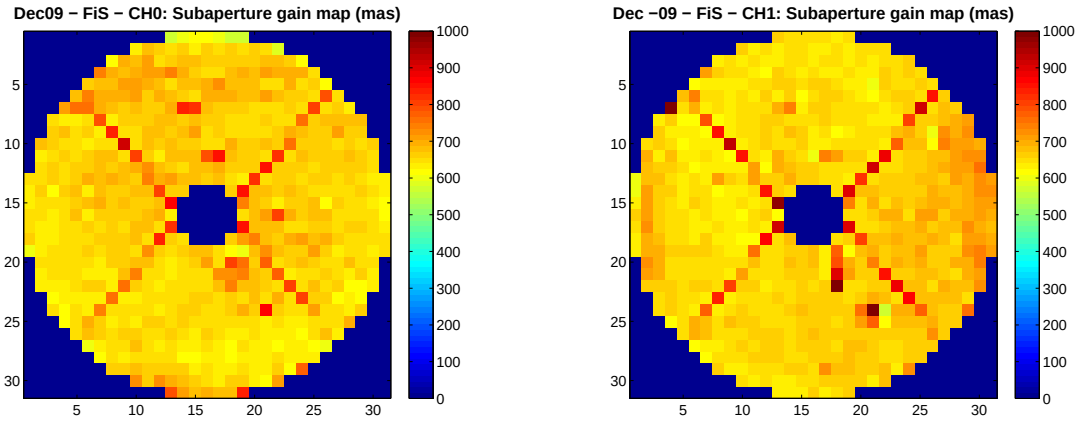

Figure 3.27: Subaperture map showing the gain (slope) over the linear range of the response curve for the field stop case (dec 2009). **Left:** Channel 0 **Right:** Channel 1.

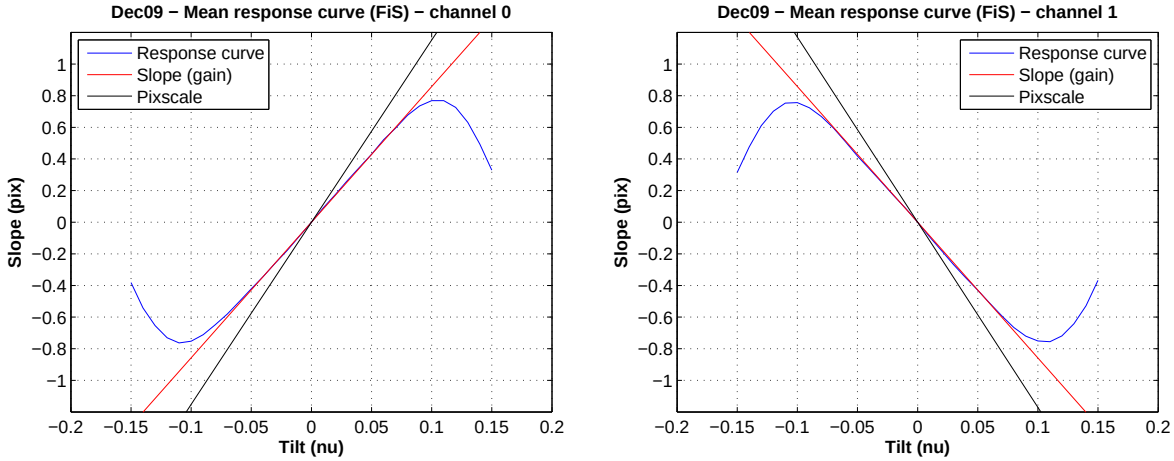

Figure 3.28: Field stop configuration (dec 2009). Mean response curve (blue line) and slope of the curve (red line) fitted in the linear range (corresponding to a 70% of the max-min difference). The pixscale is also included (black line). **Left:** Channel 0 **Right:** Channel 1.

Table 3.4: SHS linearity parameters with field stop - Dec 09

	channel 0	**channel 1**
Max slope	0.77pix	0.76 pix
Min slope	-0.76 pix	-0.76 pix
Slope dynamical range	1.26 pix	1.19 pix
Linear range/global range	82%	79%
Max tilt	0.10 nu	0.11 nu
Min tilt	-0.11 nu	-0.10 nu
Tilt dynamical range	0.15 nu	0.14 nu
gain	0.665 arcsec/pix	0.665 arcsec/pix

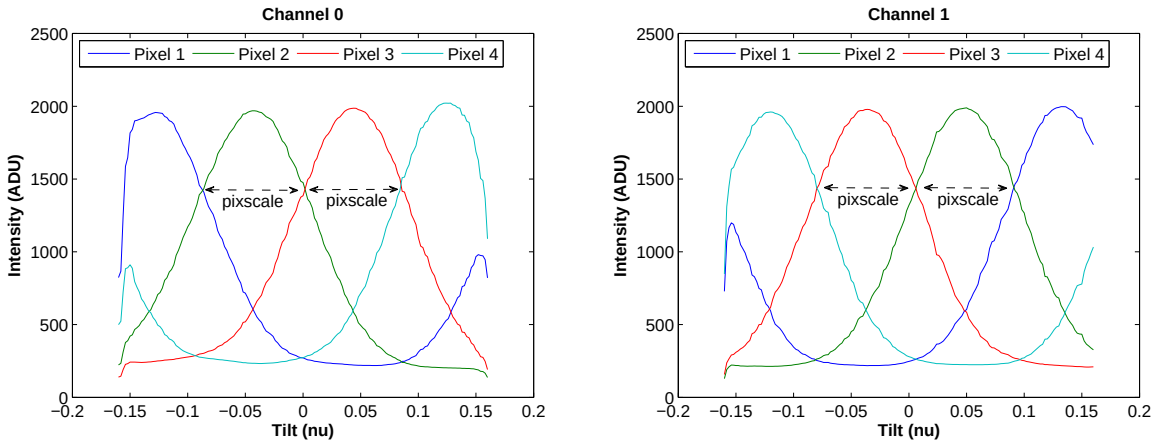

Figure 3.29: Intensity curves as a function of the tilt displacement, for the 4 pixels of the subaperture. **Left:** Channel 0 **Right:** Channel 1.

Pixel scale determination

The pixel scale was obtained initially, visually, and only for one subaperture. A new method was used to obtain a more accurate value of the pixel scale. As before, the TTM mount is displaced in both directions, but, in this case, instead of the slopes, the pixel intensity is recorded. In this way an intensity curve for each pixel of the different subapertures is obtained.

For each subaperture, the pixels are averaged along the columns, to obtain the intensity distribution along the X axis, and along the rows, to obtain the intensity distribution along the Y axis. Thus, an intensity distribution for each of the 4 averaged pixels is obtained (for X and Y directions). Finally, the intensity curves are averaged over all the subapertures.

The four curves are plotted simultaneously on figure 3.29. The distance between the interception points of the curves, as well as the distance between the maxima, represents the tilt displacement required to shift the centroid by one pixel, therefore, giving the pixel scale. The mean pixel scale for channel 0 is **0.495** arcsec/pixel, while for channel 1 is a bit smaller, **0.487** arcsec/pixel. These values are smaller than the theoretical value of 0.52 arcsec/pixel.

3.5 Turbulence analysis

The phase screens were already characterized previously in terms of spatial resolution with the HASO 64 (section 2.2.2). Now the SHS was used to characterized the temporal behavior of the turbulence in terms of equivalent speed and correlation time following Conan *et al.* 1995 ([66]) and Gendron *et al.* 1995a and 1995b ([67],[68]).

The phase screens rotate thanks to two motors with adjustable speed. The motors could rotate both in the same or opposite directions. In our case the limited RTC speed requires setting the minimum possible speed for the phase screens.

3.5.1 Zernike temporal spectra

The equivalent turbulence speed could be measured from the temporal power spectrum of the Zernike modes. The Zernike spectra are characterized by a cutoff frequency that increases with the radial degree of the polynomial as:

$$fc \approx 0.3(n+1)\frac{V}{D} \tag{3.3}$$

At high-frequencies, all of the modes spectra follow a $f^{-17/3}$ law, while at low-frequencies the behavior depends on the Zernike polynomial. For the radially symmetric polynomials,defocus (n=3) and spherical aberration (n=9) it follows a f^0. For the astigmatism (n=4) and coma (n=5) the behavior follows a $f^{-2/3}$ and a f^2 law respectively. The cut-off frequency is defined as the frequency where the regime changes from low to high frequency.

Figure 3.30 shows the spectra for the first Zernikes. A set of several SHS slope measurements (40000 frames) were taken on open loop at a rate frequency of 60 Hz. For each slope frame the modal decomposition was computed. For some low order Zernikes the power spectral density (PSD) was computed finding the low and high frequency regimes, as well as the cut-off frequency. This value is only approximate since the turning point where the behavior changes is not clear. The cut-off frequencies and turbulence speed, as well as the frequency dependency law are shown on table 3.5.

The mean speed deduced from this method is 1.5 m/s (considering 8 m pupil) which represents approximately one order of magnitude of difference with respect to real atmospheric conditions. An interesting point is the behavior at high frequency. The measured law is closer to a -10/3 law instead of the -17/3 predicted by theory. Only for the higher order mode, the spherical aberration is this law verified. This behavior of the high frequency regime was also observed for real atmospheric turbulence using the COMEON-plus instrument (Conan *et al.* 1994 [69]).

The coma mode also shows a different behavior for the low regime. For a single-layer atmosphere, the behavior should be positive, but for our case is zero, being closer to a multi-layer case. It could

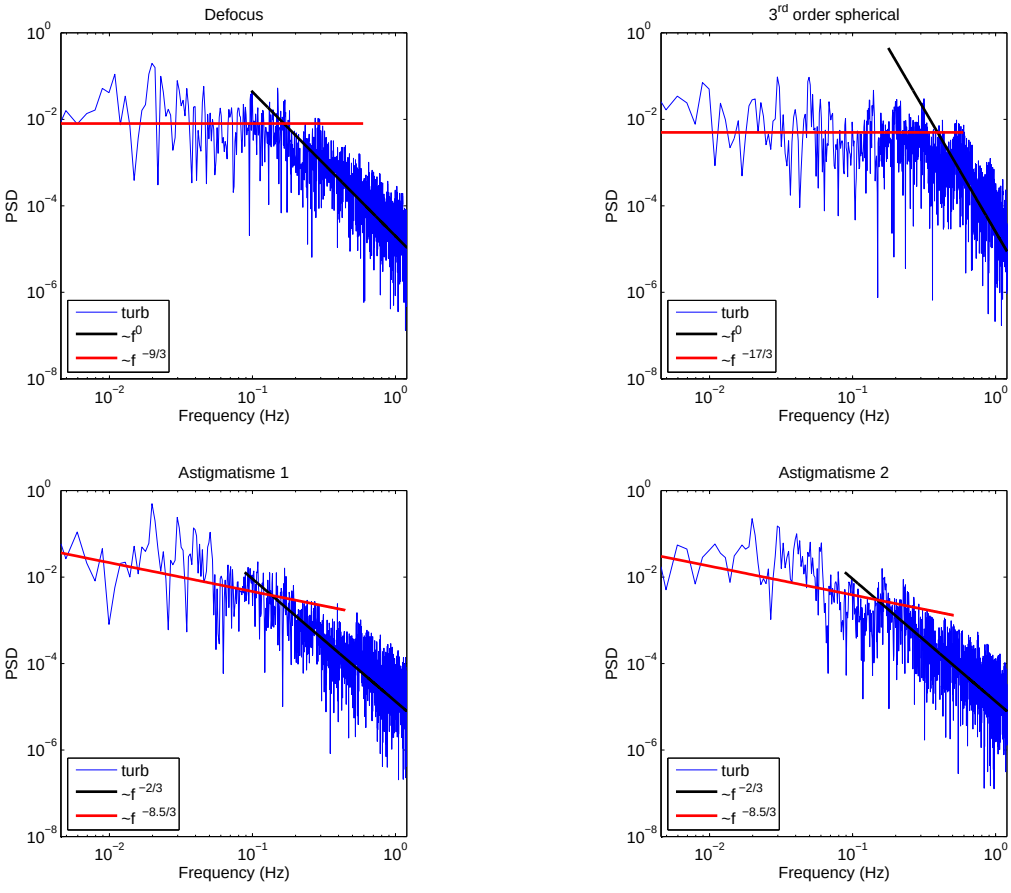

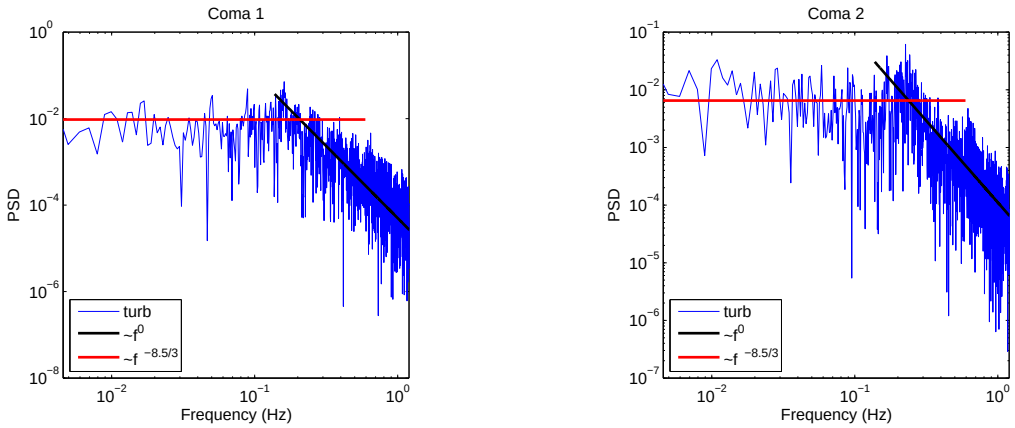

Figure 3.30: Mean temporal power spectra of some low order Zernike polynomials of the turbulence measured from the SHS slopes. The Spectra are normalized to the turbulence variance for each mode.

Table 3.5: Temporal behavior for some Zernike modes

Mode	f_c **[Hz]**	**Speed [m/s]**	**Low order regime** $[f^x]$	**High order regime** $[f^x]$
Defocus	0.17	1.5	0	-10/3
Spherical aberration	0.39	2.0	0	-17/3
astigmatism 0^o	0.14	1.2	-2/3	-8.5/3
astigmatism 45^o	0.15	1.3	-2/3	-8.5/3
Coma 0^o	0.20	1.3	0	-8.5/3
Coma 45^o	0.23	1.6	0	-8.5/3

be possible to see two regimes superimposed for the low frequency regime (zero and positive), but it is difficult to confirm.

3.5.2 Correlation time estimation

The τ_o could be obtained from the temporal autocorrelation of the subapertures. We define the correlation time of the slopes as half of the full-width-half-maximum of the mean temporal autocorrelation of the angle of arrival.

Figure 3.31(top-left) shows the mean temporal autocorrelation curve from the slope measurements of the subapertures in the case of only one phase screen turning. It is possible to see several autocorrelation peaks (for a large temporal scale) since our turbulence is cyclical. The time difference between peaks gives the rotation speed of the phase screen: **138 sec/cycle**. Now, turning both screens only one correlation peak is observed (3.31, up-right), so the cyclicity of the turbulence is avoided.

Figure 3.31 (bottom) shows the autocorrelation peak for the angle of arrival along x and y. The correlation time obtained from the FWHM are 110 ms and 200 ms for X and Y directions respectively. The difference between both axes is expected since the phase screen movement is predominant in one of the directions.

Figure 3.32 shows the HWHM (*Half Width at Half Maximum*) of the coefficients modal decomposition autocorrelation as a function of the modal number (K-L modes, see next chapter 4.3.1). A fast decrease of the correlation time vs mode number can be seen. Two different laws were found: $m^{-1/3}$ for

low order modes (m<60) and $m^{-0.65}$ for higher order modes. Different behavior was expected for low and high order modes due to the phase screen design where low spatial frequencies are reduced. For high order modes, following a Kolmogorov turbulence, the behavior expected is $m^{-1/2}$ as deduced from Fusco *et al.* 2004 ([70]).

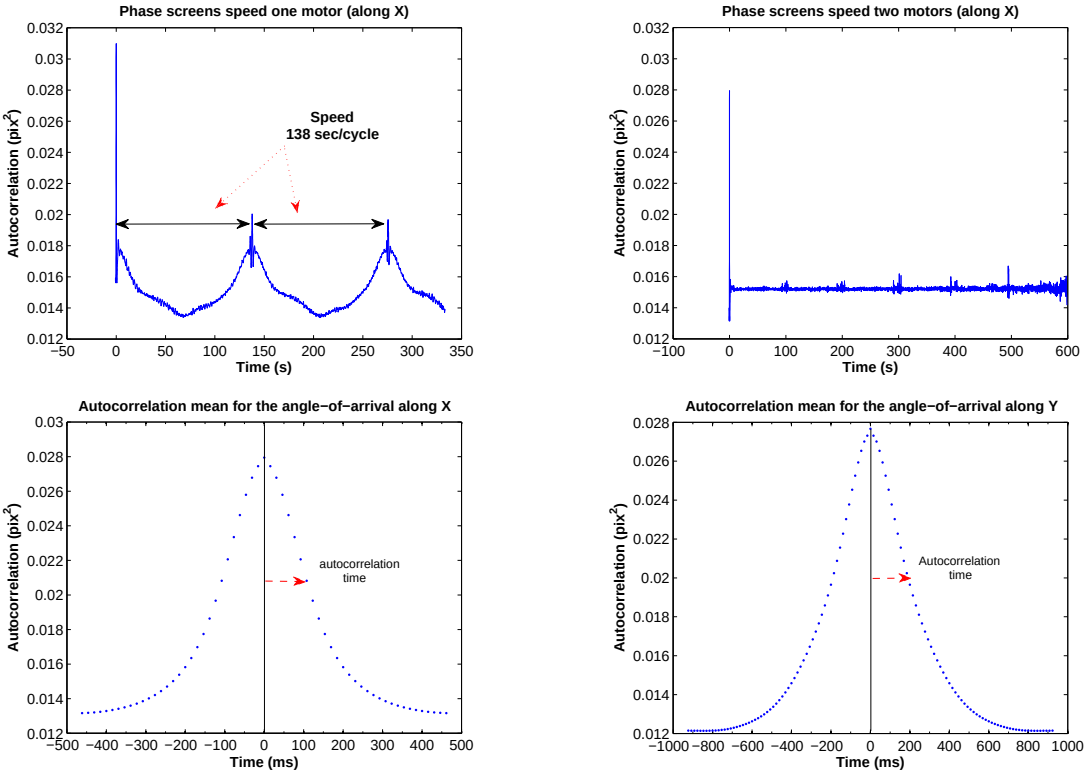

Figure 3.31: Autocorrelation mean of the angle of arrival. **Top:** Large temporal scale showing the difference between one and two motors. For the first case several autocorrelation peaks are visible at a separation of 138 s. **Bottom:** Detail of the autocorrelation peak (X and Y directions) for the case of two motors. The HWHM gives the autocorrelation time.

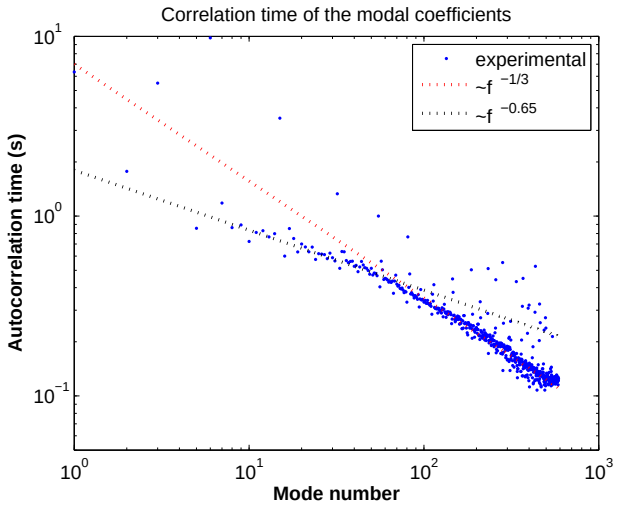

Figure 3.32: Correlation time of the coefficients modal decomposition.

3.5.3 Wind speed: Frozen turbulence hypothesis

The phase screens are placed in a unique plane conjugated to the pupil and moving at constant speed, therefore, following the *"Taylor model"* (Taylor 1938 [71]) or *"frozen turbulence hypothesis"*. This hypothesis states that a turbulent layer of finite vertical thickness behave as a frozen phase screen translated horizontally at the constant speed of the wind and modulating with time the phase of the incoming wavefront.

Under the Taylor hypothesis, it is possible to measure the equivalent turbulence speed computing the cross-correlation function for the wavefront slopes (Gendron *et al.* 1996, [72]). At any time t, the WFS gives a frame of slopes $\vec{S}(\chi, \epsilon, t)$ over the pupil. This later is characterized by the classical pupil function $P(\chi, \epsilon)$ (1 inside, 0 outside). We compute the time averaged cross-correlation of two frames of slopes distant of τ in time, i.e:

$$A(x, y, \tau) = \left\langle \frac{\int d\epsilon \int \eta \vec{S}(\epsilon, \eta, t) \vec{S}(\epsilon + u, \eta + v, t + \tau)}{\int d\epsilon \int \eta \vec{S}(\epsilon, \eta) \vec{S}(\epsilon + u, \eta + v)} \right\rangle_t \tag{3.4}$$

Two cases were studied: both screens turning in the same and opposite directions. Fig 3.33. show $A(x, y, \tau)$ for the first case, for values of τ ranging from 0 to 9 frames, i.e. 0 to 1.8s by steps of 0.2s. An

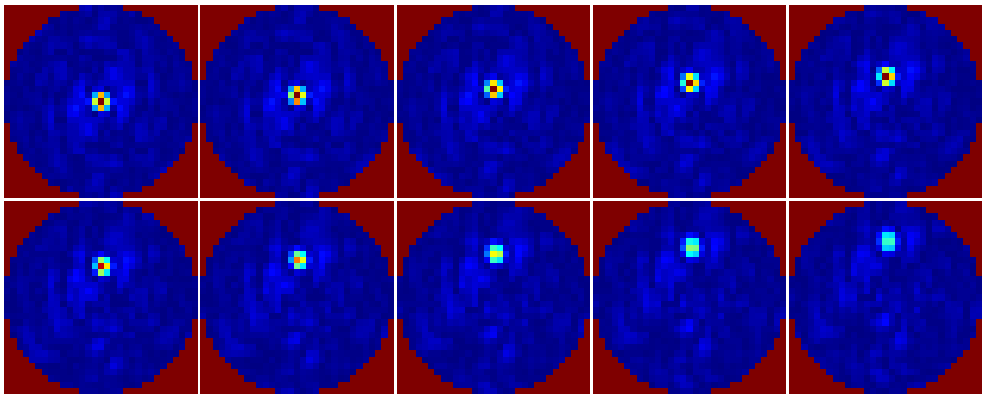

Figure 3.33: Series of 10 images representing the spatiotemporal cross-correlation function taking 0.2s apart for the case of two motors turning in the same direction. A peak is clearly visible and moves uniformly away following the Y direction at a speed of 1.26 m/s.

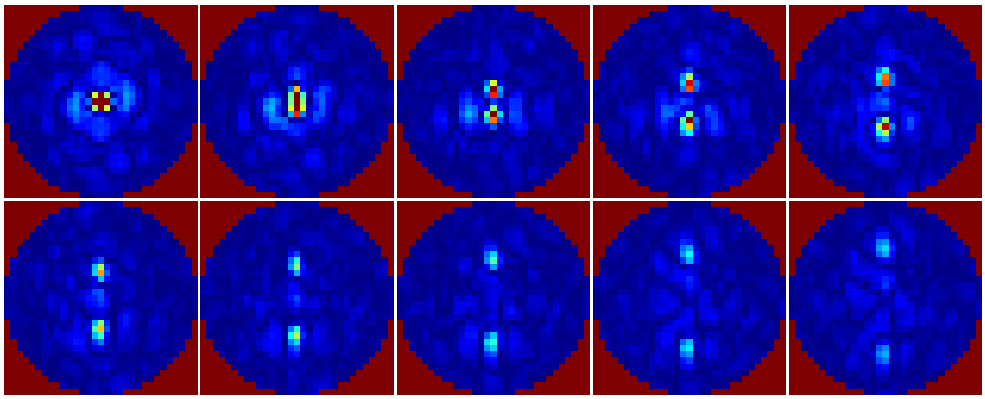

Figure 3.34: Series of 10 images representing the spatiotemporal cross-correlation function taking 0.22s apart for the case of two motors turning in opposite directions. Two peaks are clearly visible and moves away in opposite directions following the Y direction at a speed of 1.21 and 1.1 m/s.

obvious correlation peak appears, moving on a defined direction at a speed of **1.26 m/s**.

Figure 3.34 shows the second case for values of τ from 0 to 2.2s by steps of 0.22s. In this case, two correlation peaks appear showing the presence of two atmospheric layers moving at opposite directions with speeds of **1.21 a 1.10 m/s**.

For both cases the peaks movement are oriented through the Y axis, as expected from the design of the turbulence generator. The speed along the X axis was verified to be smaller than 0.1 m/s.

The turbulence speed estimated by this method is more accurate. The estimation using the Zernikes power spectrum is limited by the accuracy on the determination of the cut-off frequency, which is not easy to measure. However both methods estimate the same order of magnitude for the wind speed (slightly smaller on the cross-correlation method). The purpose of these measurements is not an accurate measurement, instead only an estimation to ensure that the loop speed is in agreement with it.

4

Control implementation

The objective of AO control is to find the DM commands that minimize the WFS measurements. Section 1.2.3 explains how the *reconstructor* gives the linear relation between measurements and commands. The simplest way to obtain it is through the inversion of the zonal IM of the system (equation 1.34). Although an optimal reconstructor should take into account not only the relation between measurements (WFS) and corrective devices (DM), but also the statistics of the wavefront distortion to be corrected.

In a modal control approach both elements are considered. The power spectrum of the atmospheric turbulence is taken into account in the modal basis construction from the actuators IF's. Afterwards, the modal basis is used to obtain a modal IM or could be projected onto the zonal IM.

The *ADONIS* method [1] consists of measuring a modal IM: instead of poking each actuator individually, we poke actuator patterns that recreate each of the modes of the base. The measurement vector is then stored as a column on this new IM. In this way the reconstructor could be recovered as:

$$R = BGD^{+} \tag{4.1}$$

where D is the modal interaction matrix (equation 1.45), B is the modal basis (equation 1.44, columns representing the DM commands to recreate each mode) and G is a diagonal matrix where the i^{th} element is the gain on the mode i (considering the simplest case without modal gain optimization, this matrix is the identity).

In the *PUEO* method [2] we have already measured a zonal IM (equation 1.29) that gives the linear relation between actuators and measurements. The reconstructor could be obtained from the knowledge of the modal basis as:

$$R = BGB^{+}M^{+} \tag{4.2}$$

where M is the zonal IM, B the modal basis and G the gain matrix explained before.

The reconstructor approx chosen for HOT (as shown in Aller-Carpentier *et al.* 2008 and 2009 ([62], [63])) follows the PUEO method. In this case, we could use a Hadamard zonal interaction matrix, which minimizes the SNR in the calibration process (see section 4.2.1). In addition, it is possible to use the same gain for all the Hadamard patterns since the signal produced on the WFS is always of the same order of magnitude.

On the contrary, a modal calibration would imply lower gains when increasing the mode order since higher-order modes produce higher signal amplitudes due to their stronger local gradients. Therefore, it would be necessary to optimize a gain algorithm for the calibration in order to produce the higher SNR avoiding sensor saturation.

[1] Takes its name from the ESO adaptive optics system *ADONIS* [73]

[2] Takes its name from the *PUEO* adaptive optics system installed at the Canada-France-Hawaii telescope(CFHT) [74]

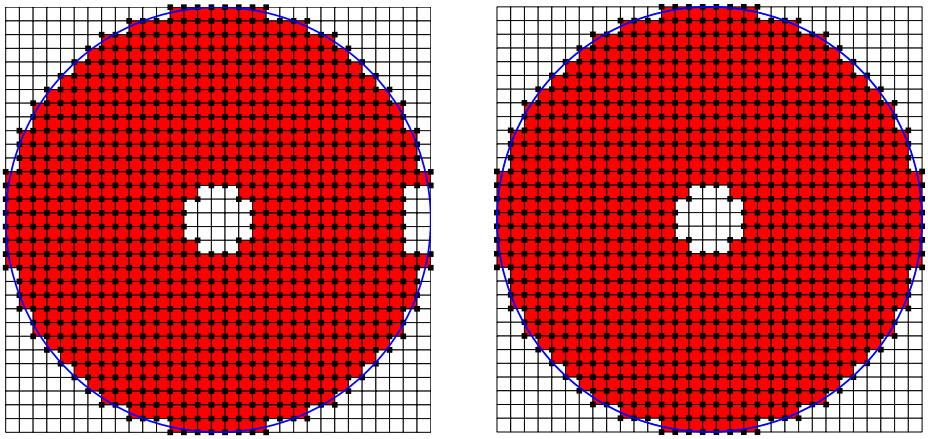

Figure 4.1: Valid subaperture map (big red squares) showing the valid actuators (small black squares). **Left:** BMM2 case. **Right:** BMM3 case.

The valid subaperture and actuator configuration used for both cases, BMM2 (patched pupil mask) and BMM3 (full VLT pupil mask) is shown in figure 4.1. A subaperture is considered valid if it receives at least 50% of the light of a fully illuminated subaperture. The valid actuators are the ones surrounding all the valid subapertures. For the first configuration, 718 subapertures and 792 actuators are considered, while for the second case it corresponds to 728 subapertures and 800 actuators.

4.1 BMM quadratic control

For a MEMS DM (as explained in section 1.2.2) the relation between position (displacement) and force (voltage) is not linear, but quadratic. To compute the position of the actuator we considered a simplified quadratic law, instead of using the real displacement vs voltage curves measured.

The HVA controller range is -1 to 1 (this scale is called *normalized units* (n.u.)) , which corresponds to 0 to 200 V. Considering now a displacement range (D) from 0 to 1 corresponding to the voltage range (V) -1 to 1, the simplified quadratic law is given by:

$$D = \frac{(V+1)^2}{4} \tag{4.3}$$

$$V = 2\sqrt{D} - 1 \tag{4.4}$$

Figure 4.2 shown this simplified quadratic law. Now, the bias value (rest position) of 0.14 n.u corresponds with 0.325 displacement units, and the maximum voltage of 0.63 n.u to 0.664 displacement units.

The conversion step between displacement and voltage is done just before sending the commands to the DM. In this way, all command computations are done in displacement units. The interaction matrix gives the relation between slopes and displacement, while the modal basis gives the relation between modes and displacement. This approximation allows to simplify the control and calibration since the real behavior of the DM is transparent and only linear relations are used for the matrix operations.

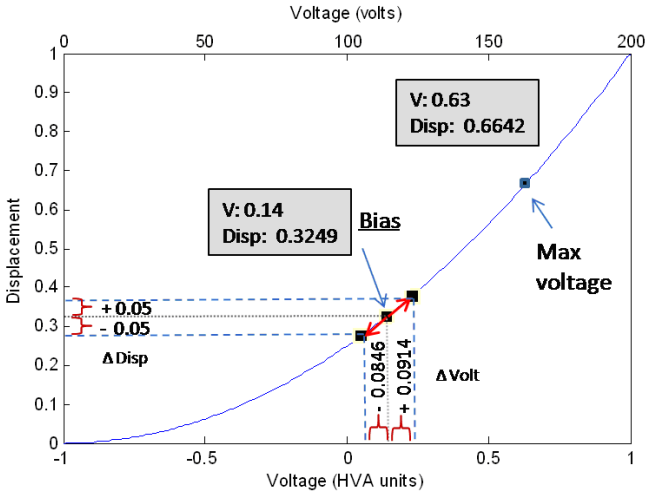

Figure 4.2: Curve showing the quadractic law used for the BMM control. The red arrows show the delta displacement from the bias used for the calibration. A displacement delta of 0.05 is used as input for the Hadamard pattern. The curve gives the equivalent values in voltage units to be applied to the actuators.

4.2 Calibration

4.2.1 Hadamard zonal calibration

The purpose of the AO calibration procedure is to measure the effect that each DM actuator has on the WFS measurement. Several parameters can be optimized on this process: the type of signal applied to the DM, the strength of this signal and its sequential measurement by the WFS.

An identity matrix is used in the classic zonal calibration, i.e, when applying sequentially each of the columns of the matrix, only one actuator is pushed and therefore only a small region of the WFS measures the perturbation produced by the DM, while the most part of the WFS measures noise. This effect is obviously worst for high-order systems.

To increase the SNR, it would be necessary to take several runs of measurements, with the consequent increase of time. Instead, a Hadamard matrix could be used. This matrix is a square matrix containing only 1's and -1's such that when any two columns or rows are placed side by side, half the adjacent cells are the same sign and half the other. Hence, the rows and columns are orthogonal and the Hadamard matrix (H) is hermitian and also invertible:

$$HH^t = 1 \tag{4.5}$$

$$HH^{-1} = 1 \tag{4.6}$$

Calibration using Hadamard matrices is demonstrated by Kasper *et al.* 2004 ([75]) to give the best theoretical SNR for the same number of measurements. Conceptually it is easy to understand since all actuators are pushed simultaneously, and therefore the full WFS measures the DM perturbation.

The raw measured IM gives the relation between WFS signals (rows) and each of the Hadamard modes (columns). The final IM giving the response of each individual actuator, could be recovered using the orthogonality property of the Hadamard matrix:

$$D = D_{raw}H^{-1} \tag{4.7}$$

Hadamard calibration could be misunderstood as modal calibration, since a sequence of "modes" are applied to the DM. The main differences lies in the inversion. The Hadamard matrix D is invertible,

and therefore the matrix D could be found unequivocally from D_{raw}, while for the usual modal bases (zernike, K-L) this is not true.

4.2.2 Acquisition

The IM is acquired using a diffraction-limited source (the so-called *alternative source*) thanks to an alternative path that avoids the presence of the phase screens. The IM is measured using the *push-pull* method ([76]). The j^{th} column of the raw interaction matrix, denoted as $D_{raw}(j)$ and corresponding to the sensor signal vector S associated with the j^{th} Hadamard pattern h_j, was computed as:

$$D_{raw}(j) = \frac{S(+Ah_j) - S(-Ah_j)}{2A} \tag{4.8}$$

where A is the amplitude factor. Thus, for each DM pattern two opposed sensor signals are measured corresponding to the up and down positions. In this way, the signal due to the static aberrations is filtered out. Such method *freezes the turbulence* removing the contribution of the slow evolving bench air if both signals are measured sequentially at high speed.

4.2.3 Speed optimization

The measurement of the 1024 columns of the IM is done sequentially. An elapsed time is necessary after applying each command to ensure that the actuator signal is well recorded by the WFS. Instead of introducing an arbitrary delay, it is more convenient to do a continuous frame acquisition at a defined frequency and to remove a certain number of frames considered not valid. The speed of the acquisition can be improved finding the optimal combination between CCD frequency and minimum number of

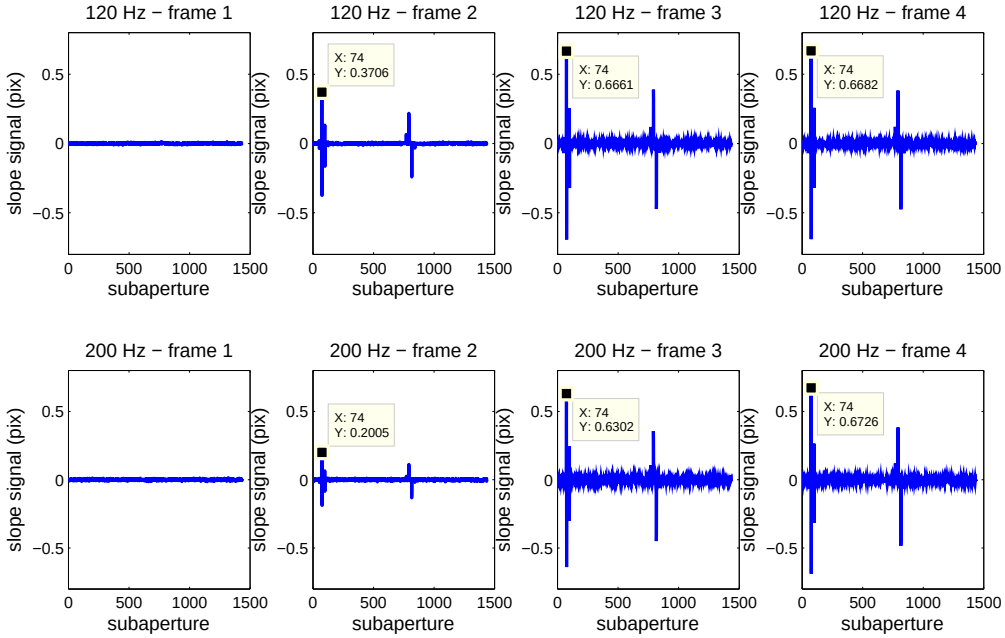

Figure 4.3: Example of frame acquisition for the 120 (top) and 200 Hz (bottom) cases. A sequence of 4 plots show the max signal produce on the detector for the 4 first frames after applying a voltage to one of the actuators (the command is applied between frame 0 and 1). For each subaperture position (on the X axis, 1-718 corresponds to X direction and 719-1436 the Y direction) we plot the signal measured on the detector.

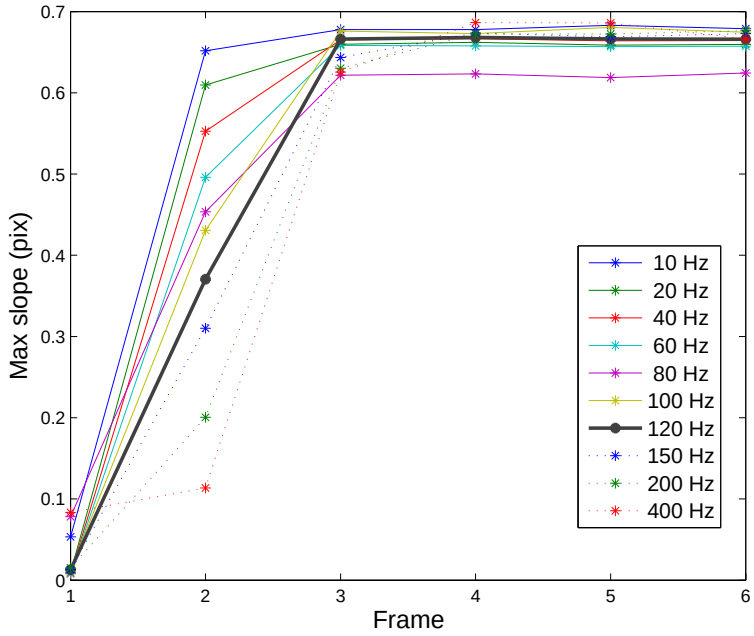

Figure 4.4: Plot showing the data of table 4.5; maximum slope (pix units) measured during the frame series for different CCD frequencies. For frequencies down to 120 Hz it is necessary to skip two frames while for frequencies up to 150 Hz it is necessary to skip three.

frames to skip in order to obtain the first useful frame (the first frame where the full actuator signal is seen by the sensor).

To find the optimal relation, a continuous set of frames was acquired for different CCD frequencies. In the middle of each sequence an actuator is pushed and we look for the first frame with the maximum signal. Figure 4.3 shows the recorded slope frames for the CCD integration time cases of 120 Hz and 200 Hz. The first frame after sending the command do not show any signal since it corresponds with the previous CCD integration period. For the next frame it is clear that the signal recorded by the WFS is not the maximum possible value. This effect is due to the fact that for an integration time of the CCD

freq [Hz]	frame 1 slope [pix]	frame 2 slope [pix]	frame 3 slope [pix]	frame 4 slope [pix]	frame 5 slope [pix]	frame 6 slope [pix]	Skipped	Speed [Hz]
10	0.05	0.65	0.68	0.68	0.68	0.68	2	3.33
20	0.01	0.61	0.66	0.66	0.66	0.66	2	6.67
40	0.01	0.55	0.67	0.67	0.66	0.66	2	13.33
60	0.01	0.50	0.66	0.66	0.66	0.66	2	20.00
80	0.08	0.45	0.62	0.62	0.62	0.62	2	26.67
100	0.01	0.43	0.68	0.67	0.68	0.67	2	33.33
120	0.01	0.37	0.67	0.67	0.67	0.67	2	**40.00**
150	0.01	0.31	0.64	0.67	0.67	0.67	3	37.50
200	0.02	0.20	0.63	0.67	0.67	0.68	3	50.00
400	0.08	0.11	0.63	0.69	0.69	0.67	3	100.00

Figure 4.5: Table showing the maximum slope measured during the frame series for different CCD frequencies. The actuator command is sent between frame 0 and 1. The 7th column shows the minimum number of frames to skip on the IM acquisition. The last column shows the effective speed of the loop for each CCD frequency and skipping the minimum number of frames. The optimal case is found at CCD speed of 120 Hz and skipping 2 frames. The result is a loop frequency of 40 Hz.

two positions of the actuator are averaged (rest and energized). Thus the resulting measured slope is proportional to the integration time that the actuator is active. In the fast case of 200 Hz also the third frame does not record the maximum slope.

Table 4.5 and figure 4.4 show for different integration times, the slope produced by the WFS along the consecutive frames after applying the same command. The last column shows the effective acquisition speed taking into account the integration time and the required skipped frames. The optimal case is found for a CCD integration time of **120 Hz** and skipping 2 frames which gives an effective acquisition speed of **40 Hz**.

Thus, the IM is acquired at a frame rate of 120 Hz, needing to acquire 3 frames for each DM position (rejecting the 2 firsts). Considering 10 push-pull series of measurements for each Hadamard mode, the final time required to calibrate the 1024 actuators is $\approx$ **10 min**.

4.2.4 Amplitude optimization

The amplitude parameter A on equation 4.8 (giving the stroke of the Hadamard pattern applied to the DM) should be optimized to produce the maximum signal on the WFS but avoiding saturation. To find the optimal value we use different amplitude factors for the calibration, recording the sensor signal vectors $S(+Am_j)$ and $S(-Am_j)$. Afterwards, using the response curve of each subaperture (section 3.4.3), we verify that the sensor signals do not exceed the linear range. The maximum amplitude factor avoiding saturation was 0.06. A value of **0.05** was used for the calibration process in order to keep a margin of error.

4.2.5 Interaction matrix analysis

The size of the IM measured is 1456 (slopes x,y) x 1024 (actuators). It is necessary to keep only the columns corresponding to the actuators inside the pupil. We verified from the IM that these actuators produce enough signal. Thus, the final IM matrix size is 1456 x 800 actuators. Figure 4.6 shows the final interaction matrix measured with Hadamard. For each half of the IM (corresponding to S_x and S_y), the main part of the signal is distributed on the diagonal, and for each actuator, is concentrated in four subapertures while the rest of the subapertures measure only noise.

Firstly the Hadamard IM is compared with the zonal case. Two zonal IM are acquired, one with the same gain (displacement) applied to the Hadamard and another applying the double (since on the Hadamard pattern two actuators are displaced in opposite directions, then the signal produced is double, hence it is necessary to compare the Hadamard case with a zonal IM with double gain).

In order to measure the noise variance, we compute the standard deviation over the upper and lower triangular area of the IM (splitting between X and Y signals and removing the diagonal region where the signal is distributed). Table 4.1 shows the variance for the 3 cases. The noise improvement factor between the Hadamard and zonal (applying the same displacement) should be $\approx n$, the number of actuators (as shown Kasper *et al.* 2004 [75]). In our case the measured factor is $\approx$ 850 which is in accord with the number of valid actuators, 800.

An equivalent method to measure the noise variance consists in computing the histogram of all the elements of the IM. The central region of the histogram is only affected by the noise and therefore will follow a Gaussian distribution. The noise variance is computed from the HWHM of the fitted Gaussian. The results are also shown in table 4.1. The improvement factor is $\approx$ 857, equal to the previous value. The improvement in SNR can be seen in Figure 4.7. Showing the IM in a logarithmic scale, the difference in variance noise is clear. In the Hadamard IM we can see additional diagonals (signal produced over subapertures faraway from the corresponding actuator) showing that the noise level is lower than for the zonal case.

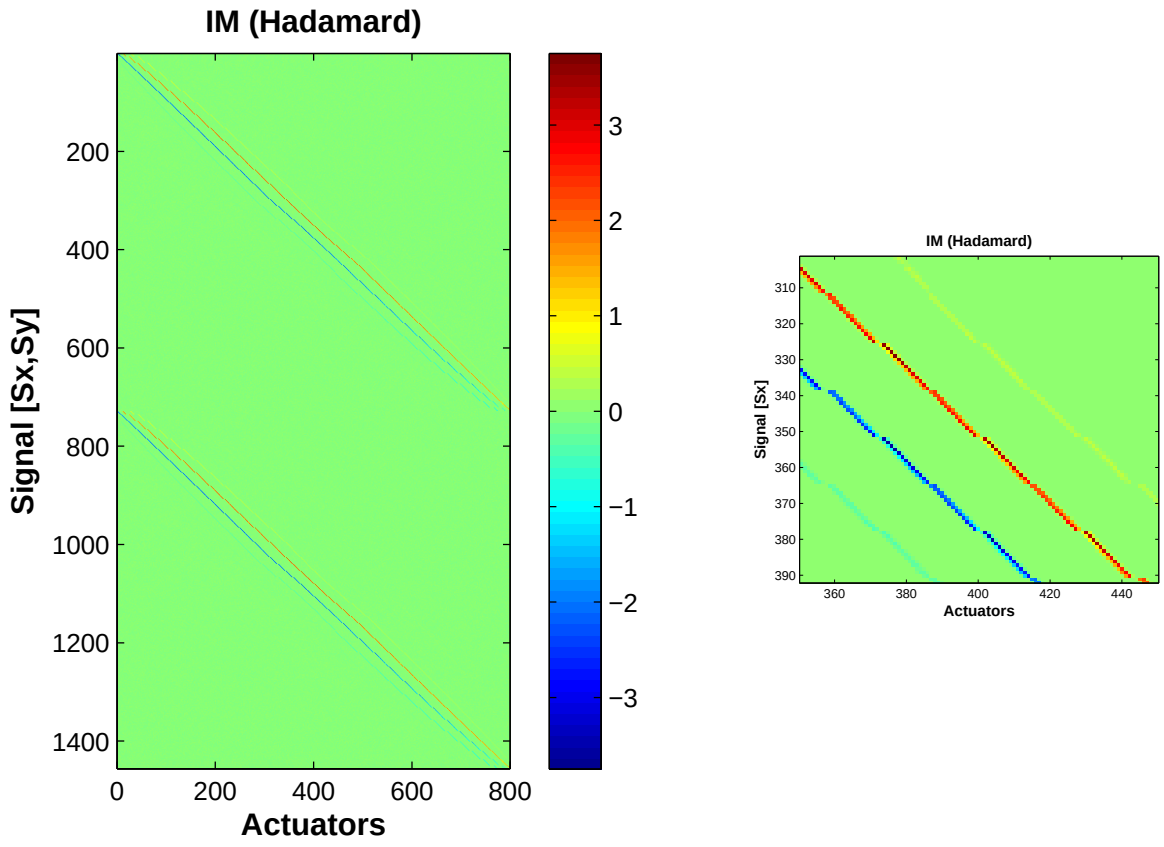

Figure 4.6: **Left:** Hadamard IM showing a clear diagonal structure. **Right:** Zoom over the center of the upper half of the IM (S_x signals).

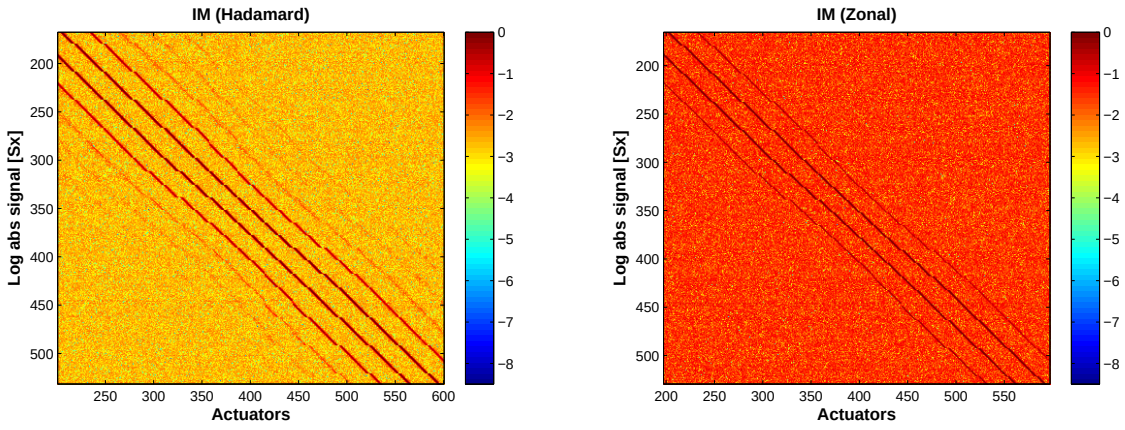

Figure 4.7: Logarithmic of the IM for the Hadamard (left) and zonal (right) case. It is clear that the zonal IM is more noisy.

It was also considered as quality criterion of the IM the computation of the conditioning number (ratio of the highest and lowest singular values from the *"Single value decomposition"*). The less noisy the IM, lower will be the condition number. Such criterion is true only for some cases (e.g. MACAO system [75]). In our case this is not true (as well as in Fusco *et al.* 2007 [77]). The condition number for the 3 interaction matrices are shown in table 4.2. Thus, for the Hadamard case (less noisy) the condition number is the highest.

Looking at figure 4.8, showing the eigenvalues obtained in the SVD, it is clear that the condition number for the Hadamard case is higher because the eigenvalues of the unseen modes drop fast close to zero. If we consider for the condition number only the eigenmodes used to compute the inverse matrix ($\approx$ 700 modes) we see that the expected behavior is recovered (table 4.2). This means that a better criterion to analyze the IM quality would be to consider the condition number over the eigenmodes considered as visible, instead of the eigenmodes over the full SVD.

Table 4.1: IM noise variance

	Hadamard	Zonal (double)	Zonal (single)
Noise variance [pix^2] (Diagonal method)	1.10e-05	0.0024	0.0094
Noise variance [pix^2] (FWHM method)	1.07e-05	0.0023	0.0092
Improvement factor (Diagonal method)	1	215	850
Improvement factor (FWHM method)	1	215	857

Table 4.2: IM conditioning number

	Hadamard	Zonal (double)	Zonal (single)
Condition number (full modes)	104.3	9.3	6.8
Condition number (700 modes)	3.1	3.2	3.9

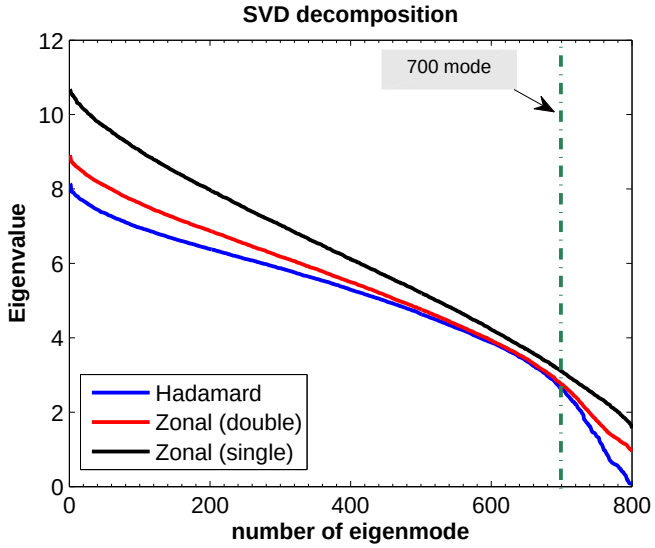

Figure 4.8: Eigenvalues plot obtained on the SVD decomposition for the Hadamard and zonal IM.

4.3 Modal basis

4.3.1 The Karhunen-Loeve basis

The modal basis construction is inspired by the method developed by E. Gendron ([68]), and applied previously, for example, on the Keck AO system ([78]), but has not been tested before for larger actuator AO systems. The specific algorithm applied is the same used to obtain the modal basis for the XAO system of SPHERE ([77]).

As explained in section 1.2.3, the classical Karhunen-Loeve (K-L) base is statistically independent and orthogonal, since it is computed from the diagonalization of the Zernike covariance matrix. This basis is derived only from the turbulence characteristics and does not seem totally suitable as it is computed without respect to the whole AO system properties, especially the DM characteristics.

Since a Karhunen-Loeve base could be constructed from any base and not necessary from the Zernike base, we could use the base defined by the DM influence functions to obtain a modal basis taking into account both the system properties and the particular distribution of the turbulent energy according to spatial frequencies.

However the IF base is not orthogonal. On the other hand, applying the classic K-L algorithm we will recover a basis with uncorrelated modes but not orthogonal. The problem is solved by applying a double diagonalization algorithm: by diagonalizing the geometric covariance matrix we recover a orthogonal basis, while the eigenvectors of the statistical covariance matrix produce uncorrelated modes. The exact algorithm used is explained in detailed in appendix B.

4.3.2 K-L base computation

We consider the BMM influence functions measured in section 3.2.4. Since the behavior is approximately the same for all actuators, and the only difference is the position on the IF matrix, we could consider a mean IF computed from all the IF's. Afterwards, this mean IF substitutes for the individual IF's, keeping the position of the IF matrix. Thus, the errors in the IF measurements are eliminated although minor individual actuator information is lost. This mean IF matrix is used as input for the K-L basis computation.

We consider a circular pupil without obstruction perfectly centered on the BMM. To choose the valid actuators for the mode computation the pupil is projected on the IF and only the actuators whose effective IF reach 50% of the peak of the complete IF are selected. Thus, 812 actuators are considered.

An atmosphere following a von Karman spectrum with $L_0 = 50$ m and $r_0 = 0.2$ m is considered for the computation (piston and tip-tilt removed).

4.3.3 Truncation

The computed modal basis B has 812 modes. But not all the modes could be used on the reconstructor due to stability problems in the control. In addition, higher order modes require higher stroke, so it is necessary to apply a gain or truncate them directly.

It is necessary to find a trade-off between the number of modes and stability. Using a higher number of modes, the theoretical performance should be higher (for high flux conditions) but at the expense of stability and saturation. On the other hand, using few modes the performance is lower since the high spatial frequencies of the turbulence are not corrected.

We decide to use two truncated modal bases: A low order base with ≈ 400 modes and a high order base with ≈ 700 modes. The low order base is very stable and gives good performance on close loop (see next chapter). On the other hand, the high order base is not stable: the performance diminishes along the

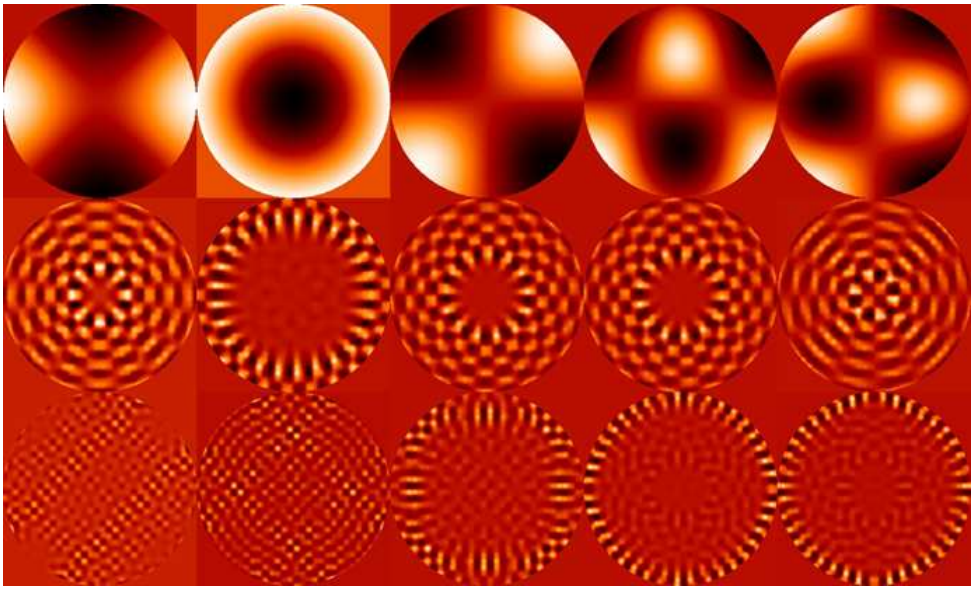

Figure 4.9: Example of K-L modes for three different ranges, first row low orders(<50); second row middle order(200); third row high order(>400).

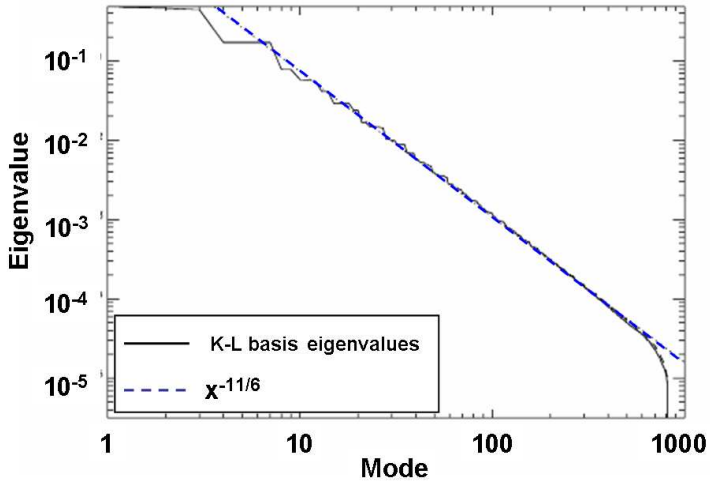

Figure 4.10: K-L basis eigenvalues reconstructed from the BMM IF's. As expected the eigenvalues follow the von Karman law $x^{-11/6}$.

loop. In addition the shape of the DM shows an unexpected waffle shape. As well, bases with 500 and 600 modes were tested, but similar problems appear.

To understand the problem we plot the maximum displacement required by each mode as a function of the modal order (figure 4.11). The maximum displacement is computed as the maximum absolute value of each column of the B matrix. The expected behavior is a monotonous increase of the required displacement. Looking at the plot, this is true only until the mode 412, while for higher orders several modes show "anomalous" high order values.

If we look at the wavefront representation of these modes from the matrix Q (figure 4.12), it is clear that basically these are waffle or partial waffle modes. In principle these modes should appear at higher number order (> 700) and not for middle order (≈ 400). Figure 4.10 shows the eigenvalues distribution

of the basis, which follows a perfect Von-Karman spectrum. We would expect these waffle modes to be related to the lower eigenvalues since waffle is not representative of the turbulence and therefore the energy associated to them should be close to zero. This behavior is not yet full understood and should be studied in more detail.

To overcome the problem we decide to truncate the basis taking into account the maximum displacement required. From the first 400 modes the linear expected tendency displacement versus modal order is used to define an increased threshold (red line on figure 4.11). Modes with higher displacement are rejected.

223 modes are rejected, thus, the final high order basis has 589 modes. The new basis solves the previous instability problems and gives better performances with respect to the low order 412 modes basis (see next chapter).

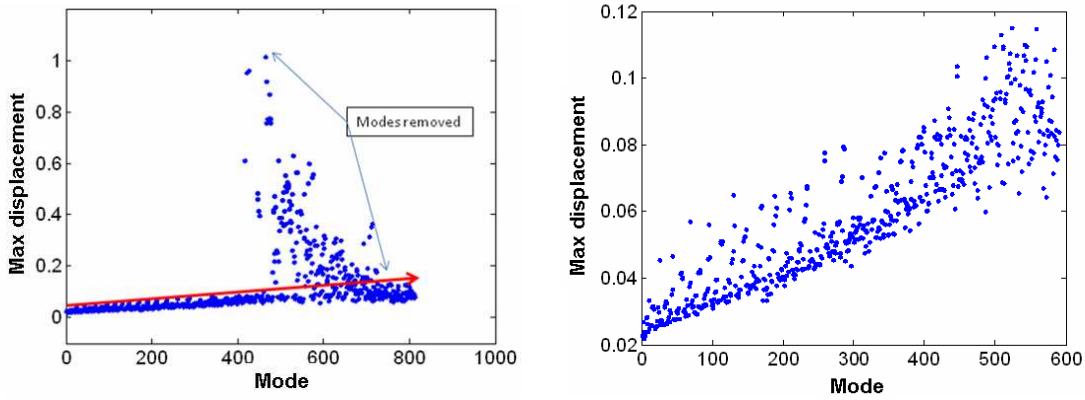

Figure 4.11: **Left:** Max displacement required by the mode as a function of the modal order. The red line shows the threshold apply to select the valid modes (increasing as the modal order). **Right:** Max displacement required as a function of the modal order for the final truncated modal basis (589 modes).

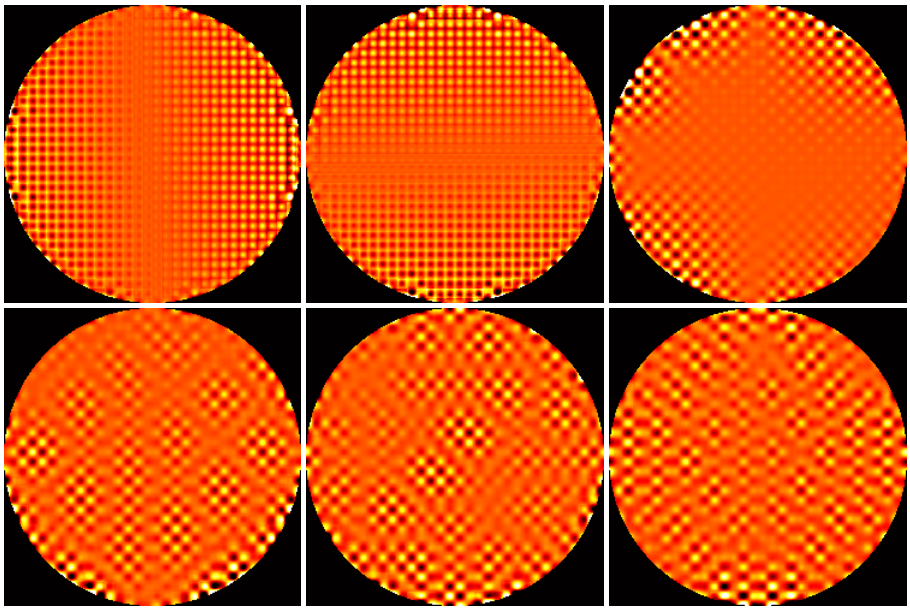

Figure 4.12: Example of rejected waffle modes (first row: modes 420, 425 and 467. Second Row: modes 518, 524 and 571).

4.4 Slaving

The main problem of the BMM deformable mirror is the short stroke capability. This limitation could produce possible stroke saturation problems especially correcting high order modes which are strongly stroke demanding by the actuators on the pupil edge. To increase the stability of the system we will slave the extra actuators outside the pupil (not consider actives) to the actuators on the pupil edge. Thus, the stroke capability of the actuators on the pupil edge (*masters*) will increase.

We consider as *masters*, the actuators that are not fully surrounded by other active actuators. For each *master* we consider as *slave* actuators the non active actuators surrounding it. Hence, there are 104 *slave* actuators distributed in two rings outside the pupil and 66 *master* actuators. This means that there are several *masters* associated to 2 *slaves*.

Slaving requires some modifications to the interaction matrix. It is necessary to take into account in the IM the increase of stroke of the *masters*. For it, the columns of the IM corresponding to the *masters* will be substituted by the addition of the *master* and *slaves* IM columns. The new IM will be called *slaved IM*.

In addition, in the control loop the commands computed for the master will be also applied to the slaved actuators.

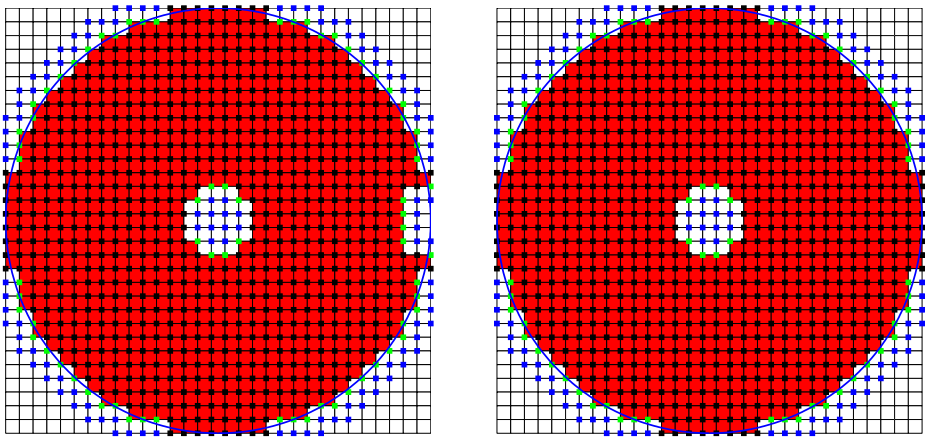

Figure 4.13: Slaving actuators map. *Black squares*, regular active actuators; *green square*, masters actuators; *blue squares*, slave actuators. **Left:** BMM2 case. **Right:** BMM3 case.

4.5 Reconstructor computation

Two control matrices are computed following equation 4.2 using the 412 mode basis and the 589 mode basis. The inverted matrices B^+ and the slaved interaction matrix M^+ are computed applying SVD where truncation is necessary.

In the case of the IM, if few modes are truncated (<20), the final reconstructor is unstable in close loop operation. On other hand, if too many modes are truncated (>40), the system is under performing. We found an optimum value of 30 modes.

The matrix B has a condition number of 58, for the high order base (589 modes) and 30 for the low order base (412 modes). The eigenvalue distribution from the SVD inversion (figure 4.14) exhibits an inflexion point which gives the optimal truncation number of modes. 8 and 6 modes for the high and low order bases, respectively. Both cases correspond to the same eigenvalue.

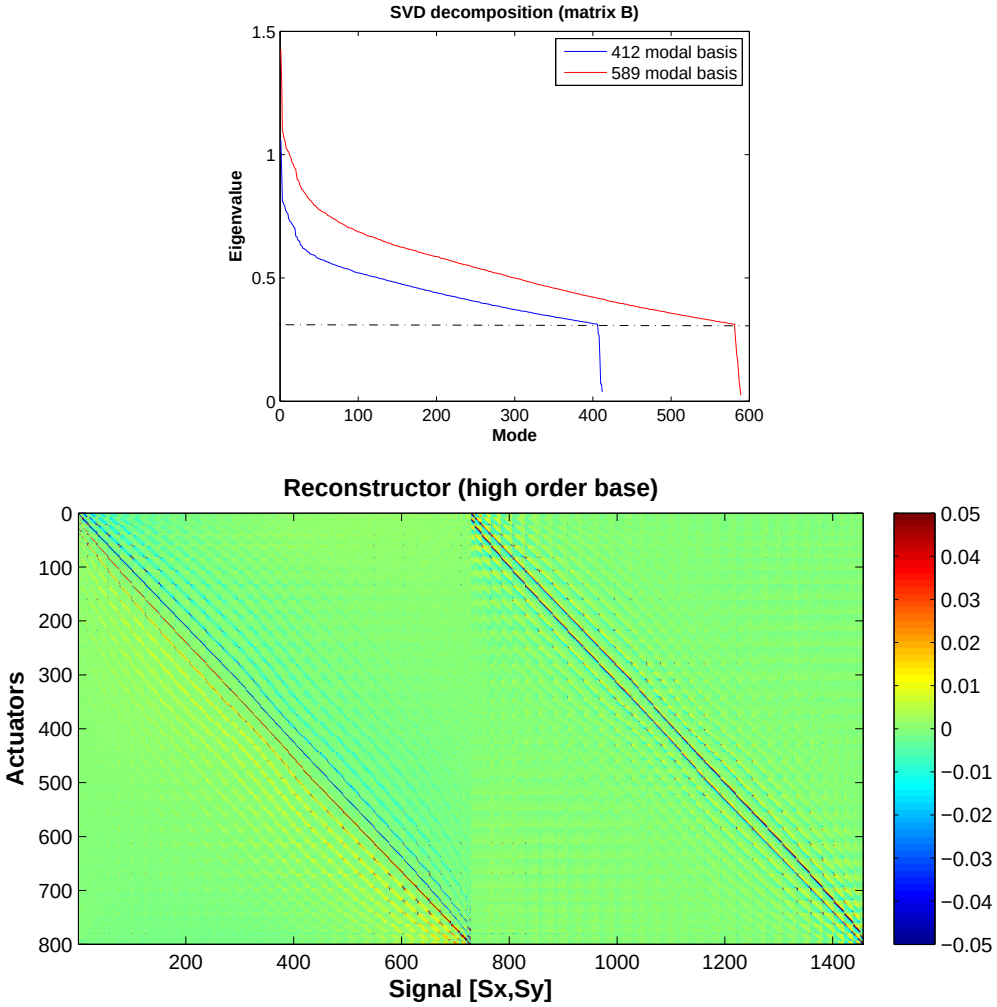

Figure 4.14: **Top:** Eigenvalues distribution from the SVD inversion of the matrix *B* (589 and 412 modes). In both cases an inflexion point shows the optimal truncation value (8 and 6 modes respectively). **Bottom:** Reconstructor matrix using the high order modal basis. A clear diagonal structure can be seen (the scale was expressed between -0.05 and 0.05 in order to saturate the high values, the min value is -0.3 and the maximum 0.4).

4.6 Loop control

A simple algorithm is implemented for the loop control. Since the TTM is used to correct the tip-tilt contribution of the atmosphere, the control of the BMM is tip-tilt free. An independent IM for the TTM is acquired and through a simple inversion the TTM reconstructor is recovered. On each iteration of the loop, the tip-tilt mount commands are computed from the slopes measurements using the TTM reconstructor. Then, the residual tip-tilt free wavefront is obtained and used as input for the main BMM loop.

The controller used is a regular integrator modified with a simple anti-windup circuit (gain 1) as shown in figure 4.16 to avoid possible saturations. The loop works in a serial mode: after the complete pixel frame is acquired, the slope vector is computed and injected in the loop in order to obtain the new command vector. The speed of the system is controlled by the CCD integration time. The loop waits until the next frame is acquired thanks to an internal CCD frame counter that also avoid frame loss. The speed of the system is limited to 80 Hz due to matlab speed limitations coming mostly from the graphical

interface.

A GUI (*graphical user interface*) under matlab was implemented to be able to control easily the AO system. The main tasks of the *SHS Guide Control* are:

- Close and open the loop (a). Several loop parameters can be configure as gain and speed.
- Select the configuration files (c): Reconstructor, IM, valid and slaving actuators mapping, reference slopes, initial actuators voltage and modal basis matrix.
- Update slope offsets in real time (d).
- Save to disk commands and slope vectors series (b).
- Control the actual BMM commands sent to the mirror and TTM (e) (the actuator map is shown only on demand to not introduce an additional delay in the system).

In addition to the matlab GUI, the RTD display shows in real time the frame of the CCD pixels.

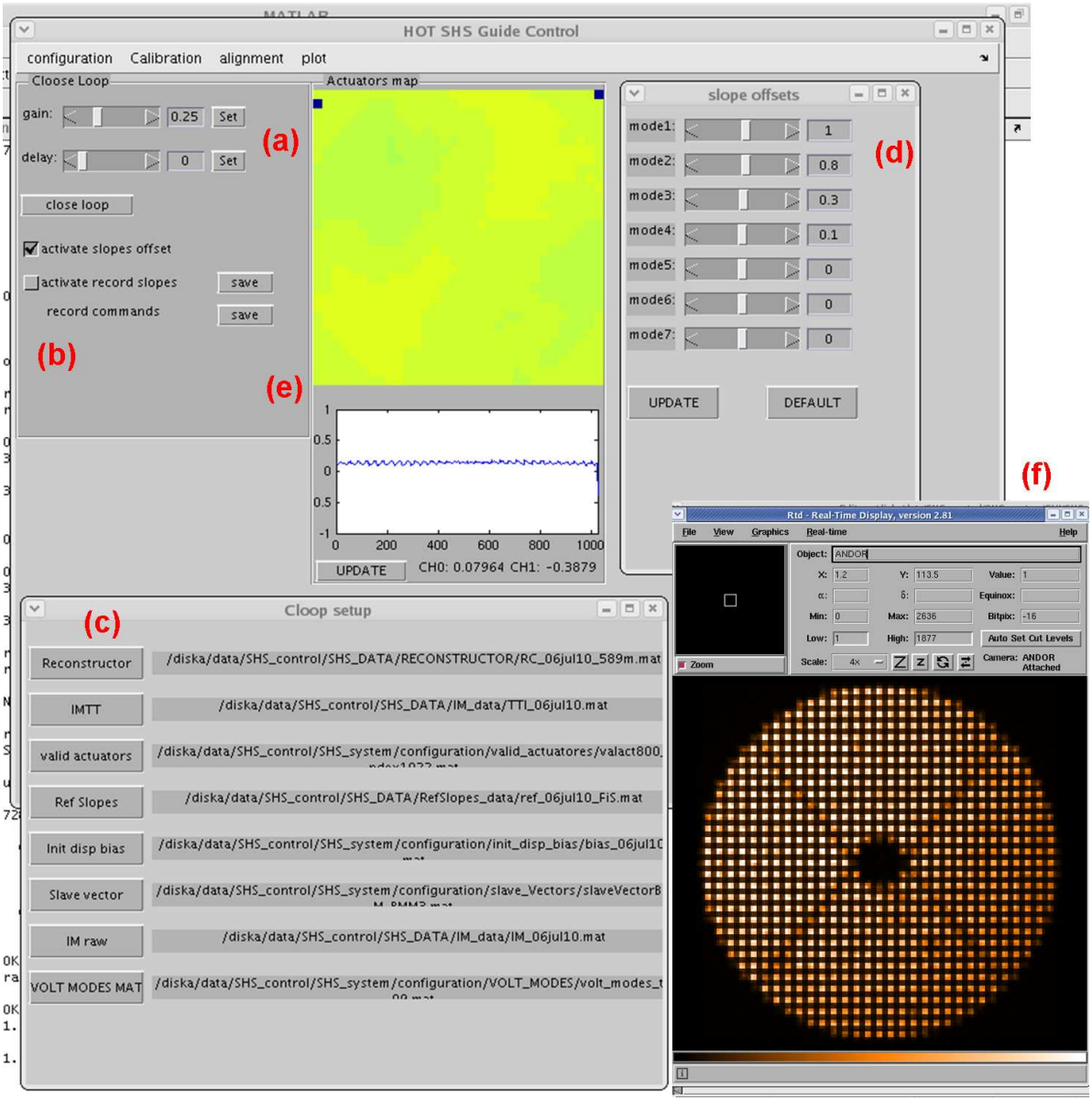

Figure 4.15: Display of the *SHS Guide control* and RTD (*real time display*).

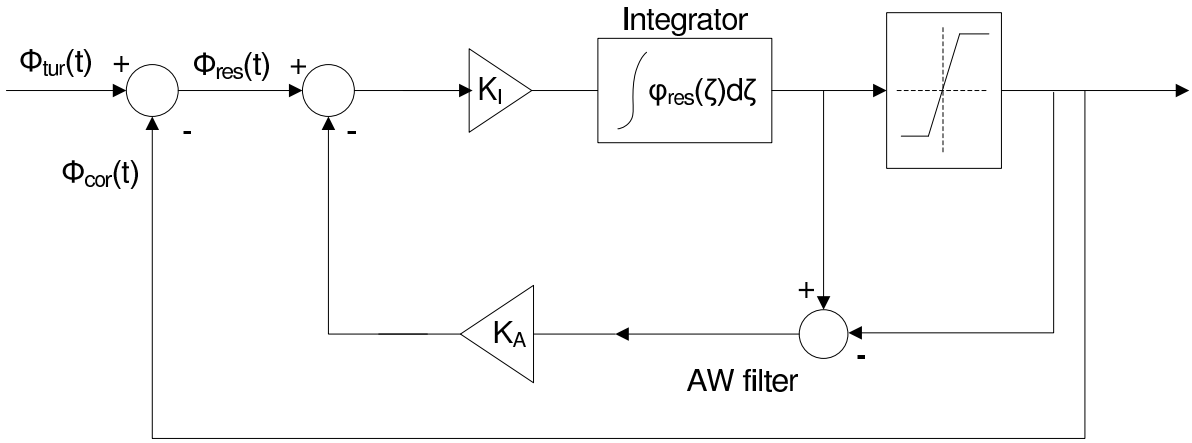

Figure 4.16: Block diagram of the integrator controller used on HOT. An antiwind-up circuit with gain $K_A = 1$ and clipping are also included. K_I is the integrator gain.

5

XAO experimental results

The estimation of the real performance of an adaptive optic system is always a discussed question. Along this chapter we will show the performance of our system as a function of the star magnitude. In our case, this relation takes a relevant importance since it is the first time to verify the improvement obtained at low flux levels thanks to the technological development of the electro-multiplicative CCDs.

The performance estimation as well as the gain optimization, will be done taking into account both, the strehl ratio (measured on the IR path) and the residual wavefront measurement (transfer function, modal correction, etc).

5.1 Experimental conditions

5.1.1 Star magnitude

White light is used to feed the turbulence generator through a fiber of 9 μm. The light is generated by an halogen lamp using a power supply to regulate the intensity. The regulation of the intensity at low intensity is quite difficult due to resistance variations of the lamp. Thus, we decided to use a set of neutral density filters (ND) installed on the SHS path (after the collimator), while the lamp is kept at maximum power.

In addition, the estimation of the flux is more accurate since we measure the high flux case with the WFS camera and without ND (less impact of the background and RON error). Then, the flux for the faint star magnitude is extrapolated since the ND attenuation is well known.

The flux (without ND) measured was $1.55 \cdot 10^9$ ph/sec equivalent to $2.66 \cdot 10^4$ $ph/sub/frame$ (at a camera frame speed of 80 Hz). Taking into account the loop frequency of SPHERE ,1.2 kHz, (in order to consider a realistic XAO case), the equivalent simulated star magnitude is 2.1. The NDs used to study the SR versus magnitude curve are: 1.5, 2.5, 3.0 and 3.5. Table 5.1 shows the flux variation and equivalent magnitude for the 5 experimental cases.

5.1.2 CCD L3 gain and equivalent RON

The ANDOR CCD camera was set to the optimal conditions following the recommendations of [53]. The preamplifier gain was set to value 1 corresponding to a system sensitivity of 32.5 e/ADU (absence of L3 gain).

It is possible to configure the amplitude of the clock voltages thereby amplifying the signal. Gain index values between 0 and 4096 are permitted, but it is not recommended to use gains over 3500. Figure 5.1 shows the system sensitivity as a function of the L3 gain index. The working camera temperature is minus 82 degrees.

The L3 gain index is selected for each magnitude star in order to maximize the signal while avoiding saturation. The maximum value used is around 9000 ADU, since the signal starts to go non-linear at 10,000 ADU (clipped at 16383 by the ADC range).

The camera was characterized at the beginning of the project to check the specifications ([53]). The intrinsic noise of the camera is very high; up to 200 e^- RMS. With the L3 gain turned up high, this became insignificant, 0.07 e- RMS at 3500 index.

In an initially test step, we found a poor performance of the system for low flux conditions which could be tracked down to the noise level: RON or background contamination. The real impact of the L3 gain index on the noise level was studied in order to know if an increase of the gain produce a real decrease on the noise contribution. For this, we acquired a set of CCD frames without light for different gain levels. The standard deviation of the signal for each frame gives an idea of the noise level. Plotting the rate between gain and standard deviation for each gain, shows the efficiency of the gain in the reduction of the noise.

Figure 5.2 shows the curves for the three cases studied: shutter close, shutter open and shutter open with better bench closure. In this last case we improved the light-tightness of the bench to avoid background contamination by ambient light coming from the lab.

It can be observed, for the three cases, that a maximum of performance (reduction of effective noise) is reached at a gain level of ≈ 380 (L3gain index 3100). For higher gain the noise reduction is constant (or decrease slightly). Hence, it is not recommended to use higher L3 gain index than 3000 since a noise

Table 5.1: Star magnitude

Star	ND	Δ mag	Magnitude	ph/sub/frame
A	0	0	2.1	$2.66 \cdot 10^4$
B	1.5	3.75	5.9	842
C	2.5	6.25	8.4	84
D	3	7.5	9.6	27
E	3.5	8.75	10.9	9

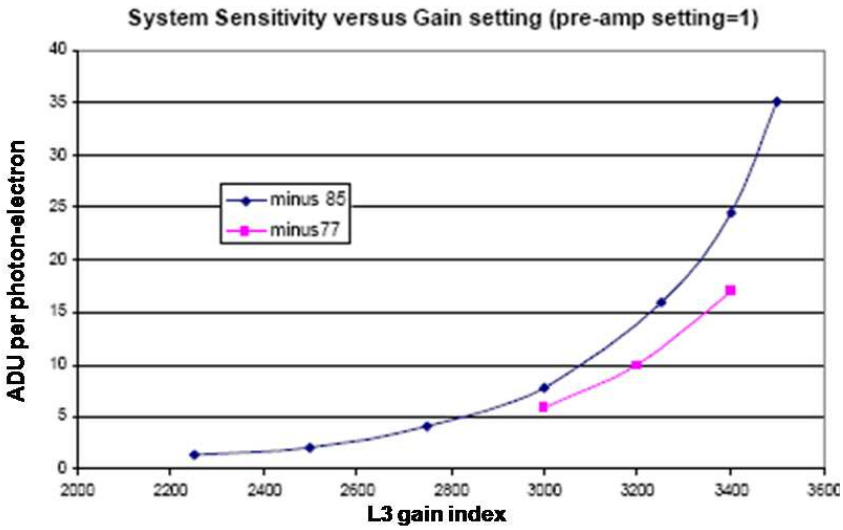

Figure 5.1: Curve showing the sensitivity behavior as a function of the L3 gain index for cooling temperatures of minus 85 and minus 77 degrees.

reduction will not be obtained.

On the ideal case (shutter close) the minimum noise reached is 0.54 e. For this case the noise is due to dark and RON, without photon noise contribution. In the cases with the shutter open, the noise level is higher, due to background light contamination of the bench.

After improving the bench closure, the noise level decrease drastically reaching values closer to the ideal case. The photon contribution was reduced in a factor 2.3 (noise goes from 1.54 e to 0.67 e). Background photons contamination in the bench explains the poor performance at low flux conditions. Table 5.2 shows the final gain index used for each star magnitude as well as the maximum signal reached on the detector.

Table 5.2: L3 gain index used and maximum signal reach on the CCD for each flux level.

Star	ND	L3 gain index	CCD max level
A	0	1200	2600
B	1.5	2600	1500
C	2.5	2900	600
D	3	2900	400
E	3.5	3000	300

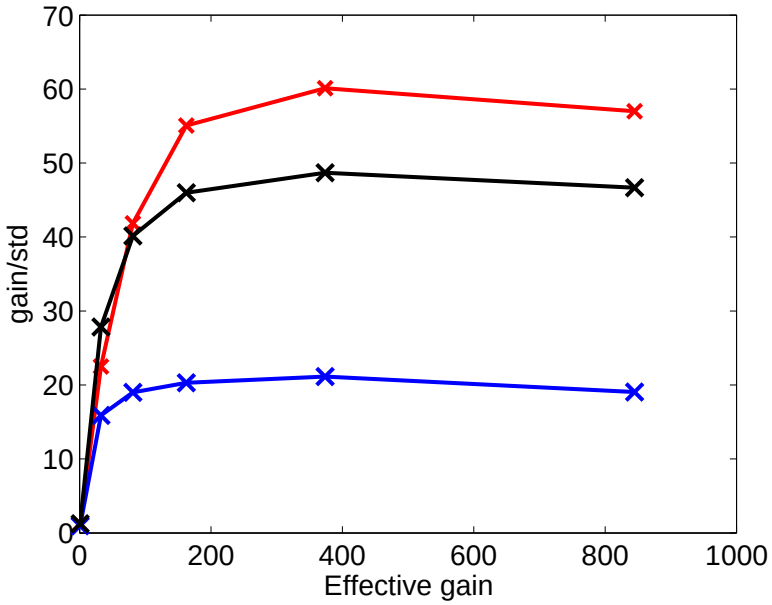

Figure 5.2: Plot showing the rate gain/std (noise improvement) for each gain level. The red curve shows the ideal case with the shutter close while the blue and black curve show the cases with the shutter open, before and after improving the bench closure respectively.

5.1.3 AO configuration

Table 5.3 summarizes the AO configuration used for the experiment and already explained in previous sections. Seeing, loop frequency, reconstructors, gain and other configurable parameters are included.

Table 5.3: AO configuration

Parameter	Configuration
Seeing	0.5 ” seeing (with reduced low order aberrations).
Wind speed	1.2 m/s
Loop frequency	80 Hz.
Loop gain	0.2 - 0.35
Bandwidth	1.8 - 3.5
Reconstructor	589 modes
	412 modes
Reference slopes	Fiber reference slopes .
Offsets	Slopes offsets included to reduce low order aberrations (def, astig, coma, trefoil) on the non common path.

5.2 Performance metrics

5.2.1 PSF analysis

The PSF images for the different study cases were recorded with the ITC camera in the IR path (H-band, narrow filter 1.4%). The ITC linear range is up to ≈ 10000 ADU; hence, a neutral density wheel in front of the detector was necessary to keep the signal on the CCD below this limit.

The ITC integration time (individual frames) was set at 2 seconds and the density wheel set at the position for which the peak signal is around 8000 counts. The images were acquired with an exposure time of 3 min 19 sec which ensure a good signal to noise ratio.

PSF profile and pixel scale estimation

A standard image processing is applied to the raw PSF image consisting on dark subtraction, sky subtraction and spike filtering ($\sigma_{sky} \approx 3.2$ counts).

The PSF profile is computed as an azimuthally-averaged profile covering 1.06 arcsec (200 pixels). So, the diffraction effect of the spider and a small ghost are also included.

The pixel scale was estimated measuring the position of the 3^{rd} minimum (dark ring) in the PSF profile: 25 pixels. For a circular pupil with 14% central obstruction ratio this minimum corresponds to a distance of 3.142 λ/D. Thus, the pixel scale obtained is 5.314 mas/pix (λ=1640 nm).

Strehl ratio estimation

The SR is estimate using an algorithm implemented in Matlab and used before to study the performance on NACO. The algorithm computes the SR as the ratio between the peak intensities of the measured PSF (normalized to the total flux) and the theoretical PSF. The theoretical PSF is computed by applying the Fourier transform to a circular pupil with 14% central obstruction ratio and taking into account the pixel scale.

The profile obtained from the theoretical PSF is superposed to the measured one in order to cross-check the pixel scale measured before. As shown in figure 5.3 both profiles coincide (see profiles plots in the next section 5.3.2).

The SR estimation, especially for high SR values, is quite sensitive to two parameters: the pixel scale and the integrated flux radius. A variation of the pixel scale of 0.1 mas produces an error on the SR estimation of the order of 2% − 3%. The estimated error using the previous mentioned method is inferior to this value, but, anycase could be an uncertainty due to difference of pixel scale along different directions.

To compute the SR it is necessary to measure the PSF flux to normalize the peak value. If a small radius is considered, part of the PSF energy will not be take into account and therefore the SR will be overestimated. On the other hand, if the radius considered is too large, a high number of background photons will be considered and the SR will be underestimated. The estimated error due to this effect is around 3%. In addition, the presence of ghosts close to the PSF contribute to underestimate the PSF strehl ratio.

We consider a diameter for the integrated flux of 200 pixels (1.06 arcsec) for stars A, B and C, 240 pixels (1.28 arcsec) for star D and 300 pixels (1.59 arcsec) for star E. A larger radius is considered for the lower magnitude stars since the SR will be lower. The flux will be spread in a larger area and therefore is more important to avoid a possible SR over estimation.

Finally, we consider a 3% as a good estimation of the SR global error.

5.2.2 Residual wavefront error analysis

For each studied case, series of 3000 slope frames were recorded in open loop (OL) and closed loop (CL). Based on the acquired real-time data we estimated the following WFS performance metrics:

- **Sensor signals rms**.
- **Modal variance distribution** in open and close loop. The sensor signals (slopes) are project onto the modal base to recover the contribution of each mode to the turbulence. Thus, a time sequence of modal coefficients is obtained and for each mode the modal variance is computed. The *residual variance* (RV) is estimated as the sum of the closed-loop modal coefficient variances.
- **Rejection transfer function**. The modulus of the turbulence rejection transfer function (RTF) of the j^{th} mode can be estimated as:

$$RTF_j(f) = \sqrt{\frac{PSD_{CL,j}(f)}{PSD_{OL,j}(f)}} \tag{5.1}$$

  where $PSD_{CL,j}(f)$ and $PSD_{OL,j}(f)$ denote respectively the closed-loop and the open-loop temporal power spectral density of the j^{th} mode. When the integrator's gain is the same for all the controlled modes (like in our case), it is possible to estimate an average RTF. Now, it is possible to define the correction bandwidth (BW) as the frequency at which the averaged rejection transfer function reaches 0 dB.

5.3 Experimental results

5.3.1 Gain optimization

For each star magnitude and for each reconstructor the optimal integrator gain was found. IR images and wavefront sequences were recorded for gains between 0.2 and 0.4 with 0.05 step. The main parameter

Table 5.4: Optimal gain for the different performance metrics (SR, RMS, RV) on the different flux conditions and reconstructor.

	589 modes				412 modes			
Mag	SR	RMS	RV	Optimal	SR	RMS	RV	Optimal
2.1	0.25/0.30	0.35	0.35	**0.35**	0.30	0.40	0.40	**0.40**
5.9	0.35	0.35	0.35	**0.35**	0.25/0.30	0.35	0.35	**0.35**
8.4	0.35	0.30	0.35	**0.35**	0.25	0.30	0.30	**0.30**
9.6	0.30	0.35	0.30	**0.30**	0.25/0.30	0.25/0.30	0.30	**0.30**
10.9	0.30	0.25	0.25	**0.25**	0.25/0.30	0.25	0.25	**0.25**

defining the optimal gain is the SR, but since the SR's obtained are closer it is necessary to take into account also the signal rms and the residual variance. So we choose the optimal gain as the one optimizing more number of these parameters.

Table 5.4 shows the gain values which optimize the different parameters and the selected optimal gain for both reconstructors. The performance in terms of SR, rms and RV for all the gains and all cases could be found in table 5.5.

Same gain is considered for all modes. Although, taking an eye on the modal variance distribution (for example from star magnitude 5.9 (section 5.4.2)), we realized that 0.4 gain minimizes the modal variance on the range of the high order modes, while, in the case of the low order modes a better improvement is achieved using 0.35 gain. This suggests that a modal gain could improve the performance of the system including on the reconstructor a gain matrix as a function of the mode order.

5.3.2 PSF analysis: SR Performance

Table 5.5 shows the SR computed for each of the star magnitudes and the reconstructor. The first conclusion is that for high flux conditions (mag 2.1 and 5.9) the optimal reconstructor is the 589 modes, while for low flux the optimum is to use the 412 modes. In the case of star magnitude 8.4 both reconstructors exhibit the same results. This shows that the number of modes should be optimized as a function of the star flux.

figure 5.3 shows the best SR (589 or 412 modes) as a function of the star magnitude. For high flux conditions the SR obtained is > 90%. Hence, the main goal of the experiment was achieved. The SR begin to decrease for the case of mag 8.4 (SR = 88.5).

Figure 5.3 (bottom) shows the relative SR difference between star magnitudes. These results are on quite good agreement with the performance simulations of SPHERE ([77]). For SPHERE, the estimated

Table 5.5: AO performance as a function of the star magnitude for different metrics.

	589 modes				412 modes			
Mag	SR [%]	RMS [pix]	RV [au]	BW [Hz]	SR [%]	RMS [pix]	RV [au]	BW [Hz]
2.1	92.0	0.116	1.05	3.52	90.5	0.127	1.50	3.35
5.9	93.5	0.115	1.07	3.36	92.0	0.133	1.90	3.59
8.4	88.5	0.143	2.32	3.59	88.5	0.151	2.98	2.03
9.6	79.5	0.165	3.58	3.20	81.0	0.170	3.87	2.50
10.9	76.5	0.202	5.97	2.10	77.5	0.201	5.97	1.80

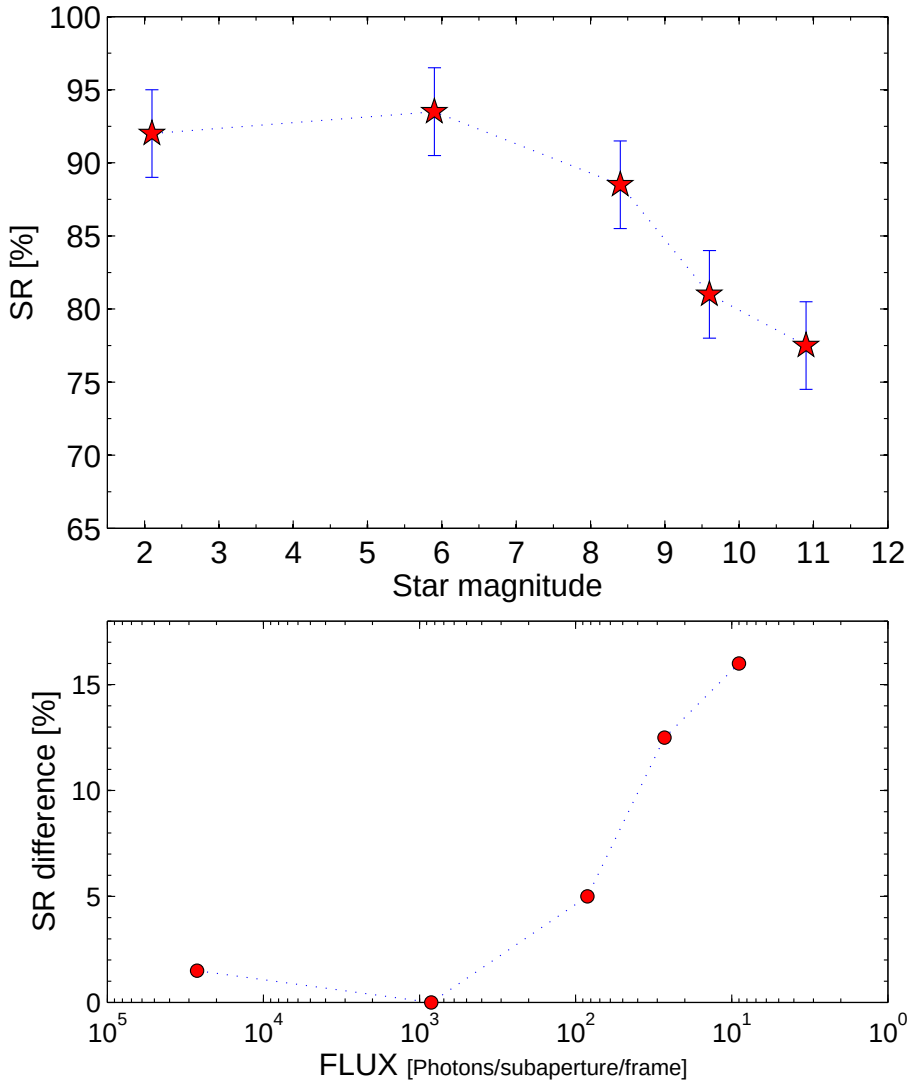

Figure 5.3: **Top:** SR performance as a function of the star magnitude. **bottom:** SR difference (respect to the most performing case) as a function of the flux.

loss of performance between high and intermediate flux is approximately 3% (for 85 photons/sub/frame) and 10% (for 27 photons/sub/frame), while in our case the measured differences are 5 and 12%.

For the lowest flux case the agreement is not so good, 16% in our case, while around 40% foreseen for SPHERE. On the other hand, the comparison in this flux range ($\approx$ 10photons/sub/frame) is quite difficult, since the performance drops very fast and it is very dependent on the number of photons; a difference of 1 photon produces a difference of around 8% of SR.

5.3.3 PSF analysis: Contrast curves

Figure 5.4 shows the contrast profiles for the most performing case and for the lowest flux case using 412 and 589 modes reconstructor. 10 rings are visible for the first case, while in the second case we could distinguish until the 8^{th} ring. Comparing with the theoretical PSF profile, we could see that the correspondence between the rings position is good, confirming the pixscale used for the SR estimation.

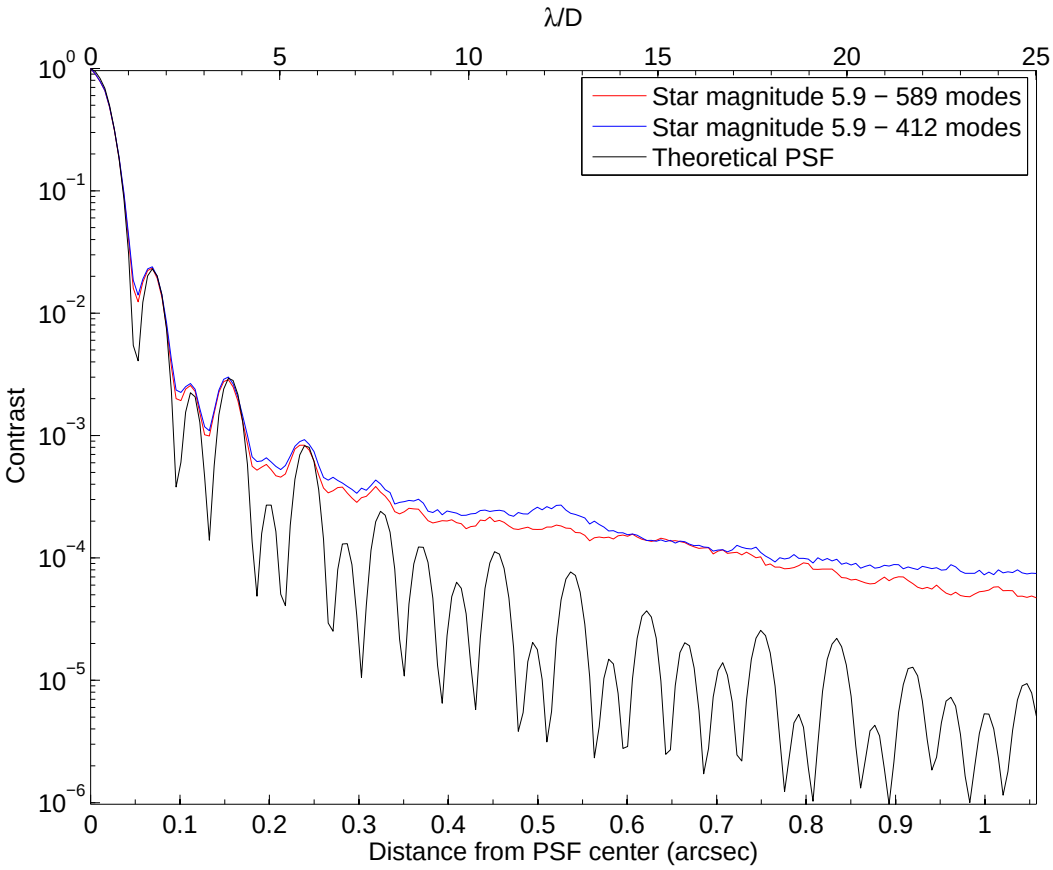

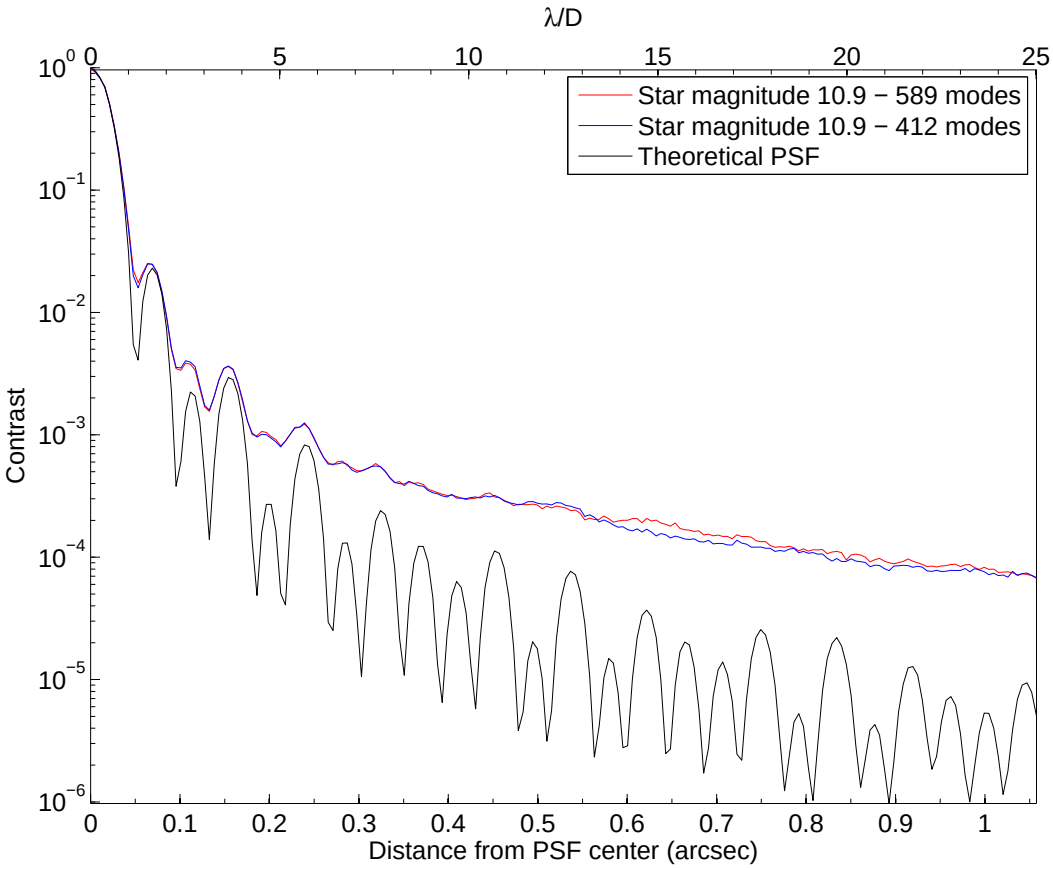

Figure 5.4: Contrast curves for magnitude stars 5.9 and 10.9. The theoretical profiles is included for comparison purpose.

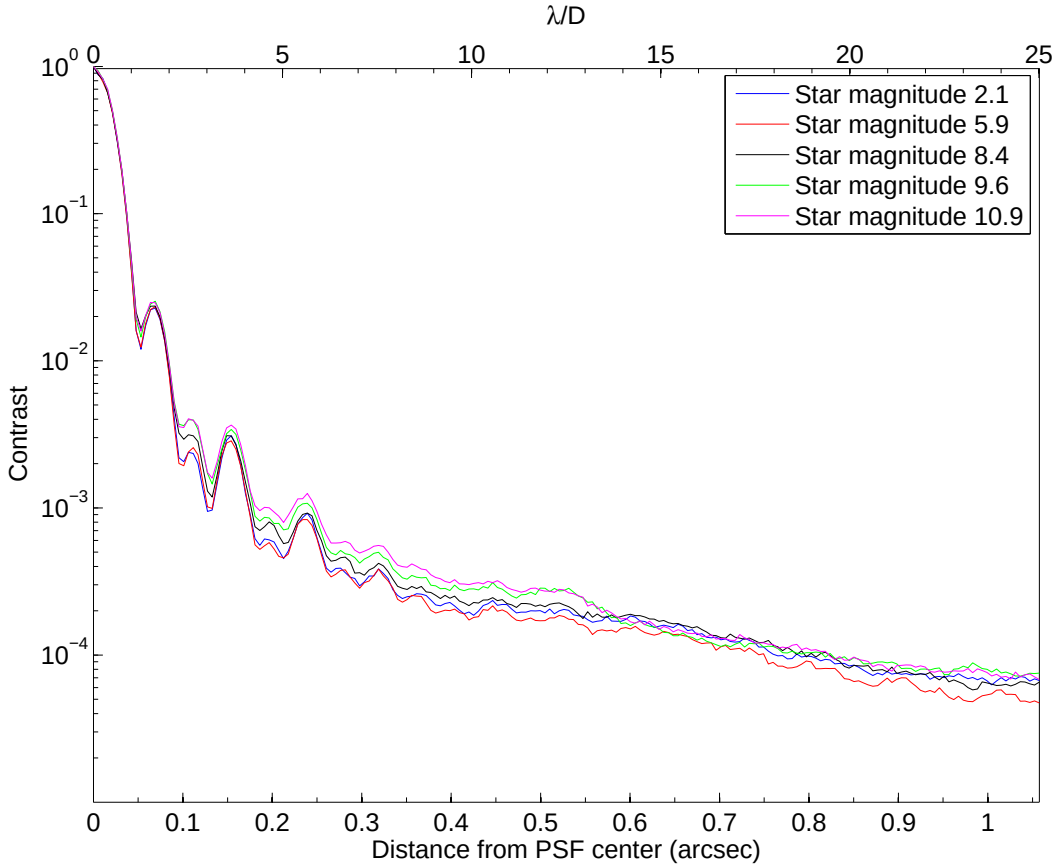

Figure 5.5: Contrast curves comparison between different star magnitudes. The optimal reconstructor (412 or 589 modes) was used for each case.

Table 5.6: Contrast obtained at 0.1, 0.2 and 0.5 arcsec for the different flux conditions.

Mag	**Contrast**		
	[0.1”]	[0.2”]	[0.5”]
2.1	$2.19 \cdot 10^{-3}$	$6.06 \cdot 10^{-4}$	$2.00 \cdot 10^{-4}$
5.9	$2.00 \cdot 10^{-3}$	$5.81 \cdot 10^{-4}$	$1.72 \cdot 10^{-4}$
8.4	$3.22 \cdot 10^{-3}$	$8.03 \cdot 10^{-4}$	$2.15 \cdot 10^{-4}$
9.6	$3.71 \cdot 10^{-3}$	$8.54 \cdot 10^{-4}$	$2.57 \cdot 10^{-4}$
10.9	$3.56 \cdot 10^{-3}$	$1.00 \cdot 10^{-3}$	$2.85 \cdot 10^{-4}$

The superposition of the theoretical and the experimental curves is very good for close angle (< 0.2 ”) (where the signal is very high). The main difference consists in a difference of contrast between bright and dark rings. for example, for the high flux case, the contrast difference between the first minimum and maximum is 0.531, while looking at the theoretical profile the contrast difference would be 0.177. This means a loss of contrast of 33%.

Figure 5.5 shows the superimposed contrast curves for all the star magnitude cases. As expected, the loss of contrast is dependent on the flux as for the SR. Table 5.6 summarize the contrast obtained at 0.1”, 0.2” and 0.5” for the different cases.

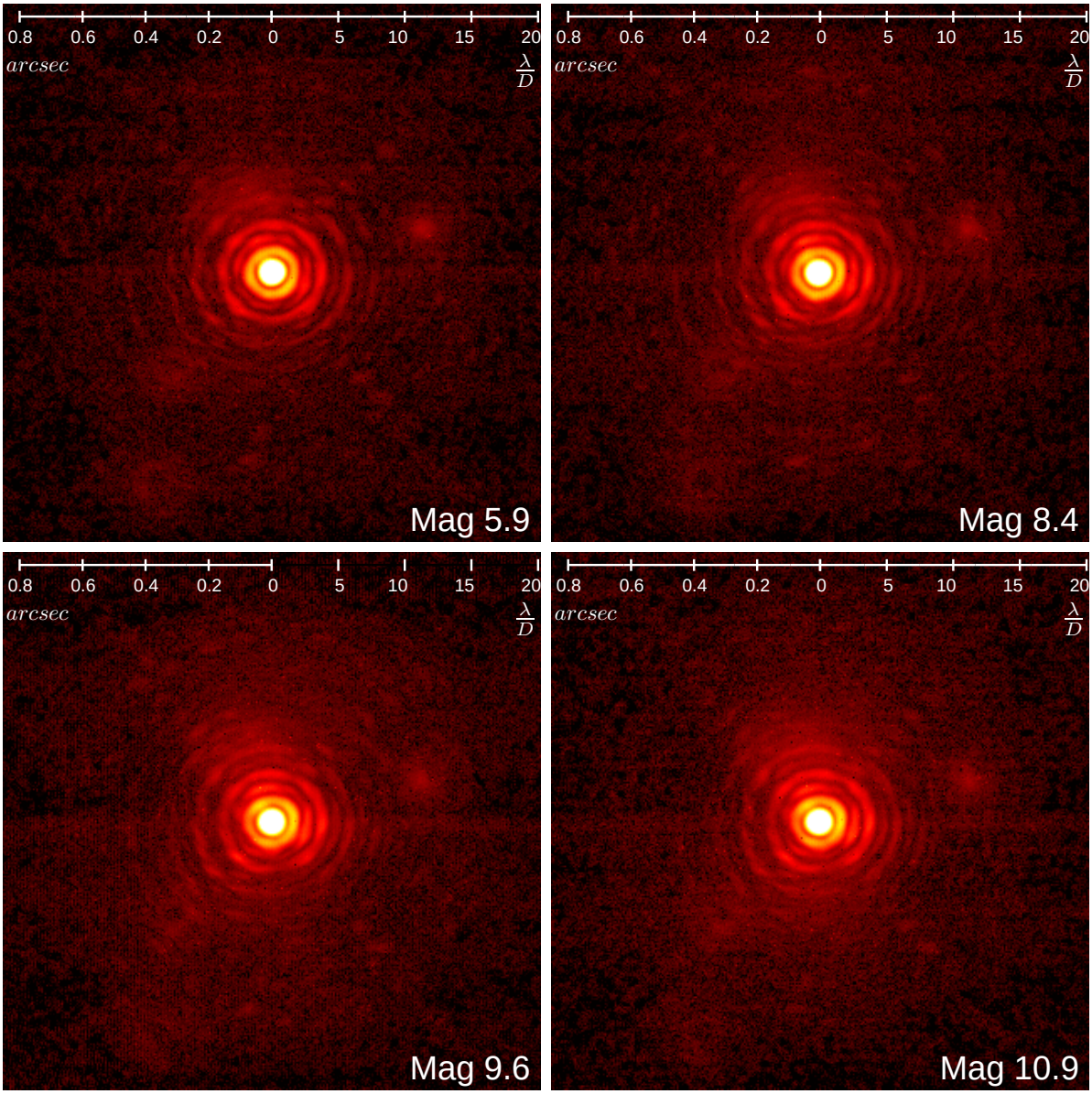

Figure 5.6: Best PSF images for stars magnitude 5.9, 8.4, 9.6 and 10.9. The color scale used is $ADU^{1/4}$.

5.3.4 WFS signal analysis: Rejection transfer function and bandwidth.

The bandwidth was measured for all gain values and for all star magnitudes as shown on section 5.4. As expected, the correction bandwidth increases with the gain of the integrator controller and that, beyond the bandwidth, the RTF exhibits an overshoot that also raises in amplitude with the gain.

Figure 5.7 shows the superimposed RTF curves for all star magnitudes choosing the corresponding optimal gain (589 modes reconstructor). Figure 5.7 (left) shows for these cases the corresponding bandwidth as a function of the star magnitude.

The bandwidth range is comprised between 3.5 and 1.8 Hz. It can be seen that for high flux conditions the bandwidth is similar for both reconstructors, while for the low flux cases the bandwidth obtained using the 589 modes reconstructor is higher.

In order to compare same gain conditions, figure 5.8 (right) shows the BW as a function of the gain for the highest and lowest flux cases.

The bandwidth is always highest for the highest flux cases. If we compare both reconstructors, for low gain values the BW match up, while it diverge at higher gains. For the high flux case the BW is superior for the 589 modes reconstructor while for the low flux case is the opposite.

Table 5.5 summarized the performance in terms of bandwidth, residual variance and sensor signal rms for all star magnitudes and reconstructors. In section 5.4 it could be found the complete tables and figures, for each flux level at different gains.

5.3.5 WFS signal analysis: Modal variance distribution.

Figure 5.10 shows the superimposed modal variance distribution curves for the different star magnitudes comparing with the open loop case. As expected the correction decrease when the flux decrease. For high flux cases (magnitudes 2.1 and 5.9) the correction is maximal, achieving correction for all modes.

For magnitude 8.4 an important jump in the correction could be seen (also observed on the SR

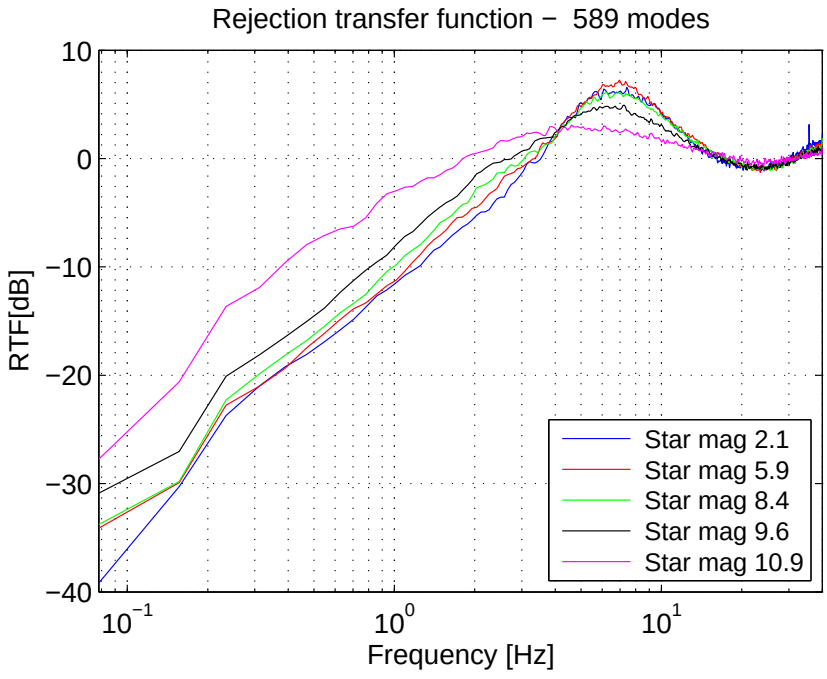

Figure 5.7: Superimposed rejection transfer functions for all the star magnitudes at the optimal gain (589 modes reconstructor).

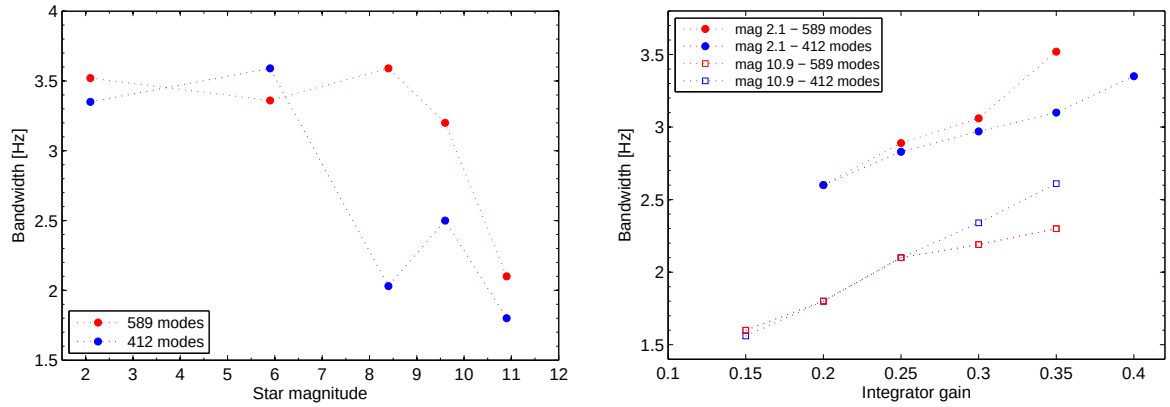

Figure 5.8: **Left:** Bandwidth as a functions of the star magnitude comparing the reconstructor cases of 589 an 412 modes. **Right:**. Bandwidth as a functions of the integrator gain for star magnitudes 2.1 and 10.9 comparing both reconstructors.

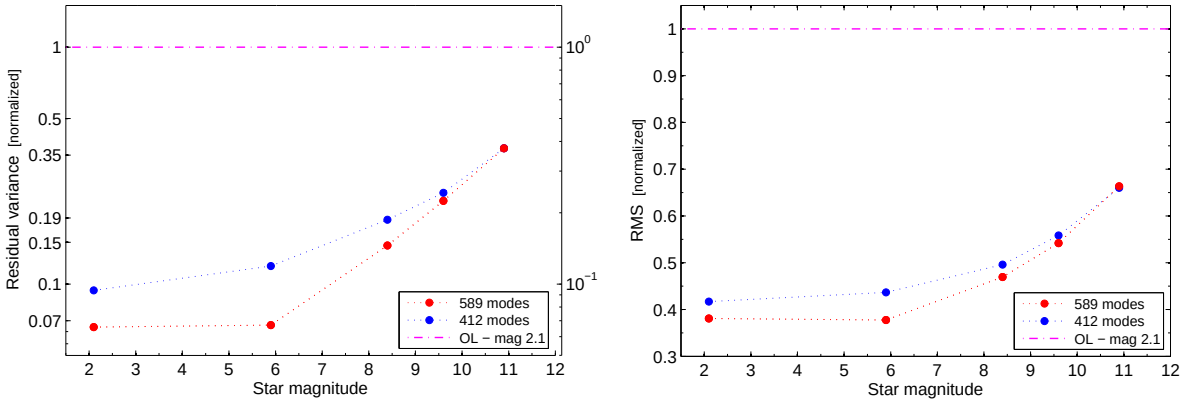

Figure 5.9: **Left:** Residual variance as a function of the star magnitude for both reconstructors. The scale is logarithmic and the RV was normalized to the open loop value (horizontal line). **Right:** Normalized sensor signal rms as a function of the star magnitude for both reconstructors. The scale is linear.

performance) achieving correction only until mode ≈ 500. While for low flux conditions (magnitudes 9.6 and 10.9) a good correction is obtained only until mode ≈400, being the modal variance in the case 10.9 even worse than in open loop.

Figure 5.9 (left) shows the behavior of the residual variance as a function of the flux level in a logarithmic scale. We normalized the values to the open loop case for comparison purpose. For high flux conditions the improvement factor is around 15 while for low flux cases is around 2.7.

It is clear that the residual variance follows a logarithmic law, specially for the high order reconstructor. Comparing both reconstructors we realized that the residual variance curves converge for the lowest flux level.

This means that the best performance for each flux level would be achieved optimizing the number of modes of the reconstructor as well as applying a modal optimization of the gain.

Figure 5.9 (right) shows the sensor signal RMS as a function of the star magnitude (linear scale). The observed behavior is similar to the previous case.

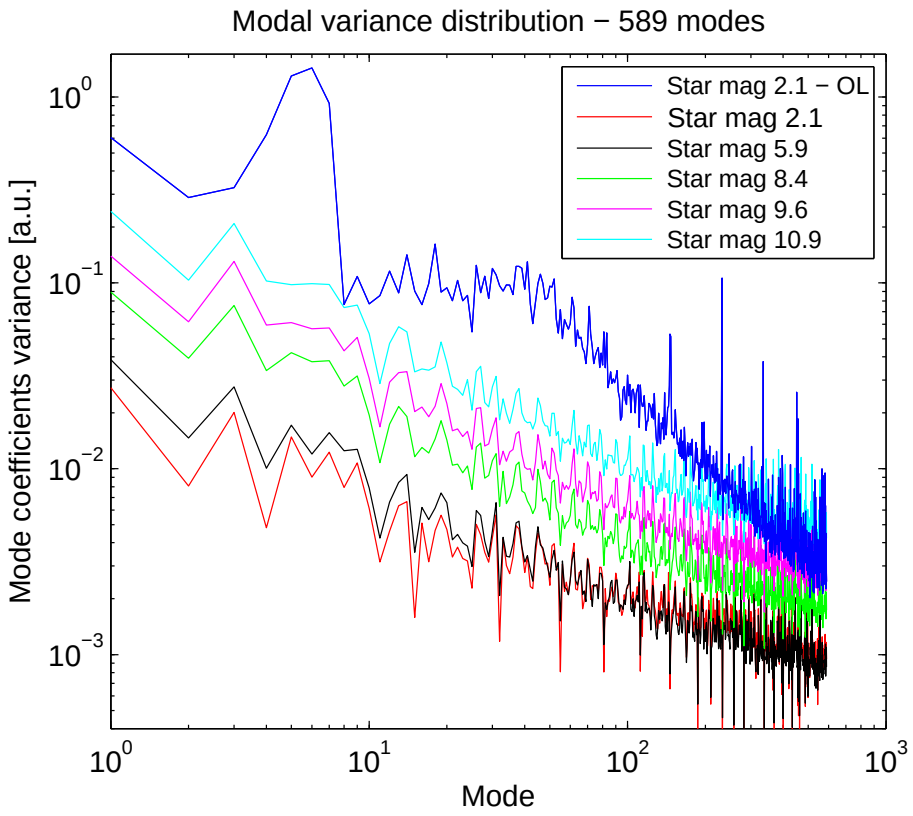

Figure 5.10: Modal variance distribution for the different flux conditions using the 589 modes reconstructor.

5.4 Performance for different flux levels: plots and tables

In this section we summarize the experimental data obtained on the gain optimization study for each flux level. For each reconstructor case we plot the RTF curves (left figures) and the modal variance distribution (right figures) corresponding to the different studied integrator gains. The bottom table summarize the results obtained for each performance metric as a function of the integrator gain.

5.4.1 Star magnitude 2.1

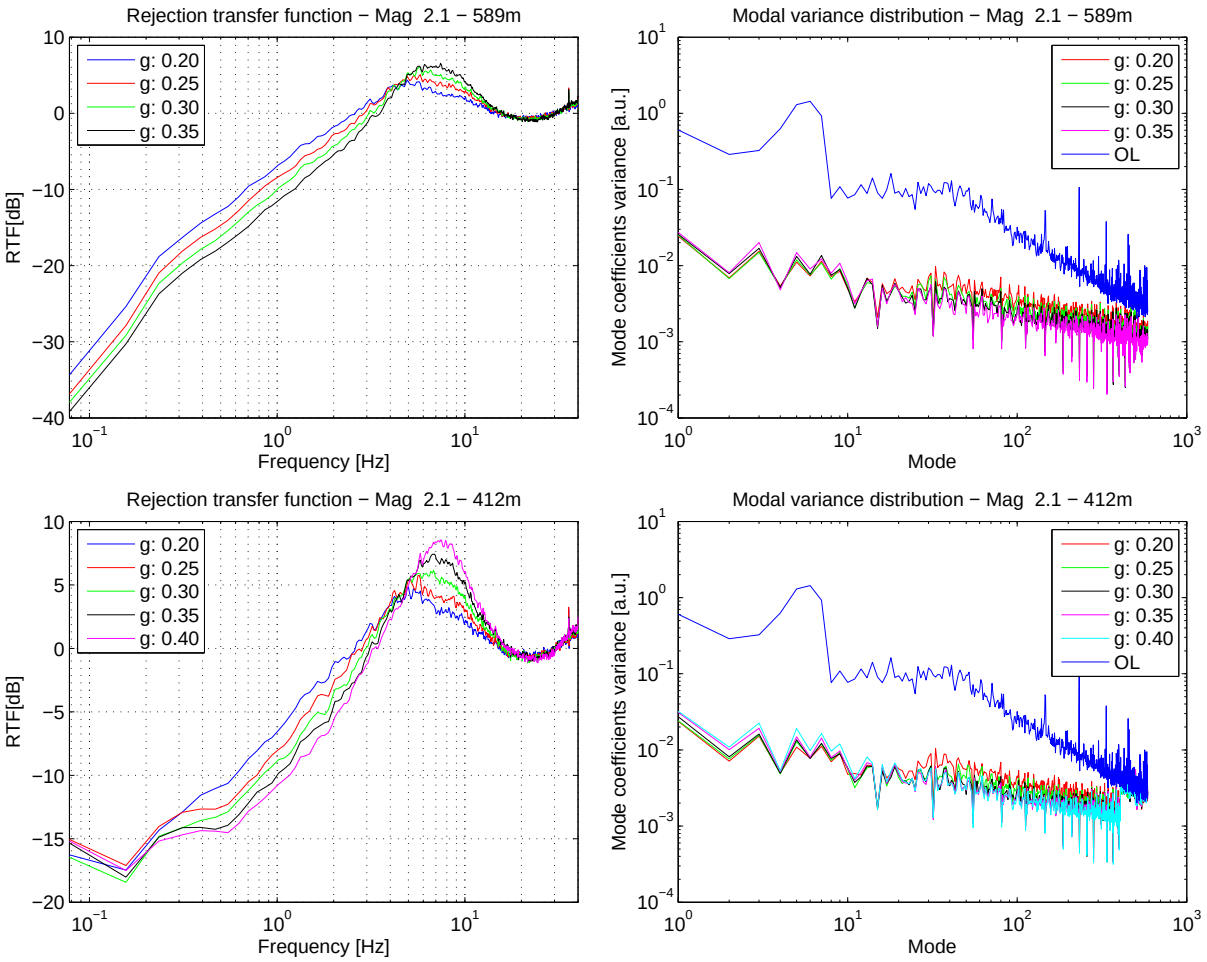

Table 5.7: Star magnitude 2.1.

	589 modes				412 modes			
Gain	SR [%]	RMS [pix]	RV [au]	BW [Hz]	SR [%]	RMS [pix]	RV [au]	BW [Hz]
0.20	90.0	0.124	1.56	2.60	89.0	0.133	1.90	2.60
0.25	92.0	0.121	1.31	2.89	89.5	0.130	1.67	2.83
0.30	91.0	0.120	1.17	3.06	90.5	0.128	1.54	2.97
0.35	92.0	0.116	1.05	3.52	90.0	0.128	1.52	3.10
0.40	-	-	-	-	89.0	0.127	1.50	3.35

5.4.2 Star magnitude 5.9

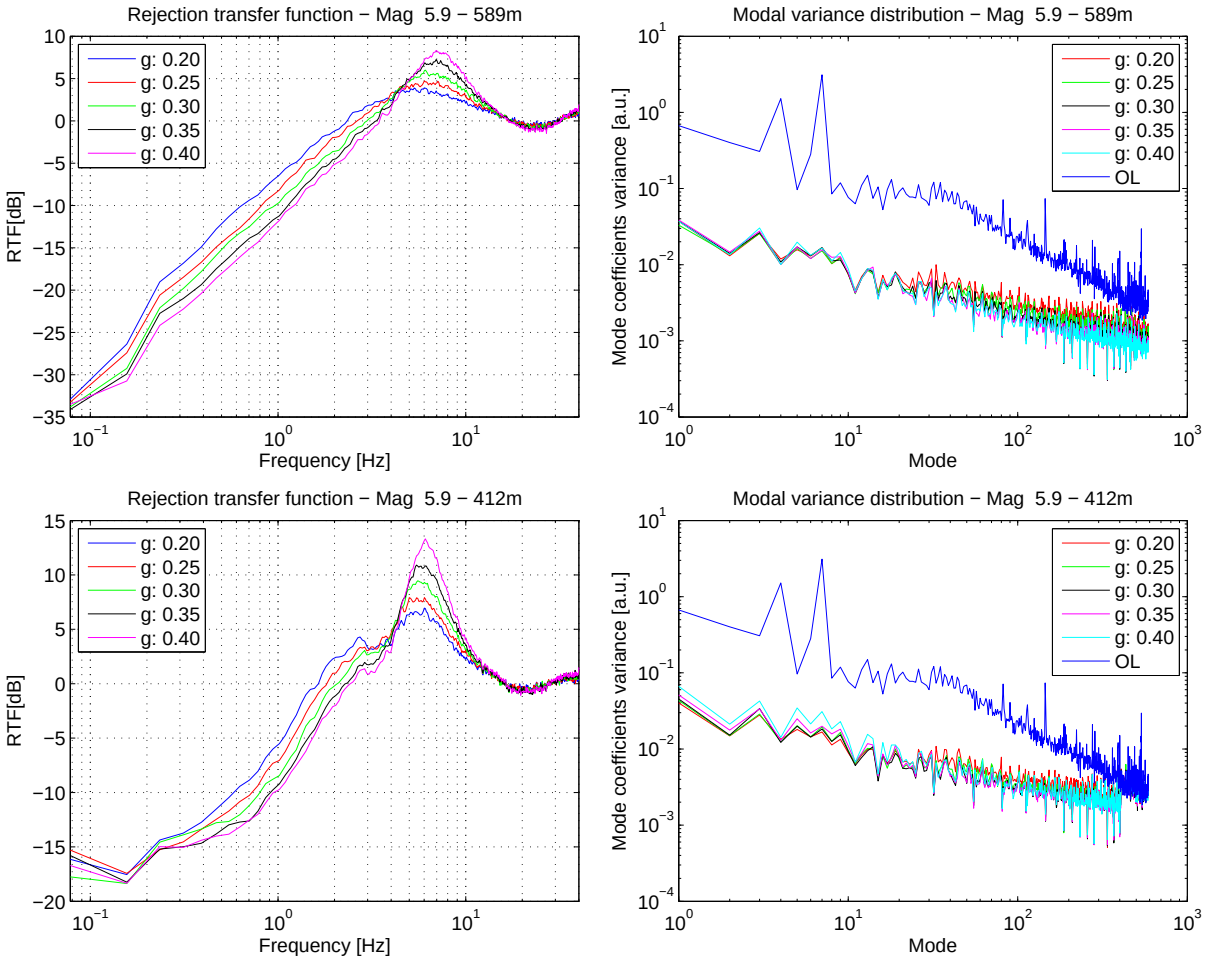

Table 5.8: Star magnitude: 5.9 .

	589 modes				412 modes			
Gain	SR [%]	RMS [pix]	RV [au]	BW [Hz]	SR [%]	RMS [pix]	RV [au]	BW [Hz]
0.20	90.0	0.122	1.52	2.34	91.0	0.137	2.20	2.34
0.25	92.0	0.121	1.29	2.66	92.0	0.135	2.01	2.66
0.30	92.5	0.117	1.15	2.97	92.0	0.133	1.90	2.89
0.35	93.5	0.115	1.07	3.36	90.0	0.133	1.91	3.59
0.40	93.0	0.116	1.04	3.67	88.0	0.135	2.05	3.83

5.4.3 Star magnitude 8.4

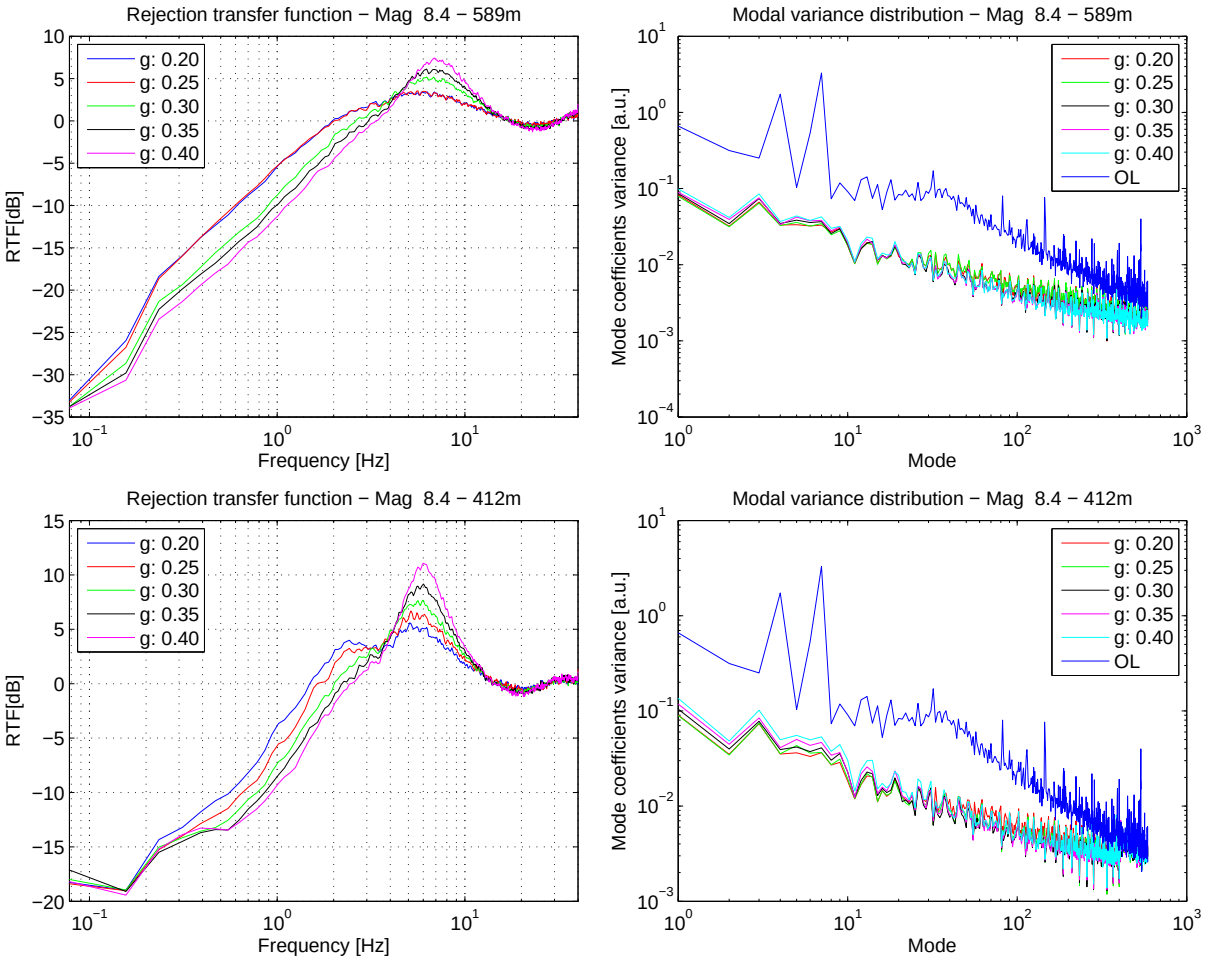

Table 5.9: Star magnitude: 8.4.

	589 modes				412 modes			
Gain	SR [%]	RMS [pix]	RV [au]	BW [Hz]	SR [%]	RMS [pix]	RV [au]	BW [Hz]
0.20	88.0	0.146	2.65	2.42	87.0	0.157	3.28	1.48
0.25	88.5	0.145	2.64	2.42	88.5	0.154	3.07	1.64
0.30	86.0	0.143	2.34	3.13	88.0	0.151	2.97	2.03
0.35	88.0	0.144	2.32	3.59	87.0	0.153	3.08	2.19
0.40	87.0	0.145	2.36	3.83	85.0	0.155	3.34	2.42

5.4.4 Star magnitude 9.6

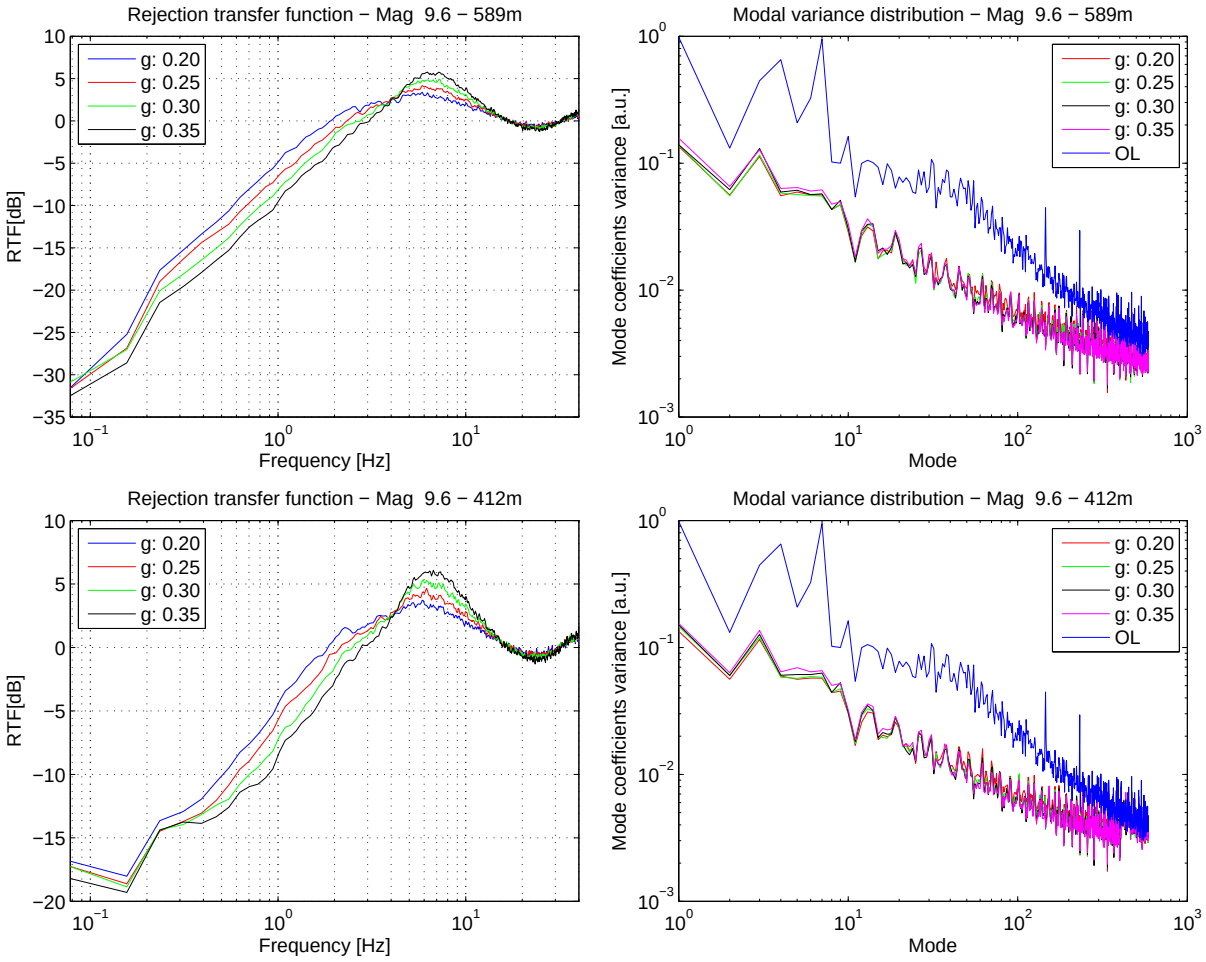

Table 5.10: Star magnitude: 9.6.

	589 modes				412 modes			
Gain	SR [%]	RMS [pix]	RV [au]	BW [Hz]	SR [%]	RMS [pix]	RV [au]	BW [Hz]
0.20	79.0	0.167	3.79	2.19	80.5	0.173	4.03	1.86
0.25	79.0	0.166	3.59	2.66	81.0	0.170	3.89	2.15
0.30	79.5	0.169	3.58	3.20	81.0	0.170	3.87	2.50
0.35	79.0	0.165	3.60	3.36	79.0	0.168	3.90	2.77

5.4.5 Star magnitude 10.9

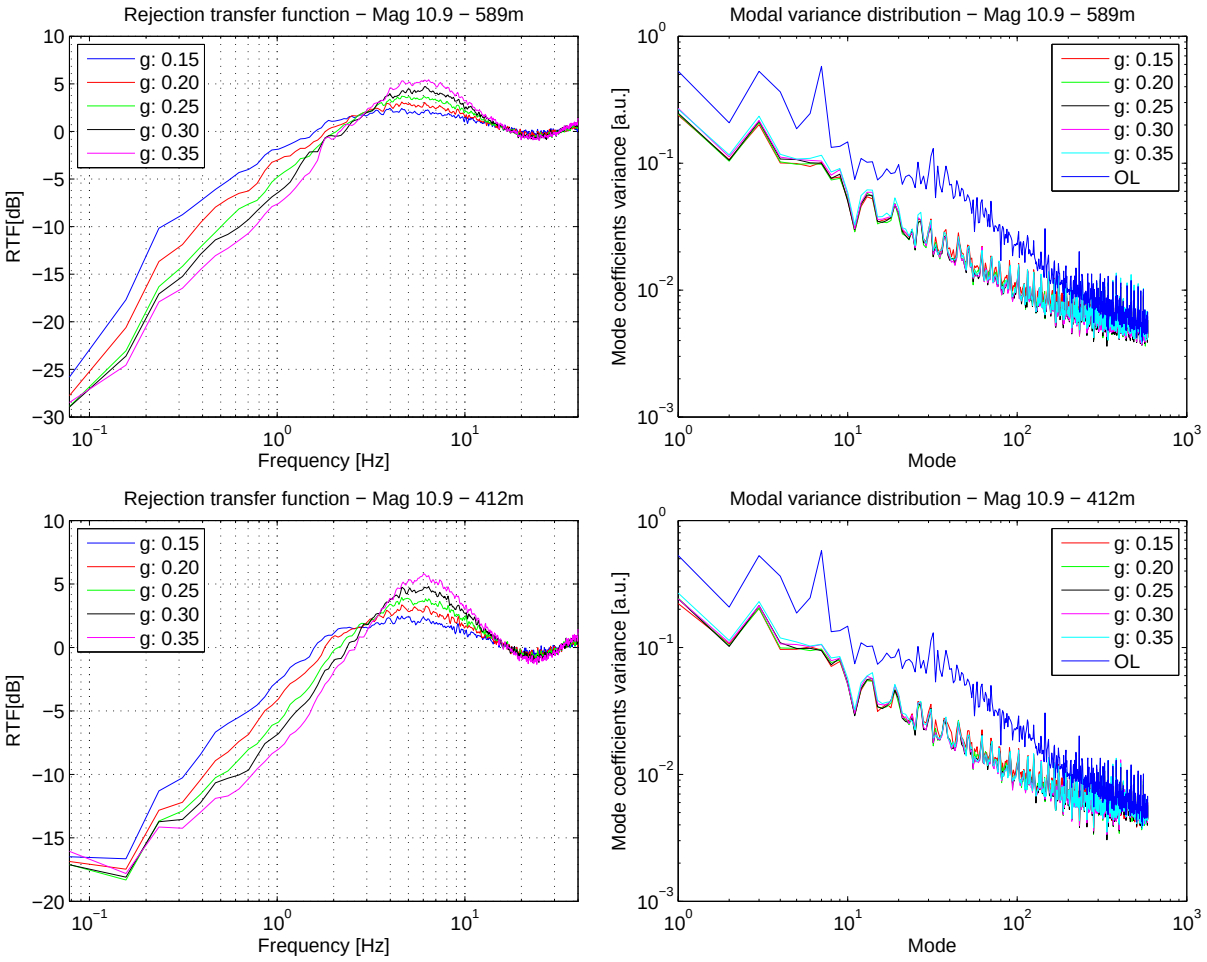

Table 5.11: Star magnitude: 10.9.

	589 modes				412 modes			
Gain	SR [%]	RMS [pix]	RV [au]	BW [Hz]	SR [%]	RMS [pix]	RV [au]	BW [Hz]
0.15	76.0	0.205	6.26	1.60	76.0	0.202	6.19	1.56
0.20	76.5	0.202	5.99	1.80	77.5	0.201	6.01	1.80
0.25	76.0	0.202	5.97	2.10	76.0	0.200	5.97	2.10
0.30	76.0	0.205	6.13	2.19	75.0	0.201	6.08	2.34
0.35	-	0.211	6.40	2.30	74.5	0.203	6.28	2.61

6

High contrast experimental results

6.1 Coronagraphy with XAO

Four types of coronagraphs were compared on the HOT bench under the same AO conditions (same conditions as for the AO performance study). The comparison experiment was done by recording sequentially coronagraphic and non coronagraphic images (PSF images) with turbulence and AO closed-loop operation.

All PSF images have been recorded with the use of a neutral density to avoid detector saturation and ensuring the maximum signal for both, PSF and coronagraphic image. A large panel of neutral density combination was available. The neutral density value for each combination has been experimentally determined for the working wavelength (λ = 1.64 μm) to ensure accuracy of the coronagraphic performance evaluation.

The complete results could be found in the ESO report [79]. We will summarize thereafter the main results taking in special consideration the APLC coronagraph.

6.1.1 Apodized pupil Lyot coronagraph

The APLC studied consists on an apodizer, a stop of 92% of the VLT pupil transmission and a focal mask of 4.5 λ/D size diameter. The inner working angle (IWA) of this coronagraph is 2.3 λ/D.

The performance of the APLC was studied under two flux conditions: star magnitude 2.1 (high flux) and 10.9 (low flux). As well we compared both reconstructor cases: 589 and 412 modes.

Figure 6.1 shows the PSF and the coronagraphic curve for each studied case (in this chapter the PSF is considered taking into account the apodizer and the reduced pupil stop). All contrast profiles are azimuthally averaged plots avoiding the angular area where the ghosts are present.

The peak rejection factor is similar for all the cases, between 135 and 190. On the other hand, the contrast improvement in the halo region (5 - 10 λ/D) for the low flux cases is quite small (even in this case an improvement is achieved because the coronagraph shows the residual speckles that could be subtracted by differential imaging).

For all the coronagraphic curves it is clear the existence of a *"bump"* around 15λ/D corresponding to the AO cut-off frequency. This decrease of contrast after this point is expected since the AO has no more effect after this region. By comparing both reconstructors we could see that the *bump* position is slightly shifted for the case of 412 modes (12.5 λ/D) with respect to the 589 modes reconstructor (14.5 λ/D). This is normal because using less modes is equivalent to have less actuators and therefore the AO correction region shrinks.

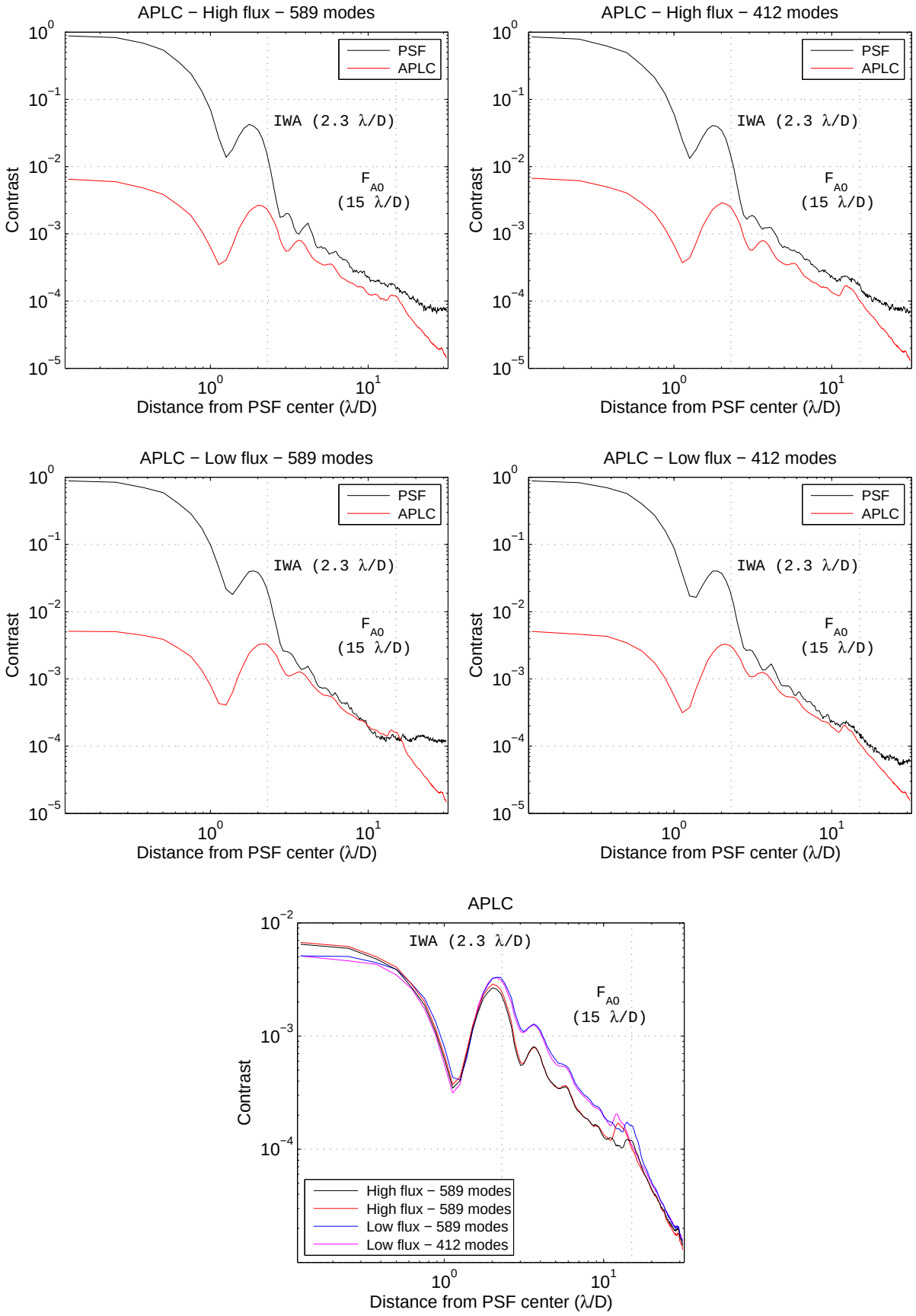

Figure 6.1: APLC contrast curves obtained for the different reconstructors and flux conditions.

6.1.2 Coronagraphs comparison

For high flux conditions we measured the performance of the FQPM, Lyot and band limited. These measurements and the previous APLC results were done on the same conditions of alignment (same focus position of the focal plane mask).

Figure 6.2 (right) shows the performance for the FQPM case. The FQPM coronagraph consists on a phase mask on the focal plane and a pupil stop (70 % of the VLT pupil transmission). For this case the IWA is 1 λ/D.

The FQPM contrast is slightly better than for the APLC as shown on table 6.1. As before the cut-off frequency position depends on the number of modes corrected. The limit of the control area is also observable on the coronagraphic image as a visible external ring (figure 6.2, left).

Figure 6.3 compares the contrast curves for the 4 coronagraphs (high flux, 589 modes). The Lyot coronagraph curve corresponds to the Lyot 360 μm (4.5 λ/D) with a pupil stop of 60% transmission (IWA of 2.2 λ/D). On the other hand, the band limited coronagraph has an IWA of 5 λ/D (using the same Lyot pupil stop). The four coronagraphs exhibit similar performance as shown on table 6.1. All coronographs achieve a contrast level $\approx 10^{-4}$ at $12\lambda/D$. Only the band limited is slightly inferior because the pupil stop was not the optimal for this band limited coronagraph.

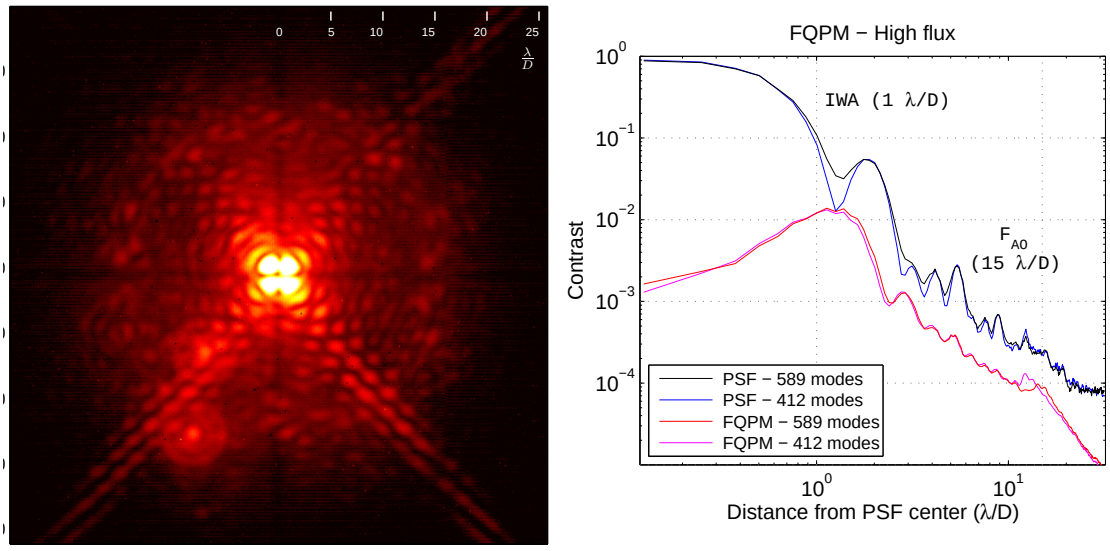

Figure 6.2: **Left:** Coronagraphic image obtained with the FQPM (high flux, 589 modes). The color scale used is ADU$^{1/4}$. **Right:** FQPM contrast curves obtained for the different reconstructors at high flux.

Table 6.1: Contrast obtained at 3, 9 ,12 and 20 λ/D for the different coronagraphs compared with the real PSF (high flux and 589 modes reconstructor).

Coronagraph	**Contrast**			
	[3 λ/D]	[9 λ/D]	[12 λ/D]	[20 λ/D]
PSF	$1.02 \cdot 10^{-3}$	$1.93 \cdot 10^{-4}$	$1.71 \cdot 10^{-4}$	$6.85 \cdot 10^{-5}$
APLC	$5.49 \cdot 10^{-4}$	$1.64 \cdot 10^{-4}$	$1.07 \cdot 10^{-4}$	$4.46 \cdot 10^{-5}$
FQPM	$1.16 \cdot 10^{-3}$	$1.30 \cdot 10^{-4}$	$8.06 \cdot 10^{-5}$	$3.47 \cdot 10^{-5}$
Lyot	$8.28 \cdot 10^{-4}$	$1.95 \cdot 10^{-4}$	$1.34 \cdot 10^{-4}$	$5.99 \cdot 10^{-5}$
Band Limited	$1.61 \cdot 10^{-4}$	$2.55 \cdot 10^{-4}$	$1.46 \cdot 10^{-4}$	$6.64 \cdot 10^{-5}$

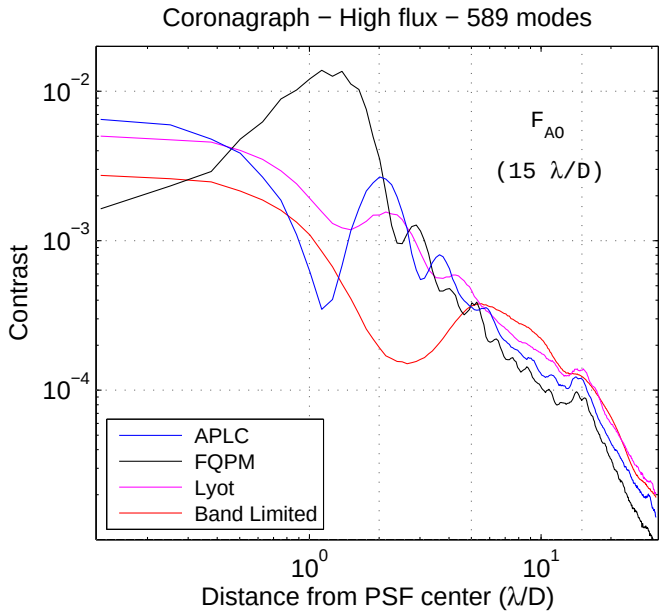

Figure 6.3: Contrast profiles obtained by different coronagraphs in high flux conditions and using the 589 modes reconstructor. the IWA angles for the corresponding case are: 2.3, 1, 2.2 and 5 λ/D. (* The band limited profile corresponds to a broad band case, R=5.

6.1.3 APLC: contrast and detectability

New measurements of the APLC were done after a better realignment of the infrared arm, including repositioning of the apodizer, pupil stop and focal mask. The global contrast, and especially the peak rejection factor, is very sensitive to the focus position of the focal mask.

A better global contrast was achieved in this case (figure 6.5 (right), table 6.2) with a peak rejection factor of ≈ 280. Figure 6.4 shows the PSF and the coronagraphic image, with a pronounced ring at the cut-off frequency. We will take advantage of this measurements to study the detectability limit of our system.

For it, we apply a high-pass filtering technique that removes the smooth structures in the coronagraphic image (atmospheric halo), leaving the small-scale higher frequencies components unaffected (e.g. planets) and therefore increasing the speckle contrast (see figure 6.5).

A smooth PSF image is computed applying a median filter to the coronagraphic image. The resulting low-pass filtered image is subtracted from the original coronagraphic image to obtain the final high-pass filtered image (HPF) shown in figure 6.5 (left). Now, the ring at the limit of the control area is emphasized and a sea of residual speckles within the control area is visible.

Figure 6.5 (right) shows the detectability curve, obtained as the azimuthally standard deviation (1σ). Thus, the detectability between 8 and 13 λ/D reaches 10^{-5} (table 6.2) which means an improvement of one order of magnitude respect to the raw APLC.

The same detectability level has been demonstrated on HOT with the APLC without the use of a high-pass filter, but using a sequential differential imaging technique as shown in Martinez *et al.* [80].

An approximate comparison with the expected contrast of SPHERE could be done. Considering a double differential imaging (spectral and angular), the expected SPHERE contrasts at 5σ for 0.1" and 0.5" are 10^{-5} and $5\cdot10^{-7}$. For HOT, after applying the high pass filter, the obtained contrasts are $1.5\cdot10^{-3}$ and $4.4\cdot10^{-5}$ for the same angular separation.

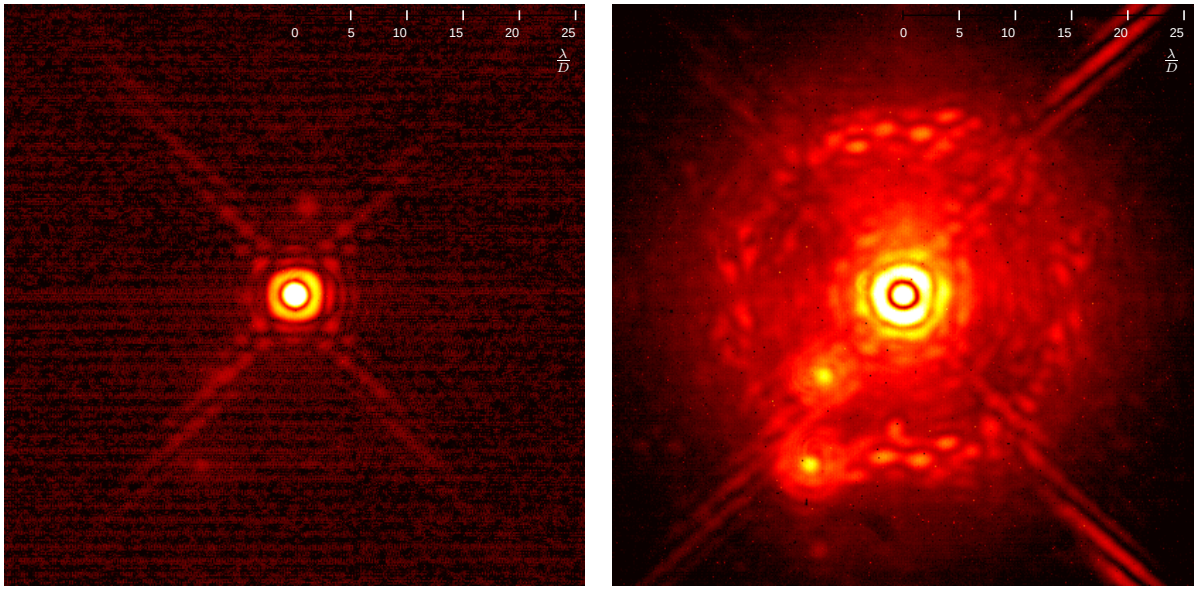

Figure 6.4: **Left:** PSF image for the APLC coronagraph. **Right:** APLC coronagraphic image.

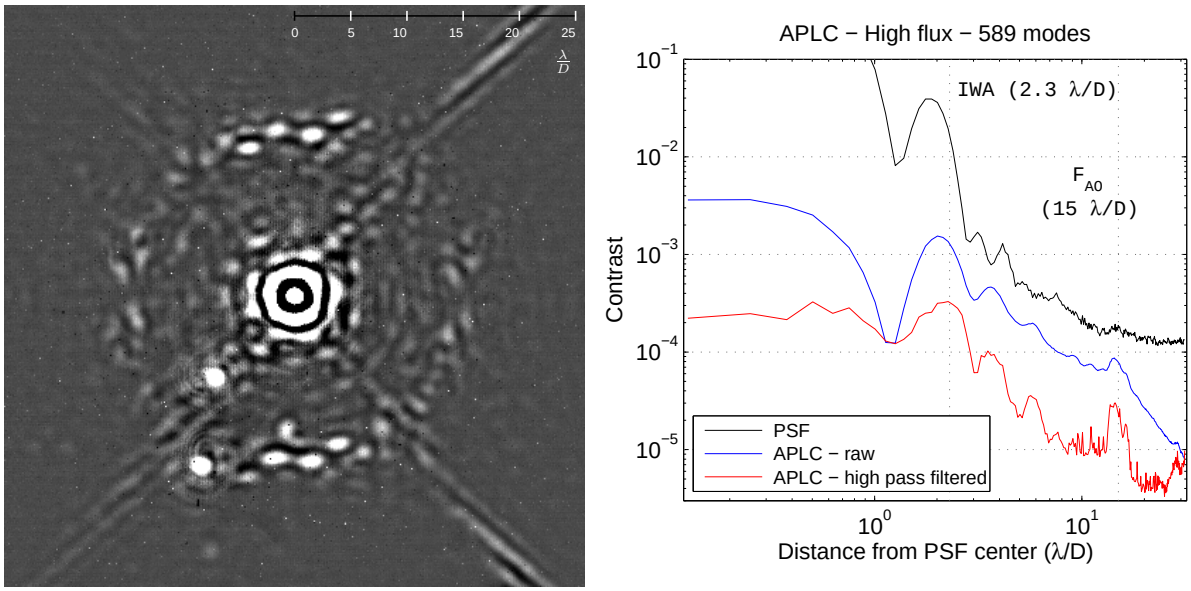

Figure 6.5: **Left:** High pass filtered APLC coronagraphic image. **Right:** Contrast and detectability curves for the APLC coronagraph.

Table 6.2: Contrast obtained at 3, 9 ,12 and 20 λ/D for the APLC after realignment of the IR path.

Case	**Contrast**			
	[3 λ/D]	[9 λ/D]	[12 λ/D]	[20 λ/D]
PSF	$1.02 \cdot 10^{-3}$	$1.93 \cdot 10^{-4}$	$1.71 \cdot 10^{-4}$	$6.85 \cdot 10^{-5}$
APLC (raw)	$3.40 \cdot 10^{-4}$	$9.25 \cdot 10^{-5}$	$6.45 \cdot 10^{-5}$	$2.68 \cdot 10^{-5}$
APLC (HPF)	$6.13 \cdot 10^{-5}$	$1.30 \cdot 10^{-5}$	$8.83 \cdot 10^{-6}$	$4.10 \cdot 10^{-6}$

6.2 Segment phasing experiments

Extreme Adaptive Optics (XAO) at the E-ELT requires dealing with a primary segmented mirror. The wave front control of the ELT includes three main units: adaptive optics, active optics and phasing camera. Each wave front control is affected to some extend by the total wavefront, but, on the other hand the different control units can "help" each other. The wavefront sensor of the AO unit will see the telescope aberrations and segments misalignments; hence the AO deformable mirror will try to compensate for them.

The goal of the present study is to determine the capability of the adaptive optics to deal with the segmentation piston errors. At present, there are several segmented telescope working with AO systems but the experience from them could not be use for extrapolation to a XAO system.

As shown in Yaitskova and Verinaud 2006 ([81]), the ability of the AO system to correct for the segmentation errors strictly depends on the design of the DM and the wave front sensor. The density of the actuators, the coupling factor and the geometry of actuators distribution directly impact on the performance.

The ELT primary mirror will be composed of around 1000 hexagonal segments of 1.5 m with a gap of 10 mm. 5-7 actuators per segment are expected considering a deformable mirror of 200x200 actuators. The experiments were carried out on the Bench taking into account the ELT geometry.

The segmentation will be simulated introducing a piston phase plate on the bench and study the impact on the AO system (stability, variations of SR ...). We will use high flux condition (2.1 star magnitude) and working with the higher reconstructor 589 modes). The APLC coronagraph presented in the previous section will be used to study the impact on the limited contrast. I will summarize on this section the results presented on the AO for ELT meeting (Paris, June 2009) (Aller-Carpentier *et al.* 2009 ([82]).

6.2.1 The piston phase plate

The residual piston phase error on the E-ELT after segment co-phasing correction is simulated on the HOT bench using a piston phase plate (PPP) manufactured with the same technology as the present phase screens. Thus, the impact on the AO performance and the residual error on the PSF could be studied.

Since the segmentation should be studied in the pupil plane, the PPP is installed on the turbulence generator replacing one of the turbulence phase screen. The only disadvantage is that the turbulence strength will decrease. Using only one phase screens that produce a seeing 0.85" when combined, the effective seeing would be reduced by a factor $\approx$2 to around 0.4" seeing. This reduction of seeing is acceptable since the prime objective of this experiment is to investigate the effects of segmentation piston errors.

19 hexagonal segments cover the equivalent pupil on the PPP (6.7 mm), providing an actuator/segment rate of 6-7 actuators as expected for the XAO instrument at the E-ELT. Segments are distributed at 4 piston levels (0, 15, 35, 75 nm) providing an RMS wave-front error of 52 nm (EPICS specification on E-ELT is 36 nm RMS). The complete PPP disk of 50 mm diameter is covered by segments and can rotate on its mount, offering the possibility of studying different alignments between segments and actuators.

6.2.2 Experimental results: segmentation effects

The impact of the PPP on the AO performance was studied on closed loop (with turbulence) analyzing the PSF and SHS slopes rms. The first conclusion is that the AO system could deal well with the

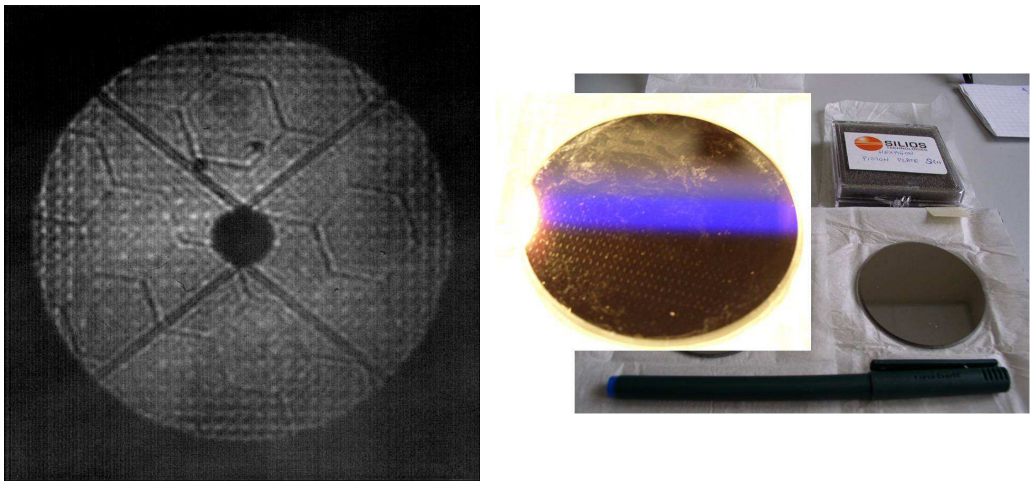

Figure 6.6: **Left:**Pupil plane image showing the segmentation **Right:**Piston phase plate (PPP).

segmentation errors, thus no stability problems appears on the system or anomalous saturation effects were seen.

The performance did not differ from the results obtained on chapter 5 achieving a SR ≈90% (using the same AO parameters). To see the effect of the segmentation it was necessary to increase the contrast. Hence, coronagraphic images were acquired with and without turbulence and with and without segmentation for comparison purpose (figure 6.7)) (the case without turbulence is obtained replacing the phase screen by a flat mirror).

The effects of the segmentation can be seen only outside the AO control frequency region (> 15 λ/D) on the coronagraphic images. The resulted images show the diffraction pattern with three axes at 60 degrees observed at a contrast level between $3.5\text{x}10^{-5}$ and $8\text{x}10^{-6}$. Azimuthally averaged contrast profiles for the studied cases are presented in figure 6.8. The profiles show that the contrast reached is not affected by the PPP.

In addition, for both cases, three images were recorded with different segments orientations (figure 6.9). The original image without segmentation has then been subtracted to identify the segmentation effect. As expected, a rotation on the diffraction pattern produced by the segments can be seen (all images were acquired on closed loop to avoid internal turbulence).

Coronagraphic images were simulated taking into account the effect of the segmentation following the PPP geometry (19 segments – 52 nm rms) (figure 6.10). The segmentation effect is observed at contrast level around $5\text{x}10^{-6}$ – $5\text{x}10^{-7}$, being in agreement with the experimental data (assuming no other error sources).

To know whether the AO system is able to correct the segmentation errors it is necessary to look inside the AO control area. But in our case, the contrast level in this area is limited by speckle, being approximately one order of magnitude higher than the segmentation effect.

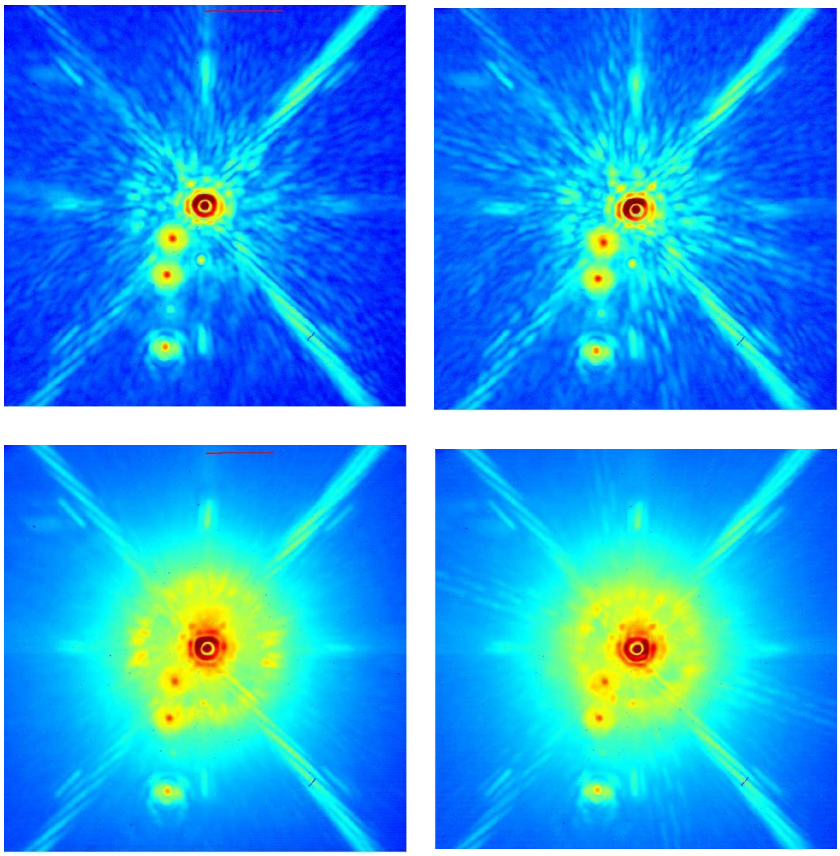

Figure 6.7: **Top:** Coronagraphic images without (right) and with (left) piston phase plate in absence of turbulence. **Bottom:** Same cases but in presence of turbulence. In the PPP cases an additional diffraction pattern with three axes at 60 degrees is observed.

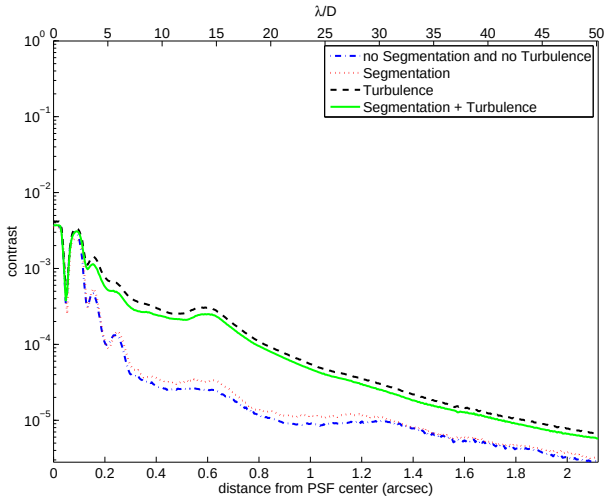

Figure 6.8: Contrast curves for the 4 studied cases (PPP and no PPP, with and whithout turbulence). The contrast reached is not affected by the PPP.

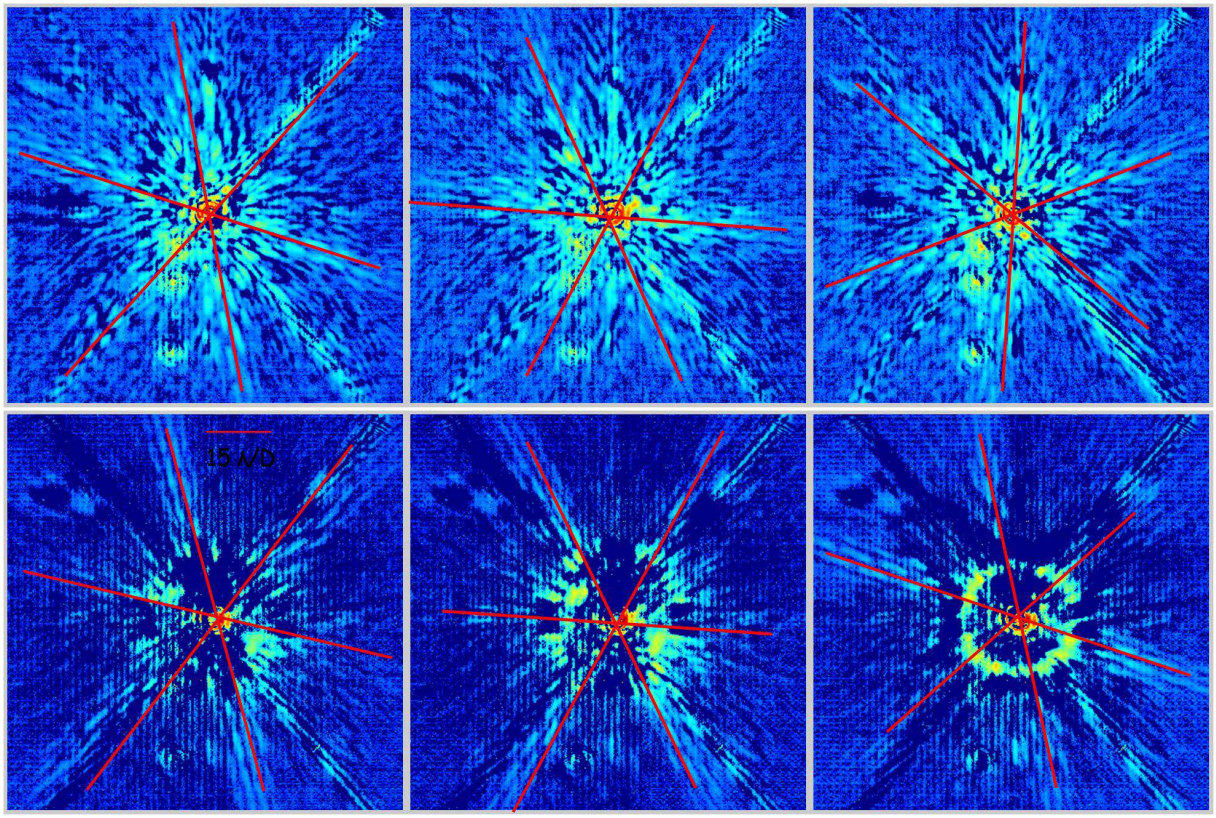

Figure 6.9: **Top:** Subtracted coronagraphic PPP images from the non segmented case in absence of turbulence. The three images corresponds to different segments orientations. **Bottom:** Same cases but in presence of turbulence. As expected, a rotation on the diffraction pattern produced by the segments can be observed.

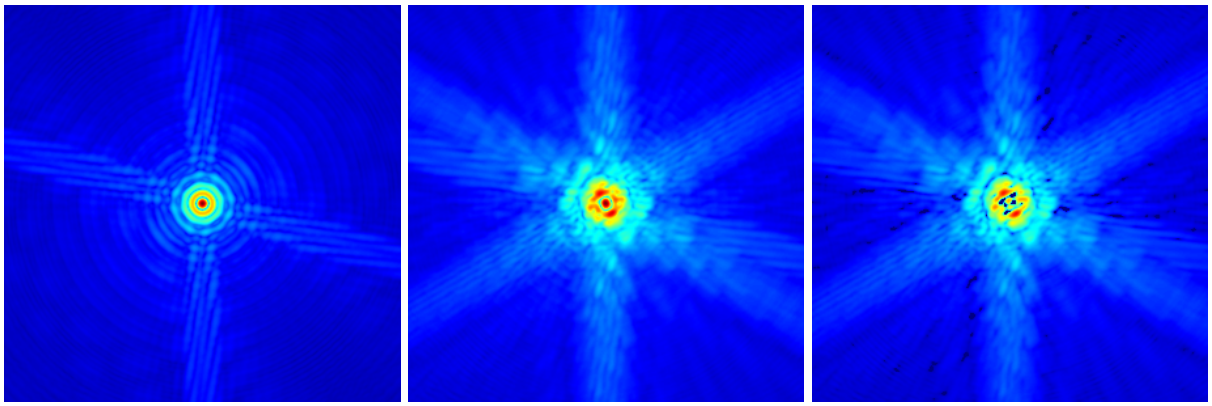

Figure 6.10: Simulated APLC coronagraphic images in absence of turbulence **Left:** Raw coronagraphic image. **Center:** Coronagraphic image including cophasing errors (52 nm rms). **Right:** Subtracted images.

6.3 Speckle nulling experiment

High-contrast imaging with a sensitivity adequate to detect earth-like planets around nearby stars requires contrasts levels between star and planet better than 10^{-9}. Extreme adaptive optics and high performing coronagraphs are required, but not sufficient, to achieve this goal. The main limiting factors are the non common path aberrations and static speckle noise in the final scientific image. Static speckles and planets show similar characteristics on intensity and shape, limiting the detectability. Detectability can be increased either implementing techniques to discriminate the planet signal to the speckle patterns, making use of spectral de-convolution or spectroscopic/polarimetric techniques (based upon the simultaneous differential imaging paradigm), or directly by suppressing the speckle pattern with the use of a suited DM.

6.3.1 Concept

Speckle nulling is a post focal technique (after coronagraph) that performs correction based upon measurements from the final science camera. The purpose of speckle nulling is to reduce the speckle noise in a specific region of the image plane (the "dark hole", DK) below the planet level by using a DM that makes speckles interfere destructively. The algorithm measures the complex amplitude of the speckle. Afterwards, the complex amplitude (CA) is used to compute the mirror shape that suppresses the speckles. All the speckle nulling algorithms require two basic conditions:

- That the system works in a regime where aberrations are reduced to a small fraction of the wavelength, i.e. SR > 90%. For this regime, we can replace the $e^{i\phi}$ on the complex amplitude, by its first order expansion $1 + i\phi$.
- Persistent quasi-static speckles. Speckles, produced by optical defects on the telescope and instrument, must be stable on the regime of several hours.

6.3.2 Electric field conjugation

Classical speckle nulling need to suppress speckles one by one and, therefore, requires many iterations and thus takes a great deal of time. To overcome this limitation a new algorithm was proposed by Give'on (Give'on *et al.* 2007, [83]) consisting of conjugating the electric field in a selected area of the image plane.

This method, the so-called Electric Field Conjugation (EFC), consists of two parts functionally independent: estimation and correction. The complex electric field amplitude (CA) in the image plane is estimated, then the estimated CA is processed to determine a correction to the DM actuators, that superposes the negative of the electric field onto the image plane, conceptually making the image intensity zero (i.e. conjugating the DM with the electric field on the image plane). Appendix B summarize the EFC algorithm principle followed in our experiment.

Before going in the details is important to clarify the notation: Electric field and complex amplitude are used to express the same concept depending on the authors, even if it is not case. In a strict notation, electric field should be expressed as:

$$E = A_c e^{-i\omega t} \tag{6.1}$$

where the electric field is the complex amplitude (A_C) multiplied by the temporal component, and the complex amplitude itself is defined as:

$$A_c = A e^{-i\phi} \tag{6.2}$$

Since for static speckles study there is no interest on the temporal component of the electric field, we will refer to complex amplitude when talking about electric field.

6.3.3 Experimental implementation

I will describe in this section the speckle-nulling experiment implemented on the HOT bench on the context of the EPICS phase A study (see Aller-Carpentier *et al.* 2010 ([84])

The main elements of the experiment are list hereafter:

- No turbulence, two flat mirrors replaced the phase screens. Only the internal turbulence was present.
- Micro-deformable mirror BMM. The mirror is only used to measure and correct the speckles.
- Infrared image plane (PSF). Optical quality on the IR path is > 90% (after correcting static errors on the bench using the bimorph mirror). The ITC IR camera in used to imaged the PSF using the narrow band on H band (1640 nm, 1.4% band).
- APLC coronagraph achieving a contrast $\approx 10^{-4}$ on the region of interest.
- Stability of the static speckles produced by the system. Figure 6.11 shows coronagraphic images taken on an interval of two days: the speckle pattern produced is constant on this period. Further experiments showed that the intensity stability of the speckles is $\approx 10^{-5}$.
- IR source. A high luminous IR source was acquired to have enough signal on the speckles (even if the PSF center is saturated). The IR source is coupled with a white source to feed the SH sensor.
- TT control. Tip and tilt are the main components of the turbulence inside the bench. The SH sensor is used to drive the TTM in close loop, hence, the stability of the speckle position is enhanced.

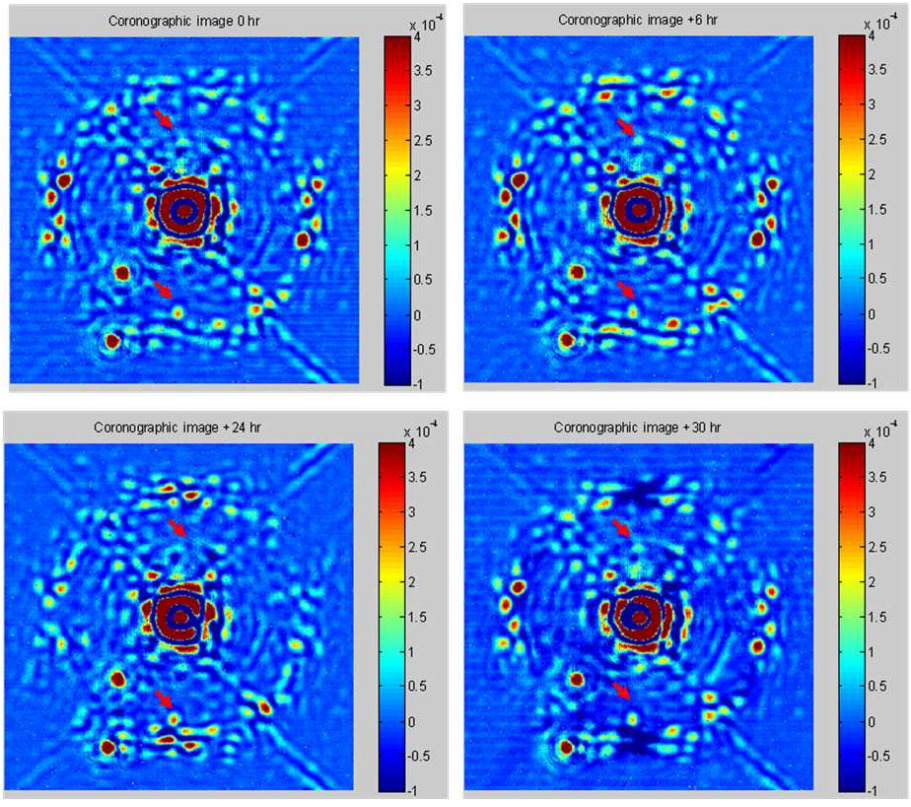

Figure 6.11: High-pass filtered coronagraphic images (AO close loop with turbulence) showing the residual speckle mapping. The images were taken with an interval of 30 hrs. The images show the speckle stability.

6.3.4 EFC algorithm implementation

The implementation of the EFC algorithm follows the next steps:

- Complex amplitude conjugation. FFT (*Fast Fourier Transform* is used as linear operator (C) to transform pupil plane CA to image plane CA.
- Computation of the complex amplitude IM, G. The influence functions of the BMM measured with an interferometer were used for the computation.
- Resizing of the IR images to adjust the size required by the CA conjugation and matrix G dimension.
- Determined the region Ω where the CA will be minimized.
- Computation of the BMM patterns used for calibration and computation of the CA produced on the image plane.
- Computation of the CA in the region Ω from the calibration images.
- Compute the actuators vector minimizing the CA proper to the speckle pattern.

The next considerations and simplifications were taken into account:

- Perfect coronagraph is considered when conjugating pupil plane CA to image plane CA.
- The influence function datacube has a size of 124x124x812. There are 812 actuators inside the pupil. Each influence function frame has a dimension of 124x124 pixels.
- We define a circular pupil with 124 pixels (to adjust to the IF scale). The pad is adjusted to get the desired pixels scale on the FFT operation. we work with the minimum value to minimize the size of the matrices (2 pixel per λ/D. i.e. 248x248 pixels pad).

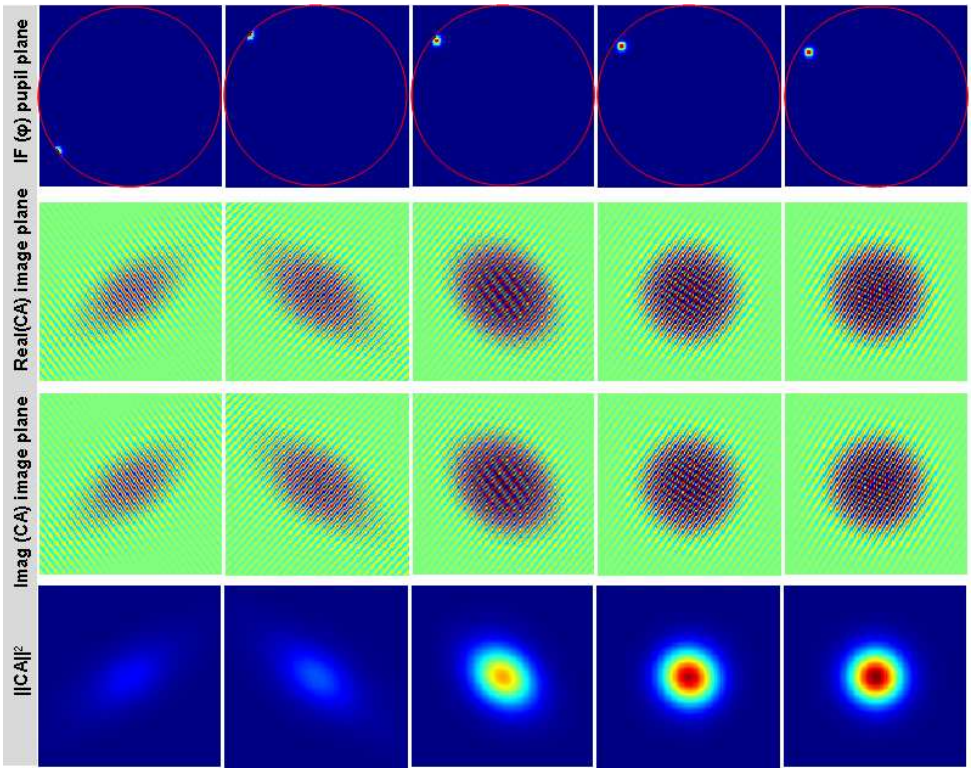

Figure 6.12: G matrix computation: first row corresponds to 5 actuators IF, second and third row show the real and imaginary complex amplitude on the image plane when pushing the actuator. Last row show the equivalent intensity on the image plane ($||CA||^2$). The IF's have a resolution of 124x124 pixel while the CA images resolution is 248x248 pixel (only 124x124 central pixels are shown).

Computation of the complex amplitude interaction matrix

To obtain the interaction matrix G we compute the CA produced by each actuator on the image plane, on the same way an AO system compute the IM pushing each actuator and measuring the response on the WFS.

In this case, the interaction matrix G is a synthetic matrix. It is not possible to push an actuator on the BMM and measure the CA, since the only effect on the image plane is an intensity variation. Instead, we compute the response in terms of CA corresponding to each influence function shape using the conjugation operator (FFT). Figure 6.12 shows the case of 5 actuators IF's and the corresponding CA value on the image plane (shown as real and image component).

For each CA image, we select only the pixels corresponding to the interest region Ω. Reordering the pixels in a matrix we recover the G matrix with dimension $N_{act} x N_{pix}$, that gives the relation:

$$CA_{pix} = G \cdot a_{act} \tag{6.3}$$

Afterwards G is inverted using SVD (several modes should be truncated on the inversion).

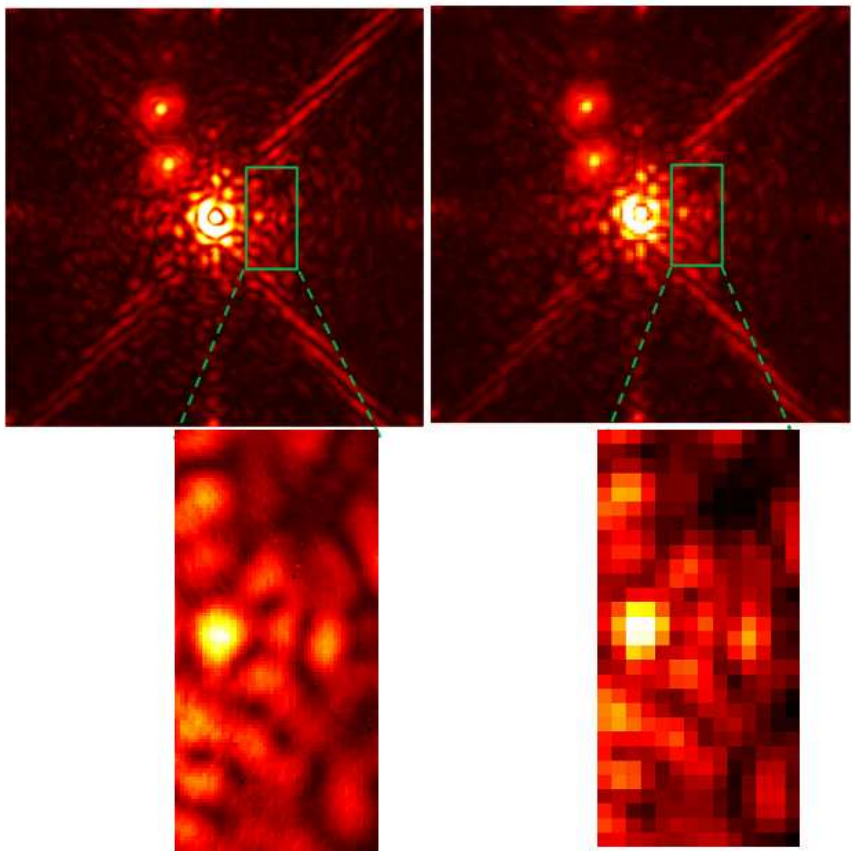

Figure 6.13: Coronagraphic images. **Left:** Original ITC image showing the probe region. **Right:** Coronagraphic image showing the final resolution used for the EFC algorithm. **Bottom:** Zoom of the region on interest for both images. Images are show on a root square intensity scale.

IR images resolution and probe region determination

The IR camera has a resolution of 1024x1024 pixels and a pixel scale of 5.3 mas/pix (0.1257 λ/D per pixel). The easiest way is to resize the IR image to recover the pixel scale of the simulated image plane, i.e. 0.5 λ/D per pixel. Figure 6.13 shows the original coronagraphic PSF and the result after resizing. The loss of resolution is not significant.

The probe region is localized on the right side of the PSF image (see Figure 6.13) in order to avoid the ghosts. In this region we can find several speckles, one of them quite intense. The region has a dimension of 29x14 pixels, center on the Y axe and displaced 10 pixels from the PSF center on the X direction in order to avoid residual energy from the center. The area Ω covers 406 pixels, so the CA_{pix} vector will have 812 elements. Dimension of G is 812 actuators x 812 signals, which implies a good compromise on terms of memory and time computing on the inversion operation.

Calibration patterns

Due to some calibration errors on the knowledge over the DM, it is better to use probe patterns relatively simple. In practice, we choose a pattern that gives near-uniform additive amplitude in a rectangular region in the image plane. The DM shape (ϕ) that produce this uniform amplitude on the image plane is given by:

$$\phi(u,v) = A sinc(\Delta X u) sinc(\Delta Y v) sin(X_c u + \theta) \tag{6.4}$$

where u and v are surface coordinates on the pupil plane, ΔX and ΔY are, respectively, the width and height of the rectangular probe region. X_c is the center of the rectangular, θ is the probe spatial phase, and A is the amplitude of ϕ. Two probe patters are used with $\theta = 0$ and $\theta = \pi/2$ (and the corresponding negative values).

Once the pupil plane shape is determined, we compute the corresponding voltage pattern using the DM influence functions (see figure 6.14). The final amplitude of the voltage pattern is adjust in sort that

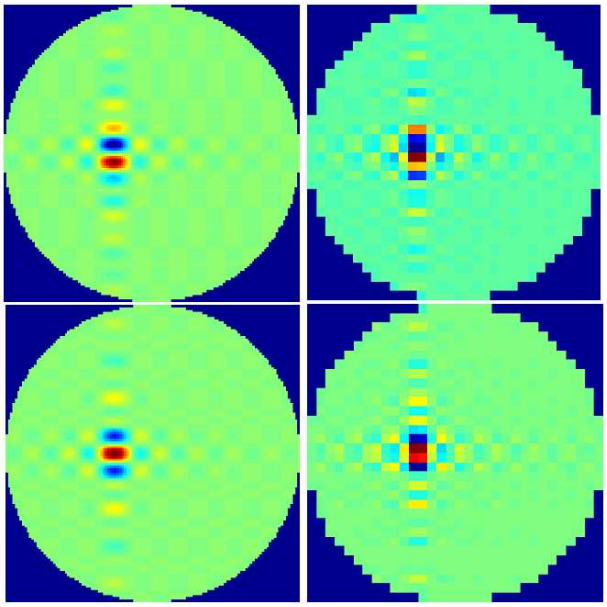

Figure 6.14: Wavefront patterns used for complex amplitude calibration. Left images represent the calibration wavefront (ϕ) while the right images show the voltage pattern on the DM to recover these wavefronts. **Top:** Pattern with $\theta = 0$ **Bottom:** Pattern with $\theta = \pi/2$.

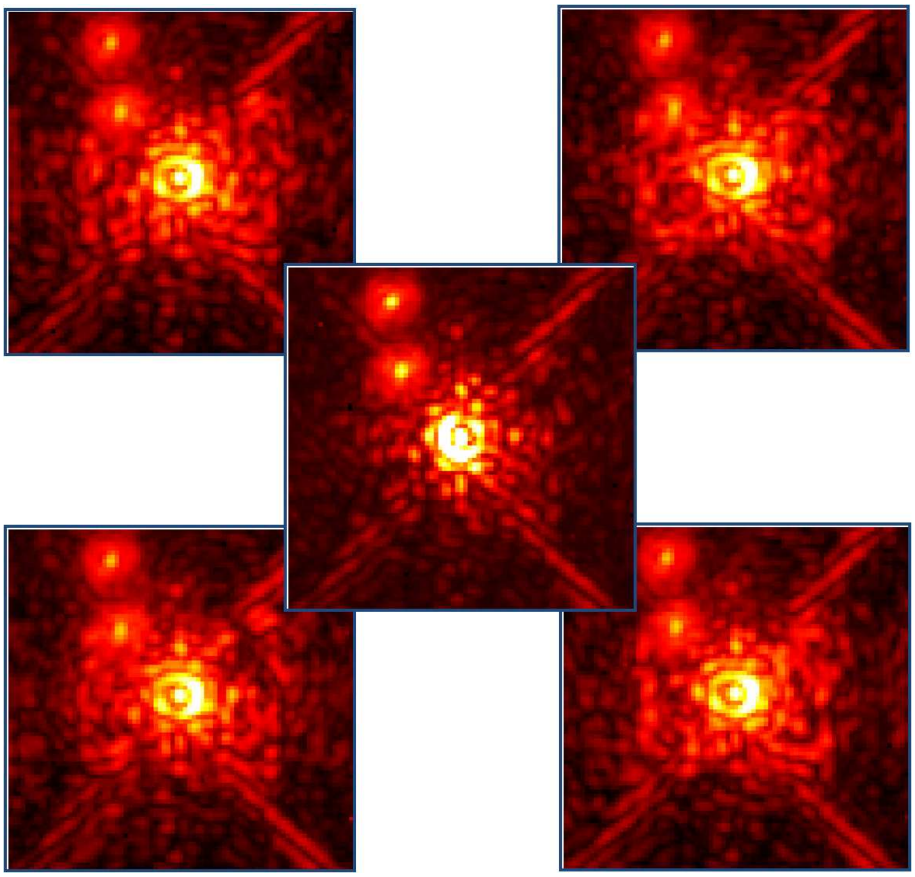

Figure 6.15: IR calibration images. **Top:** $I^+ \rightarrow \phi$ ($\theta = 0$) and $I^- \rightarrow \phi$ ($\theta = 0$) (left and right images respectively). **Bottom:** $I^+ \rightarrow \phi$ ($\theta = \pi/2$) and $I^- \rightarrow \phi$ ($\theta = \pi/2$) (left and right images respectively). **Center:** Standard coronagraphic image for comparison ($\phi = 0$). Images are shown on a root square intensity scale.

the intensity of the probe amplitude is similar to the speckles intensity to be corrected. Figure 6.15 shows the corresponding IR images acquired.

Complex amplitude estimation

The first term of equation C.10 is obtained from the experimental IR images, while the second term (matrix) is computed from the calibration wavefront patterns in the pupil plane. For both, only the pixels of the probe region are used.

The final computed complex amplitude in the probe region is shown in Figure 6.16. It is shown that the reconstructed complex amplitude reproduces the speckle mapping distribution of the original IR image. The main difference is the relative intensity between speckles. For instance, in the original IR image the most intense speckle is on the left-center of the image, while on the reconstructed case the most intense is placed at the left-down.

Corrective voltage computation

The final BMM voltage pattern that minimize the energy on the probe region is computed using the synthetic matrix G and the CA computed in section 6.3.4.

The equation, $a_{act} = G^+ \cdot CA_{pix}$, is used on an iterative process to obtain the voltage vector. A voltage vector is computed for each iteration. Using the IF and the conjugation operator, the CA amplitude on

the image plane produced by the voltage pattern is obtained. This new CA is used to re-compute a new voltage vector. The loop continues until the difference between the CA computed in two consecutive steps reach a minimum error. A small gain is used on the iterative process to avoid possible divergences on the loop.

The number of truncate modes on the SVD inversion of G is quite high. The optimal number of modes found is ≈ 250 (of 850 modes). If more modes are used on the inversion the final correction is smaller and also produce errors on the iterative process. The voltage vector found is on arbitrary units and, therefore, there is an amplitude factor to be taken into account. To find the amplitude factor we apply the voltage vector with different amplitudes until we minimized the speckles intensity on the IR image.

6.3.5 Results

Figure 6.17 shows the probe area for the corrected IR images compared with the original IR image (full resolution images). Two corrective patterns were used, the first with a voltage amplitude of 12 and the second of 20 (center an right images respectively). The intensity of the bigger speckles decreased. But some energy seems to be displaced to other areas, especially on the 2nd case where a ring appears around the central core. The correction factors for the big speckles are: 3.6 (center-left), 11.5 (up), 3.4 (center-right).

Figure 6.18 shows a better result obtained some days later. In this case the residual ring do not appear. As before the speckle intensity decreased, except for one speckle (center of the image, circled in white) that increased. The correction factors for the big speckles area: 8 (center-left), 8.96 (up-left), 7.9 (center-right), -1.36 (center-center). An additional result is the stability on the speckle pattern as shown from the non-corrected images with a difference of 24 hours.

The results show the real capability of the speckle nulling technique. We demonstrate that the speckle intensity could be decrease between 0.5 and 1 order of magnitude. This experiment is only a first step, and further optimization will be required to increase the speckle suppression. On the other hand, experimental results should be obtained under real turbulence conditions.

The next issues should be optimized:

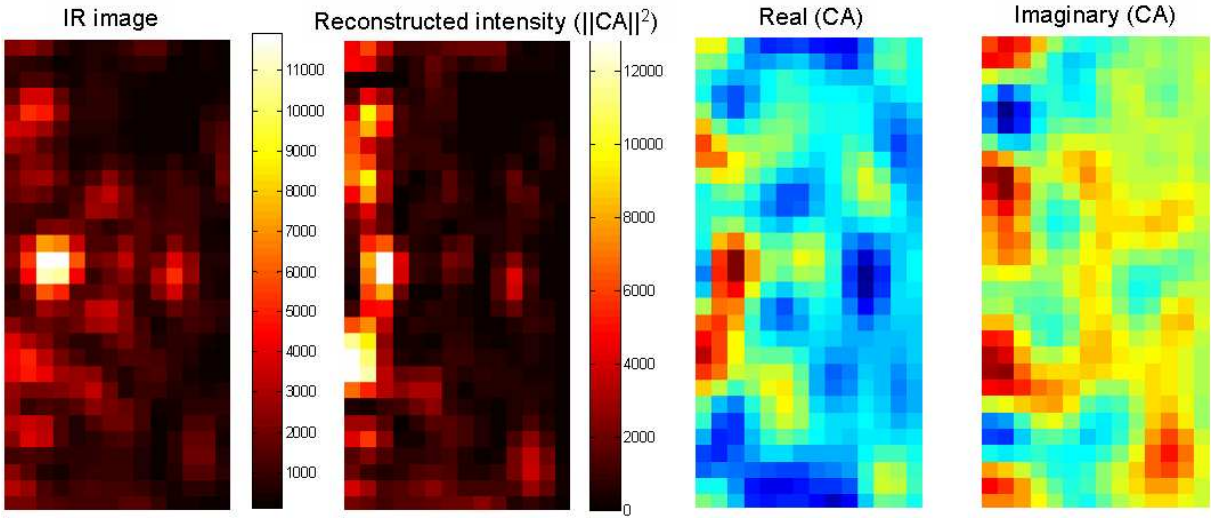

Figure 6.16: The first image show the probe region on the original coronagraphic image showing the speckle map. The other images show the re-constructed complex amplitude, the second image corresponds to the intensity level ($||CA||^2$), while the third and fourth images corresponds respectively to the real and imaginary part of the CA . Images are shown on a linear scale.

- Iterative process. After the first correction, a new set of calibration images could be taken adjusting the amplitude pattern to calibrate the residual speckles and compute a new corrective voltage. This process could be done iteratively.
- Realistic coronagraph. A more realistic model for the coronagraph could be used taken into account the APLC configuration and a real pupil including the spiders.
- CA calibration could be done using several patterns (using additional θ values).

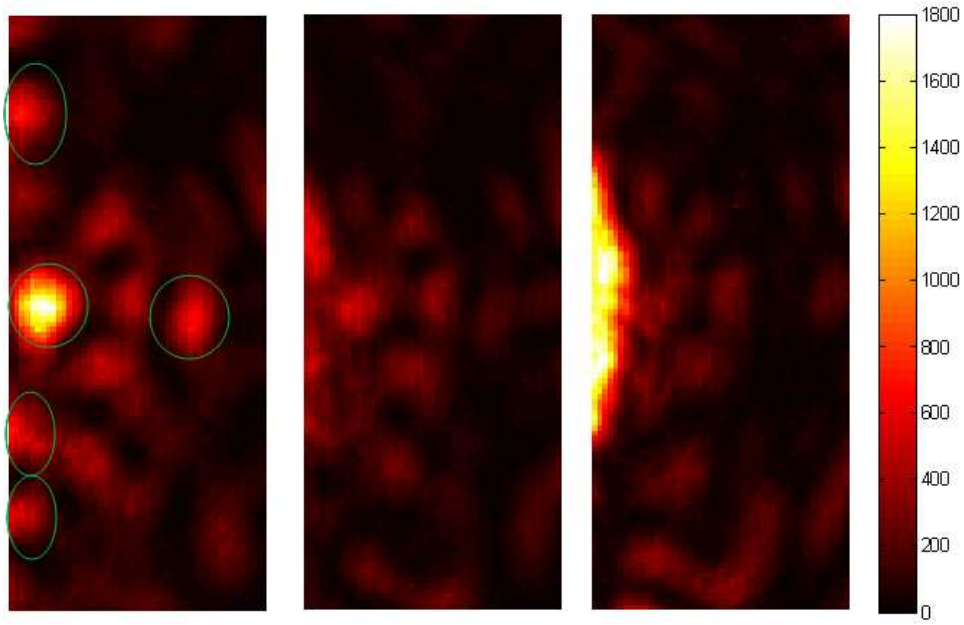

Figure 6.17: Probe region image (14 dec 09). **Left:** Uncorrected image. **Center:** Corrected image (voltage amplitude factor 12). **Right:** Corrected image (voltage amplitude factor 20).

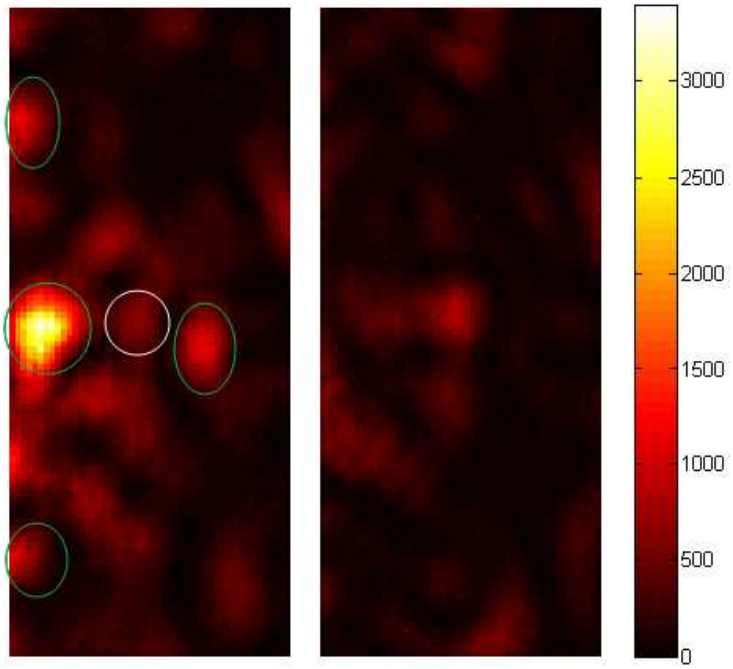

Figure 6.18: Probe region image (15 dec 09). **Left:** Uncorrected image. **Right:** Corrected image.

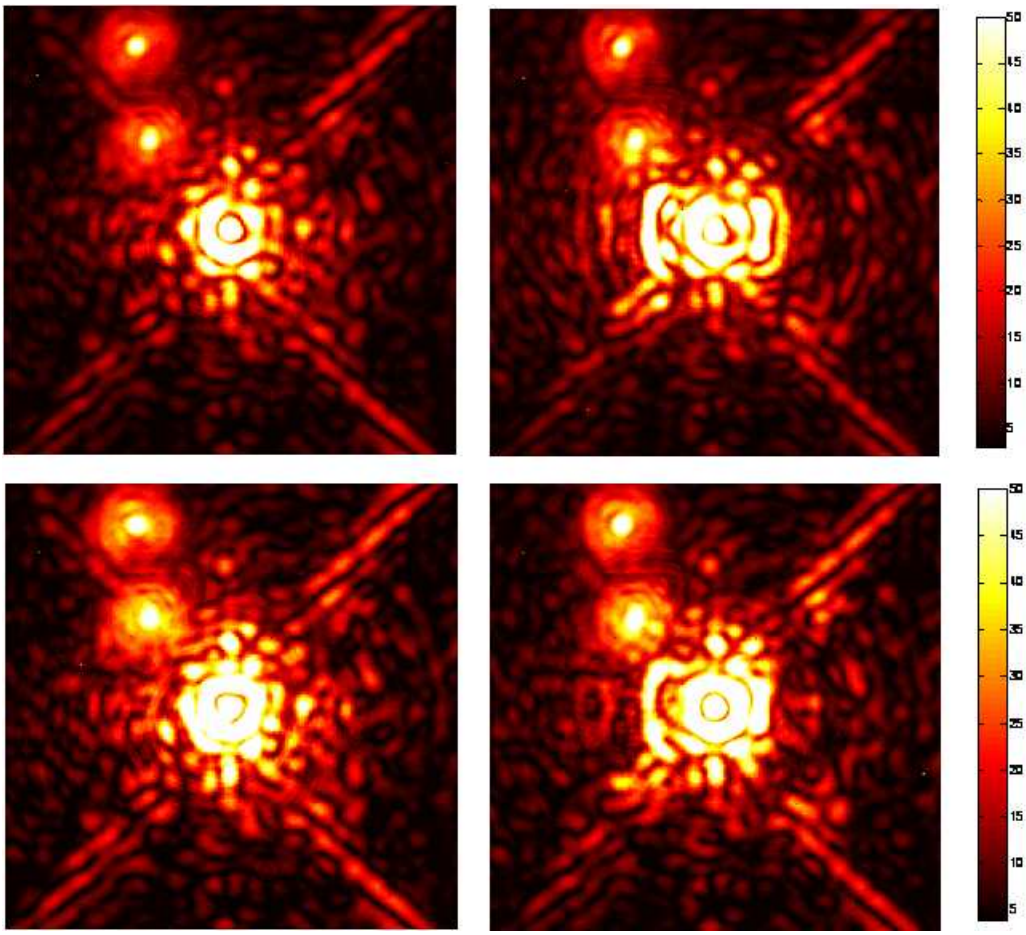

Figure 6.19: Coronagraphic images acquired the 14 dec 09 (top) and 15 dec 09 (bottom). **Left:** Uncorrected image. **Right:** Corrected image. The up-right image shows a clear new ring structure around the PSF (image corresponding to the amplitude voltage of 20).

- SVD truncation and amplitude factors should be study with more attention.

Guyon *et al.* 2010 ([85]) proposed a new algorithm for the CA computation. This method was already implemented on simulation and will be also tested in further experiment on the bench.

Conclusion

Direct imaging of extrasolar planets requires the development of adaptive optics systems to achieve quite perfect PSF images of the parental star. In addition, high performing coronagraphs are mandatory to suppress the light of the parental star, showing the presence of the planet.

Next generation of planet finders, as SPHERE (VLT telescope) or EPICS (E-ELT telescope), will combine XAO and coronagraph systems with additional instrumentation used to discriminate the planet with respect to the residual speckle noise. Simulations predict good performance but XAO systems still needed to be proven in laboratory.

The *"High Order Test Bench"* implements an end-to-end XAO system under realistic telescope conditions. Its objectives are to confirm the expected performance, studying possible limitations for an XAO system, and to test new technologies. The high quality PSF image is used to study the contrast performance of a new generation of coronagraphs and to develop new techniques for speckle suppression.

The work developed in this thesis could be mainly summarized in three points: *(a)* characterization of the individual subsystems, *(b)* implementation of a full operating AO system and *(c)* evaluation the AO and the postfocal contrast performance.

All the subsystems were characterized and integrated successfully on the bench achieving a full operating AO system. A new type of deformable mirror for astronomical AO was characterized in terms of flatness, stroke behavior, bias and influence functions shape. The MEMS deformable mirror of Boston Micromachines shows an optimal flatness in the central region but strong slopes over the edges. Thus, in general, it would be recommended to use only the inner region for wavefront correction. In our case, 32 actuators are required to work in a high order regime. The bimorph mirror of HOT is used to compensate partially for this problem.

The number of defective actuators is lower ($< 5\%$) than requested to the manufacturer. The stroke behavior follows a quadratic law as expected. The maximum stroke is obtained before the maximum voltage range of the DM, being different with respect the manufacturer especifications. High resolution interferometric images of the DM influence functions were taken and used later to construct the modal base. These images show the same shape for all the actuators.

The durability and life time is the main problem of this BMM deformable mirror. An oxidation process can occur and may cause the dead of the actuators, producing a local peak in the reflected wavefront. We suppose that a leak in the protective window allows the entrance of water vapor producing the oxidation. The last BMM acquired two years ago does not exhibit any oxidation problem, by the moment, probably due to an improvement of the isolation of the protective window.

The Shack-Hartmann sensor, using an electron multiplicative CCD, was demonstrated to be suitable for high order wave-front sensing. It was characterized in terms of linearity to ensure a correct behavior. The linearity measurements are required to find the optimal stroke value used for the calibration step. As well, the pixel scale was measured experimentally applying a new method based on the measurement of the intensity pixels variations of the subapertures when applying a known tilt to the wavefront. This measurements have helped us to understand better the difference between subaperture slope gain and pixel scale. This method will be also applied to the *Adaptive Optics Facility* of the VLT.

The SHS was used to characterized the temporal behavior of the simulated turbulence by the rotating phase screens. The SHS measurements show that the turbulence follows the *frozen turbulence hypothesis*. One or two peaks are clearly visible on the spatio-temporal cross-correlation map depending on the phase screens moving either on the same, or on the opposite sense.

A turbulence speed of 1.26 m/s is derived from the peaks displacement. This speed is about one order of magnitude slower than the real atmospheric turbulence. The control loop framerate($\approx$ 80 Hz) is also one order of magnitude slower than a real XAO system, hence, well matching the reduced turbulence speed.

The power spectrum of the low order Zernike modes was computed. The estimated frequency dependency law shows a behavior slightly different to the theoretical values, but in agreement with other measurements obtained from real atmospheric turbulence using low order AO instruments. The correlation time of the modal coefficients as a function of the mode order was obtained for a Karhunen-Loeve basis of $\approx$ 600 modes.

The calibration and modal control of the AO system was inspired by the SPHERE methodology. A Hadamard zonal calibration was optimized applying a push-pull method. Hence a full calibration is done in $\approx$ 10 minutes. We have demonstrated experimentally that the noise improvement of the Hadamard method with respect to a classic zonal calibration follows the theoretical dependence (proportional to the actuator number) for a high order system.

A Karhunen-Loeve modal basis is projected onto the interaction matrix to recover a modal control. The K-L basis is built from the influence functions measurements applying a double diagonalization method that ensures modes orthogonal and statistically independent. A high number of noisy modes had to be rejected since they exhibit a waffle pattern. These modes were expected to be at the end of the modal base with a high order number and low eigenvalues. By the contrary, they appear at the middle of the base. This effect was not yet understood and require further studies. Finally, a maximum of 589 modes of the 812 possibles have been controlled. This means that $\approx$ 28% of the modes could not be controlled. This limitation should be understood better, especially, in the context of future AO systems with many degrees of freedom.

The loop control follows a simple integrator algorithm with an anti-windup circuit. Through the whole process, the DM is linearly controlled even if the displacement is quadratically proportional to the voltage. A simple quadratic law is applied for this purpose. This method allows to simplify the control and calibration. Matlab programming language has shown to be suitable to control the full system working simultaneously with *Sparta-light* components (standard ESO platform for low demanding AO systems).

The AO performance of the system was studied as a function of the star guide magnitude. Five flux cases corresponding to magnitudes between 2 and 11 were chosen (properly scaled to realistic framerates). The performance of the system was estimated from narrow band IR PSF images (H-band) and the residual wavefront measurements. The PSF exhibits a SR of $\approx$ 93% in high flux conditions and $\approx$ 78% in low flux conditions in good agreement with the expected performance of SPHERE.

For the lowest flux case, only 9 photons per subaperture and frame are detected, being a photon counting system. The performance at this low flux regime is obtained thanks to the electron multiplied CCD capabilities with subelectronic RON ($\approx$ 0.7 e^-). If the multiplicative gain is set to zero the AO system is not even able to close the loop. This result confirms experimentally the capabilities of this technology for AO.

Azimuthal profiles were computed from the PSF images. For all flux cases a diffraction-limited image is obtained showing up to 8 Airy rings. The contrast level obtained at high flux is $\approx 6 \cdot 10^{-4}$ for an angular separation of 0.2 arcsec.

The residual wavefront measured by the SHS is used to study the temporal and spatial behavior. The rejection transfer function shows a bandwidth correction of $\approx$ 3.5 Hz. This value is in agreement with

the loop and turbulence speed, one order of magnitude lower than it would be for a real AO system. The modal variance distribution measured for the open and closed loop cases shows the correction achieved for all the modes of the modal basis. The correction is efficient for all modes of our chosen basis meaning that the residual variance is reduced in closed loop.

The high quality PSF obtained in the HOT bench is used to study the coronagraph performance with XAO conditions. Several coronagraphs were analyzed (APLC, FQPM, BL). The *Apodized Pupil Lyot Coronagraph*, manufactured with a new technique (*halftone-dot process*), achieves a peak rejection factor of ≈ 280 and a contrast of $3{\cdot}10^{-4}$ at 3 λ/D. A high pass filtered coronagraphic image is obtained by subtracting a median filtered image. In this way, the smooth structures in the coronagraphic PSF such as the AO residual seeing halo are removed. The detectability (1 σ) then reaches 10^{-5} between 8 and 13 λ/D.

Coronagraphic images also show the spatial cut-off frequency of the AO system as a bump in the contrast profiles. The cut-off frequency is slightly different depending in the number of modes corrected. For the high order reconstructor (589 modes) the cut-off appears at 14.5 λ/D, while for the low order case (412 modes) it appears at 12.5 λ/D. This difference confirms that the bump is really due to the AO cut-off.

The contrast limitation of 10^{-5} (after coronagraph) is due to residual speckle noise in the halo. Preliminary experiments were carried out to reduce the speckle intensity by using the *speckle nulling* postfocal technique. The *Electrical Field Conjugation (EFC)* concept was applied to estimate the complex field amplitude in a selected area of the image plane. This information is processed to determine a correction to the DM that suppresses the speckles. Initial results show a reduction of around one order of magnitude for the most intense speckles. Several issues, as addressed in the last chapter, should be considered in the implementation of the method to achieve a real improvement in the detectability. Specifically, the speckle temporal stability should be studied more carefully.

Resumen y conclusiones

La observación directa de planetas extrasolares requiere el desarrollo de Óptica Adaptativa Extrema (XAO) para conseguir imágenes de alta resolución de la estrella progenitora. Además, coronógrafos de última generación son imprescindibles para suprimir la luz de la estrella central, haciendo visible la presencia del planeta.

La próxima generación de instrumentos dedicados a la búsqueda de planetas extrasolares como SPHERE (VLT) o EPICS (E-ELT) combinarán sistemas XAO y coronógrafos incluyendo instrumentación específica para poder discriminar el planeta respecto de los *speckles* residuales. Las simulaciones predicen un alto rendimiento para los sistemas XAO pero todavía tienen que ser probados en el laboratorio.

El banco de pruebas HOT ("High Order Test Bench") reproduce un sistema XAO completo que permite el estudio y caracterización en condiciones normales de observación. Sus objetivos son confirmar el rendimiento previsto, verificando posibles limitaciones de los sistemas XAO y estudiar nuevas tecnologías. La alta calidad de imagen generada por el sistema de óptica adaptativa es utilizada para estudiar el contraste de una nueva generación de coronógrafos y para desarrollar nuevas técnicas de supresión de *speckles*.

El trabajo desarrollado a lo largo de esta tesis puede resumirse en tres puntos principales: (a) caracterización de los diversos subsistemas, (b) implementación de un sistema completo y totalmente operativo de óptica adaptativa (c) evaluación del rendimiento de la óptica adaptativa y del contraste final en la imagen científica.

Todos los subsistemas han sido caracterizados e integrados con exito en el banco óptico dando lugar a un sistema completo de AO. Un nuevo espejo deformable para uso astronómico ha sido caracterizado en cuanto a planicidad, comportamiento del actuador, posición de reposo y funciones de influencia. El espejo deformable de tipo MEMS de *Boston Micromachines* exhibe una región interna plana, al contrario que en los bordes donde la pendiente es muy pronunciada. Por lo tanto, en general seria recomendable utilizar solo la región interna para corregir el frente de ondas. En nuestro caso el máximo numero de actuadores, 32, tiene que ser utilizado para poder trabajar en el régimen de alta resolución. El espejo deformable bimorfo de HOT es utilizado para resolver parcialmente este problema.

El número de actuadores defectuosos es inferior ($< 5\%$) al mínimo requerido al fabricante. El desplazamiento (*stroke*) producido por el actuador al aplicarle un voltaje sigue una ley cuadrática como era de esperar. El máximo desplazamiento se obtiene para un voltaje inferior al máximo tolerado por el espejo deformable y representa una diferencia respecto a las especificaciones del fabricante. Imágenes de las funciones de influencias para todos los actuadores fueron obtenidas mediante interferometría de alta resolución. Estas imágenes muestran que todas las funciones de influencia tienen una forma similar. Posteriormente, estas funciones de influencia han sido utilizadas para construir nuestra base modal.

La durabilidad y vida media de estos dispositivos representan su mayor inconveniente. Procesos de oxidación pueden provocar la inacción de los actuadores, dando lugar a un pico local en el frente de ondas reflejado. Suponemos que debido a un fallo en el aislamiento de la ventana protectiva, vapor de agua entró en contacto con el espejo deformable, dando lugar a la oxidación. El último BMM adquirido hace ya más de dos años no ha mostrado todavía ningún síntoma de oxidación, probablemente debido a

una mejora en el aislamiento del espejo.

El sensor Shack-Hartmann (SHS) utilizando como detector una cámara EMCCD (*electrón multiplicative CCD*) ha demostrado ser óptima para medir el frente de ondas con una alta resolución. El sensor ha sido caracterizado en cuanto a linearidad para garantizar un correcto funcionamiento. Las curvas de linearidad son necesarias para encontrar el desplazamiento correcto del actuador durante la calibración. También, el tamaño aparente del píxel (*píxel scale*) ha sido medido experimentalmente utilizando un nuevo método basado en el estudio de la variación producida en la intensidad de los píxeles pertenecientes a la subapertura al aplicar una inclinación (*tilt*) conocida al frente de ondas. Las medidas obtenidas de esta forma han sido de gran utilidad para entender mejor la diferencia entre la pendiente de la curva de linearidad (ganancia) y el tamaño aparente del píxel. Este método será aplicado también para el proyecto de óptica adaptativa del VLT, conocido como AOF (*Adaptive Optics Facility*).

Hemos utilizado el SHS para caracterizar el comportamiento temporal de la turbulencia generada por las dos pantallas de turbulencia (*phase screen*) en rotación. Las medidas obtenidas demuestran que la turbulencia simulada sigue la hipótesis de la turbulencia rígida (*frozen turbulence hypothesis*). Uno o dos picos son claramente visibles en la correlación espacio-temporal dependiendo de si las pantallas de turbulencia giran en la misma o en direcciones opuestas.

La velocidad de la turbulencia obtenida a partir del movimiento de los picos, es de 1.26 m/s. Este valor equivale a un orden de magnitud inferior a la velocidad de la turbulencia atmosférica real. La velocidad de control de nuestro sistema ($\approx$ 80 Hz) es también un orden de magnitud inferior a la de un instrumento XAO, por lo tanto, ajustándose perfectamente a la velocidad reducida de nuestra turbulencia simulada.

Hemos calculado el espectro de potencias de los modos Zernikes de más bajo orden. El comportamiento del espectro, en función de la frecuencia, es ligeramente diferente al comportamiento teórico esperado, pero similar al obtenido con otros sistemas de AO a partir de medidas reales en el cielo. También, hemos calculado el tiempo de correlación, en función del orden del modo, para una base de $\approx$ 600 modos Karhunen-Loeve (K-L).

El control modal y la calibración están basados en la metodología aplicada en SPHERE. Una calibración zonal de tipo Hadamard ha sido optimizada mediante un método de push-pull. De esta manera el tiempo total para la fase de calibración es de aproximadamente unos 10 minutos. Hemos demostrado experimentalmente que la disminución del ruido de la matriz de interacción aplicando una calibración Hadamard con respecto a una calibración zonal clásica se ajusta a la expresión teórica (proporcional al número de actuadores) también para un sistema de alto orden.

El comportamiento modal del control del sistema se recupera al proyectar sobre la matriz de interacción una base modal de Karhunen-Loeve. La base se construye a partir de las medidas de las funciones de influencia aplicando un método de doble diagonalización que garantiza modos ortogonales y estadísticamente independientes. Un gran número de modos han tenido que ser eliminados debido a que exhibían un patrón de tipo *waffle* (es decir, en forma de tablero de ajedrez). Estos modos deberían tener un orden superior y bajo valor propio, apareciendo por tanto al final de la base. Por el contrario, aparecen a mitad de la base. El origen de este comportamiento es todavía desconocido y por tanto tendrá que ser estudiado en más detalle. Al final, de un total de 812 modos se han conseguido controlar 589. Esto significa que aproximadamente el 28% de los modos no pueden ser controlados. Esta limitación debe ser entendida mejor, especialmente en el contexto de futuros sistemas de óptica adaptativa con gran número de grados de libertad.

El bucle de control se basa en un simple integrador modificado con un circuito de anti-windup. A través de todo el proceso, el espejo es controlado linealmente incluso si el desplazamiento es cuadráticamente proporcional al voltaje aplicado. Para ello, hemos aplicado una simple ley cuadrática. Esta aproximación permite simplificar el control y el proceso de calibración. Hemos podido gestionar de forma óptima el control de todo el sistema utilizando el lenguaje de programación de alto nivel *Mat-*

lab simultáneamente con componentes de *Sparta-light* (plataforma estándar de la ESO para sistemas de óptica adaptativa de bajo requerimiento).

El rendimiento del sistema ha sido estudiado en función de la magnitud de la estrella guía. Para este estudio se han escogido 5 condiciones de flujo, correspondientes a estrellas con magnitud entre 2 y 11 (reescaladas correctamente a una velocidad de bucle real). El rendimiento del sistema ha sido medido a partir de imágenes infrarrojas (banda - H) de banda estrecha de la PSF. El Strehl Ratio medido a partir de la PSF es de ≈93% en condiciones de alto flujo y de ≈78% en bajo flujo. Estos resultados concuerdan con el rendimiento estimado para SPHERE.

Para condiciones de muy bajo flujo, solo 9 fotones por subapertura y fotograma son detectados, comportándose así como un sistema de detección individual de fotones. El rendimiento en estas condiciones de flujo es el resultado de la capacidad electro-multiplicativa de la cámara CCD (ruido subelectrónico $\approx 0.7\ e^-$). Si la ganancia electromultiplicativa se desactiva, el control de la óptica adaptativa no es ni siquiera capaz de cerrar el bucle. Este resultado confirma experimentalmente la capacidad de esta tecnología para la óptica adaptativa.

Perfiles azimutales han sido medidos a partir de las imágenes de la PSF. Para todos los casos estudiados se ha obtenido una imagen difractiva en la que se observan hasta 8 discos de Airy. El contraste obtenido en condiciones de alto flujo es de $\approx 6 \cdot 10^{-4}$ a una distancia angular de 0.2 segundos de arco.

El frente de ondas residual medido por el SHS es utilizado para estudiar el comportamiento espacial y temporal. La función de transferencia muestra una banda de correción de ≈ 3.5 Hz. Este resultado concuerda con la velocidad del bucle y de la turbulencia que es un orden de magnitud menor de lo que sería para un sistema real. La distribución de la varianza modal medida en bucle abierto y cerrado muestra el rendimiento obtenido para cada uno de los modos de la base modal. Se obtiene una corrección eficaz para todos los modos de la base que hemos escogido, lo que quiere decir que la varianza disminuye en bucle cerrado.

La gran calidad de imagen obtenida por HOT es utilizada para estudiar la eficiencia de la coronografía en condiciones XAO. Varios coronógrafos han sido analizados (APLC, FQPM, BL). El coronógrafo de tipo Lyot con pupila apodizada fabricado con una nueva técnica (*halftone-dot process*) consigue una atenuación central de ≈ 280 y un contraste de $3{\cdot}10^{-4}$ a una distancia angular de 3 λ/D. Aplicando un filtro medio a la imagen coronográfica obtenemos una imagen en la que se muestran sólo las estructuras de alta frecuencia espacial. De esta manera el halo residual puede ser eliminado. La detectabilidad (1 σ) así obtenida es de 10^{-5} entre 8 y 13 λ/D.

Las imágenes coronográficas también muestran la frecuencia de corte espacial del sistema de AO como un bache en el perfil de contraste. La frecuencia de corte está ligeramente desplazada dependiendo del número de modos corregidos. Para el reconstructor de alto orden (589 modos) la frecuenta de corte aparece a una distancia angular de 14.5 λ/D, mientras que para el reconstructor de bajo orden (412 modos) aparece a 12.5 λ/D. Esta diferencia confirma que el bache tiene realmente su origen en la frecuencia de corte espacial del sistema de óptica adaptativa.

La limitación de 10^{-5} en el contraste (después del coronógrafo) es debida a la presencia de los *speckles* residuales en el halo. Experimentos preliminares se han llevado a cabo para reducir la intensidad de estos *speckles* mediante técnicas posfocales de *speckle nulling*. Se ha aplicado el concepto de la conjugación del campo electrico (EFC, del inglés *Electrical Field Conjugation*) para estimar la amplitud compleja en una región concreta del plano imagen. Esta información es utilizada para determinar la corrección a aplicar al espejo deformable que suprime los *speckles*. Resultados preliminares muestran una reducción de intensidad de aproximadamente un orden de magnitud para los speckles más brillantes. Varias cuestiones, como ya hemos mencionado en el último capítulo, deben tenerse en cuenta en la implementación de este método para poder conseguir una mejora real en la detectabilidad. Especialmente, la estabilidad temporal de los speckles tiene que ser estudiada más detenidamente.

A

Coronagraphy principle

Coronagraphy was introduced by B. Lyot in the 1930's for solar application. Since that time, the concept has evolved to stellar application. A coronagraph is an instrument that strives to control the diffracted light from a bright astrophysical object to image faint off-axis companion in its close environment. A stellar coronagraph is therefore a starlight suppression device designed to reduce the on-axis starlight as much as possible by preserving the off-axis companion signal (Figure A.1).

In its classical scheme, a coronagraph is a combination of a low-frequencies filter (the coronagraph mask, main component placed in the first focal plane) with a high-frequencies filer (so-called Lyot stop placed in the second pupil plane). The light distribution in the relayed pupil (second pupil plane) is different than in the input pupil. The light is diverted outside the pupil.

The action of the Lyot stop is precisely to select the geometric pupil (or smaller) in which the on-axis

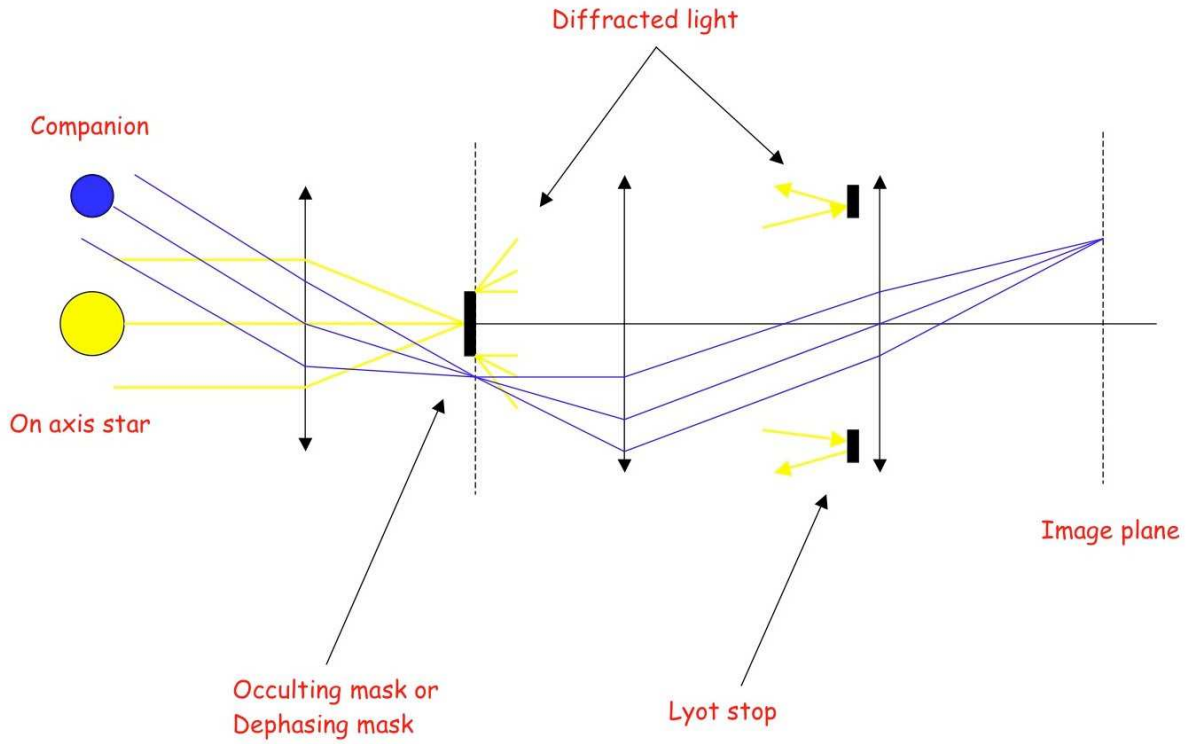

Figure A.1: Scheme of the coronagraphic process.

starlight is rejected. Downstream, an image of the field can be formed with the starlight attenuated. In contrary, an off-axis object (companion) missing the effect of the coronagraph (low-frequencies filter) has its pupil unaltered and is re-imaged in the final detector plane.

The coronagraph mask could work as an amplitude mask (Lyot coronagraph, APLC) or as a phase mask (Four quadrant phase mask coronagraph (FQPM)).

A variation of the classical Lyot coronagraph is the APLC (*"Apodized pupil Lyot coronagraph"*), where the entrance is modify by an amplitude mask with a given transmission profile (for a circular pupil the entrance apodized pupil has a radially varying transmission profile). The effect of the apodized pupil is to produce a PSF with a larger core compared to the classical Airy pattern but with attenuated diffraction rings, hence increasing the contrast between both regions.

B

Karhunen-Loeve basis construction

The K-L basis considered for the modal control is derived from the DM influence functions and the turbulence spatial properties. We consider the projection of the turbulent wavefront space onto the space defined by the DM influence functions, noted E_{wf}.

We want to find the K-L basis noted Q of the subspace E_{wf} with respect to the tip-tilt free turbulence wavefronts. We note C_{phi} the covariance matrix of the tip-tilt free turbulence wavefronts:

$$C_\phi = \langle \phi(\mathbf{r})\phi(\mathbf{r}') \rangle \tag{B.1}$$

Then the problem is to define Q so that:

$$Q^t C_\phi Q = \Lambda \tag{B.2}$$

$$Q^t Q = I \tag{B.3}$$

where Λ is a diagonal matrix and I is the identity matrix. The equation B.2 gives the statistical covariance matrix of the K-L base Q:

$$\left\langle a_i a_j \right\rangle = \int_P \langle \phi(\mathbf{r})\phi(\mathbf{r}') \rangle \, Q_i(\mathbf{r}) Q_j(\mathbf{r}) d^2 r \tag{B.4}$$

Thus, being a diagonal matrix the uncorrelation between modes is ensured. In other hand, B.3 imply the orthogonality of the basis.

We denote F the influence function matrix which describes the pixels map of the wavefront produced by each actuator. F is an isomorphism between the space of control voltages E_{cv} and E_{wf} . We define B, the matrix of vectors of E_{cv} so that:

$$Q = FB \tag{B.5}$$

Thus, B is the K-L basis expressed in the control voltage space. We denote Δ the geometrical covariance matrix of the influence functions as:

$$\Delta = F^t F \tag{B.6}$$

Or, expressed in integral form:

$$\Delta_{ij} = \left\langle f_i f_j \right\rangle = \int_P F_i(\mathbf{r}) F_j(\mathbf{r}) d^2 r \tag{B.7}$$

and G the statistical covariance matrix of the influence functions:

$$G = F^t C_\phi F \tag{B.8}$$

Of course, the matrix Δ is not the identity and the matrix G is not diagonal. The simultaneous double diagonalization is obtained with the following procedure:

- Diagonalize Δ so that $M'^{t}\Delta M' = D^2$, where M' is the eigenmodes matrix of Δ and D^2 is the square root of the diagonal matrix of the eigenvalues.
- Normalize the eigenvectors M' of Δ with respect to the square root of their eigenvalues: $M = M'D^{-1}$.
- Express G in the normalized eigenmodes basis M of the deformable mirror: $G' = M^{t}GM$.
- Diagonalize G' such as $A^{t}G'A = \Lambda$ where A is the eigenmodes matrix of G' and Λ is the eigenvalues matrix of G', i.e. of both the DM and the turbulence, and A is given in the eigen space of the DM.
- Express A in the control voltage space: $B = MA$. The size of B is: $n_{actuators}$ x m_{modes}.
- Compute the K-L modal basis $Q = FB$. The j^{th} column of Q gives the wavefront representation of the j^{th} mode.

Orthogonality and uncorrelation properties of the basis B could be verified developing equations B.2 and B.3 in terms of A and M.

C

Electric field conjugation algorithm

C.1 EFC correction

Considering an optical imaging system with a deformable mirror on the pupil plane, the corrected electric field in the image plane over some region Ω is modeled as:

$$E_{cor} = \mathbb{C}\{Ae^{\alpha+i\beta}e^{i\phi}\} \tag{C.1}$$

where:

- A is the real aperture illumination function.
- α and β are the amplitude and phase aberrations in the pupil plane, i.e. in the DM plane.
- ϕ is the shape of the DM.
- C is the linear operator that takes the electric field from the DM plane to the electric field in the image plane over the region Ω (on practice C is a Fourier transform operation).

Using the first-order Taylor expansion of the DM effect and assuming small aberrations, we may write:

$$E_{cor} \approx \mathbb{C}\{Ae^{\alpha+i\beta}\} + i\mathbb{C}\{e^{\phi}\} = E_{ab} + i\mathbb{C}\{A\phi\} \tag{C.2}$$

where E_{ab} is the electric field in the image plane due to the static aberrations.

The term $C\{A\phi\}$ represents the effect of the DM shape on the electric field at the image plane. Considering this effect as the superposition of the influence functions of the DM it could be expressed as a linear operation:

$$\mathbb{C}\{A\phi\} = G\mathbf{a} \tag{C.3}$$

where a is the DM's actuator vector and G is a linear operator (corresponding to an interaction matrix between DM and the complex amplitude in the region Ω). Substituting this expression on equation C.2 and nulling the electric field over Ω, we could write:

$$G\mathbf{a} = iE_{ab} \tag{C.4}$$

Using the matrix formalism, the DM actuators vectors nulling the complex amplitude is given by:

$$C.4\mathbf{a} = \begin{pmatrix} \mathcal{R}\{G\} \\ \dots \\ \mathcal{I}\{G\} \end{pmatrix}^{-1} \begin{bmatrix} \mathcal{R}\{iE_{ab}\} \\ \dots \\ \mathcal{I}\{iE_{ab}\} \end{bmatrix} \tag{C.5}$$

where the first component is the inverted matrix G and the second component is the electric field in the region Ω expressed as a vector. For both components, the real and imaginary parts were separated to limit the solution to be real valued. Matrix G, being over-determined, it then requires an SVD inversion. Thus, the final solution minimize the total energy given by $||E_{ab} + iC\{\phi\}||^2$.

C.2 EFC estimation

To compute the DM actuator vector it is first necessary to estimate E_{ab}. The suited algorithm is based on pairs of images taken at the image plane using different DM configurations introducing a known complex amplitude, fixed a priori, over the region Ω of the focal plane.

Considering a DM configuration k producing a phase Φ_k, the electric field and the intensity produced in the final science camera plane are given by:

$$E_k \approx E_{ab} + i\mathbb{C}\{A\psi_k\} \tag{C.6}$$

$$I_k \approx \|E_{ab} + i\mathbb{C}\{A\psi_k\}\|^2 \tag{C.7}$$

Taking images in pairs with $+\Phi_k$ and $-\Phi_k$ the intensity of the images are related as:

$$I_k^+ - I_k^- = 4\mathcal{R}\{E_{ab}^* i\{A\psi_k\}\} \tag{C.8}$$

Taking several k pairs of images and considering each point of the region Ω , this relationship could be write on a matrix as:

$$\begin{bmatrix} I_1^+ - I_1^- \\ \vdots \\ I_k^+ - I_k^- \end{bmatrix} = 4 \begin{pmatrix} \mathcal{R}\{i\mathbb{C}\{A\psi_1\}\} & \mathcal{I}\{i\mathbb{C}\{A\psi_1\}\} \\ & \vdots \\ \mathcal{R}\{i\mathbb{C}\{A\psi_k\}\} & \mathcal{I}\{i\mathbb{C}\{A\psi_k\}\} \end{pmatrix} \begin{bmatrix} \mathcal{R}\{E_{ab}\}\vdots \\ \mathcal{I}\{E_{ab}\} \end{bmatrix} \tag{C.9}$$

The complex amplitude of the image plane is recovered inverting this relationship:

$$\underbrace{\begin{bmatrix} \mathcal{R}\{E_{ab}\}\vdots \\ \mathcal{I}\{E_{ab}\} \end{bmatrix}}_{\substack{\text{image plane CA of} \\ \text{the aberrated wavefront}}} = \frac{1}{4} \underbrace{\begin{pmatrix} \mathcal{R}\{i\mathbb{C}\{A\psi_1\}\} & \mathcal{I}\{i\mathbb{C}\{A\psi_1\}\} \\ & \vdots \\ \mathcal{R}\{i\mathbb{C}\{A\psi_k\}\} & \mathcal{I}\{i\mathbb{C}\{A\psi_k\}\} \end{pmatrix}^+}_{\substack{\text{image plane CA} \\ \text{produced by a known} \\ \text{phase in the DM}}} \underbrace{\begin{bmatrix} I_1^+ - I_1^- \\ \vdots \\ I_k^+ - I_k^- \end{bmatrix}}_{\substack{\text{Intensity images} \\ \text{in the science camera}}} \tag{C.10}$$

D

Acronyms

ADONIS ADaptive Optics Near Infrared System

AO Adaptive Optics

AGN Active Galactic Nuclei

APD Avalanche Photodiode

APLC Apodized Lyot Coronagraph

AR Anti-reflecting

AS Alternative Source

A4Q Achromatic four-quadrant phase mask Coronagraph

BLC Band-Limited coronagraph

BMM Boston Micro-deformable Mirror

BW Bandwidth

CA Complex Amplitude

CCD Electron Multiplying Charge Coupled Device

CH Channel

CL Close Loop

CLC Classical Lyot Coronagraph

COME-ON CGE-Observatoire de Meudon-Onera

CODE Corrective Optics Driver Electronics

CWS Curvature Wavefront Sensor

DBI Dual Band Imaging

DK Dark Hole

DM Deformable Mirror

DSP Digital Signal Processor

E-ELT European Extremely Large Telescope

EFC Electric Field Conjugation

EMCCD Electron Multiplying Charge Coupled Device

EPICS ExoPlanet imaging Camera and Spectrograph

ESO European Southern Observatory

FFT Fast Fourier Transform

FiS Field Stop

FLC Liquid Crystal polarization modulator

FoV Field of View

FPDP Front Panel Data Port

FPGA Field Programmable Gate Array

FQPM Four-quadrant phase mask

FWHM Full Width at Half Maximum

GALACSI Ground Atmospheric Layer Adaptive Corrector for Spectroscopic Imaging

GLAO Ground Layer Adaptive Optics

GPI Gemini planet finder

GRAAL GRound layer Adaptive optics Assisted by Lasers

GUI Graphical User Interface

HAWK-I Cryogenic widefield imager

HCI High Contrast Imaging

HKL House-keeping Link

HOT High Order Test-bench

HPF High-Pass Filter

HR HertzsprungRussell diagram

HSDL High Speed Data Link

HST Hubble Space Telescope

HVA High Voltage Amplifier

HWHM Half Width at Half Maximum

HWP Half-wave plate

IF Influence Function

IFS Integral Field Spectrograph

IM Interaction Matrix

IR Infrared

IRDIS Infrared Dualbeam Imager and Spectrograph

ISAAC Infrared Spectrometer And Array Camera

ITC Infrared Test Camera

IWA Inner Working Angle

K-L Karhuhen-Loeve

LA Lenslet Array

LBT Large Binocular Telescope

LGS Laser Guide Star

MACAO Multi-Application Curvature Adaptive Optics

MAD Multi-Conjugate Adaptive Optics Demonstrator

MCAO Multi-Conjugate Adaptive Optics

MDM Micro Deformable Mirror

MEMS Micro Electro-Mechanical Systems

MOAO Multi-Object Adaptive Optics

MOEMS Micro Opto-Electro-Mechanical Systems

MUSE Multi Unit Spectroscopic Explorer

NACO Naos - Conica

ND Neutral Density

NGS Natural Guide Star

NIR Near Infrared

n.u. Normalized Units

OD Optical density

OL Open loop

OPD Optical Path Difference

OSIRIS OH-Suppressing Infrared Integral Field Spectrograph

PPP Piston Phase Plate

PS Phase Screen

PSF Point Spread Function

PSD Power Spectral Density

PTV Peak-to-Valey

PWS Pyramid Wavefront Sensor

PZT Piezoelectric - Pb(Zr,Ti)O3

RMS Root Mean Square

RSD Real Slope Display

RTC Real Time Computing

RTD Real Time Display

RTF Rejection Transfer Function

RV Radial-Velocity

RV Residual Variance

SAXO Sphere Extreme Adaptive Optics

SCAO Single Conjugate adaptive optics

SCC Self-Coherent Camera

SF Spatial Filter

SFSHS Spatial Filter Shack-Hartmann Sensor

SHS Shack-Hartmann Sensor

SNR Signal to Noise Ratio

SOFI Son OF ISAAC, infrared spectrograph and imaging camera on the NTT

SPARTA Standard Platform for Adaptive optics Real Time Applications

SPHERE Spectro-polarimetric High-contrast Exoplanet REsearch

SPN Speckle Nulling

SR Strehl Ratio

SS Standard Source

SVD	Single Value Decomposition
TCP	Transmission Control Protocol
TT	Tip Tilt
TTM	Tip-Tilt Mount
VLT	Very Large Telescope
VLTI	Very Large Telescope Interferometer
WF	Wavefront
WFE	Wavefront Error
WFS	Wavefront Sensor
WPU	Weight Processing Unit
XAO	eXtreme Adaptive Optics
ZIMPOL	Zurich Imaging Polarimeter

Bibliography

[1] H. W. Babcock. The Possibility of Compensating Astronomical Seeing. *PASP*, 65:229–+, October 1953.

[2] K.-P. Markus. Overall science goals and top level AO requirements for the E-ELT. In *Adaptative Optics for Extremely Large Telescopes*, 2010.

[3] A. Lagrange and J. Beuzit. Future of Adaptive Optics on Single Aperture Telescopes. Astrophysical cases. In V. Coudé du Foresto, D. Rouan, & G. Rousset, editor, *Visions for Infrared Astronomy, Instrumentation, Mesure, Métrologie*, pages 163–171, 2006.

[4] B. Macintosh, M. Troy, R. Doyon, J. Graham, K. Baker, B. Bauman, C. Marois, D. Palmer, D. Phillion, L. Poyneer, I. Crossfield, P. Dumont, B. M. Levine, M. Shao, G. Serabyn, C. Shelton, G. Vasisht, J. K. Wallace, J.-F. Lavigne, P. Valee, N. Rowlands, K. Tam, and D. Hackett. Extreme adaptive optics for the Thirty Meter Telescope. volume 6272 of *Society of Photo-Optical Instrumentation Engineers (SPIE) Conference Series*, July 2006.

[5] R. Bacon and other 60 authors. Probing Unexplored Territories with MUSE: a Second-Generation Instrument for the VLT. *The Messenger*, 124:5–+, June 2006.

[6] C. Max, E. McGrath, D. Gavel, D. Le Mignant, P. Wizinowich, and R. Dekany. The science case for the Next Generation AO system at W. M. Keck Observatory. volume 7015 of *Society of Photo-Optical Instrumentation Engineers (SPIE) Conference Series*, July 2008.

[7] M. C. Liu. Astronomical science with laser guide star adaptive optics: a brief review, a current snapshot, and a bright future. volume 6272 of *Society of Photo-Optical Instrumentation Engineers (SPIE) Conference Series*, July 2006.

[8] F. Roddier (Ed.). *Adaptive optics in astronomy*. Cambridge University Press, 1999.

[9] J. W. Hardy. *Adaptive Optics for Astronomical Telescopes*. Oxford Series in Optical and imaging Science, July 1998.

[10] R. K. Tyson. *Principles of adaptive optics*. Academic Press, 1998.

[11] R. K. Tyson and B. W. Frazier. *Field guide to adaptive optics*. SPIE Press, 1998.

[12] J.C. Dainty. Adaptive Optics. In Torok, Peter and Kao, Fu-Jen, editor, *Optical Imaging and Microscopy*, volume 87 of *Springer Series in Optical Sciences*, pages 307–327. Springer Berlin / Heidelberg, 2007.

[13] N. Devaney. Review of astronomical adaptive optics systems and plans. volume 6584 of *Society of Photo-Optical Instrumentation Engineers (SPIE) Conference Series*, May 2007.

[14] N. Devaney. Adaptive Optics; Principles, Performance and Challenges. In R. Foy & F. C. Foy, editor, *NATO ASIB Proc. 198: Optics in astrophysics*, page 181, January 2005.

[15] P. Léna. Adaptive optics: a breakthrough in astronomy. *Experimental Astronomy*, 26:35–48, August 2009.

[16] H. I. Campbell and A. H. Greenaway. Wavefront Sensing: From Historical Roots to the State-of-the-Art. volume 22 of *EAS Publications Series*, pages 165–185, 2006.

[17] R. Ragazzoni. Pupil plane wavefront sensing with an oscillating prism. *Journal of Modern Optics*, 43:289–293, February 1996.

[18] R. Ragazzoni and J. Farinato. Sensitivity of a pyramidic Wave Front sensor in closed loop Adaptive Optics. *A&A*, 350:L23–L26, October 1999.

[19] J. B. Costa, R. Ragazzoni, A. Ghedina, M. Carbillet, C. Vérinaud, M. Feldt, S. Esposito, E. Puga, and J. Farinato. Is there need of any modulation in the pyramid wavefront sensor? In P. L. Wizinowich & D. Bonaccini, editor, *Society of Photo-Optical Instrumentation Engineers (SPIE) Conference Series*, volume 4839, pages 288–298, February 2003.

[20] F. Roddier and C. Roddier. Curvature sensing and compensation: a new concept in adaptive optics. In *Very Large Telescopes and their Instrumentation, Vol. 2*, volume 2, pages 667–673, October 1988.

[21] ME. Motamedi (Ed.). *MOEMS: Micro-Opto-Electro-Mechanical Systems*. SPIE Press, 2005.

[22] R. Krishnamoorthy Mali, T. G. Bifano, N. Vandelli, and M. N. Horenstein. Development of micro-electromechanical deformable mirrors for phase modulation of light. *Optical Engineering*, 36:542–548, February 1997.

[23] F. Zamkotsian. MOEMS, Micro-Optics for Astronomical Instrumentation. In R. Foy & F. C. Foy, editor, *NATO ASIB Proc. 198: Optics in astrophysics*, pages 107–+, January 2005.

[24] N. Hubin, B. L. Ellerbroek, R. Arsenault, R. M. Clare, R. Dekany, L. Gilles, M. Kasper, G. Herriot, M. Le Louarn, E. Marchetti, S. Oberti, J. Stoesz, J. P. Veran, and C. Vérinaud. Adaptive optics for Extremely Large Telescopes. In P. Whitelock, M. Dennefeld, & B. Leibundgut, editor, *The Scientific Requirements for Extremely Large Telescopes*, volume 232 of *IAU Symposium*, pages 60–85, 2006.

[25] M. Carbillet. Adaptive Optics for High-Contrast Imaging. volume 22 of *EAS Publications Series*, pages 121–138, 2006.

[26] B. A. Macintosh, S. S. Olivier, B. J. Bauman, J. M. Brase, E. Carr, C. J. Carrano, D. T. Gavel, C. E. Max, and J. Patience. Practical high-order adaptive optics systems for extrasolar planet searches. volume 4494 of *Society of Photo-Optical Instrumentation Engineers (SPIE) Conference Series*, pages 60–68, February 2002.

[27] K. Dohlen, M. Langlois, M. Saisse, L. Hill, A. Origne, M. Jacquet, C. Fabron, J.-C. Blanc, M. Llored, M. Carle, C. Moutou, A. Vigan, A. Boccaletti, M. Carbillet, D. Mouillet, and J.-L. Beuzit. The infra-red dual imaging and spectrograph for SPHERE: design and performance. In *Society of Photo-Optical Instrumentation Engineers (SPIE) Conference Series*, volume 7014 of *Society of Photo-Optical Instrumentation Engineers (SPIE) Conference Series*, August 2008.

[28] W.H. Smith. Spectral differential imaging detection of planets about nearby stars. *PASP*, 99:1344–1353, December 1987.

[29] R. U. Claudi, M. Turatto, R. G. Gratton, J. Antichi, M. Bonavita, P. Bruno, E. Cascone, V. De Caprio, S. Desidera, E. Giro, D. Mesa, S. Scuderi, K. Dohlen, J. L. Beuzit, and P. Puget. SPHERE IFS: the spectro differential imager of the VLT for exoplanets search. In *Society of Photo-Optical Instrumentation Engineers (SPIE) Conference Series*, volume 7014 of *Society of Photo-Optical Instrumentation Engineers (SPIE) Conference Series*, August 2008.

[30] S. Gladysz and J. C. Christou. Detection of Faint Companions through Stochastic Speckle Discrimination. *Ap.J*, 684:1486–1495, September 2008.

[31] G. Szymon, P. Martinez, and J. Aller-Carpentier, E. Christou. Statistical signal enhancement in adaptive-optics observations of exoplanets. page AOTuC2. Optical Society of America, 2009.

[32] O. Guyon. Limits of Adaptive Optics for High-Contrast Imaging. *Ap.J*, 629:592–614, August 2005.

[33] L. A. Poyneer and B. Macintosh. Spatially filtered wave-front sensor for high-order adaptive optics. *Journal of the Optical Society of America A*, 21:810–819, May 2004.

[34] C. Vérinaud, M. Le Louarn, V. Korkiakoski, and M. Carbillet. Adaptive optics for high-contrast imaging: pyramid sensor versus spatially filtered Shack-Hartmann sensor. *MNRAS*, 357:L26–L30, February 2005.

[35] A.-M. Lagrange, J.-L. Beuzit, G. Chauvin, and D. Mouillet. Adaptive optics and extrasolar planetary systems. In *Society of Photo-Optical Instrumentation Engineers (SPIE) Conference Series*, volume 7015, July 2008.

[36] C. Moutou. Ground-based direct imaging of exoplanets. Science objectives of extreme AO systems. volume 12 of *EAS Publications Series*, pages 337–345, 2004.

[37] C. Moutou, A.-M. Lagrange, J.-L. Beuzit, and D. Mouillet. Direct Detection of Exoplanets with Future Adaptive Optics Systems. In W. Brandner & M. E. Kasper, editor, *Science with Adaptive Optics*, pages 152–+, 2005.

[38] J.-L. Beuzit, M. Feldt, K. Dohlen, D. Mouillet, P. Puget, F. Wildi, L. Abe, J. Antichi, A. Baruffolo, P. Baudoz, A. Boccaletti, M. Carbillet, J. Charton, R. Claudi, M. Downing, C. Fabron, P. Feautrier, E. Fedrigo, T. Fusco, J.-L. Gach, R. Gratton, T. Henning, N. Hubin, F. Joos, M. Kasper, M. Langlois, R. Lenzen, C. Moutou, A. Pavlov, C. Petit, J. Pragt, P. Rabou, F. Rigal, R. Roelfsema, G. Rousset, M. Saisse, H.-M. Schmid, E. Stadler, C. Thalmann, M. Turatto, S. Udry, F. Vakili, and R. Waters. SPHERE: a planet finder instrument for the VLT. In *Society of Photo-Optical Instrumentation Engineers (SPIE) Conference Series*, volume 7014, August 2008.

[39] A.-M. Lagrange, D. Gratadour, G. Chauvin, T. Fusco, D. Ehrenreich, D. Mouillet, G. Rousset, D. Rouan, F. Allard, É. Gendron, J. Charton, L. Mugnier, P. Rabou, J. Montri, and F. Lacombe. A probable giant planet imaged in the β Pictoris disk. VLT/NaCo deep L'-band imaging. *A&A*, 493:L21–L25, January 2009.

[40] B. Macintosh, J. Graham, D. Palmer, R. Doyon, D. Gavel, J. Larkin, B. Oppenheimer, L. Saddlemyer, J. K. Wallace, B. Bauman, J. Evans, D. Erikson, K. Morzinski, D. Phillion, L. Poyneer, A. Sivaramakrishnan, R. Soummer, S. Thibault, and J.-P. Veran. The Gemini Planet Imager. volume 6272 of *Society of Photo-Optical Instrumentation Engineers (SPIE) Conference Series*, July 2006.

[41] M. Kasper, J.-L. Beuzit, C. Verinaud, R. G. Gratton, F. Kerber, N. Yaitskova, A. Boccaletti, N. Thatte, H. M. Schmid, C. Keller, P. Baudoz, L. Abe, E. Aller-Carpentier, J. Antichi, M. Bonavita, K. Dohlen, E. Fedrigo, H. Hanenburg, N. Hubin, R. Jager, V. Korkiakoski, P. Martinez, D. Mesa, O. Preis, P. Rabou, R. Roelfsema, G. Salter, M. Tecza, and L. Venema. EPICS: direct imaging of exoplanets with the E-ELT. volume 7735 of *Society of Photo-Optical Instrumentation Engineers (SPIE) Conference Series*, July 2010.

[42] E. Vernet, L. Jochum, P. La Penna, N. Hubin, R. Muradore, J. M. Casalta, I. Kjelberg, J.-C. Sinquin, F. Locre, P. Morin, R. Cousty, J.-M. Lurçon, J.-J. Roland, B. Crepy, E. Gabriel, R. Biasi, M. Andrighettoni, G. Angerer, D. Gallieni, M. Mantegazza, M. Tintori, E. Molinari, D. Tresoldi, G. Toso, P. Spanó, M. Riva, G. Crimi, A. Riccardi, G. Marque, J.-L. Carel, and E. Ruch. The field stabilization and adaptive optics mirrors for the European Extremely Large Telescope. volume 7015 of *Society of Photo-Optical Instrumentation Engineers (SPIE) Conference Series*, July 2008.

[43] P. Baudoz, A. Boccaletti, J. Baudrand, and D. Rouan. The Self-Coherent Camera: a new tool for planet detection. In C. Aime & F. Vakili, editor, *IAU Colloq. 200: Direct Imaging of Exoplanets: Science and Techniques*, pages 553–558, 2006.

[44] E. Vernet, M. Kasper, C. Vérinaud, E. Fedrigo, S. Tordo, N. Hubin, S. Esposito, E. Pinna, A. Puglisi, A. Tozzi, A. G. Basden, S. J. Goodsell, G. D. Love, and R. M. Myers. Extreme adaptive optics system optimization with the high order test bench. volume 6272 of *Society of Photo-Optical Instrumentation Engineers (SPIE) Conference Series*, July 2006.

[45] R. Arsenault, J. Alonso, H. Bonnet, J. Brynnel, B. Delabre, R. Donaldson, C. Dupuy, E. Fedrigo, J. Spyromilio, T. Erm, J. Farinato, N. Hubin, L. Ivanescu, M. Kasper, S. Oberti, J. Paufique, S. Rossi, S. Tordo, S. Stroebele, J.-L. Lizon, P. Gigan, F. Pouplard, F. Delplancke, A. Silber, M. Quattri, and R. Reiss. MACAO-VLTI first light: adaptive optics at the service of interferometry. *The Messenger*, 112:7–12, June 2003.

[46] C. Vérinaud and M. Kasper (App.). *High Order Testbench Experiment plan Overview*. HOT review. ESO internal documentation, 2006. VLT-TRE-ESO-14690-4081.

[47] M. Kasper and N. Hubin (App.). *High Order Testbench: Top Level Requirements*. HOT review. ESO internal documentation, 2006. VLT-TRE-ESO-14690-3414.

[48] E. Vernet and M. Kasper (App.). *High Order Testbench Assembly, Integration, Testing Plan and Results*. HOT review. ESO internal documentation, 2006. VLT-TRE-ESO-14690-4079.

[49] S. Tordo and R. Arsenault (App.). *Assembly Integration and test plans for MACAO-VLTI*. MACAO-VLTI Prelimary design review. ESO internal documentation, 2001. VLT-PLA-ESO-15600-2241.

[50] E. Vernet, C. Vérinaud, and M. Kasper (App.). *High Order Testbench Phase screens*. HOT review. ESO internal documentation, 2006. VLT-TRE-ESO-14690-3705.

[51] S. Tulloch and M. Kasper (App.). *High Order Testbench BMM Deformable Mirror Characterisation*. HOT review. ESO internal documentation, 2006. VLT-TRE-ESO-16100-4082.

[52] A. Basden. *Design of the Shack-Hartmann Wavefront Sensor for HOT*. HOT review. ESO internal documentation, 2006.

[53] S. Tulloch and M. Kasper (App.). *Andor iXON L3 Camera Characterisation*. HOT review. ESO internal documentation, 2006. VLT-TRE-ESO-16100-4083.

[54] E. Pinna, A. T. Puglisi, F. Quiros-Pacheco, L. Busoni, A. Tozzi, S. Esposito, E. Aller-Carpentier, and M. Kasper. The pyramid wavefront sensor for the high order testbench (HOT). In *Society of Photo-Optical Instrumentation Engineers (SPIE) Conference Series*, volume 7015 of *Presented at the Society of Photo-Optical Instrumentation Engineers (SPIE) Conference*, July 2008.

[55] S. Esposito, A. Tozzi, A. Puglisi, and Busoni S. *Pyramid wavefront sensor for HOT*. HOT review. ESO internal documentation, 2006.

[56] S. Esposito, A. Tozzi, D. Ferruzzi, M. Carbillet, A. Riccardi, L. Fini, C. Vérinaud, M. Accardo, G. Brusa, D. Gallieni, R. Biasi, C. Baffa, V. Biliotti, I. Foppiani, A. Puglisi, R. Ragazzoni, P. Ranfagni, P. Stefanini, P. Salinari, W. Seifert, and J. Storm. First Light Adaptive Optics System for Large Binocular Telescope. In P. L. Wizinowich & D. Bonaccini, editor, *Society of Photo-Optical Instrumentation Engineers (SPIE) Conference Series*, volume 4839 of *Presented at the Society of Photo-Optical Instrumentation Engineers (SPIE) Conference*, pages 164–173, February 2003.

[57] P. Martinez, E. Vernet, C. Dorrer, E. Aller Carpentier, A. Boccaletti, M. Kasper, J. Baudrand, and C. Chaumont. Phase and Lyot-type coronagraphs for the High Order Testbench: prototyping and first laboratory results. volume 7015 of *Society of Photo-Optical Instrumentation Engineers (SPIE) Conference Series*, July 2008.

[58] P. Martinez, C. Dorrer, E. Aller Carpentier, M. Kasper, A. Boccaletti, K. Dohlen, and N. Yaitskova. Design, analysis, and testing of a microdot apodizer for the Apodized Pupil Lyot Coronagraph. *A&A*, 495:363–370, February 2009.

[59] P. Martinez, C. Dorrer, E. Aller-Carpentier, M. Kasper, A. Boccaletti, and K. Dohlen. Halftoning for High-contrast Imaging: Developments for the SPHERE and EPICS Instruments. *The Messenger*, 137:18–23, September 2009.

[60] P. Martinez, C. Dorrer, M. Kasper, A. Boccaletti, and K. Dohlen. Design, analysis, and testing of a microdot apodizer for the apodized pupil Lyot coronagraph. II. Impact of the dot size. *A&A*, 500:1281–1285, June 2009.

[61] E. Fedrigo and M. Kasper (App.). *SPARTA for HOT Conceptual Design*. HOT review. ESO internal documentation, 2006. VLT-TRE-ESO-16100-3983.

[62] E. Aller-Carpentier, M. Kasper, P. Martinez, E. Vernet, E. Fedrigo, C. Soenke, S. Tordo, N. Hubin, C. Verinaud, S. Esposito, E. Pinna, A. Puglisi, A. Tozzi, F. Quiros, A. G. Basden, S. J. Goodsell, G. D. Love, and R. M. Myers. High order test bench for extreme adaptive optics system optimization. In *Society of Photo-Optical Instrumentation Engineers (SPIE) Conference Series*, volume 7015, July 2008.

[63] E. Aller-Carpentier and M. Kasper (App.). *SHS and Pyramid comparison test report*. FP6-OPTICON-JRA1 deliverable documentation. ESO internal documentation, 2009. VLT-TRE-ESO-14690-4724.

[64] H. R. Shea, A. Gasparyan, C. D. White, R. B. Comizzoli, D. Abusch-Magder, and S. C. Arney. Anodic oxidation and reliability of MEMS polysilicon electrodes at high relative humidity and high voltages. volume 4180 of *Society of Photo-Optical Instrumentation Engineers (SPIE) Conference Series*, pages 117–122, August 2000.

[65] H. R. Shea, A. Gasparyan, Ho Bun Chan, S. Arney, R.E. S., D. Lopez, Sungho Jin, and R.P. McConnell. Effects of electrical leakage currents on MEMS reliability and performance. volume 4180 of *Device and Materials Reliability, IEEE Transactions on*, pages 198–207, June 2004.

[66] J.-M. Conan, G. Rousset, and P.-Y. Madec. Wave-front temporal spectra in high-resolution imaging through turbulence. *Journal of the Optical Society of America A*, 12:1559–1570, July 1995.

[67] E. Gendron and P. Lena. Astronomical adaptive optics. II. Experimental results of an optimized modal control. *A&A S.*, 111:153–+, May 1995.

[68] E. Gendron. *Optimization de la commande modale en optique adaptative: applications a l'astronomie.* PhD thesis, Universite Denis Diderot - Paris VII, 1995.

[69] J-M Conan. *Etude de la correction partielle en optique adaptative.* PhD thesis, Universite de Paris-Sud (X1 Orsay) - U.F.R. Scientific d'Orsay, 1994.

[70] T. Fusco, G. Rousset, D. Rabaud, E. Gendron, D Mouillet, F. Lacombe, G. Zins, P-Y. Madec, A-M. Lagrange, Charton J., D. Rouan, N. Hubin, and N. Ageorges. Naos on-line characterization of turbulence parameters and adaptive optics performance. *Journal of Optics A: Pure and Applied Optics*, 6(6):585, 2004.

[71] G. I. Taylor. The Spectrum of Turbulence. *Royal Society of London Proceedings Series A*, 164:476–490, February 1938.

[72] E. Gendron and P. Léna. Single Layer Atmospheric Turbulence Demonstrated by Adaptive Optics Observations. *Ap&SS*, 239:221–228, September 1996.

[73] J.-L. Beuzit, L. Demailly, E. Gendron, P. Gigan, F. Lacombe, D. Rouan, N. Hubin, D. Bonaccini, E. Prieto, F. Chazallet, D. Rabaud, P.-Y. Madec, G. Rousset, R. Hofmann, and F. Eisenhauer. Adaptive Optics on a 3.6-Meter Telescope. The ADONIS System. *Experimental Astronomy*, 7:285–292, 1997.

[74] R. Arsenault, D. A. Salmon, J. M. Kerr, F. J. Rigaut, D. Crampton, and W. A. Grundmann. PUEO: the Canada-France-Hawaii Telescope adaptive optics bonnette I: system description. volume 2201 of *Presented at the Society of Photo-Optical Instrumentation Engineers (SPIE) Conference*, pages 833–842, May 1994.

[75] M. Kasper, E. Fedrigo, D. P. Looze, H. Bonnet, L. Ivanescu, and S. Oberti. Fast calibration of high-order adaptive optics systems. *Journal of the Optical Society of America A*, 21:1004–1008, June 2004.

[76] S. Esposito, E. Riccardi, F. Quiros-Pacheco, E. Pinna, A. Puglisi, M. Xompero, Briguglio R., Busoni L., Fini F., Stefanini P., Brusa G., Tozzi A., Ranfagni P., Pieralli F., Guerra J.G., Arcidiacono C., and Salinari P. Laboratory characterization and performance of the high-order AO system for the LBT telescope. *Journal of the Optical Society of America A*, 2010. Accepted for publicaction.

[77] T. Fusco and J. Charton (App.). *Sphere AO analysis report*. SPHERE final design review. ESO internal documentation, 2007. VLT-TRE-SPH-14690-0248.

[78] O. Lai, P. J. Stomski, and E. Gendron. MANO: the modal analysis and noise optimization program for the W.M. Keck Observatory adaptive optics system. In P. L. Wizinowich, editor, *Society of Photo-Optical Instrumentation Engineers (SPIE) Conference Series*, volume 4007 of *Presented at*

the Society of Photo-Optical Instrumentation Engineers (SPIE) Conference, pages 620–631, July 2000.

[79] P. Martinez and M. Kasper (App.). *Coronagraphs Test Report*. FP6-European Extremely Large Telescope design study documentation . ESO internal documentation, 2009. ELT-TRE-INS-04500.

[80] P. Martinez, E. Aller-Carpentier, and M. Kasper. Laboratory Demonstration of Efficient XAO Coronagraphy in the Context of SPHERE. *PASP*, 122:916–923, August 2010.

[81] N. Yaitskova and C. Verinaud. Adaptive optics correction of the wavefront distortions induced by segments misalignment in Extremely Large Telescope. volume 6267 of *Society of Photo-Optical Instrumentation Engineers (SPIE) Conference Series*, July 2006.

[82] E. Aller-Carpentier, M. Kasper, and P. Martinez. Segment phasing experiments on the High Order Test bench. In *Adaptative Optics for Extremely Large Telescopes*, 2010.

[83] A. Give'on, B. Kern, S. Shaklan, D. C. Moody, and L. Pueyo. Broadband wavefront correction algorithm for high-contrast imaging systems. volume 6691 of *Society of Photo-Optical Instrumentation Engineers (SPIE) Conference Series*, September 2007.

[84] P. Aller-Carpentier, J Antichi, and M. Kasper (App.). *XAO and wave-front control experiment reports*. EPICS phase A study review. ESO internal documentation, 2010. E-TRE-ESO-556-0629.

[85] O. Guyon, E. Pluzhnik, F. Martinache, J. Totems, S. Tanaka, T. Matsuo, C. Blain, and R. Belikov. High-Contrast Imaging and Wavefront Control with a PIAA Coronagraph: Laboratory System Validation. *PASP*, 122:71–84, January 2010.

[86] R. Arsenault, P.-Y. Madec, N. Hubin, J. Paufique, S. Stroebele, C. Soenke, R. Donaldson, E. Fedrigo, S. Oberti, S. Tordo, M. Downing, M. Kiekebusch, R. Conzelmann, M. Duchateau, A. Jost, W. Hackenberg, D. Bonaccini Calia, B. Delabre, R. Stuik, R. Biasi, D. Gallieni, P. Lazzarini, M. Lelouarn, and A. Glindeman. ESO adaptive optics facility. In *Society of Photo-Optical Instrumentation Engineers (SPIE) Conference Series*, volume 7015 of *Society of Photo-Optical Instrumentation Engineers (SPIE) Conference Series*, July 2008.

[87] M. Kasper and N. Hubin (App.). *High Order Testbench Design Report*. HOT review. ESO internal documentation, 2006. VLT-TRE-ESO-14690-3857.

[88] C. Vérinaud and M. Kasper (App.). *High Order Testbench Simulations*. HOT review. ESO internal documentation, 2006. VLT-TRE-ESO-14690-4080.

[89] E. Gendron and P. Lena. Astronomical adaptive optics. 1: Modal control optimization. *A&A*, 291:337–347, November 1994.